Università Politecnica delle Marche
Scuola di Dottorato di Ricerca in Scienze dell'Ingegneria
Curriculum in Meccanica

Clustering Inverse Beamforming and multi-domain acoustic imaging approaches for vehicles NVH

Ph.D. Dissertation of:

Claudio Colangeli

Advisor:

Prof. Paolo Castellini

Co-advisors:

Dr. Karl Janssens

Dr. Paolo Chiariotti

XV edition - new series

Università Politecnica delle Marche
Scuola di Dottorato di Ricerca in Scienze dell'Ingegneria
Curriculum in Meccanica

Clustering Inverse Beamforming and multi-domain acoustic imaging approaches for vehicles NVH

Ph.D. Dissertation of:

Claudio Colangeli

Advisor:

Prof. Paolo Castellini

Co-advisors:

Dr. Karl Janssens

Dr. Paolo Chiariotti

XV edition - new series

Università Politecnica delle Marche
Dipartimento di Ingegneria Industriale e Scienze Matematiche
Via Brecce Bianche — 60131 - Ancona, Italy

“Io e’ compagni eravam vecchi e tardi
quando venimmo a quella foce stretta
dov’Ercule segnò li suoi riguardi,

acciò che l’uom più oltre non si metta:
da la man destra mi lasciai Sibilia,
da l’altra già m’avea lasciata Setta.”

Dante Alighieri
Inferno, Canto XXVI

“…quando c’è bisogno non solo di intelligenza agile e di spirito versatile, ma di volontà ferma, di persistenza e di resistenza, io mi sono detto a voce alta: tu sei abruzzese!”

Benedetto Croce

to Gabriele
and to all the dreams broken up there in Rigopiano

Acknowledgements

Once upon a time, in a far, far land, called Farindola, a young man, with no high education, sold part of the flock of sheeps he had, to let his boy continuing his studies. That man was my great grandfather. That boy: my grandfather. The boy grew up and became a teacher. He married a charming woman from the south of Italy. After the second world war was ended, they gave birth to my father. He became a teacher, too.

And here I am. I wish to start my acknowledgements giving to my history its fair share of merit. I wish, therefore, to thank my great grandfather, who lived before the “Europe” that we know today had been even imagined. I wish to thank him, first, because he filled my pen with ink and my soul with dreams. And, together with him, I wish to thank all those simple men and women who resisted the darkness of their hard times and fought so hard for a peaceful and united Europe. Without them my research was not even imaginable.

And here I am. This time for real. I have a long list of people, places, ideas, dreams, tastes, flavours, sounds, etc., to thank and I would never be able to name them all. But first things first: my first passionate, moved and sincere thought of gratitude goes to my girlfriend, soon to be wife, Sara. I wish her to know that, besides being an amazing woman, she’s the engine of my passions, the spark of my intuitions, the muse of my inspirations. I know, dear reader, what you are thinking: that it is unfair to thank her before my parents. Perhaps you’re right, but I did it on purpose: to tell to my beloved parents that they did a great job with me, accomplishing the mission that every parent wish to accomplish: let their children grow strong and happy so that, one day, they will be able to find their way to happiness and make the World a better place. And of course, when that happens, all dads and moms on Earth hope that their grown kids turn back and look with gratitude to who made their life possible. For this reason, dear Mom and Dad, I look back to you to thank you, from the deep of my heart, for so many things…but above all for the following three gifts you gave me: faith, trust in people and curiosity. Curiosity for every little thing! Well…and of course thank you for another priceless gift: my brother, Giorgio. The solid rock! One of my few reference points. My example of life, my wing.

I have at least two more families to thank: the one that I found in Ancona and the one that I found in Leuven. I don’t want to let anybody out of these thoughts. Therefore I won’t name anybody, but I will give you two pictures instead. Picture this: …it’s kind of late in the evening, but there’s still some light, it’s summer and it’s warm. Everything went wrong, today, or maybe everything was good…it doesn’t really matter. We are seated in front of the sea. We don’t speak that much, we just enjoy the beauty of what we see, the sound of the waves, the call of the seagulls. Splash! If you can picture this, well: you’re family! Now picture this: …we’re riding on our bikes. It’s kind of late in the evening. Everything went wrong, today, or maybe everything was good. It doesn’t matter. The air is not so warm anymore, but that freshness is regenerative, liberating. We watch the sunset while laying on the grass. We walk home. We talk about the future, the past, silly stuff,… It gets dark, then it gets very late. “See you tomorrow!”. If you can picture this, then you’re family!

As you can imagine, dear reader, during my years of Ph.D. research I have benefited from the support of many scientific guides. Many mentors, many brilliant minds and bright

examples of excellent women and man and of passionate researchers. To each of them goes my deep gratitude. Forever. I'll mention some, in particular, to name the quality that, in them, I admire the most. Since romance is not (yet) dead, let me start with a lady: I'd like to thank Prof. Milena Martarelli because she was my first example of passionate researcher. She believed in me. She was the one who teached me all about signal processing for the first time. A special thought of gratitude goes to the advisor of my thesis, Prof. Paolo Castellini, for instilling in me the profound convinction that "progress is better than perfection". There would be no words to thank enough Dr. Karl Janssens. Long before being the co-advisor of my thesis, before being my boss at work, besides being an excellent manager and a brilliant mind, I wish to thank Karl for his incredible capability of pulling the good out of people. Including myself. For having taught me how to turn my weaknesses into strengths. Finally, for having taught me the value of being critic, but not ruthless; determined but not ambitious; pragmatic but never superficial. I'd like, moreover, to thank my other co-advisor, Paolo Chiariotti, for his priceless support and for his curiosity and precious contribution towards every technical detail of my research work. But most of all I'd like to thank Paolo for his friendship and for having taught me the value of persistence and commitment. Like he'd say: "no pain, no gain!".
Among the many brilliant members of the scientific community, to which I, humbly, belong, there are several persons to whom I owe a lot of what I managed to accomplish so far and in particular in this thesis. In many cases, in fact, meeting them inspired good ideas and fruitful research pathways to follow. In some cases, on the contrary, I had the chance to realise how stupid and ruthless people can become when they are not moved by curiosity and passion, but rather by fear and pride. These (few,) were priceless experiences, too.
Last, but absolutely not least, I'd like to express my sincere gratitude to the reviewers of my Ph.D. manuscript: Prof. Jérôme Antoni and Prof. Wim De Roeck. Their opinion, their interest on the subjects that I have proposed and their constructive remarks are the best reward for all my efforts in writing it. I'd like to address a few more special words to Prof. Antoni to thank him for his wise advices and, most importantly, to thank him for being a brilliant example of a scientist animated by insatiable curiosity and intellectual vitality. I sincerely hope that our scientific trajectories will have many chances to cross again in the future.
To conclude this little and completely insufficient compendium of acknowledgments, I'd like to thank each single travelling companion that I met during the last three amazing years. It might be trivial to say, but it is true: I am made of all those hands that I have shaken, the smiles that I have received, the thoughts, fears and hopes that I have been sharing. I will always carry them with me, in the jurney of my life. Finally: thanks to The Rolling Stones, the AC/DC, The Beatles, the Pink Floyd, Eric Clapton, Etta James, The Guns n'roses, Norah Jones, The Eagles, The Doors, BB King, Buddy Guy, Stevie Ray Vaughan, The Queen, the birds in the morning and the neighbours at night,… for having been, of this jurney, the soundtrack.

Claudio

This work was supported by the Marie Curie ITN project ENHANCED (joined Experimental and Numerical methods for HumAN CEntered interior noise Design). The project has received funding from the European Union Seventh Framework Programme under grant agreement n° 606800. The whole consortium is gratefully acknowledged.

Abstract

The interior sound perceived in vehicle cabins is a very important attribute for the user. This implies that the study of the acoustic and vibration performance of a vehicle should be considered since the early stages of the design. Experimental methods have a key role both in helping validating the modelling and the virtual prototyping of the designed vehicles and in troubleshooting, understanding causes and effects of noise and vibration problems occurring inside the vehicle enclosure. Acoustic imaging and sound source localization methods such as beamforming and Near-field Acoustic Holography are used in vehicles NVH because they are capable of locating and ranking the noise sources contributing to the overall noise perceived inside the cabin. However these techniques are often relegated to the troubleshooting phase, thus requiring additional experiments for more detailed NVH analyses. It is therefore desirable that such methods evolve towards more refined solutions capable of providing a larger and more detailed amount of information. In order to meet these requirements, this thesis proposes a modular and multi-domain approach involving direct and inverse acoustic imaging techniques. These techniques are combined with pre- and post- processing algorithms for providing quantitative and accurate results in frequency, time and angle domain, thus targeting relevant types of problems in vehicles NVH such as the identification of interior and exterior (affecting interior noise) noise sources and the analysis of noise sources produced by rotating machines such as internal combustion engines. In this framework, an improved version of Generalized Inverse Beamforming algorithm, working in frequency domain, is presented. The improvement raises from the exploitation of PCA-based adaptive pre- processing yielding larger dynamic range and better performance in terms of source quantification. A criterion for the separation of the sought sources into uncorrelated distributions is also presented. The core finding of this thesis is represented by a novel inverse acoustic imaging method working in frequency domain, named Clustering Inverse Beamforming (CIB). The method grounds on a statistical processing based on an Equivalent Source Method formulation. In this way, an accurate localization, a reliable ranking of the identified sources and their separation into uncorrelated phenomena, thanks to a new entity called clustering mask matrix, is obtained. The clustering mask matrix is a function defined in the source region whose values, ranging from 0 to 1, can be interpreted as the confidence level of finding a sought physical source in the corresponding location. The CIB approach is validated on several simulated and real experiments. The clustering mask matrix is also exploited in this work for scaling the under-determined inverse acoustic problem up to an equivalent over determined version, allowing the reconstruction of the time evolution of the sources sought. It has limited effect in presence of distributed sources and spatially joint uncorrelated sources. Finally a methodology for decomposing the acoustic image of the sound field generated by a rotating machine as a function of the angular evolution of the machine shaft is proposed. The approach is validated on simulated data for several operating conditions with promising results. This set of findings aims at contributing to the advent of a new paradigm of acoustic imaging applications in vehicles NVH, supporting all the stages of the vehicle design with time-saving and cost-efficient experimental techniques.

Contents

List of Figures

List of Tables

Chapter 1.

Introduction

The ambition of this thesis work is contributing to the advent of a new paradigm of acoustic imaging applications in vehicles NVH. The acronym NVH stays for: Noise, Vibration and Harshness. This discipline studies acoustic and vibratory problems in industry. It plays a key role in the design and development of performing and comfortable vehicles for ground/air/marine transportation. In fact, thanks to NVH, the manifold causes of noise and vibration affecting the passengers' comfort can be taken into account and tackled since the earliest stages of the design of the vehicle, granting an harmonious development of the assembly combining sound and vibration quality with the required performance. In-vehicle acoustic discomfort can be due to causes that occur at the exterior or at the interior of the vehicle's cabin. In general it is easier, in the design process, to optimize and reduce as much as possible the NVH problems due to interior components because their behaviour is controllable and their influence more predictable. On the contrary, the exterior causes of noise and vibration problems, affecting the in-vehicle passengers experience, are very often due to complex mechanisms of propagation from the exterior towards the interior and/or to the interaction of the vehicle with the external environment. The latter cause is less predictable and controllable. For this reason exterior sources affecting the in-vehicle noise and vibration must be studied with particular effort.
This document will mainly focus on the noise issues caused by exterior phenomena and in particular on the experimental techniques that can help the localization task, i.e. to answer the question: "where the noise sources come from?" A first answer can be obtained by classifying the category of potential exterior noise sources. Taking, from now on, the example of cars, the main exterior noise sources are:

- Road noise: due to the interaction of the tires and the road.
- Wind noise: due to the air flow impinging on the vehicles structure.
- Engine noise: due to the functioning of the engine. Typical components are: combustion noise, mechanical noise due to the rotating elements, etc.

The interior sound perceived in an automotive cabin is a very important attribute in vehicle engineering. This implies that the study of the acoustic and vibration performance of a vehicle should be considered since the early stages of the design. If not, making changes on the product would become more expensive and of limited options. In order to perform a early study of the acoustic and vibration performance of the vehicle, the ideal would be being able to predict the behavior of the product with simulation models. To understand the modelling challenges and improve the modelling know-how, experimental acoustic methods play an important role. Moreover, experimental methods are instrumental also for

troubleshooting and for understanding both the causes – paths - and the effects – sources - of the noise and vibration problems occurring inside a vehicle cabin.
The main techniques that serve these needs are:

- Acoustic imaging techniques, capable of locating and quantifying the noise sources contributing to the overall noise level inside a vehicle.
- Transfer Path Analysis (TPA), that is able to assess the possible ways of energy transfer from the various causes of noise and vibration and to evaluate their individual effects at a given target location providing insight into the mechanisms responsible for the problems.
- Acoustic Modal Analysis (AMA), that relates the acoustic response to the intrinsic system behaviour of the car cabin.

Without using these techniques, the only option - which was actually the one used in the past - to reduce the noise and vibration issues occurring in a vehicle's cabin prototype is the so-called "masking" method. This approach consists in covering all the interior surfaces with acoustic absorbing material and to uncover the target regions sequentially, in order to evaluate the contribution to the overall noise level of each single region. The "masking" method allows only qualitative results and only in a very advanced stage of the vehicle's production cycle. The synergy between AMA, TPA and acoustic imaging, on the contrary, makes it possible to predict the acoustic behaviour of the car cabin since the early stages of its design. This is particularly due to the exploitation of simulation models that can be made more and more reliable through the updating processes linked to AMA [1]. The use of TPA and advanced acoustic imaging techniques allows analysing the (virtual or real) prototype of the vehicle's cabin giving to the designer a deep insight about the mechanisms that generates the observed noise and vibration problems, thus easing their solutions.

This thesis proposes a modular and multi-domain (frequency, time and angle domain) approach to acoustic imaging for advanced vehicles NVH analyses pursuing time and economical efficiency.
Acoustic imaging techniques such as beamforming and Near-field Acoustic Holography are considered robust and simple experimental tools. However, due to their limitations, they have been often relegated to troubleshooting and qualitative studies in vehicles and in particular in automotive NVH. This limited exploitability makes the use of these techniques not always convenient compared to the costs of the equipment and the human effort required to conduct the tests. It is therefore desirable that such methods evolve towards more refined solutions capable of providing a larger and more detailed amount of information. If on the one hand this must be pursued by enhancing the single acoustic imaging approaches, on the other hand it is important to improve the synergy between acoustic imaging and other NVH techniques (such as TPA, AMA, Sound Quality assessment, etc.) oriented to the design of multi-purpose test setups and the modular exploitation of the results of each analysis. For the sake of time and economic efficiency, another requirement to this new paradigm of NVH experimental analyses is the possibility, on the one hand, to apply multiple techniques at the same time adopting the same

experimental setup and on the other hand adopting the same technique with similar equipment, but on different configurations and application cases. Such solutions would improve the effectiveness of acoustic imaging in the vehicle NVH development process ([2, 3] Fig. 1. 1).

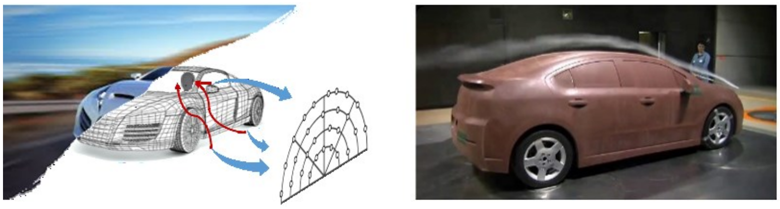

Fig. 1. 1 : towards virtual prototyping of the acoustic package of a vehicle.

The ideas reported in this thesis have been conceived with this paradigm in mind. Three experimental contexts, where improved acoustic imaging solutions can be beneficially exploited, have been targeted: study of exterior sources affecting in-vehicle noise, interior noise sources identification and components noise assessment. The information obtained through such acoustic imaging applications may serve several other NVH analyses. To give some examples: the accurate identification of the spectra of the exterior noise sources affecting in-vehicle noise and/or of the interior sources allow the estimate of their partial contribution to the driver (dis)comfort adopting source-transfer-receiver-based methods.

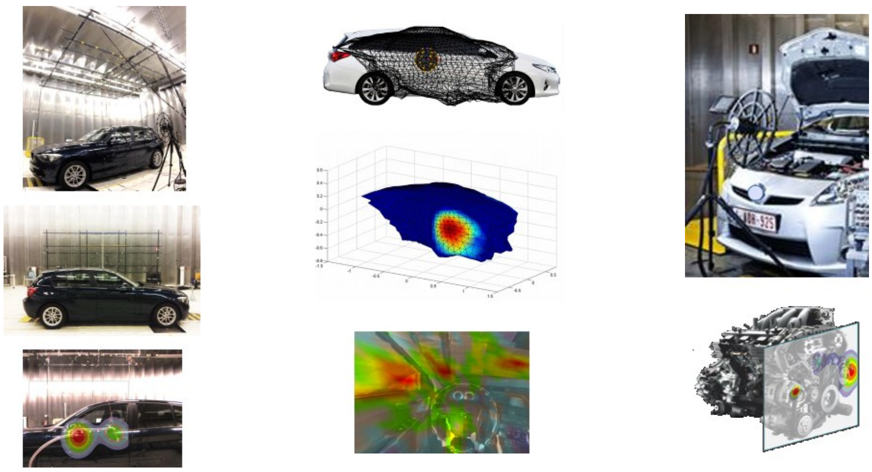

(a) *(b)* *(c)*

Fig. 1. 2 : acoustic imaging in automotive. Applications to (a): exterior, (b): interior and (c): components noise sources identification.

The availability of the time evolution of such noise sources enable auralization and Sound Quality studies. The decomposition into their angular evolution over the cycle of the engine would help understanding the mechanism of generation of the noise sources produced by ICE, etc. This variety of desiderata suggests to tune the type of acoustic imaging analysis on the specific information required. In order to do so, a multi-domain framework has been imagined in which frequency-based, time-based and angle-based techniques have been developed to be chosen, modularly, according to the problem under study.

1.1. Literature survey

Among the manifold techniques suitable for the localization of exterior sources affecting in-vehicle noise, in this document we will focus on the acoustic imaging methods involving microphone arrays, thus leaving apart the ones based on Sound Intensity measurements [4]. For this purpose a state-of-the-art overview about the main acoustic imaging techniques will be given in paragraphs 1.1.1 and 1.1.2. The more experienced readers will find in these paragraphs a comprehensive overview of the main references in the domain, accompanied with a brief discussion of the mentioned acoustic imaging methods. The non-initiated readers can refer to section 1.2 for a better understanding of the more fundamental aspects related to acoustic imaging. Moreover, despite they will not be explicitly treated in this thesis, for the sake of clearness and completeness a short description of the main literature available regarding TPA and AMA will be given in paragraphs 1.1.3 and 1.1.4 respectively.

1.1.1. Exterior acoustic imaging

Acoustic imaging techniques are used for localizing and ranking (based on their strength) the noise sources active in the acoustic field under study. A typical acoustic imaging experimental setup involves the presence of an array of microphones that can be placed at large distance with respect to the object under study - far-filed beamforming - in the proximity of the object - Near-field Acoustic Holography (NAH), Inverse Boundary Element Method (IBEM) - and/or in enclosures such as vehicle cabins, rooms, etc… In the latter case, literature often refers to interior beamforming. Such techniques divide into two main categories: direct methods and inverse methods. A systematic definition of the two categories is given by Leclère et al. in [5]. In the case of a direct method the location/strength of each source is identified independently from the others by scanning over the source area covering the location of potential sources and assigning to each of them a strength as a function of position and of course the microphones signals. Inverse methods are considering the problem for all sources at once. In this way the interference between potential coherent sources is taken into account. The main drawback is that inverse methods are more sensitive to noise and to numerical instabilities.
The shape of the array and the geometrical placement of the microphones on the array depend on the application pursued and on the type of processing algorithm used. Some examples are the following. Regular (equally spacing between microphones) arrays are used in the case of NAH based on 2D spatial Fourier transform (see references [6] and [7]). Planar optimized shapes (i.e. spiral, wheel, half-wheel, cross/star shapes, etc…) are mainly

used for far-field applications when adopting those beamforming techniques falling into the category of direct methods. Spherical distributions (open sphere or rigid scattering sphere) are more suited for interior applications. When adopting inverse methods the influence of the shape of the array is less dramatic and, at least theoretically, there is no influence on the accuracy in the results as a function of frequency. In this case, irregular and randomly spaced microphone distributions are the most adopted.

Among the direct methods, the algorithms working in frequency domain descending from the so-called Conventional Beamforming (CB) are the most used. The working principle of the CB algorithm consists in scanning the source area by means of "steering vectors" (see [8] and [9]) applied to the Cross-Spectral Matrix (CSM) estimated between the signals recorded by the microphone array. This idea has been conceived for the first time, and formalized in both time domain and frequency domain, by Billingsley et Al. in 1974-1976 under the name of "the acoustic telescope" ([10], as reported also in [11]) and Fisher et Al. in 1977 under the definition of "polar correlation" and applied to jet engine noise (see references [12] and [13]). CB presents some intrinsic limitations related to the fact that the acoustic sources active at the calculation plane appear in the beamforming output not as clean beams, but rather contaminated by corresponding Point Spread Functions (PSFs). A PSF is the spatial impulse response of the beamformer to an acoustic source in a specific source location, "observed" by a specific microphone array. A typical PSF presents a main lobe in correspondence of the theoretical location of the acoustic source and sidelobes elsewhere. Such sidelobes degrade the beamforming output and make the acoustic map difficult to interpret. In order to overcome such limitations advanced approaches have been lately developed. Among them it is worth mentioning: the Functional Beamforming (FB) [14], deconvolution methods such as CLEAN and its evolutions (i.e. PSF-CLEAN, CLEAN-SC, HR-CLEAN-SC) [15, 16], DAMAS and its evolutions (i.e. DAMAS2, DAMAS3,…) [17, 18, 19, 20], the Non Negative Least Square approaches (NNLS, FFT-NNLS) [21], the deconvolution methods based on the Richardson-Lucy (RL) algorithm [22, 23, 24], etc. Functional Beamforming aims at eliminating the sidelobes by adopting a modified CSM which is manipulated by raising it to the power of an exponent parameter. All the deconvolution methods aim at removing the unwanted effect of the sidelobes by iteratively removing the PSFs from the beamforming map calculated by means of CB in order to improve the spatial resolution, to increase the dynamic range and better quantifying the source strengths (methods for quantification of the source strengths after deconvolution are described in [9] and [17]). For a comparison of their performance the interested reader can refer to [25] where different versions of DAMAS, NNLS and CLEAN have been described and compared with the aim of giving guidelines on their application. A similar work has been presented by Ehrenfried and Koop in [26] where the authors compare the DAMAS2 algorithm to DAMAS, NNLS and RL algorithms in term of computational effort, sensitivity to noise and robustness to user-dependent parameters such as the number of iterations to set. Yardibi et Al. give, in reference [27], a systematic comparison of DAMAS and CLEAN-SC in terms of the estimation of the absolute signal power of the sources, capability of identifying correlated and uncorrelated sources and computational effort. Another approach that completes the panorama of the deconvolution methods is the so-called Localization and Optimization of Array REsults (LORE) whose main idea, described in reference [28], consists in recognising patterns in the beamformed outputs (obtained with CB) and relating them to the noise sources that would produce the map. Since most of the deconvolution methods involve the solution of an inverse problem after the direct CB step, they are sometimes classified as inverse methods (see for example: [11]). In this thesis they are still considered as direct methods because they all start from a so-called "dirty map" computed by means of CB. This implies that the scanning of the acoustic scene requires the assumption that all the scanned points are assumed to be incoherent sources that emit sound independently. This is a big limitation when dealing with correlated and/or distributed sources as pointed out by Chu and Yang in [25]. Moreover the CB processing intrinsically implies the presence of Point Spread Functions, requiring deconvolution for obtaining clean maps. These are the aspects that encourages the use of different philosophies for acoustic imaging which are not affected by such limitations, such as inverse methods.

All inverse methods have in common the idea of finding the best linear combination of sources that reconstruct the measured pressure distribution at the array level in an optimal way. Contrarily to direct methods, inverse methods are intrinsically able to deal with correlated as well as uncorrelated source distributions, and with sparse as well as spatially-distributed acoustic sources (see for example [29]). This versatility explains the reason of their use and the increasing interest in their development. The choice of the nature of sources, the implementation of the inversion of the acoustic problem and the geometry of the problem will define different methods in literature. Relevant examples are IBEM and Equivalent Source Methods (ESM). IBEM [30, 31] uses functions obtained adopting the Boundary Element Method for formulating the radiation problem, therefore relates the acoustic field at a certain region in space with the vibration velocity of an emitting object. The ESM replaces the emitting object with a cloud of monopoles (equivalent, or elementary, sources) and assigns to each elementary source the proper strength and phase relationship, required to match the acoustic field sampled at the measurement plane by the microphone array [32]. Under the category of ESM several methods can be accounted. The nomenclature is not unified because historically such methods have been developed by many scientific communities with slightly different purposes. To give some examples: the irregular NAH [33] is an ESM applied in the near-field; the Airborne Source Quantification (ASQ) [34] or the Inverse FRF (IFRF) method [35] are techniques adopted in cases in which the inverse acoustic problem is not severely under-determined (see also: [32]); the Generalized Inverse Beamforming (GIBF) [36, 37, 38, 39], generally applied in far-field applications, solves severely under-determined inverse acoustic problems by multiple iterations. And they can all be considered ESM. In the case of GIBF at each iteration the number of equivalent sources describing the acoustic scene is reduced according to a wanted criterion (normally the equivalent sources' strength). In this way numerical issues are reduced and sparsity is enforced. Notice that in this case the term beamforming is inapposite because the working principle of the method does not require the use of scanning acoustic beams. Nevertheless this terminology is widely adopted in literature. ESM are also used in near-field applications like in the case of the wideband acoustical holography described in reference [40].

The main advantages of adopting ESM for Sound Source Localization (SSL) is that such techniques aim at associating a reliable quantitative output to the source localized by means of a distribution of elementary sources (monopoles or even multi-poles). The reason why the approach is versatile is twofold. On the one hand it allows to reproduce complex source distributions as a combination of simple source models; on the other hand, with the same principle, one is able to model, in a theoretical way, simple scenarios (such as monopole radiation) by means of multiple elementary sources as long as the pressure field produced by such distribution is equivalent to the real one. A consequence of this equivalence is that the power radiated by the equivalent sources distribution should be the same radiated by the real sources to be modelled. These interesting properties make it possible to exploit such methods not only for troubleshooting purposes, but also for accurate quantitative assessments. However, despite effective, these approaches can lead to numerical instabilities mainly due to the ill-posedness of the inverse problem to be solved. In fact, the number of equivalent source points, also called "scan points" - characterized by their own amplitude and phase - that discretize the calculation plane is generally higher than the number of microphones used in the beamforming array. Therefore, the number of unknowns is higher than the number of equations. For solving such underdetermined problem, a pseudo-inverse and a regularization strategy are required. There is a vast literature about this subject and many approaches have been studied and applied also in similar domains such as Near-field Acoustic Holography (see for example: [41]). Colangeli et al. [39] performed a sensitivity analysis on a Generalized Inverse Beamforming (GIBF) algorithm in order to identify the best regularization strategy to be adopted with GIBF. A similar study, on a different ESM-like approach, was performed by Kim and Nelson in [42]. Other approaches where the regularization strategy is somehow triggered by the characteristics of the acoustic fields are described in [43, 44]. The interested reader might refer to [45] for a deeper discussion on regularization methods. The problem of regularization in inverse beamforming is often tackled together with the problem of decomposition of the active field in uncorrelated noise sources distributions. The ill-conditioning of the numerical problem is not only due to the lack of information in the measurements, but it can also be caused by other factors such as possible uncertainties in the propagation model and noise disturbances. Especially for the latter issues, a Principal Component Analysis (PCA) of the acoustic field under study can help for improving the results of acoustic inverse methods (some typical scenarios are depicted in references [46, 47]). Colangeli et al. used such approach in [39] in order to solve complex acoustic fields and severe background noise conditions.

A Bayesian formulation of the inverse acoustic problem is proposed by Antoni in [48, 49, 50]. In this approach, physical and probabilistic information about the investigated acoustic problem are combined to obtain an equivalent sources reconstruction of the acoustic scene. Such method relies on the so-called Bayesian regularization strategy that relates the choice of the optimal regularization to probabilistic assumptions about the source field and the measurement noise. Moreover it is proven in [48, 49] that the possibility of exploiting a priori spatial information on the source field greatly improves the spatial resolution thanks to the so-called "*Bayesian focusin*g". The method is based on rephrasing the inverse problem formulation in order to obtain the reconstruction of the source field through the expansion of optimal basis functions. Due to this aspect, this technique goes beyond the ESM concept. However, it still remains an Equivalent Source Method because such optimal basis is obtained from the discretization of the source region into elementary equivalent sources. In fact in [51], where Pereira et Al. compared the Bayesian method with a classical ESM formulation with different regularization strategies, it is shown that such classical formulation can be obtained as a particular case of the Bayesian formulation. It is moreover noteworthy that the Bayesian nature of this approach allows assigning a probabilistic value to the obtained results by quantifying the level of uncertainty [52].

1.1.2. Interior acoustic imaging

For interior acoustic imaging a convenient classification of methods is proposed by Pereira in [52] (where the reader can find a more detailed description of the possible methods), based on their underlying assumptions and processing to solve the given problem:

- Beamforming methods.
- Near-field Acoustic Holography (NAH) methods.
- Inverse methods.

The beamforming principle adopted is the same as in the exterior acoustic imaging. Instead, the configuration of the array is adapted considering that the in interior applications the microphones array receives acoustic radiation coming from all the directions and not only from the one "observed" with a planar configuration. As regards interior acoustic imaging, therefore, a typical configuration of the microphone array is the rigid sphere.

In most of the applications the scattering effect of the rigid sphere is taken into consideration in the adopted radiation model, therefore in the formulation of the steering vectors (spherical beamforming [33]). This improves the accuracy and the dynamic range at mid-high frequencies because it improves the directivity of the antenna. This advantage is unfortunately lost at low frequency, where the wavelength of the acoustic waves is larger than the diameter of the sphere, making the scattering effect less efficient. In order to extend such frequency range, Lamotte et Al. propose to combine the rigid sphere with a larger open sphere (disposed concentrically). This will allow covering a larger range by adopting the following strategy (reported in reference [53]):

- High frequency (above 1500 Hz): only small rigid sphere with spherical beamforming.
- Mid-frequency (500 - 1500 Hz): combination of large open sphere (bad directivity, good resolution) and small rigid sphere (good directivity, bad resolution).

For combining the benefits of the two arrays, a patented procedure based on "spatial coherence" is applied.

Another powerful way to exploit the spherical configuration of the microphones within the array is the so-called Spherical Harmonics Beamforming described in [54]. It is based on the decomposition of the acoustic pressure field sampled on the spherical array onto a spherical harmonics basis which is used, in the spirit of the beamforming principle, to focus the array towards a set of scan positions obtaining the beamforming map very often in the azimuth and elevation angles coordinates. Roig et Al. proposed in [55] an approach that adopts the spherical harmonics decomposition to generate virtual pressures onto a spherical surface concentric and larger than the rigid spherical array. The aim is obtaining, through processing, the hardware configuration proposed in [53] with the same purposes. The advantage of these approaches is that the scattering effect of the rigid sphere can be taken into account improving the results. However, such methods still rely on a free field propagation model between the scan points and the microphones of the array. In order to improve the results one could improve the radiation model used in the beamforming solution by including the effect of reflection in the radiation model (Image Source Method,

an example is given in: [56]) and/or taking into account the modal behavior of the cavity [57]. Another strategy for improving the beamforming results, but still adopting the free field propagation assumption was proposed by Castellini and Sassaroli in [58, 59] trough the so-called "average beamforming": a statistical approach that requires to place the microphones array in several (two or more) positions within the cabin. The idea is that the effect of the reflections and the modal behaviour of the cavity depends on the position of the array while the physical sources obviously remain the same. By complementing the information carried by the standard beamforming maps with the mapping of statistical quantities it is possible to reduce the undesired effects focusing on the physical sources.
The application of acoustic holography in non-anechoic conditions is a difficult task because the noise sources are placed in both regions of the microphone array (front and back). Villot et Al. studied the radiation of plane structures inside an enclosure [60]. Tamura et Al. [61, 62] proposed the use of a double layer microphone array for making it possible to distinguish between the sources acting in front or in the back of the array. The concept was then used in [63]. Other approaches, such as: Statistically Optimized NAH [64] and Spherical NAH [65] have been proposed for improving the performance of NAH and reducing its costs in terms of time and equipment. However the latter aspects are still the main drawbacks of adopting NAH for interior noise applications despite the benefit of an improved spatial resolution with respect to beamforming methods.
Among the inverse method to be applied in interior applications the main options are: IBEM and ESM. IBEM was introduced for overcoming the limitations of NAH in dealing with arbitrarily shaped radiating surfaces [31], Kim and Ih applied for the first time the technique to a car cabin mock-up [30]. The IBEM method, that relates the acoustic pressure within a bounded domain to the normal velocity and surface pressure of the bounding surfaces thanks to a numerical discretization of the Kirchhoff-Helmholtz integral equation, has on the one hand the advantage of giving the freedom of utilizing arbitrarily shaped radiating surfaces and microphone arrays, on the other hand it has the drawback that the number of required measurement points increases in frequency and that the quality of the result is highly influenced by the numerical model adopted. The ESM ([66], originally called "wave superposition method") tends to mitigate the limitations of IBEM. It is based on the idea that the acoustic field generated by an arbitrarily shaped object can be described by means of the superposition of the fields generated by elementary sources (monopoles, dipoles, etc.) placed within the radiator. As already mentioned for exterior applications, the solution of the inverse acoustic problem formulated in terms of ESM consists in finding the optimal equivalent sources parameters (amplitude and phase) such that the resulting acoustic fields matches the one measured by the microphones array. Thanks to this formulation it is no longer required that the shape of the microphone array should be conformal to the cabin's cavity, moreover the number of measurement points can be severely reduced if compared to the IBEM case. This allows the application of such methods also adopting the rigid spherical configuration typical of the beamforming applications [67, 68]. The price to pay for this great versatility is that the inverse problem to be solved is in general severely under-determined and in most of the cases severely ill-conditioned, too. The issues related to the ill-conditioning of ESM problems and their

consequences have been addressed from several angles in literature: [32, 52, 69]. In this thesis a novel approach will be discussed in Chapter 3.
To conclude this paragraph three hybrid methods will be shortly described. The first is called: Helmholtz Least Squares (HELS, [70]), the second is called Hybrid Near-field Acoustic Holography (HNAH, [71]), the third one is called inverse Patch Transfer Function method (iPTF, [72]). The HELS method utilizes a microphones array conformal to the cabin enclosure in order to reproduce the pressure field active within the cavity as a superposition of a particular orthogonal basis of functions: the acoustic modes. This strategy gives on the one hand the advantage of a reduced number of required measurement points, on the other hand the approach badly deals with geometry of the cavity that deviate considerably from a sphere, moreover it is limited at high frequency due to the high modal density. Due to these limitations, Wu [71] proposed to use HELS as a pre-processing in a methodology called HNAH. It uses the HELS decomposition of the acoustic field within the enclosure to generate virtual microphones (in literature it is used the term "synthetic acoustic pressure") on the same surface, conformal to the enclosure bounds, where the physical sensors belong. In this way it is possible to increase the number of measurement points onto the measurement surface. This increased sampling of the measurement surface makes it possible the use of iBEM for finally computing the normal surface velocity and the pressures over the source (enclosure) surface. This method gives the advantage of performing iBEM with a reduced number of microphones, however it suffers from the same limitations of the HELS method. The iPTF method tries to overcome the limitations of the abovementioned approaches (HELS and HNAH). The iPTF approach has been proposed in several formulations: [72, 73, 74]. Its main idea is to define an arbitrary volume including the main sources within a cavity and discretizing its virtual surface in patches in which pressure and particle velocity should be measured/known. This information is finally combined with a FEM model of the virtual volume. This approach allows to identify the acoustic field inside the entire virtual volume. Thanks to its formulation and to the FEM modelling, the iPTF method overcomes most of the limitations of the previous methods allowing to deal with complex geometries of the cavity in a larger frequency range. Weak point of the method is the cumbersome measurement effort required. In order to mitigate this limitation a novel formulation has been recently presented, [75], with the name: "Mixed iPTF". This formulation keeps the basic principles of the previous version, but requires only pressure measurements becoming more cost efficient.

1.1.3. Transfer Path Analysis

The transmission towards the interior can occur through the structure of the cabin - structure-borne path - or through the acoustic propagation of the load through the air-structure coupling. The latter ones are named air-borne paths. The most suitable technique for studying the propagation of noise and vibration problems from the exterior towards the interior of a vehicle is the so-called Transfer Path Analysis (TPA). It is a procedure that allows to trace the transfer of vibro-acoustic energy from a source to a given receiver assuming that the system can be modelled by means of a set of source-transfer-receiver paths that bring energy from the "active part", where the "sources" are located, towards the

"passive part", where the receiver/s is/are located. In automotive the passive part is represented by the car cabin, while the active part is represented by the engine, wheels, suspensions, etc. TPA will not be assessed in this document and for a complete description of this approach the reader can refer to: [76, 77, 78]. Different approaches for the assessment of the structure-borne and air-borne paths are required. While for structure-born paths assessment the most convenient approaches are better defined and more robust (mount-stiffness method, matrix inversion method, OPAX, etc. [76, 77, 78, 79]), it is not the same for the study of air-borne paths. In this case several solutions have been proposed, but very often they have to be specialized to specific cases (powertrain airborne noise contribution [34, 80], airborne tire noise contribution [81], panel contribution analysis [82], etc.). For the airborne transfer paths analysis, is often used the definition: "Airborne Sound Quantification" (ASQ). With ASQ is generally defined an inverse method based on the estimation of Noise Transfer Functions (NTF) between the source location (where the acoustic loading takes place) and the target location(s) (where the acoustic loading's influence is of interest) [83, 84, 85, 86]. It has been often used also for exterior noise assessment such as pass-by noise engineering [87, 88, 89].
If the study of the transmission is a crucial aspect to reduce the discomfort of the vehicle's passengers, it is equally very important to have a deep knowledge about the exterior source location and their characteristics. This knowledge, in fact, will help on the one hand to refine the TPA models making them more effective and on the other hand to understand in detail the mechanisms of generation of the exterior noise loads, their nature, their causes. To give some examples related to automotive, this sort of analyses will help understanding the role of the leading and trailing edge [90] and the degree of correlation between front and rear wheel in the road noise airborne propagation (see section 3.3); understanding the contribution to the wind noise of specific car components [91]; understanding the contribution of combustion and mechanical noise produced by an Internal Combustion Engine (ICE) [92].

1.1.4. Acoustic Modal Analysis

AMA aims at decomposing the behaviour of the car cavity into a set of individual resonance phenomena, each characterized by a resonance frequency, damping ratio, participation factor and mode shape. The experimental data set to derive this model consists of a set of Frequency Response Functions (FRFs) between a set of reference (i.e. acoustic source input) degrees of freedom and all response (i.e. microphone output) degrees of freedom. The analogy with the structural Experimental Modal Analysis (EMA) is straightforward [93, 94, 95]. A broader view and a deeper insight on this topic can be obtained thanks to the literature produced by Accardo and co-workers listed in the references section: [96, 97, 98, 99].

1.2. General theoretical aspects

In this section there are reported some theoretical aspects related to simple sources radiation and to how a radiation problem is related to acoustic imaging. This short dissertation does not aim at giving a deep insight on these topics, but rather at defining tools that will be largely used in the following chapters, in order to facilitate the reader in the manuscript consultation. In particular, the interdependency of the acoustic quantities related to the radiation problem of simple sources will be recalled in paragraph 1.2.1, while the direct and inverse formulations of an acoustic imaging problem will be discussed in paragraph 1.2.2. For a more detailed treatment, the reader can refer, within the vast literature on these subjects, to [100] regarding the fundamentals of acoustics and to [101] regarding the manifold array based methods and their formulation.

1.2.1. Monopole propagation and related acoustic quantities

An acoustic monopole radiates sound equally in all directions. In practice, any sound source whose dimensions are much smaller than the wavelength of the sound being radiated will act as a monopole. This explain our interest in such a model of propagation of sound. If the source is small with respect to a wavelength and several wavelengths apart, it can be treated as a *simple source* (at the same frequency). In this case its acoustical radiation properties can be considered identical to the ones of a pulsating sphere of the same source strength *Q*. This assumption will allow to describe these sources through the monopole propagation model. In particular it will be possible to know the pressure field, for any given frequency, at any given distance as in Eq.(1. 1).

$$p(r,\omega) = \rho \frac{j\omega Q}{4\pi r} e^{-j\frac{\omega}{c}r} \tag{1. 1}$$

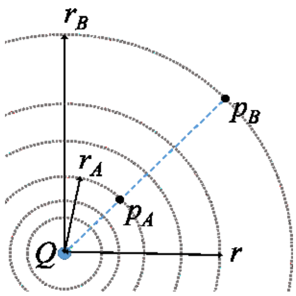

Fig. 1. 3 : scheme of the radiation of a monopole of strength Q in free field.

The quantities represented in Eq.(1. 1) are:

- p: acoustic pressure [Pa];
- ρ: density of the air [kg/m^3];
- ω: angular frequency defined as $2\pi f$ [rad/s];
- Q: acoustic strength, also called volume velocity, [m^3/s];
- r: module of the distance between the source location and the investigated point.

It is convenient to refer to $j\omega Q$ as the volume acceleration, [m^3/s^2] of the source.
Referring to Fig. 1. 3 it is possible to notice that Eq.(1. 1) allows also to define through Eq.(1. 2) the pressure produced by the source of strength Q in a location B when the pressure field is known in the location A and vice versa.

$$p_B = p_A \frac{r_A}{r_B} e^{-j\frac{\omega}{c}(r_B - r_A)} \tag{1. 2}$$

The acoustic power emitted by the monopole source of strength Q is quantified in Eq.(1. 3).

$$W(\omega) = \frac{1}{8\pi} \frac{\rho}{c} (\omega Q)^2 \tag{1. 3}$$

Thanks to Eq.(1. 1) and Eq.(1. 3) it is also possible to evaluate, through Eq.(1. 4), the acoustic power radiated by a monopole source if it is known the pressure field produced by the source in the location r.

$$W(\omega) = \frac{2\pi r^2}{\rho c} (p(r,\omega))^2 \tag{1. 4}$$

Assuming that Q is the only source active in the acoustic field, from Eq.(1. 4) descends that the power level L_W of the source is theoretically known once it is known the Sound Pressure Level (SPL) at a given distance from the source. Defining in fact the SPL as in Eq.(1. 5), the power level of the source can be obtained through Eq.(1. 6) by reworking Eq.(1. 4) in a dB scale and setting the reference values of W_0 = 1 pW and p_0 = 20 μPa.

$$SPL = 20\log_{10}\left(\frac{p}{p_0}\right) \tag{1. 5}$$

$$L_W = 10\log_{10}\left(\frac{W}{W_0}\right) = SPL + 10\log_{10}\left(\frac{2\pi r^2}{\Omega_0}\right) \quad (1.\ 6)$$

The reported equations are to be considered valid only in the case of ideal monopole sources in ideal free-field conditions. In reality the acoustic power radiated by real sources should be evaluated through more detailed and refined measurement procedures prescribed by the standards (ISO 3741, ISO 3744, ISO 3746, ISO 9614-1/2, etc. [102]).
In acoustic imaging the ideal monopole radiation model represents a central concept for many formulations. In fact, several acoustic imaging problems, and in particular the one of interest in this thesis - the direct beamformer and the equivalent source model - have in common the assumption that the acoustic field sensed by the microphones belonging to the array is caused by a distribution of monopole sources placed in a so-called source region. Such problems formulation exploits equations (1. 1)-(1. 6). Some authors extended the acoustic imaging formulation to cases of more complex radiating sources such as dipoles and quadripoles [36, 103, 104, 105, 106], these cases will not be deeply investigated in this thesis.

1.2.2. The direct beamformer and the equivalent sources radiation problem

The problem of the radiation of acoustic sources towards measurement locations where an array of microphones is installed will be introduced in this paragraph. As already described in paragraph 1.1.1, the configuration of a microphone array pointed towards an acoustic scene is the typical experimental setup required for performing any kind of acoustic imaging based on simple pressure measurements. The aim of this paragraph is to describe the direct and the inverse approach to the investigation of the radiation of sound sources through acoustic imaging. In fact, it will be clarified to the reader the difference between these two points of view, explaining how the same information available (geometry of the problem and measured acoustic pressure at the microphones locations) can be exploited for obtaining a direct formulation or an inverse formulation, finally pointing out pros and cons of the two choices.
Fig. 1. 4 reports, through an example, the three steps common to any acoustic imaging problem formulation. In our example, in fact, Fig. 1. 4(a) represents a microphone array installed for observing the acoustic scene generated by two generic sources, of strength Q_I and Q_{II}, radiating towards the array. Fig. 1. 4(b) reports the first assumptions to simplify the problem: the sources (initially not known) are assumed to be “simple”, for example monopoles. Such sources are assumed to belong to a source region called *scan plane* and a geometrical relationship between the *array plane* and the *source plane* is defined. Finally, as depicted by Fig. 1. 4(c), a radiation model can be generated thanks to the physical and geometrical hypothesis assumed so far. In particular, the scan plane is discretized into a set of elementary monopole sources and their radiation towards each microphone of the array is obtained.

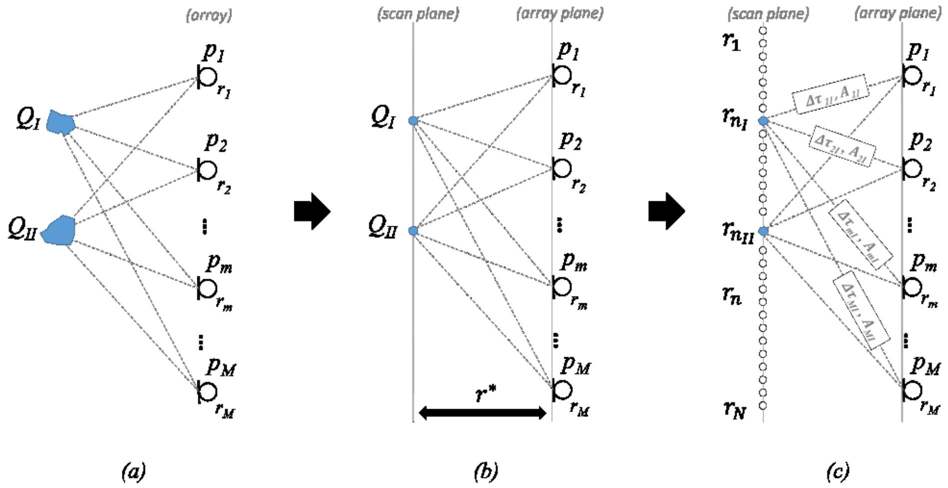

Fig. 1. 4 : problem statement for acoustic imaging. (a): acoustic source radiation towards a microphone array. (b) the sources are assumed to be "simple" and belonging to a source region called "scan plane". (c) building the radiation model on the basis of the physical information available (geometrical: array position with respect to the scan plane; acoustical: far-field, near-field, etc.).

This radiation problem can be formalized as in Eq.(1. 7) in which the so-called *radiation matrix A* allows to determine, at any given frequency, the complex pressure at the microphone locations, stored in the vector $\underline{p}$, if the characteristics of each monopole that discretized the scan plane, represented by the coefficients of the vector a, are known.

$$A(\omega)\underline{a}(\omega) = \underline{p}(\omega) \tag{1. 7}$$

If the elementary monopole sources are characterized by their strength (Q_n [m^3/s]), the elements of the radiation matrix A assume the form of Eq.(1. 8)

$$A_{mn} = \rho c \frac{j\omega}{4\pi |r_m - r_n|} e^{-j\frac{\omega}{c}|r_m - r_n|} . \tag{1. 8}$$

Moreover it is possible to interpret the phase shift prescribed by Eq.(1. 8) as the time delay, $\Delta\tau_{mI}=|r_m-r_I|/c$ and $\Delta\tau_{mII}=|r_m-r_{II}|/c$, that occurs due to the travelling of the acoustic wave from the sources Q_I and Q_{II} to the receivers p_m. In our example the ideal formulation of the investigated radiation problem yields what reported in Eq.(1. 9).

$$\begin{pmatrix} A_{11} & \cdots & A_{1I} & \cdots & A_{1II} & \cdots & A_{1N} \\ \vdots & & \vdots & & \vdots & & \vdots \\ A_{m1} & \cdots & A_{mI} & \cdots & A_{mII} & \cdots & A_{mN} \\ \vdots & & \vdots & & \vdots & & \vdots \\ A_{M1} & \cdots & A_{MI} & \cdots & A_{MII} & \cdots & A_{MN} \end{pmatrix}_{[M\times N]} \begin{pmatrix} 0 \\ \vdots \\ Q_I \\ \vdots \\ Q_{II} \\ \vdots \\ 0 \end{pmatrix}_{[N\times 1]} = \begin{pmatrix} p_1 \\ \vdots \\ p_m \\ \vdots \\ p_M \end{pmatrix}_{[M\times 1]} \tag{1. 9}$$

The pressure filed at the array level is ideally produced by two monopolar sources Q_I and Q_{II} placed in the corresponding locations indicated by r_{nI} and r_{nII} as in Fig. 1. 4(c). In reality the coefficients of the vector $\underline{a}$ in Eq.(1. 7) are unknown and their determination is not a trivial task because it requires the inversion of the problem stated in Eq.(1. 7).
Such problem can be approached in two manners: inversion of the radiation matrix A (inverse methods) or through focused beamforming (direct methods).
Fig. 1. 5 reports a scheme that explains the approach to the problem through focused beamforming.

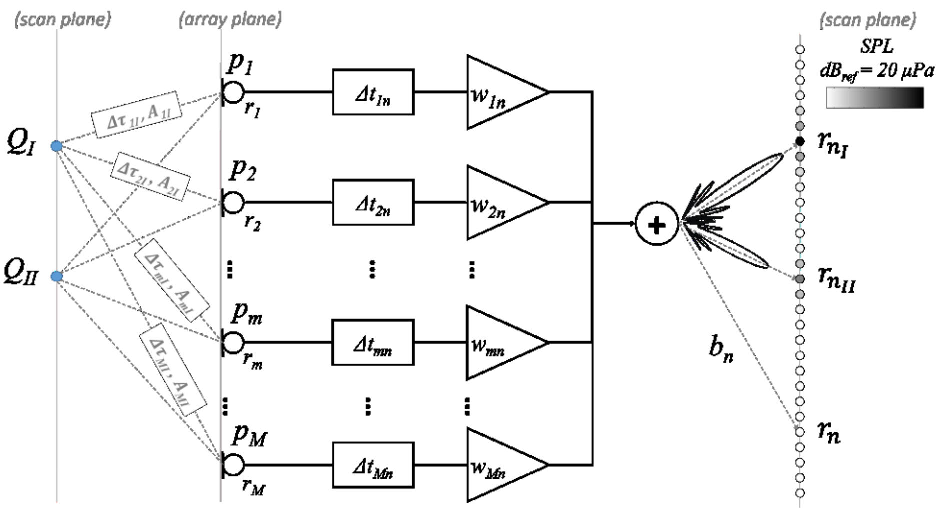

Fig. 1. 5 : scheme explaining the beamforming formulation.

The *focused beamforming* is an averaging procedure that determines the acoustic contribution of the sources sought within the scan plane thanks to mathematical entities called *steering vectors*. The steering vectors $\underline{w}(\omega,r_n)$, or $\underline{w}_n$ when the dependency by the frequency is made implicit and the relationship with the n[th] focused scan point r_n is synthetically explicated by the subscript n, allow to use the complex acoustic pressure sampled at the array level to form a *beam* that is *focused* onto each of the n scan points through the expression of Eq.(1. 10):

$$b_n = \underline{w}^H(\omega, r_n)\underline{p}(\omega). \tag{1. 10}$$

This beam-forming effect is obtained by assigning to each steering vector a set of phase shifts (or time delays) { $\omega\Delta t_{1n}$, … , $\omega\Delta t_{mn}$, … , $\omega\Delta t_{Mn}$ } that, properly combined with the complex pressures { p_1 , … , p_M }, emphasizes the sound coming towards the array from the position r_n and suppresses the sound coming from elsewhere. This is done per each scanned point of the scan plane, under the assumption that each elementary monopolar source composing the scan plane can be considered uncorrelated from the others. The b_n coefficients, for all the N scan points, are the elements of the vector $\underline{b}$ that is often called *beam pattern*, i.e. the set of the N focused acoustic beams. The steering vectors $\underline{w}_n$ can be assumed proportional to the columns of the radiation matrix A (Eq.(1. 11)).

$$\underline{w}_n \propto \begin{pmatrix} A_{1n} \\ \vdots \\ A_{mn} \\ \vdots \\ A_{Mn} \end{pmatrix}_{[M\times 1]} \tag{1. 11}$$

Many alternative steering vectors formulations are available in literature. The interested reader can refer to [107] for a complete overview. The classic approach is: rescaling the element of the radiation matrix (Eq.(1. 12)) on their module emphasizing the phase relationship between the sound radiated by the nth scan point and the signal sensed at the microphones array locations.

$$w_{mn} = \frac{1}{M}\frac{A_{mn}}{|A_{mn}|} = \frac{1}{M}e^{-j\frac{\omega}{c}|r_m - r_n|} \tag{1. 12}$$

Defining with B_n , see Eq.(1. 13), as the product of each element of the beam pattern with its complex conjugate

$$B_n = b_n b_n^* \tag{1. 13}$$

and recalling that the Cross-Spectral Matrix (CSM) between the microphones array signals is estimated, by averaging over multiple realizations, through the Hermitian product of the complex pressure vector $\underline{p}$ with itself as shown in Eq.(1. 14):

$$C_M = \left\langle \underline{p}\,\underline{p}^H \right\rangle_{[M\times M]}, \tag{1. 14}$$

it remains proven, through Eq.(1. 10), the equation Eq.(1. 15):

$$C_b = w^H C_M w. \tag{1. 15}$$

The vector $\underline{B}$, containing the diagonal elements of the matrix C_b is the acoustic image obtained through direct beamforming. Its elements are described in Eq.(1. 13) and have unit: [Pa^2]. The columns of w (steering matrix) contain the steering vector previously defined (Eq.(1. 16)).

$$\underline{B} = \begin{pmatrix} b_1 b_1^* \\ \vdots \\ b_n b_n^* \\ \vdots \\ b_N b_N^* \end{pmatrix}_{[N\times 1]} \quad , \quad w = \begin{bmatrix} \underline{w}_1 & \cdots & \underline{w}_n & \cdots & \underline{w}_N \end{bmatrix}_{[M\times N]} \tag{1. 16}$$

The method that adopts Eq.(1. 15) for obtaining the acoustic image of the scene observed by the microphone array is often called in literature: *Conventional Beamforming* [26]. Its results are often plotted in dB reporting the SPL values obtained beam-forming the microphones array information towards each of the scan points used to discretize the source region. Notice that this method relies on the assumption that each elementary monopolar source in the scan plane has to be considered as uncorrelated from the others and no relationship between them is taken into account. Moreover, it is worth to point out that the steering vectors allow to map the *effect* (SPL) of such elementary sources distribution at the scan plane and not their actual strength. These assumptions make direct methods on the one hand very robust in accomplishing the sources localization task, whereas on the other hand, despite theoretically ([108]) absolute levels of the sources strengths can be obtained through post-processing of the results of Eq.(1. 15), direct methods yield only qualitative indications on the acoustic power radiated by the investigated sources. Furthermore the assumption that the elementary monopolar sources belonging to the scan plane are uncorrelated, limits the technique in presence of complex acoustic fields in which correlated and distributed sources are active.

The condition of no correlation between the elementary sources of the scan plane is not required in the Equivalent Source Method (ESM) formulation. ESM still relies on the discretization of the source region into elementary monopolar sources, but, contrarily to the previous category of methods, it aims at estimating the coefficient of the vector $\underline{a}$ of Eq.(1. 7) through the pseudo-inversion of the radiation matrix A (Eq.(1. 17)).

$$\underline{a} = A^{+} \underline{p} \tag{1. 17}$$

This inverse methods have the advantage of considering the elementary monopolar sources of the scan plane all at once. The phase relationship between them is therefore taken into account allowing to better dealing with correlated source distributions. Considering all the elementary sources at once has also the advantage that the mutual interaction of the acoustic fields produced by each of them at the microphones array locations can be taken into account. This will allow to determine the source strength of each of them by fitting in a least-squares sense their effect into the acoustic field sampled at the array level. From this assumption descends the definition of *equivalent sources*.

At this point it should be clear to the reader the marked difference between the *beam pattern* obtained through a direct approach and the *equivalent sources distribution* obtained through inverse methods. In the first case a pressure value, representative of the array information beam-steered towards each scan point, is assigned to each elementary source of the scan plane, whereas in the second case the strength (or a coefficient proportional to it) of an equivalent source is assigned to each scan point. In fact, despite the term "inverse beamforming" is widely used in literature, it is actually inappropriate in the case of ESM because such techniques do not rely on a beam-steering process, but rather on a least-squares fitting of the pressure information at the array level. However, for uniformity with the literature terminology, in this thesis the wording "inverse beamforming" will be kept when referring to existing or novel inverse acoustic imaging methods.

Despite the two branches of methodologies (inverse and direct approaches) are intrinsically different, they both originate from the same acoustic problem described in Eq.(1. 7). This suggests to investigate more deeply the mathematical aspects that differentiate the two approaches in order to efficiently position strengths and limitations. In order to do so the inverse problem formulation of Eq. (1. 17) can be reworked observing that the Moore-Penrose generalized inverse of the radiation matrix A can be obtained through its Singular Values Decomposition (SVD) [109, 110] as shown in Eq.(1. 18):

$$A_{[M\times N]} = U_{[M\times M]} \Sigma_{[M\times N]} V^{H}_{[N\times N]} \quad \Rightarrow \quad A^{+} = V\Sigma^{-1}U^{H} \,. \tag{1. 18}$$

The matrix Σ is populated by the singular values of A.

Let us define C_a as the CSM between the equivalent sources of the equivalent source distribution obtained through Eq.(1. 17):

$$C_a = \left\langle \underline{a}\underline{a}^{H} \right\rangle . \tag{1. 19}$$

The expression in Eq.(1. 20) is obtained by injecting in Eq.(1. 19) the expressions of $\underline{a}$ and A of Eq.(1. 17) and Eq.(1. 18) respectively and observing that the product $\underline{p}\underline{p}^H$ equals the CSM between the microphones array signals, C_M.

$$C_a = V\Sigma^{-1}U^H C_M U\Sigma^{-H}V^H \tag{1. 20}$$

Through this compact expression it becomes evident that the delicacy of the inverse methods lies in the nature of the singular values of the radiation matrix A. In particular, the situation becomes critical when the non-zero element of Σ range from very small to very high values because in that case A is ill-conditioned and/or ill-determined. This problem can be mitigated through *Truncated SVD* [111] of the matrix A (neglecting the least significant elements of Σ during its pseudo-inversion) or by means of other regularization strategies (see [45] and Chapter 2). In this latter case the formulation of Eq.(1. 20) changes into the one of Eq.(1. 21)

$$C_a = V\widetilde{\Sigma}^{-1}U^H C_M U\widetilde{\Sigma}^{-H}V^H \tag{1. 21}$$

where Σ^{-1} has been replaced by the expression in Eq.(1. 22):

$$\widetilde{\Sigma}^{-1} = \begin{bmatrix} \frac{\Sigma_{11}}{\Sigma_{11}^2+\lambda^2} & \cdots & 0 & \cdots & 0 \\ 0 & \ddots & \vdots & & \vdots \\ 0 & \cdots & \frac{\Sigma_{mm}}{\Sigma_{mm}^2+\lambda^2} & \cdots & 0 \\ \vdots & & & \ddots & \vdots \\ 0 & \cdots & 0 & \cdots & \frac{\Sigma_{MM}}{\Sigma_{MM}^2+\lambda^2} \\ 0 & \cdots & 0 & \cdots & 0 \\ \vdots & & \vdots & & \vdots \\ 0 & \cdots & 0 & \cdots & 0 \end{bmatrix} \tag{1. 22}$$

The coefficient λ^2 is the so-called *regularization parameter*. Several regularization strategies for the optimal choice of λ^2 have been proposed in literature [45]. In section 2.2 of Chapter 2 this aspect will be discussed with regard to the possible choices available in the case of the adoption of the GIBF algorithm for solving the inverse problem.
In the case of a focused beamforming formulation, instead, recalling Eq.(1. 15) and defining C_b as the CSM between the elements of the beam pattern:

$$C_b = \underline{b}\underline{b}^H \,, \tag{1. 23}$$

Eq.(1. 23) is obtained:

$$C_b = \hat{V}\hat{\Sigma}^H \hat{U}^H C_M \hat{U}\hat{\Sigma}\hat{V}^H \,, \tag{1. 24}$$

where the steering matrix w has been decomposed through singular values factorization:

$$w_{[M\times N]} = \hat{U}_{[M\times M]}\hat{\Sigma}_{[M\times N]}\hat{V}^H_{[N\times N]} \,. \tag{1. 25}$$

It can be observed that in the case of direct approaches (Eq.(1. 24)) the singular values matrix is not inverted.

In [112], where Dougherty proposed a simplified solution of the *generalized inverse problem* (called GINV) especially tailored for jet noise, based on Eq. (1. 20), it is observed that the structures of Eq.(1. 20) and Eq.(1. 24) are so similar to even allow an hybrid approach (Eq.(1. 26)) in which a compromise between the reciprocal and the original value of each singular value of A could be used to fill the non-zero elements of $Z_{[NxM]}$:

$$C_c = VZU^H C_M UZ^H V^H \,. \tag{1. 26}$$

However, this hybrid approach as such yields results comparable to the focused beamforming (already defined: Conventional Beamforming) CB in which on the one hand the spatial resolution is slightly improved by tuning the matrix Z, on the other hand the solution completely diverges if Z is not tuned properly.

The case of the Bayesian approach proposed by Antoni in [49] can be obtained through Eq.(1. 27):

$$C_d = \widetilde{V}\widetilde{Z}\widetilde{U}^H C_M \widetilde{U}\widetilde{Z}^H \widetilde{V}^H \tag{1. 27}$$

by putting:

$$\widetilde{U}_{[M\times M]} = \Omega^{-1/2}_{noise[M\times M]} U_{[M\times M]} \,, \tag{1. 28}$$

$$\widetilde{Z}_{[N\times M]} = \begin{bmatrix} \frac{\Sigma_{11}}{\Sigma_{11}^2+\eta^2} & \cdots & 0 & \cdots & 0 \\ 0 & \ddots & \vdots & & \vdots \\ 0 & \cdots & \frac{\Sigma_{mm}}{\Sigma_{mm}^2+\eta^2} & \cdots & 0 \\ \vdots & & & \ddots & \vdots \\ 0 & \cdots & 0 & \cdots & \frac{\Sigma_{MM}}{\Sigma_{MM}^2+\eta^2} \\ 0 & \cdots & 0 & \cdots & 0 \\ \vdots & & \vdots & & \vdots \\ 0 & \cdots & 0 & \cdots & 0 \end{bmatrix}, \tag{1. 29}$$

and:

$$\widetilde{V}_{[N\times N]} \propto V\,. \tag{1. 30}$$

It is in fact explained in [49] that:

- Ω_{noise} in Eq.(1. 28) is such that the product $\beta^2\Omega_{noise}$ is the covariant matrix of the measurement noise at the microphones of the array with the coefficient β^2 representing the mean energy of such noise.
- η^2 is in this case obtained through the so-called Bayesian regularization as a function of the abovementioned coefficient β^2 and the mean energy of the source field quantified by another parameter, α^2, estimated taking into account a priori information on the source field.

The structure of $\tilde{V}$ will not be described here. The interested reader can find the detailed description of the method in [48, 49, 51]. Eq.(1. 30) only reports that $\tilde{V}$ can be considered proportional to the eigen-functions V of the matrix A.
Notice that, as Pereira et Al. observed in [51], the Bayesian formulation in Eq.(1. 27) admits the formulation of Eq.(1. 21) as a particular case in which are considered: $\Omega_{noise}=I$ (identity matrix), $\eta^2= \lambda^2$ (i.e. the Bayesian regularization strategy is replaced with other approaches [45]) and $\tilde{V}\equiv V$. In [51] the authors compared the two formulations (Eq.(1. 21) and Eq.(1. 27)) coming to the conclusion that the Bayesian approach outperforms the other (at least in the cases reported in the paper) thanks to the Bayesian regularization mechanism.

Inverse methods allow, with a compact formulation, quantitative results, accurate localization and the resolution of complex acoustic fields. These methods are moreover

easy to extend towards more refined modelling of the radiation properties of the sought equivalent sources including multi-pole behavior or other extensions of the free-field assumptions (reflections, reverberation, etc.). Besides these advantages, the downside of adopting inverse methods consists in the fact that the corresponding inverse problems are often severely under-determined and ill-conditioned. These drawbacks may have a dramatic impact on the final results if not properly considered and tackled. These aspects will be discussed extensively in Chapters 2 and 3.
Despite the just mentioned risks, the interest towards inverse methods is fully justified by their great potential in resolving correlated and uncorrelated sources distribution with high spatial accuracy and high dynamic range. Fig. 1. 6 describes a numerical simulation of an array of randomly distributed microphones (Fig. 1. 6(a)) placed 1 m far from a random noise source located in the center of the circle depicted in Fig. 1. 6(b) describing the acoustic scene and the considered scan plane.

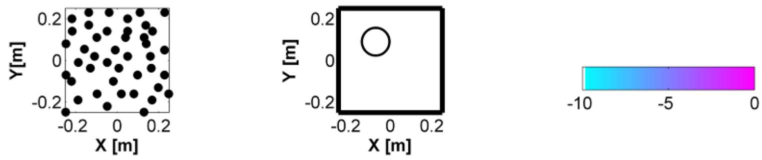

(a) (b) (c)

Fig. 1. 6 : simulated beamforming problem for comparing CB and GIBF performance. Problem statement. (a): microphones array geometry. (b): Theoretical location of the sought random noise source. (c): colour code. The acoustic images are normalized to their maximum value and plotted with 10 dB dynamic range.

A comparison between the results obtained with CB, direct method, and GIBF, the inverse method that will be studied and enhanced in this thesis, is reported in Fig. 1. 7. It was already pointed out that the beam pattern obtained through direct methods and the equivalent sources distribution obtained by means of inverse methods have slightly different interpretations. In order to directly compare the results of the two methods in terms of localization accuracy and dynamic range capabilities, the acoustic images have been normalized to their maximum value and plotted in dB with a fixed range of 10 dB.

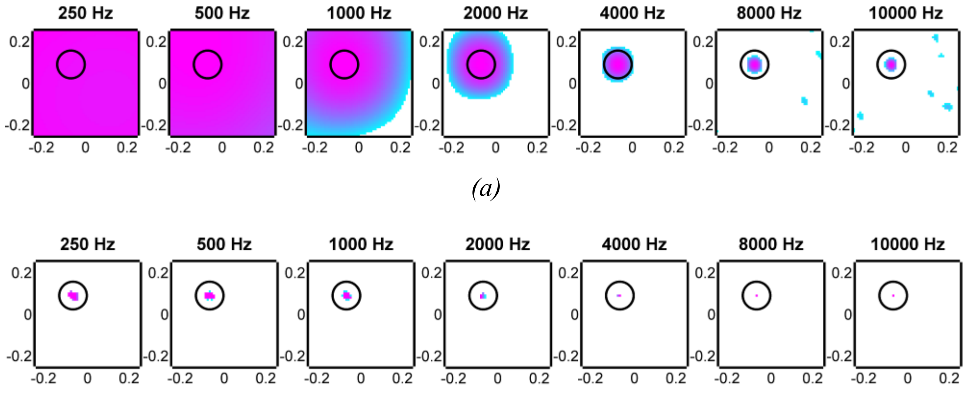

(a)

(b)

Fig. 1. 7 : comparison of results in the range 250 Hz – 10000 Hz for the acoustic imaging problem stated in Fig. 1. 6. (a): Conventional Beamforming (CB) results. (b): Generalized Inverse Beamforming (GIBF) results.

The two methodologies have been tested for frequencies ranging from 250 Hz to 10000 Hz. It can be noticed that the dynamic range allowed by GIBF is constantly larger than 10 dB (it is much larger actually), while it becomes acceptable for CB as from 2000 Hz and it becomes again smaller than the 10 dB scale due to the sidelobes introduced by the point spread function [101].

The literature review regarding the acoustic imaging techniques reported in paragraphs 1.1.1 and 1.1.2 showed that many alternative methods have been proposed ever since the idea of the "acoustic telescope" [10] was applied for the first time to visualize acoustic sources. Historically the direct methods were investigated first, targeting qualitative and troubleshooting applications, whereas lately the interest towards inverse methods is constantly increasing (in parallel with the improvement of the mature direct methods) because of their high performance and the possibility of absolute quantitative results. However, the optimal method to choose depends on the pursued application and the choice of using a direct or an inverse approach for acoustic imaging should be driven by the ultimate goal of the analysis.

In this thesis, for example, the main focus will be on inverse methods because novel pre- and post- processing techniques to enhance the results of a GIBF algorithm will be proposed in Chapter 2, whereas in Chapter 3 and Chapter 4 a novel inverse technique, called Clustering Inverse Beamforming, will be introduced and applied in frequency and time domain. However it will be also shown that the use of an inverse method is not always the most convenient choice. This is the case of Chapter 5, where an acoustic imaging methodology for tackling cyclo-stationary noise problems will be described.

1.3. Structure of the manuscript

The following paragraphs describe the content of the thesis guiding the reader through its structure.

Advanced acoustic imaging in frequency domain

Chapter 2 is dedicated to the description of *Generalized Inverse Beamforming* (GIBF). This approach has been chosen among several alternative techniques based on the so-called *Equivalent Source Method* (ESM) because of its versatility and compatibility with PCA-based *blind source separation* (BSS) methods. These methods will be in fact used in this thesis for uncorrelated sources separation and for de-noising processing. GIBF utilizes an iterative optimization procedure to discard the insignificant equivalent sources from the source plane in order to turn the initially under-determined into an over-determined equivalent problem reducing numerical issues.
Three critical aspects of GIBF have been addressed with the following findings:

- The ill-conditioning problems in GIBF has been studied in a systematic way and guidelines for optimal regularization have been given.
- The ability of the method of decomposing the acoustic image into quantifiable uncorrelated sources distributions has been tested and a sufficient criterion to ascertain the compatibility between the obtained virtual decomposition of the acoustic image and the physical sources actually present has been proposed.
- Adaptive strategies for performing the iterative optimization procedure to reduce the source plane have been proposed.

Moreover several alternatives for achieving the optimized solution have been introduced obtaining a modular approach that allows to combine GIBF with pre- and post- processing techniques to improve the solution.

A novel inverse acoustic imaging method, the so-called Clustering Inverse Beamforming (CIB), working in frequency domain, will be presented in Chapter 3. CIB is an array-based acoustic imaging technique to solve inverse problems formulated by discretizing the source region into elementary equivalent sources. It is based on the statistical processing of multiple realizations of the acoustic image, related to the investigated source region, iteratively obtained solving the corresponding inverse problem on different clusters of microphones, taken from the same microphones array. The result of such statistical processing is stored in the so-called "*clustering mask matrix*". This function is defined in the source region where it is interpretable as the confidence level of finding a physical source in each location within the domain. The inner statistical nature of such approach prevents the occurrence of numerical issues related to the solution of the inverse problem. By enabling to focus on those sub-regions most likely to be the sites of physical sources, it allows accurate localization and optimal quantification. Moreover, if combined with Principal Component Analysis, the method provides a robust criterion for uncorrelated noise source separation with no need of reference sensors in the proximity of the investigated object. CIB is applicable to exterior as well as interior acoustic imaging problems. It does not require any special geometrical configuration of the microphones array. CIB is therefore useful not only for troubleshooting applications, but also for accurate NVH analyses. Another remarkable advantage is that it requires a reduced number of sensors and tests. Moreover, it allows to design flexible and multi-purpose test setup. One example is the use of a randomly distributed microphones array in the car cabin that can be used both for interior acoustic imaging and Acoustic Modal Analysis.

Inverse source reconstruction in time domain

CIB has been adopted also as preliminary step for inverse source reconstruction in time domain based on far-field measurements. This technique, presented in Chapter 4, is particularly suited in those applications that require a detailed knowledge of the main sources and the acoustic field produced by them. In NVH such cases are normally tackled using experimental technologies such as NAH and Sound Intensity that have the advantage of yielding very detailed results but at the cost of an increased time and economical effort for their implementation. Moreover these other methods require to measure in the proximity of the objects, which is not always possible in industrial applications (i.e. wind tunnel measurements). The time domain-based method described in Chapter 4, therefore, represents an appealing alternative for source reconstruction with a reduced computational and experimental effort.

Decomposition of the acoustic image in the angle domain for the study of cyclo-stationary phenomena

Chapter 5 is dedicated to the description and the sensitivity analysis of an acoustic imaging technique tailored for cyclo-stationary phenomena. This algorithm is particularly suitable for investigating noise problem produced by rotating machineries. In fact it relates the pressure field at the array level with the angular evolution of the rotating elements of the investigated machine making available an acoustic image representative of the acoustic field around the machine at any angular instant within the cycle. The study of sound and vibration phenomena related to the engine of a car often needs complex experimental setups. The engine has to be instrumented with several sensors requiring several hours (or days) of tests. The possibility to relate the identification of the noise sources produced by the ICE with the angular position of the rotating elements of the engine and the knowledge of the location of such noise sources within the cycle of the ICE, through microphones array measurements, gives therefore several advantages. In fact on the one hand it allows to understand the causality between the physical phenomena and their acoustic consequences and on the other hand it allows to optimize the effort for further more accurate studies saving, once again, time and costs.

Chapter 2.

Generalized Inverse Beamforming

In inverse beamforming the acoustic field at a calculation plane is obtained by inverting a direct radiation problem in which sources are assumed to be distributed over a scan points grid and are then radiated towards the microphones positions at the array plane. The unknowns are the strengths of each source. The number of unknowns is generally much higher than the number of microphones causing difficulties in the generalized inversion of the full-size problem. An optimization strategy, proposed for the first time by Suzuki [36] is to iteratively reduce the considered scan points discarding the ones that do not really participate to the acoustic field because of weaker amplitude. This idea gave birth to the Generalized Inverse Beamforming (GIBF) method.

Suzuki proposed in [105] an improved version of GIBF in which the problem has been reformulated to be solved as a L1-norm problem adopting an iteratively re-weighted least squares approach. It is based on a weighting matrix applied to the transfer matrix describing the propagation of the equivalent sources distributed at the calculation plane. Another GIBF formulation based on a weighting procedure has been proposed in [38]. Zavala compared several implementations of GIBF in [113] targeting moving sources and aero-acoustic source localization [104, 114] applications. The same author deepened also the themes of regularization [37] and strength estimation of correlated sources distributions [115]. To conclude the overview on the versions of GIBF available in literature, it is worth to mention the formulation given by Dougherty in [112] for assessing jet noise problems. The main idea is reworking the linear algebra of the problem in order to solve it as a generalized version of a direct beamformer solution. The same algorithm has been applied on a recent study on jet noise presented in [116].

In this chapter a GIBF formulation is presented in section 2.1. The regularization problem in GIBF has been addressed in a systematic way and guidelines for the selection of the optimal regularization strategy will be given in section 2.2. The GIBF algorithm will be used in combination with existing and novel PCA-based pre-processing methods aiming at improving the calculated acoustic images. In section 2.3 the use of PCA for uncorrelated source separation of the GIBF solution, based on the microphones array cross-spectral matrix eigen-structure, will be discussed. In sections 2.4 and 2.5 two adaptive pre-processing methods to discard insignificant equivalent source component of the obtained solution will be presented: the first one is based on a PCA of the acoustic image, the other one on the solution of an over-determined formulation of the inverse problem.

The studies presented in this chapter are preparatory to the implementation of the GIBF method in the microphone clustering approach that will be introduced in Chapter 3, providing the so-called Clustering Inverse Beamforming method.

2.1. Formulation

The GIBF algorithm proposed in this thesis works in frequency domain and starts with the computation of the Cross-Spectral Matrix (CSM) of the microphone array signals. The CSM is an M×M matrix, with M the number of microphones in the array, whose elements consist in the cross-spectra between the signals of each pair of microphones of the array. The main diagonal of the CSM contains the auto-power spectra of the signals of each microphone. In this manuscript the CSM is estimated adopting the Welch's method: i.e. assuming the microphones signals stationary and ergodic in such a way that the cross-spectra can be estimated by an averaging process over multiple blocks of the microphone signals. The eigenvalue decomposition (Eq.(2. 1)) of the microphone array CSM C_M

$$C_M = ESE^H \tag{2. 1}$$

makes it possible to decompose the acoustic field at the array plane in eigenmodes $\underline{p}^{(i)}$ (Eq.(1. 7)). E and S represent, respectively, the eigenvectors and the eigenvalues matrices of size M×M. They are composed, respectively, by:

- $\underline{e}^{(i)}$, column vector of E, whose elements are: $e^{(i)}{}_m$;
- $s^{(i)}$, diagonal elements of S, eigenvalues of C_M.

The symbol " $^+$ " indicates the conjugate (or Hermitian) transpose. Each eigenmode corresponds to an uncorrelated source distribution. A theoretical explanation of this assumption is given in [9], in [39] and in [117]. As highlighted in [39], it is recommended to calculate the CSM taking, as rule of thumb, at least 10×M averages in order to obtain a correct estimation of the Auto-Power Spectra (APS) of the uncorrelated source distributions active in the field through eigenvalue decomposition. This topic will be deepened in section 2.3.1.

$$P = [\ \underline{p}^{(1)} \quad \dots \quad \underline{p}^{(i)} \quad \dots\dots \quad \underline{p}^{(L)} \quad \dots \quad \underline{p}^{(M)}\ ] = E\sqrt{S} \tag{2. 2}$$

In Eq.(1. 7), L represents the number of not negligible eigenmodes of C_M. Physically, each distribution $\underline{p}^{(i)}$ at the array plane is the result of the sound propagation of the corresponding source distribution $\underline{a}^{(i)}$ located at the calculation plane. Assuming a radiation model suitable for monopole sources in free field conditions

$$\{A\}_{m,n} = \frac{e^{-ikr_{mn}}}{4\pi r_{mn}} \tag{2. 3}$$

r_{mn} being the distance between the mth of the M microphones and the nth of the N scan points composing the calculation plane, the radiation problem can be formulated as follows:

$$\underline{a}^{(i)} \quad s.t. \quad A\underline{a}^{(i)} = \underline{p}^{(i)} \quad \forall i = 1,...,L. \tag{2. 4}$$

This implies also that the problem can be solved also considering all the not negligible eigenvalues of the CSM at once:

$$\underline{a} \quad s.t. \quad A\underline{a} = \sum_{i=1}^{L} \underline{p}^{(i)} \; . \tag{2. 5}$$

The inverse problem is solved through the pseudo-inverse of the radiation matrix A. The radiation matrix A is generally ill-conditioned, thus a regularization strategy is required. The Tikhonov's approach is exploited for the inversion. Regularization is obtained by introducing a parameter (λ^2) in the generalized inversion as shown in Eq.(2. 6) where I is the identity matrix of size M×M.

$$\underline{a}^{(i)} = A^H (AA^H + \lambda^2 I)^{-1} \underline{p}^{(i)} \tag{2. 6}$$

Several criteria can be adopted to identify the regularization parameter [45]. Among these, the quasi-optimality function has resulted to be the most effective in GIBF problems [39]. An extensive description of the latter technique is given in section 2.2.

Suzuki [36] proposed to use an iterative process for improving the identification task. He suggested to solve Eq.(2. 6) iteratively for a fixed number of times, updating the problem at each iteration and discarding, from the equivalent source solution vector $\underline{a}^{(i),\, k=*}$, the scan point showing the weakest amplitude (thus the weakest strength). This operation should allow for better posing the inverse problem by discarding the redundant unknowns (therefore reducing numerical instabilities) leading to a more accurate identification of the source distributions.

This approach has the limitation that the threshold to be set for truncation is user-dependent. It could be improved. However it can be considered a solid strategy for optimizing the localization and dynamic range of the resulting acoustic image. Moreover it has demonstrated to be robust in presence of non-ideal conditions of test. In order to ascertain that, the robustness of the algorithm to wrong specifications of the geometry has been tested by simulating the most common errors: wrong positioning of the array in the space, wrong positioning of the microphones within the array. A simulated sine source at 1 kHz has been placed at the coordinate [0.1 m,-0.1 m, 0.6 m] of the acoustic scene depicted as in Fig. 2. 1(a). In the first analysis the array error in positioning is made varying in the range: r_{ideal}+δr_{mis}=0.6m ±0.1m with a 0.01 m step for the distance to the target grid and Φ_{ideal}+$\delta\Phi_{mis}$=0°±10° with a step of 0.1° for the error in angle positioning. Results in Fig. 2. 1(b). In the second case the position of each microphone is made randomly varying within a sphere of radius $\delta\rho_{mis}$=0.01 m. Fig. 2. 1(c).The size of the dots in the maps in Fig. 2. 1(b-c) is proportional to the number of occurrences in which the source has been localized in that position. In both analyses the localization error is within an area of about 0.05 m radius.

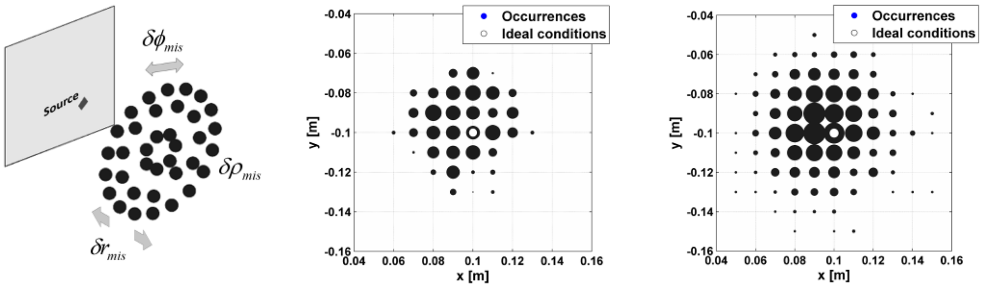

(a) (b) (c)

Fig. 2. 1 : robustness of GIBF algorithm to typical misalignments in the geometry. (a) Statement of the analysis. (b) Results for the combined misalignments δr_{mis} and $\delta\Phi_{mis}$. (c) Results for the combined misalignment $\delta\rho_{mis}$.

2.2. Regularization in GIBF

For inverting the ill-conditioned radiation matrix the Tikhonov's approach is used, as depicted in Eq.(2. 6). Several studies have been conducted in literature aiming at defining the best procedure of regularization in the case of the several version proposed for assessing inverse acoustic imaging problems.

Regarding GIBF, the first proposal came from Suzuki in [36] where it was suggested to choose the regularization parameter λ^2 as a fraction ranging from the 0.1 % to the 5% of the highest singular value of the matrix AA^H (or A^HA if dealing with and over-determined problem). The same approach was used by Zavala in [103]. Such approach may reveal to be oversimplified since the parameter is not updated, therefore not optimized, in the iterative process required by the method. The same author proposed in [37] a so-called *optimized regularization strategy* that relies on the minimization, at each iteration, of a cost function based on the L1-norm of the residual terms of the iterative inverse solution. This method proved to be more accurate in solving the ill-posed problem allowing also a much better strength estimation with respect to the previous version. Presezniak, in [38], does not specifies the adopted regularization strategy in the so-called Generalized Weighted Inverse Beamforming (GWIBF), however in his paper a weighting procedure that helps the matrix inversion to be successful is introduced. It is based on the iterative weighted pseudo-inverse approach presented in [118] and promises to achieve better dynamic range with respect to the GIBF approach as in [37]. Likewise, in [105] Suzuki relates the regularization parameter to a weighting diagonal matrix, acting on the radiation matrix A, that is optimized at each iteration thanks to a L1 norm-based Iteratively Re-weighted Least Square (IRLS) procedure. A similar approach, named "*iterative weighted equivalent source method*" is presented in [52]. Also in the version presented in [112] the regularization strategy relies on the tuning of the singular values of the inversed radiation matrix A. However the author does not propose a clear strategy to optimize this choice.

From this overview emerges that, despite the several alternatives available, the regularization strategy remains one of the most delicate aspects in the GIBF formulation. In the case of other inverse acoustic imaging methods such as IBEM, NAH and ESM in formulations alternative to GIBF, the range of alternative regularization strategies adopted in literature is considerably more circumscribed since it is mainly dominated by three approaches: Generalized Cross-Validation (GCV) [119], L-Curve [120] and the most recent Bayesian regularization [49]. Kim and Nelson compared in [42] GCV and L-Curve performances when dealing with acoustical inverse problems requiring Tikhonov regularization and they concluded that GCV is in general more robust and reliable, especially if the problem is severely ill-conditioned. However they also pointed out that L-Curve performs well in presence of low noise and a better conditioning. A similar conclusion was reached in reference [121], but not in all the possible cases. In fact, the same paper refers to [122] where the authors proved that the L-Curve strategy outperforms GCV in IBEM applications. The GCV and L-Curve strategies performance in dealing with under-determined inverse approaches were compared also by Leclère in [32]. The author found the two methods are nicely complementary and proposed, in the same article, a combination of the two approaches to optimize the regularization. Besides GCV and L-Curve another recent technique, named "*Bayesian approach*" [49] entered the scene. This method, already introduced in section 1.2.2 solves the inverse source reconstruction problem combining physical and probabilistic information on the investigated acoustic scene [50]. In particular, it brings into play any prior information available on the noise source. The integration of such information into the mathematical formulation of the problem turns out to define a novel strategy for the definition of the regularization parameter called "*Bayesian regularization*" [48, 52, 123]. In this case the choice of the optimal regularization parameter is driven by the optimization of a cost function that takes into account the measurement noise at the array level and the nature of the sound sources sought. In [51] Pereira et Al. compared the Bayesian regularization strategy with the L-Curve approach proving that the first one outperforms the other. Moreover the authors point out that the cost function used for the Bayesian regularization has not more than one minimum and for this reason it appears more robust than other options.

Bearing in mind this panorama of options, a study that aims at finding a robust alternative to the state-of-the-art for the regularization strategy of GIBF problems is presented in this section. Four options are considered: quasi-optimality function, GCV, L-Curve and Lagrange multipliers. The interested reader can find the details about those methods in reference [45].

Since it will be the one used in the applications shown in this thesis, the approach based on the so-called quasi-optimality function is shortly described hereafter. Also in this case the choice of the regularization factor λ^2 is adopted taking advantage of the properties of the SVD of A. The candidate regularization factors are chosen among a set of N_r logarithmically distributed regularization parameters between the highest and the lowest non-zero singular value of the radiation matrix A.

Let us define also the Singular Value Decomposition of the radiation matrix A as:

$$A = U\Sigma V^H = \begin{bmatrix} \underline{u}_1 & \cdots & \underline{u}_m & \cdots & \underline{u}_M \end{bmatrix} \begin{bmatrix} \Sigma_{11} & \cdots & 0 & \cdots & 0 & \cdots & 0 \\ \vdots & \ddots & \vdots & & \vdots & & \vdots \\ 0 & \cdots & \Sigma_{mm} & \cdots & 0 & \cdots & 0 \\ \vdots & & \vdots & \ddots & \vdots & & \vdots \\ 0 & \cdots & 0 & \cdots & \Sigma_{MM} & \cdots & 0 \end{bmatrix} \begin{bmatrix} \underline{v}_1 & \cdots & \underline{v}_n & \cdots & v_N \end{bmatrix}^H \quad (2.\ 7)$$

The method consists in the minimization of the following *quasi-optimality function* (Eq.(2. 13)) (see reference [45]):

$$Q(\lambda^2{}_l) = \sqrt{\sum_{m=1}^{M} \left(1 - \frac{\Sigma_{mm}^2}{\Sigma_{mm}^2 + \lambda_l^2}\right) \frac{\Sigma_{mm}^2}{\Sigma_{mm}^2 + \lambda_l^2} \frac{\underline{u}_m^H \underline{p}^{(i)}}{\Sigma_{mm}}} \ . \quad (2.\ 8)$$

Notice that the physics of the investigated acoustic problem is present through the used microphones array information $\underline{p}^{(i)}$. The optimal regularization parameter is therefore λ^2:

$$\lambda^2 \in [\min(\Sigma), \max(\Sigma)]\, s.t.\;\; Q(\lambda^2) = \min\left(Q(\lambda^2{}_l), \forall l\right). \tag{2. 9}$$

In the GIBF algorithm described above, an optimal regularization parameter (λ_k^2) is chosen at any iteration allowing the solution to be obtained in the form:

$$\underline{a}^{(i),k} = \sum_{m=1}^{M} \frac{\Sigma_m^2}{\Sigma_m^2 + \lambda_k^2} \frac{\underline{u}_m^H \underline{v}_m}{\Sigma_m} \underline{p}^{(i)} \tag{2. 10}$$

or, equivalently, as:

$$\begin{aligned} \underline{a}^{(i),k} &= A^H (AA^H + \lambda_k{}^2 I)^{-1} \underline{p}^{(i)} \quad if \quad M < N \\ \underline{a}^{(i),k} &= (A^H A + \lambda_k{}^2 I)^{-1} A^H \underline{p}^{(i)} \quad if \quad M > N \end{aligned} \tag{2. 11}$$

The four alternative methods (quasi-optimality, GCV, L-Curve, Lagrange) select from a set of candidates values the optimal regularization factor as the one that minimizes (the corner for the L-Curve) a certain function related to the inverse problem to be solved. Fig. 2. 2 presents a comparison between the methods in presence of a sinusoidal source at 1 kHz and 1 Pa amplitude placed at the coordinate: [0.01 m -0.01 m, 0.6 m] in the shown maps.

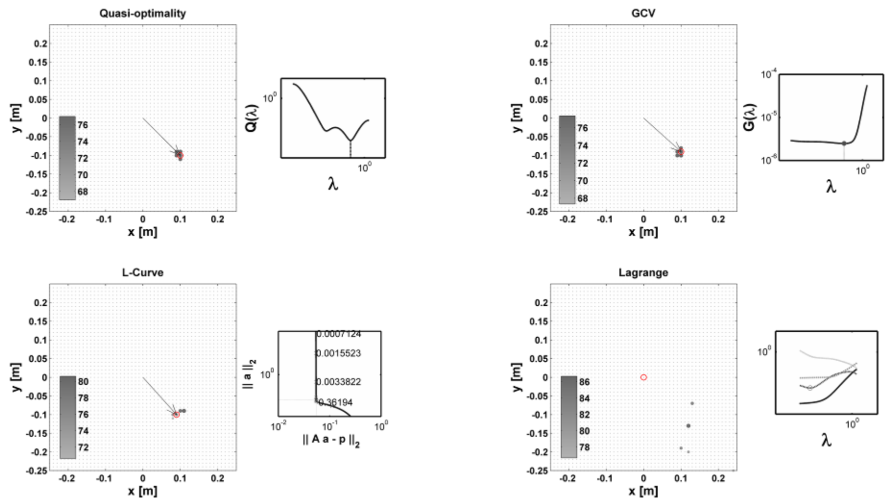

Fig. 2. 2 : comparison of GIBF results with different regularization strategies.

The most effective are the quasi-optimality and GCV functions. The L-Curve still allows localizing the source with a less clear pattern.

Fig. 2. 3 shows the trend of the chosen regularization factor during the iterative process of the GIBF algorithm in the four cases. Quasi-optimality and GCV functions yield a similar regularization factor after the first iterations.

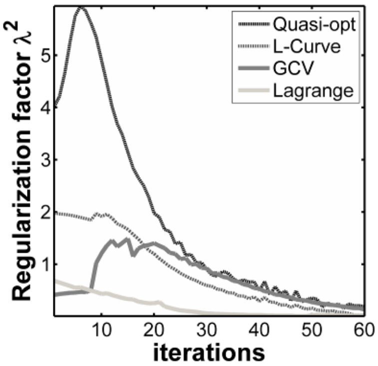

Fig. 2. 3 : trend of the regularization parameters during GIBF iterations.

As already mentioned, in the inverse acoustic imaging applications reported in this thesis the quasi-optimality function will be always utilized except in the case of the section 3.4 of Chapter 3 in which, when applying GIBF adopting a rigid scattering spherical array, other strategies such as GCV and L-Curve have proven to be more robust.

2.3. Uncorrelated noise sources separation in GIBF

The separation of a measured sound field in uncorrelated sources distributions can be very useful when dealing with sound source localization problems. In acoustic imaging this is a challenging task because the acoustic sources have, besides their time evolution and frequency content, also a spatial nature that add an additional complexity to the source separation problem. In order to obtain the separation of an acoustic image of the sought sound sources into uncorrelated distributions one can use coherence-based methods that rely on reference sensors which are physically placed in the proximity of the noise sources under study [89, 124]. However this is not always convenient because it requires additional sensors and a more complex setup. In some applications, such as wind tunnel aero-acoustic testing, the installation of reference sensors is even almost impossible. In order to overcome the limitations of this approach, it is possible to resort to Blind Source Separation (BSS) techniques. BSS methods have the advantage that they do not necessarily require reference sensors. Generally speaking such techniques rely on assumptions capable to describe the way the sought uncorrelated sources become the mixture observed by the acoustic array. Among the manifold instruments to implement BSS approaches, the PCA of the CSM between the signals of the microphones array is one of the most addressed in literature [36, 39, 46, 107, 116]. The main idea is to enforce the separation of the information available at the microphones array level in partial acoustic fields by means of the eigenvalues decomposition of the CSM as already introduced in Eq.(2. 1). Besides the advantage of being very simple to implement and it does not require any additional information on the acoustic field, this approach has the limitation that it does not ensures that the uncorrelated sources retrieved are actually corresponding to physical sound sources. Another possibility is to perform the PCA of the reconstructed acoustic image and not of the acoustic field sampled at the array level [47, 125]. This will allow to separate the acoustic image in the contributions of "*virtual sources*", but similarly to the previous case, the uniqueness of the separation is not granted and some (or all) of the virtual sources may not correspond to physical sound sources. In order to find a unique solution Dong et Al. proposed the so-called principle of "*least spatial complexity*" [126] and "*least spatial entropy*" [44] that select, among the possible virtual sources, the ones with maximum spatial compactness. The same authors, in a recent article [127], state that the PCA is a necessary but not a sufficient condition for source separation. In order to provide the sufficient condition a criterion that enforces the uncorrelated sources to be also *spatially orthogonal* is therefore given in the paper.

The use of GIBF, offers the possibility to resolve complex and partially correlated sound sources distributions if used in combination with a PCA of the acoustic field [103]. This makes it particularly suitable in problems of sound source localization whether many causes of noise, uncorrelated each other, are active at the same time [36, 113]. This for several reasons: first of all an inverse approach allows defining the most appropriate radiation model [103, 106, 112]) for the case in study, allowing also to quantify the strength of the noise sources active in the field; moreover the accuracy in localizing point as well as distributed noise sources is rather constant in frequency. In this section, the synergy between the PCA-based uncorrelated acoustic sources separation principle and the use of GIBF will be tackled. The limitations of the approach will be tested in paragraph 2.3.1. Guidelines in terms of optimal processing parameters will be given and limitations in terms of the tolerated background noise level and the characteristics of the investigated sound field will be pointed out. In paragraph 2.3.2 the absolute quantification of uncorrelated sound source distribution will be studied and a sufficient condition, based on the strength estimation provided by the eigenvalues of the CSM, will be proposed for discriminating between virtual and physical sources distributions obtained in the acoustic images of the partial fields decomposed through PCA.

2.3.1. PCA of the CSM for uncorrelated noise source separation

Let us consider, as in Fig. 2. 4, two uncorrelated sources: $s_1(t)$ and $s_2(t)$ whose spectra are: $S_1(\omega)$, $S_2(\omega)$, and two microphones m_1 and m_2 receiving the abovementioned sources. If $P_1(\omega)$ and $P_2(\omega)$ are the spectra of the measured signals, the radiation problem can be modelled as in Eq.(2. 12) and the CSM between the signals at the microphones of such a problem is given by Eq.(2. 13).

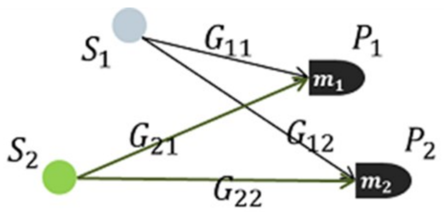

Fig. 2. 4 : sources (S_1 and S_2) radiation towards microphones (P_1 and P_2).

$$\begin{pmatrix} P_1 \\ P_2 \end{pmatrix} = \begin{bmatrix} G_{11} & G_{21} \\ G_{12} & G_{22} \end{bmatrix} \begin{pmatrix} S_1 \\ S_2 \end{pmatrix} \tag{2. 12}$$

$$C_M = \begin{bmatrix} (S_1G_{11} + S_2G_{21})(S_1G_{11} + S_2G_{21})^* & (S_1G_{11} + S_2G_{21})(S_1G_{12} + S_2G_{22})^* \\ (S_1G_{12} + S_2G_{22})(S_1G_{11} + S_2G_{21})^* & (S_1G_{12} + S_2G_{22})(S_1G_{12} + S_2G_{22})^* \end{bmatrix} \tag{2. 13}$$

Assuming uncorrelated sources, ideally we have that $i \neq j \Longrightarrow S_iS_j^* = 0$. Moreover: $G_{kl}G_{mn}^* = 1 \Leftrightarrow k = m \wedge l = n$. So:

$$C_M = \begin{bmatrix} S_1^{\,2} + S_2^{\,2} & S_1^{\,2}(G_{11}G_{12}^*) + S_2^{\,2}(G_{21}G_{22}^*) \\ S_1^{\,2}(G_{12}G_{11}^*) + S_2^{\,2}(G_{22}G_{21}^*) & S_1^{\,2} + S_2^{\,2} \end{bmatrix} \tag{2. 14}$$

Therefore it is composed by two parts, in this case: one dominated by S_1 and the other dominated by S_2:

$$C_M = S_1^{\,2}\begin{bmatrix} 1 & (G_{11}G_{12}^*) \\ (G_{12}G_{11}^*) & 1 \end{bmatrix} + S_2^{\,2}\begin{bmatrix} 1 & (G_{21}G_{22}^*) \\ (G_{22}G_{21}^*) & 1 \end{bmatrix} \tag{2. 15}$$

Recalling that C_M is by definition Hermitian, as already explained in section 2.1, Eq.(2. 1), the eigenvalue decomposition of the CSM, $C_M = ESE^H$, can be obtained, for the very specific case just described, in the form:

$$E = \begin{bmatrix} G_{11} & G_{21} \\ G_{12} & G_{22} \end{bmatrix} \quad , \quad S = \begin{bmatrix} S_1^{\,2} & 0 \\ 0 & S_2^{\,2} \end{bmatrix} \tag{2. 16}$$

Eq.(2. 12) and Eq.(2. 16) testify, in fact, that under the assumption of uncorrelated phenomena, the eigenvalue decomposition of the CSM yields the Auto-Power Spectra (APS) of each uncorrelated sources as eigenvalues, while the eigenvectors depend only on the propagation model.

This interesting result, if combined with GIBF using the just described PCA approach as in Eq.(2. 4)-(2. 6), can be exploited to:

- Ascertain the number of uncorrelated sources active in the field.
- Retrieve their strength by means of their corresponding eigenvalue of the CSM.
- Filter out the background noise by discarding the lowest eigenvalues of CSM.

This feature can be in fact exploited for deciding the number and which uncorrelated sources to be used to reconstruct the sound field. This operation will tell information also about the background noise present in the data and if the number of averages taken for computing the CSM is enough for correctly filter it out through the PCA. In order to understand the mutual influence of such parameters (number of averages for the CSM computation and SNR of the measurement data), a sensitivity analysis has been carried out on numerical simulations performed on a virtual problem in which two uncorrelated white noise sources (Source#1 and Source#2) are active in the frequency range 200 Hz – 20 kHz. An array of 36 microphones is placed at a distance of 0.6 m far from the source plane. The geometry of the problem is depicted in Fig. 2. 5.

The cross-influence of all the combinations of the following parameters on the GIBF algorithm has been studied:

- Number of averages taken for CSM (AVG): 1000,667,500,333,100,50,33,10.
- Background noise in data (SNR_{dB}): 50,40,30,20,17,10,7,0.

The signals sample rate is 20480 Hz. The beamforming simulation has been carried out in time domain by simulating the delays at the different microphone positions. In all the GIBF calculations has been considered a scan points distribution equally spaced in the calculation plane with a spatial resolution of 0.01 m.

The CSM has been calculated keeping a frequency resolution of 10 Hz. This choice is driven by an analysis on this parameter which is not reported because did not show clearly identifiable trends, but it demonstrated that 10 Hz is a good compromise for strength estimation and calculation time. If not differently specified, the results described below will be presented at a frequency of 1 kHz.

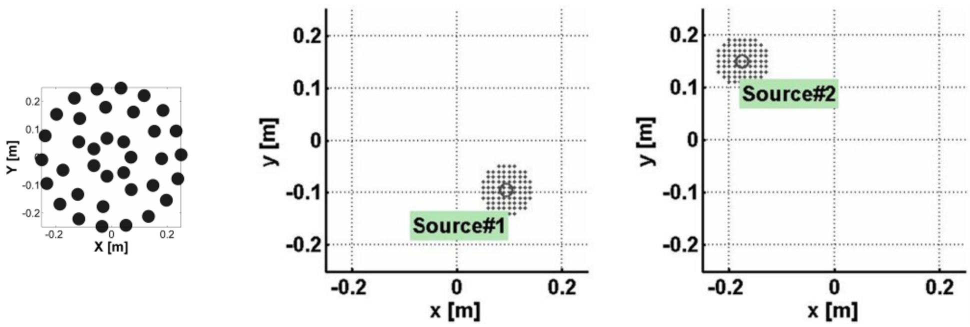

(a) *(b)*

Fig. 2. 5 : problem statement. (a) Array geometry. (b) Sources locations and respective areas of tolerance.

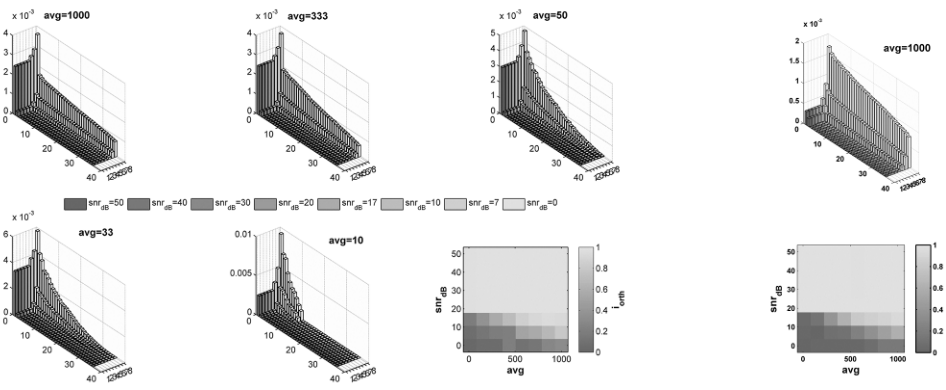

(a) *(b)*

Fig. 2. 6 : Eigenvalues trend (AVG vs. SNR) and indicator i_{orth} for two scenarios: (a) Strength Source#1 > Strength Source#2, and (b) Strength Source#1 > Strength Source#2.

According to Eq.(1. 7) and Eq.(2. 6), since the solution $\underline{a}^{(i),k=0}$ is related to the i^{th} eigenmode of the CSM ($\underline{p}^{(i)}$), its propagation $A\underline{a}^{(i),k=0}$ towards the array is by definition orthogonal to any other eigenmode of the CSM. This can be checked exploiting the so-called Modal Assurance Criterion (MAC) [128], i.e. producing the *MAC* matrix, based on the inner products between the $A\underline{a}^{(i),k=0}$ and $\underline{p}^{(j)}$ functions. In fact, if there are L relevant sources active in the field, it must be:

$$\left\langle A\underline{a}^{(i),k=0},\underline{p}^{(j)}\right\rangle = 0 \quad \forall j \neq i \quad , \quad i,j = 1,...,L. \tag{2. 17}$$

In the ideal case depicted by Eq.(2. 17) the MAC matrix coincide to the identity and its determinant is equal to 1. Its determinant becomes < 1 in any other case. This property can be used for verifying the results. Let us define the following indicator (in Eq.(2. 18)) whose trend is shown in Fig. 2. 6 in the case of two scenarios: one, *(a)*, in which one source's strength is higher than the other, the other, *(b)*, in which the two sources have equal strength.

$$i_{orth}(i,j) = \det(MAC(A\underline{a}^{(i),k=0},\underline{p}^{(j)})) = \begin{cases} 1 \rightarrow \quad \textit{solution orthogonal} \\ <1 \rightarrow \textit{solution NOT orthogonal} \end{cases} \tag{2. 18}$$

Fig. 2. 6 also shows, in two scenarios, the eigenvalues of the CSM ranked in a descended order and grouped per SNR and different number of averages showing that, for GIBF applications, the number of averages should be at least 10×M (M is the number of microphones), for having the main eigenvalues stable for quantification purposes.
As expected the SNR has a strong influence on the i_{orth} therefore on the solution. Uncorrelated sources with different frequency content permit to tolerate slightly more severe SNR conditions.

2.3.2. Exploiting the uncorrelated sources APS estimation for the interpretation of the acoustic imaging results

In addition to the correct localization of the sound sources active in the field, and their separation in uncorrelated source distributions, it is therefore possible to obtain quantitative results from the inverse beamforming solution. This section focuses on a criterion that can be exploited for this purpose and to ascertain that each separated virtual uncorrelated source distribution actually correspond to its physical counterpart.
The eigenvalues decomposition of the CSM C_M gives an estimation of the APS of the uncorrelated source distributions active in the acoustic field under study. In fact, the same APS quantitative information can be retrieved by energetically integrating the source distribution in the GIBF map. In this way, the APS of the ith uncorrelated source active in the field can be obtained using Eq.(2. 19),

$$(\Theta_i)^2 = \frac{s_i - s_M}{\rho^2 M R_r} \tag{2. 19}$$

Where:

- M is the number of microphones of the array;
- $s_i \in S$ is the ith eigenvalue of the CSM;
- s_M the minimum eigenvalue that can be considered an estimation of the background noise;

- $R_r=(1/4\pi r)^2$ is the propagation factor, where r is the distance between the array plane and the calculation plane;
- ρ is the density of the air;
- Θ_i is the volume acceleration of the ith source.

The proposed criterion is based on the assumptions that:

- A source is represented by aggregate groups of monopoles whose patterns are detectable through pattern recognition [129, 130, 150].
- The monopoles of a pattern have a uniform phase (per frequency line) within the pattern.

In order to describe the criterion, let us assume to deal with a source distribution represented by two correlated monopole sources respectively placed at (0 m,0.1 m) and (0.1 m,-0.1 m) and labelled as $\underline{a}^{(i)}(\underline{n}_{\zeta=1})$ and $\underline{a}^{(i)}(\underline{n}_{\zeta=2})$ respectively. Let's also assume that $\underline{a}^{(i)}(\underline{n}_{\zeta=3})$ and $\underline{a}^{(i)}(\underline{n}_{\zeta=4})$, are numerical issues which are not related with the source distribution. Such condition is represented in Fig. 2. 7(a).

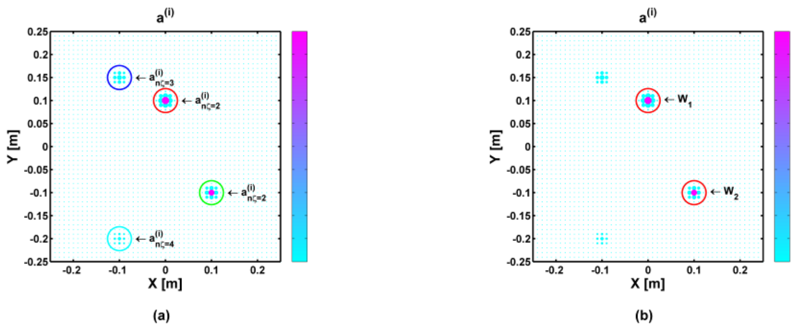

Fig. 2. 7 : example of application of the criterion of sources labelling and identification.

Assuming that in this case the unit of the coefficients of the distribution $\underline{a}^{(i)}$ is [m^3/s^2] it is possible to proceed as follows:

1) Localize the $K^{(i)}$ patterns $\underline{n}_\zeta$ in the GIBF map $\underline{a}^{(i)}$ and calculate their centroids.
2) Quantify each pattern's power through integration in the pattern area of the map:

$$W_\varsigma = \frac{\rho}{8\pi c}\sum_{n\in\underline{n}_\varsigma}(a_n^{(i)})^2 \quad . \tag{2. 20}$$

3) Identify the pattern or the set of patterns $\varphi_\gamma^{(i)}$ that minimizes the check function $\Pi^{(i)}$:

$$\Pi^{(i)} = \left| \sum_{k=1}^{K^{(i)}} \varphi_{\gamma}^{(i)}(k) W_{\varsigma} - \frac{\rho}{8\pi c} (\Theta_i)^2 \right| \tag{2. 21}$$

where:

$$\varphi_{\gamma}^{(i)}(k) = \begin{cases} 1, & \textit{pattern } \underline{n}_{\varsigma} \textit{ DOES belong to the combination } \gamma \\ 0, & \textit{pattern } \underline{n}_{\varsigma} \textit{ DOES NOT belong to the combination } \gamma \end{cases} \tag{2. 22}$$

The use of this algorithm makes is possible to obtain a reliable labelling and identification of the sources (Fig. 2. 7(b)), In the depicted case, the algorithm acts as in Eq.(2. 23).

$$\varphi_{\gamma}^{(i)} = [1 \quad 1 \quad 0 \quad 0] \rightarrow \min(\Pi^{(i)}) = \left| W_1 + W_2 - \frac{\rho}{8\pi c} (\Theta_i)^2 \right| \tag{2. 23}$$

Despite limited by the assumption of monopole source distribution (see also [39]), the proposed approach represents an interesting method for correct quantification of equivalent sources distributions. A similar method that takes advantage of the Clustering Inverse Beamforming formulation is presented in Chapter 3, while an example of application is presented below. In this numerical simulation, two uncorrelated sources have been used in the geometrical configuration depicted in Fig. 2. 5. In this case Source#1 is a random noise in the range 200 Hz – 20 kHz, while Source#2 is a recorded electric engine noise signal. The analysis reported in Fig. 2. 8 is limited in the range 800 Hz – 5 kHz.

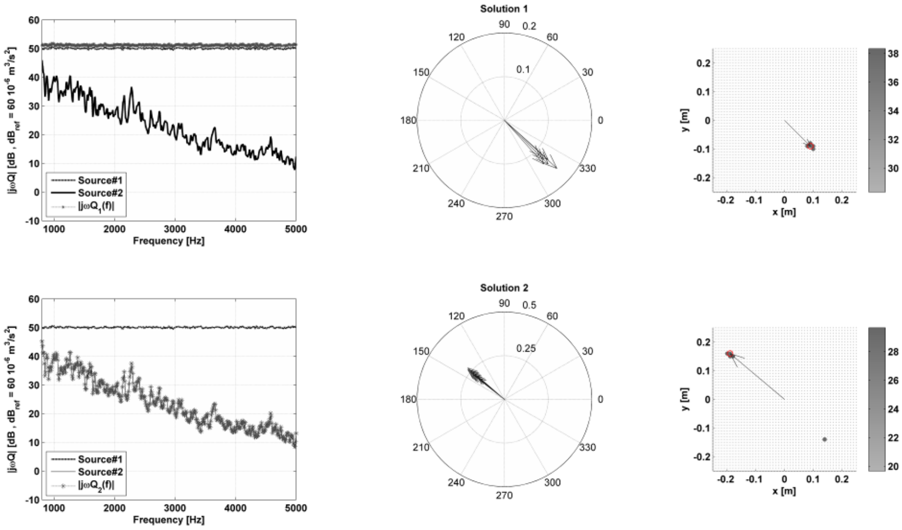

(a) *(b)* *(c)*

Fig. 2. 8 : Interpretation of the acoustic imaging results through uncorrelated APS estimation. (a) Retrieved spectra compared with the original signals. (b) Compass diagrams reporting the location of the sources retrieved at any frequency line in the range 800 Hz – 5 kHz. (c) An example of acoustic map at 1 kHz.

Fig. 2. 8 shows how the criterion described in this section helps the user in the interpretation of the obtained inverse acoustic image. In this case the results are reported in volume acceleration (unit: m^3/s^2). As it can be noticed, the criterion helps in the presence of artifact an unwanted numerical issues.

2.4. PCA-based pre-processing for improved solution

This section aims at formulating a generic pre-processing method that, combined with existing ESM methods, such as GIBF, optimizes the inverse beamforming solution leading to the identification of the source distributions on the calculation plane. The method is based on the observation that it is possible to reduce the number of scan points during the iteration step, by exploiting the dimensionality reduction capabilities of PCA (see reference [131] for an example of application in image processing) if applied on the running matrix of scan points. This approach makes it possible to design a criterion for selecting the equivalent sources on which to focus during the iteration step for reducing the numerical size of the inverse problem and its degree of under-determination. The benefits of this approach are: better dynamic range, better separation of the sound field into uncorrelated sources distributions, reduced computation effort and improved robustness of the regularization strategy.

The PCA of the CSM is not a sufficient condition for decomposing the investigated acoustic field into uncorrelated partial distribution of sources, but it has been demonstrated in the previous section that its use greatly improves the solution of GIBF. This is because it removes the back-ground noise in the array data, mitigating the issues related to the ill-conditioning of the inverse problem, and provides an accurate ranking of the sources under certain conditions. Moreover it was observed in section 2.3, and it will be reaffirmed through examples below, that the discrepancy between the virtual uncorrelated sources distributions and the physical ones is mainly due to two factors: numerical issues related to the inversion of the problem and leakage of the contribution of one uncorrelated source into the acoustic images of the others. The first ones appear in the acoustic images as non-aggregated and randomly distributed sources, while the seconds occur as aggregated patterns in the ideal location of the sources belonging to the other principal components. They therefore still keep a physical meaning, contrary to those of the former category. Both types of discrepancy are deleterious for the GIBF iterative process that narrows the under-determined inverse problem down to an optimized over-determined version. This suggests to tackle both issues before performing the iterative optimization.

The iterative optimization approach introduced in section 2.1 starts with a distribution ($\underline{a}^{(i),k=0}$) of equivalent sources which cover the whole calculation plane. Additionally, the inverse problem of Eq.(2. 6) is calculated per eigenmodes, therefore, all the equivalent sources should theoretically belong to a unique correlated source distribution related to the corresponding eigenvalue ($s^{(i)}$, corresponding in its turn to the $\underline{p}^{(i)}$ distribution at the microphone array plane) of the CSM. This is not the case for the initial solution $\underline{a}^{(i),k=0}$, assuming that the adopted radiation law (Eq.(2. 3)) is correct, when either there is uncorrelated background noise due to numerical instabilities or the separation in virtual uncorrelated contributions by the eigenvalue decomposition of the CSM does not correspond entirely to the actual physical source distributions. While the reduction of the number of scan points, as Suzuki [36] suggested, may solve the issue related to numerical instabilities, the presence of an anomalous mixture of uncorrelated phenomena in one eigenmode can irreparably compromise the quality of the final solution (i.e. the correct identification of the source distributions). This suggests adopting a strategy that is effective for tackling both problems, i.e. that is able to refine the separation of the acoustic field in uncorrelated phenomena and to avoid the numerical instabilities due to the ill-conditioning of the problem. This could be done through a modular approach that couples the BSS of the array data into virtual uncorrelated sources distribution through eigenvalues decomposition of the CSM with an adaptive pre-processing based on the PCA of the corresponding acoustic images before applying the GIBF iterative algorithm or other optimization strategies. The idea of the proposed approach is to perform a PCA on the complex $\bar{a}^{(i)}$ matrix (the superscript $k=0$ will be, from now on, omitted for making the text more readable), which is a mapping of the equivalent source vector on the scan points' location over the calculation plane. In this work the method is described in the case of a square calculation plane and the equivalent sources are equally spaced in the two dimensions of the plane. This will make the method easier to describe. In this case the $\bar{a}^{(i)}$ matrix assumes size: $n_y \times n_x$ where n_x and n_y are given by the discretization of the calculation plane in its two dimensions and the product $n_x \cdot n_y$ equals the number N of equivalent sources that discretize the calculation plane. In cases in which the calculation region assumes a different shape, even 3D, such complex geometry should be transformed and projected onto a rectangular plane discretized with equally spaced equivalent sources before performing the proposed PCA-based pre-processing. The assessment of such complex cases goes beyond the purposes of this document and will not be discussed below. However such additional complexity does not represent a limitation of the proposed technique.

The PCA approach will reduce the numerical instabilities (de-noising of the $\bar{a}^{(i)}$ map) and it will decompose the scan points matrix in uncorrelated terms. Indeed, only few principal components will be actually related to the source distribution, while the rest of the components will describe artefacts and other unwanted features of the retrieved matrix. The comparison with PCA performed on an image is straightforward, also because the $\bar{a}^{(i)}$ matrix can effectively be considered as an image mapping the source distributions. Notice that we will refer to $\bar{a}^{(i)}$ when describing the 2D matrix reshaped representation of the solution (1D) vector $\bar{a}^{(i)}$ obtained solving Eq.(2. 6) .

An adaptive criterion for defining an optimal dynamic range that makes it possible to discard, in a single iteration, those scan points that do not contribute to the acoustic field and to de-noise the initial solution from unwanted uncorrelated background noise or spurious ghost sources will be presented in the next sections. This operation is done on the full set of scan points before starting the optimization process.

For describing the approach, numerical simulations have been performed adopting an array (Fig. 2. 9) of 43 randomly distributed microphones. In the simulated scenario two uncorrelated band limited (0 Hz – 8 kHz) white noise monopole sources of the same strength are placed on a calculation plane 0.6 m far from the array. In such plane the coordinates of the source are: [-0.07 m, 0.09 m] for Source#1 and [0.18 m, -0.17 m] for Source#2. The calculation plane covers an area of 0.5 m × 0.5 m and it is discretized by scan points which are equally spaced with a step of 0.01 m in both the dimensions of the plane ($n_x = n_y = 51$, $N = n_x \cdot n_y = 2601$).

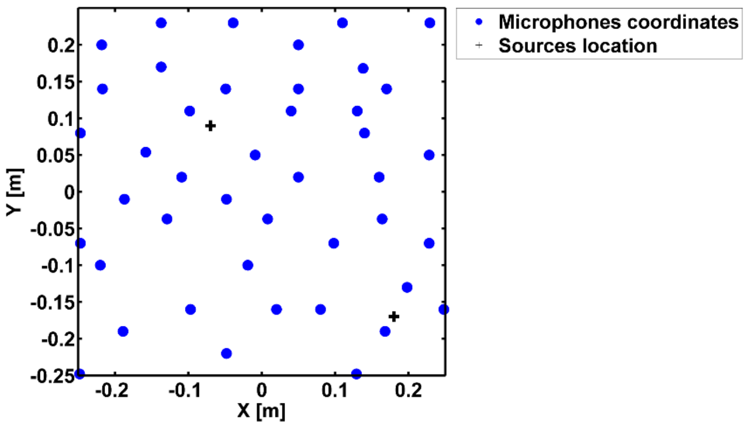

Fig. 2. 9 : Array of microphones used in the numerical simulation.

2.4.1. Adaptive selection of the main principal components of $\bar{a}^{(i)}$

A PCA on the $\bar{a}^{(i)}$ matrix can be performed by exploiting the SVD factorization, as in Eq.(2. 24),

$$\bar{a}^{(i)} = \Phi_{(i)}\Omega_{(i)}\Psi_{(i)}^{H} = \Phi_{i}\begin{bmatrix} \omega_1 & 0 & 0 & \dots & 0 \\ 0 & \omega_2 & 0 & 0 & 0 \\ 0 & 0 & \omega_j & 0 & 0 \\ \vdots & \vdots & \vdots & \ddots & \vdots \\ 0 & 0 & 0 & \dots & \omega_J \end{bmatrix}_{(i)} \Psi_{(i)}^{H} \qquad (2.\ 24)$$

that reports the singular values (SV) ω_j in descending order making explicit that the last SV is much smaller than the first one ($\omega_J << \omega_1$). The columns of Φ ($n_y \times n_y$) and Ψ ($n_x \times n_x$) are the left-singular vectors and right-singular vectors respectively. The size of Ω is $n_y \times n_x$, the same size of the decomposed matrix. Eq.(2. 24) has been specialized to the case of the proposed example $n_x = n_y$. However what described below applies also to the most general cases.

When considering the numerical simulation previously presented, where two uncorrelated noise sources actively contribute to the sound field, the overall source distribution at the calculation plane can be obtained, as a first solution, as reported in Eq.(2. 25). In this equation, q_c represents the equivalent sources strength distribution at the calculation plane, r_c is the vector defining the location of each scan point and f expresses the frequency dependence. A graphical representation is shown in Fig. 2. 10(a).

$$q_c(r_c, f) \approx \underline{a} = A^+(AA^+ + \lambda^2 I)^{-1}(\underline{p}^{(i=1)} + \underline{p}^{(i=2)}) \qquad (2.\ 25)$$

Performing a PCA on the matrix form of $\underline{a}$, i.e. $\bar{a}$, by exploiting Eq.(2. 25) will entail the first three principal components to be expressed as:

$$\bar{a}_{j=1}^{(i=1+i=2)} = \Phi_{i=1+i=2,j=1} \begin{bmatrix} \omega_1 & 0 & 0 & \dots & 0 \\ 0 & 0 & 0 & 0 & 0 \\ 0 & 0 & 0 & 0 & 0 \\ \vdots & \vdots & \vdots & \ddots & \vdots \\ 0 & 0 & 0 & \dots & 0 \end{bmatrix}_{i=1+i=2} \Psi_{i=1+i=2,j=1}^{H} \qquad (2.\ 26)$$

$$\bar{a}_{j=2}^{(i=1+i=2)} = \Phi_{i=1+i=2,j=2} \begin{bmatrix} 0 & 0 & 0 & \dots & 0 \\ 0 & \omega_2 & 0 & 0 & 0 \\ 0 & 0 & 0 & 0 & 0 \\ \vdots & \vdots & \vdots & \ddots & \vdots \\ 0 & 0 & 0 & \dots & 0 \end{bmatrix}_{i=1+i=2} \Psi_{i=1+i=2,j=2}^{H} \qquad (2.\ 27)$$

$$\bar{a}_{j=3}^{(i=1+i=2)} = \Phi_{i=1+i=2,j=3} \begin{bmatrix} 0 & 0 & 0 & \dots & 0 \\ 0 & 0 & 0 & 0 & 0 \\ 0 & 0 & \omega_3 & 0 & 0 \\ \vdots & \vdots & \vdots & \ddots & \vdots \\ 0 & 0 & 0 & \dots & 0 \end{bmatrix}_{i=1+i=2} \Psi_{i=1+i=2,j=3}^{H} \qquad (2.\ 28)$$

A graphical representation of the overall case of Eq.(2. 25) and the components obtained in equations from Eq.(2. 26) to Eq.(2. 28) for the virtual test case is reported in Fig. 2. 10(a), (b), (c) and (d) respectively.

Fig. 2. 10 shows that a PCA performed on $\bar{a}^{(i=1+i=2)}$ makes it possible to decompose the sound field in principal components that are linked to the uncorrelated sources causing the sound field. Any uncorrelated background noise is assigned to the lower order principal components. Such PCA step therefore produces similar results to those obtained by exploiting equations from Eq.(2. 1) to Eq.(2. 6), under the main difference that the analysis is performed on the calculation plane domain. Mathematically this means that, for the strongest uncorrelated components, $\bar{a}_j \sim \bar{a}^{(i)}$.

This observation opens up several interesting scenarios. Indeed, one could think to perform a further PCA step on each $\bar{a}^{(i)}$ matrix, in order to separate the actual information related to the presence of a source from any other disturbing information such as numerical issues and/or unwanted anomalous uncorrelated sources leaking in the source distribution retrieved from Eq.(2. 6). The benefits of such approach for the $\bar{a}^{(i=1)}$ and the $\bar{a}^{(i=2)}$ matrices are clear when observing Fig. 2. 11 and Fig. 2. 12 respectively. Fig. 2. 11(a) and Fig. 2. 12(a) report the original $\bar{a}^{(i=1)}$ and the $\bar{a}^{(i=2)}$ matrices (source distributions at 2 kHz) retrieved from Eq.(2. 6) for the two first eigenmodes $\underline{p}^{(i=1)}$ and $\underline{p}^{(i=2)}$.

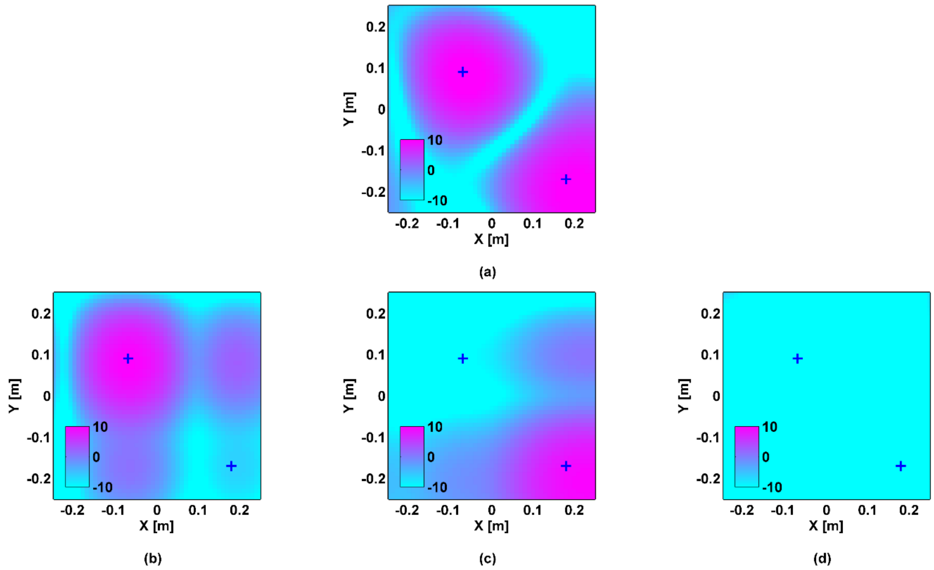

Fig. 2. 10 : Sound Pressure Level (SPL) maps @ 2 kHz (dB$_{ref}$=20 μPa) related to the $\underline{a}^{(i=1+i=2),k=0}$ *solution of Eq.(2. 25). (a)* $\overline{a}^{(i=1+i=2)}$*; (b)* $\overline{a}_{j=1}^{(i=1+i=2)}$*; (c)* $\overline{a}_{j=2}^{(i=1+i=2)}$*; (d)* $\overline{a}_{j=3}^{(i=1+i=2)}$.

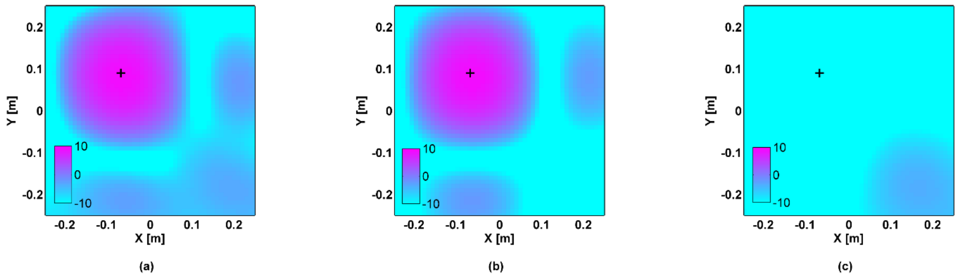

Fig. 2. 11 : SPL maps @ 2 kHz (dB_{ref}=20 μPa) related to $\underline{a}^{(i=1),k=0}$ *and its principal components: (a)* $\overline{a}^{(i=1)}$*, (b)* $\overline{a}^{(i=1)}_{j=1}$ *and (c)* $\overline{a}^{(i=1)}_{j=2}$.

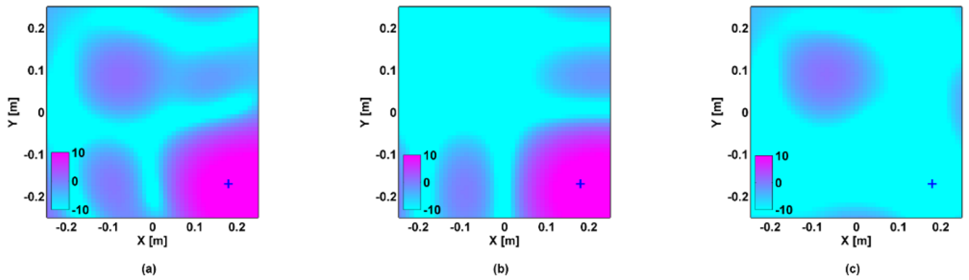

Fig. 2. 12 : SPL maps @ 2 kHz (dB_{ref}=20 μPa) related to $\underline{a}^{(i=2),k=0}$ *and its principal components: (a)* $\overline{a}^{(i=2)}$*, (b)* $\overline{a}^{(i=2)}_{j=1}$ *and (c)* $\overline{a}^{(i=2)}_{j=2}$.

Since the two main SV of the CSM of the numerical simulation proposed, which correspond to $\underline{p}^{(1)}$ and $\underline{p}^{(2)}$, are treated separately, nothing but the sources centered in [-0.07 m , 0.09 m] for $\bar{a}^{(i=1)}$ and [0.18 m , -0.17 m] for $\bar{a}^{(i=2)}$ are supposed to be present in the solutions. Nevertheless, although weaker than the main sources, ghost sources and numerical issues are recognizable. If not correctly faced, this phenomenon has proved to cause errors in the identification of the sources and in the reconstruction of the active acoustic field, as discussed in [39] and [132]. In fact the optimization process normally utilized in GIBF and described in [39] would be irreparably biased by the presence of such numerical issues. By performing a PCA on the $\bar{a}^{(i=1)}$ and the $\bar{a}^{(i=2)}$ matrices the solutions reported in Fig. 2. 11(b-c) and Fig. 2. 12(b-c) are obtained. These figures report, respectively for each $\bar{a}^{(i)}$ matrix, the first two principal components, $\overline{a}^{(i)}_{j}$ j=1,2, obtained from the SVD factorization performed on the scan points domain. Fig. 2. 11(c) and Fig. 2. 12(c) also show that the $\overline{a}^{(i)}_{j=2}$, $i=1, 2$ solutions contain information related to the weakest source, i.e. $a_{j=2}^{(i=1),k=0} \rightarrow a^{(i=2),k=0}$ and $a_{j=2}^{(i=2),k=0} \rightarrow a^{(i=1),k=0}$. The Truncated Singular Value Decomposition (TSVD) of the source map, performed as described above, therefore provides a more correct starting point for the GIBF iterative optimization process, thus making it more robust.

In order to guarantee a valid identification of the source distributions, a truncation order selection method is now required. A robust approach should ground on an adaptive criterion that makes it possible to retrieve the truncation order depending on the composition of each SV matrix $\Omega_{(i)}$. It has been observed in fact that it is possible to associate the transition from the amplitude of the SV that bring the information related to the source distribution, the relevant SV, and the others that are related to artefacts, background noise and leakage of the contribution of other uncorrelated sources active in the acoustic scene (as depicted in the example given in Fig. 2. 12), to a sudden change of the trend of the SV amplitude if they are ranked in a descending order. However such behavior is strongly related to the specific acoustic problem and it is in general not possible to know a priori the number of uncorrelated sources which are active in the acoustic scene under study, moreover the level of background noise will influence the amplitude of the lowest SV. Therefore an adaptive threshold is required. The idea is to link such threshold not only to the absolute amplitude of the relevant SV, but also to the relative amplitude with respect to the lower ones. The method proposed by the authors uses the minimization of the cost function reported in Eq.(2. 29).

$$\Gamma(j) = \begin{cases} \hat{\omega}_j & if \quad j = 1 \\ \hat{\omega}_j + \alpha(\hat{\omega}_j - \hat{\omega}_{j-1}) & if \quad j = 2,...,J \end{cases} \tag{2. 29}$$

where $\hat{\omega}_j$ can be expressed as in Eq.(2. 30):

$$\hat{\omega}_j = \frac{\omega_j}{\sum_{j=1}^{J} \omega_j} \tag{2. 30}$$

In Eq.(2. 30) the SV ω_j are normalized to 1 with respect to the sum of the entire set of J singular values. They are ranked in descendent order: $\omega_1 > \omega_2 > \cdots > \omega_J$. It will be demonstrated below that such a cost functions presents a minimum in correspondence of the change of the trend of the SV amplitude at can be used for classifying the set of singular values that bring the information related to the wanted source distribution. The proposed truncation criterion consists in selecting all the SV with index $j < \hat{j}$, where $\hat{j}$ is expressed according to Eq.(2. 31).

$$\hat{j} \quad s.t. \quad \Gamma(\hat{j}) = \min(\Gamma) \tag{2. 31}$$

The factor α used in Eq.(2. 29) is a weight given to the discrete derivative part ($\hat{\omega}_j - \hat{\omega}_{j-1}$). For defining its range of variability a Montecarlo simulation has been performed by generating distributions of $\hat{\omega}$ ordered in a descendent way with J=10. The evolution of the distribution of the simulated $\hat{\omega}$ has been adapted creating several scenarios in which the sudden change of the trend described above, separating the relevant SV from the rest, occurs progressively at j=1,2,3,4,5. 10^5 different cases for each scenario have been generated and processed with the Eq.(2. 29) varying the parameter α from 0 to 1 with steps of 0.1. An example of the generated scenarios and the corresponding cost functions is visible in Fig. 2. 13.

Fig. 2. 14 reports the result of the sensitivity analysis on the parameter α with respect to the number of relevant SV in a $\hat{\omega}$ distribution. The white area represents the range of values assumed by the parameter α for which the cost function has given the correct estimate of the number of SV actually identified as "relevant" in the totality of the cases (100% over 10^5 samples).

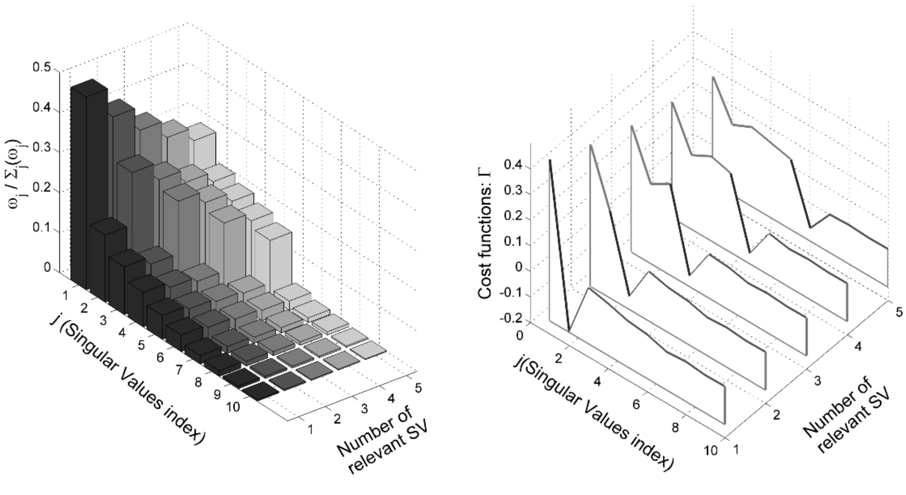

Fig. 2. 13 : Example of generated $\hat{\omega}$ scenarios with 1,2,3,4 and 5 relevant singular values respectively. (a) $\hat{\omega}$ distributions. (b) Γ_j cost functions.

It can be noticed that the lower the number of relevant SV, the higher the importance of the derivative part in the cost function. From Fig. 2. 14 it can be concluded that the best choice is setting parameter $\alpha \geq 0.7$. The higher limit of the parameter α is not discussed in this document, although it has been noticed (as intuitively predictable) that $\alpha \gg 1$ may lead to biased results because the proportional part becomes negligible. In this document it is used $\alpha = 0.7$.

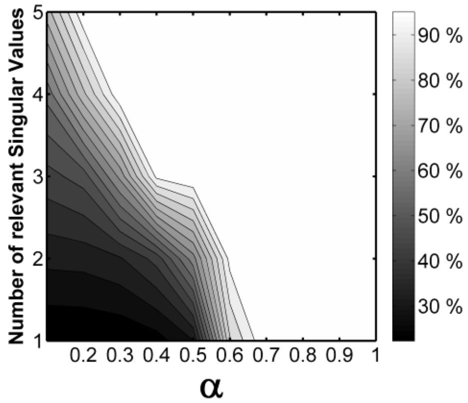

Fig. 2. 14 : Result of the Montecarlo analysis on the parameter α vs. the number of relevant singular values of a $\hat{\omega}$ distribution.

Fig. 2. 15 shows the relationship between the normalized set of SV (values expressed in percentage) of a certain $\underline{a}^{(i)}$ matrix and the corresponding cost function.

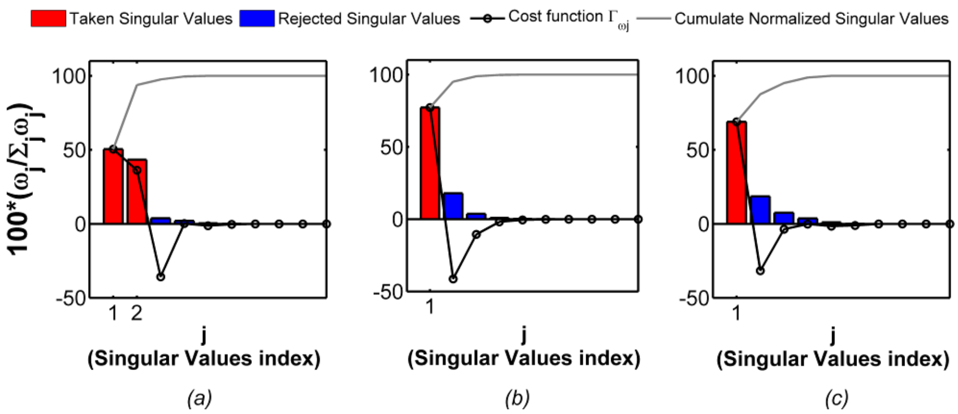

Fig. 2. 15 : Selection of the singular values for: (a) $\underline{a}^{(i=1+i=2),k=0}$, (b) $\underline{a}^{(i=1),k=0}$, (c) $\underline{a}^{(i=2),k=0}$, by means of the cost function Γ. The x-axis (singular value index) has been indicated only for $j < \breve{j}$.

The cumulative curves of the normalized SV for the cases (a), (b) and (c) are also plotted in Fig. 2. 15. These curves estimate the percentage of information (linked to the number of SV) kept over the total information contained in the processed matrix. Notice that the value of such percentage is rather different in the three cases of our example, meaning that the ratio between active noise sources and the background noise is not constant and an adaptive

criterion for their separation is actually needed. The cumulative sum of the SV of a matrix is a valuable measure of the similarity between the original matrix and its reconstruction performed adopting only a subset of its SV. If the inclusion of an additional SV does not change significantly the value assumed by the cumulative curve, most likely this SV (and the lowest ones) does not bring relevant contribution to the reconstruction of the original matrix. The described adaptive process will allow retaining the contribution linked to the physical phenomenon, discarding those related to numerical issues and background noise.
Once the number of principal components to be kept is defined, each resulting matrix

$$\breve{a}^{(i)} = \sum_{j=1}^{\breve{j}} \bar{a}_j^{(i)} \tag{2. 32}$$

has to be processed in order to reduce the number of scan points on the calculation plane, thus enhancing the inverse beamforming solution with the remaining equivalent sources. A criterion for selecting the part of each $\breve{a}^{(i)}$ to be discarded is proposed in the following paragraph. It defines an optimal dynamic range between the level of the equivalent sources that actually contribute to the sound field and the level of those that can be considered not relevant.

2.4.2. The adaptive criterion for defining an optimal dynamic range

Let us assume $\breve{a}^{(i)}$ to be the matrix obtained after the TSVD step described in the previous section. A variable $\delta = \delta_n$, where n=1,…,N' and N' are the scan points considered (e.g. N'=N for $\breve{a}^{(i),k=0}$), can be defined as reported in Eq.(2. 33):

$$\delta_n = -20\log_{10}\left(\frac{\left|a_i^0(n)\right|}{\max(\left|\breve{a}_i^0\right|)}\right). \tag{2. 33}$$

This variable normalizes the equivalent source strengths distribution of the $\breve{a}^{(i)}$ matrix to one and put it in a dB scale so that δ_n quantifies the difference of the nth scan point with respect to the maximum value. The minus in the formula makes the variable positive. δ_n is defined in the sample space (whose corresponding continuous variable is $\delta\in[0,+\infty)$) of a random variable, Δ, that generically assumes the possible values of δ in the set of occurrences of the calculation plane.
The sample distribution obtained through Eq.(2. 33) can be treated statistically by computing the associated relative frequency histogram H. This histogram can be considered an estimate of the Probability Density Function (PDF) g_Δ (Eq. (2. 34)) associated to the variable δ.

$$\frac{1}{N'} H_{\delta^*}(\delta) \cong g_\Delta(\delta) \tag{2. 34}$$

In Eq. (2. 34) δ^* represent the discretization bins used for creating the histogram, while N' is the associated total number of occurrences, i.e. the number of scan points, considered. This equation can be used for introducing an adaptive criterion being able to determine the optimal dynamic range of the $\breve{a}^{(i)}$ matrix. In this way a pruning operation on the equivalent sources can be performed. An adaptive criterion can be based on the extraction of statistical quantities from the PDF g_Δ. One possible option is defining the optimal dynamic range threshold μ adopting the function of Eq. (2. 35).

$$\mu = \beta \sum_{\delta^*}^{\max(\delta^*)} \delta^* \cdot g_\Delta(\delta^*) \tag{2. 35}$$

The idea of Eq. (2. 35) is to relate μ to intrinsic characteristics of the PDF g_Δ. For this reason the factor β is introduced to take into account scalar parameters which are representative of the PDF. It has been observed that very often this distribution resembles a multi-modal distribution. It is therefore difficult to refer to analytical models to extract g_Δ. A non-parametric method based on the Parzen estimation (see references [133, 134]) is proposed in order to provide a robust and adaptive method for identifying the β parameter. The idea of the Parzen method is estimating the PDF by fitting it with a function designed as follows:

$$D(\delta) = \frac{1}{N}\sum_{n=1}^{N} K\left(\frac{\delta - \delta_n}{h}\right) \approx g_\Delta(\delta) \tag{2. 36}$$

where K is a function called kernel. It can be suitably chosen under appropriate conditions [133] although the default option, also used in this application, is using normal distributions as kernel functions. The parameter h is defined as the width of the kernel.
The choice of the parameter h leads to a more or less smooth fitting of g_Δ. There are several approaches available in literature for properly selecting this parameter. For theoretical insights the interested reader may refer to reference [135]. The simplest approach is adopting the formula shown in Eq.(2. 37), which is theoretically correct in the case g_Δ is a normal distribution, but remains a valid option also in the general case where the nature of g_Δ is unknown (more details are given in [135]).

$$h = \left(\frac{4}{3N}\right)^{1/5} \sigma \tag{2. 37}$$

In this formula N is the number of elements of the distribution and σ is the estimate of its standard deviation.
Fig. 2. 16 gives an example of the application of the Parzen estimation to a case of a normal distribution of N elements with expectation value equal to 0 and standard deviation equal to

1. In this figure, the histogram, the analytical Gaussian curve and the Parzen estimation of the corresponding PDF are compared. It has been therefore shown how the parameter h condenses in one scalar number the characteristics of the PDF, whatever shaped it is.
Setting:

$$\beta = \frac{1}{h} \tag{2. 38}$$

the μ value can be calculated with Eq. (2. 35). It represents the wanted optimal dynamic range.
The criterion for reducing the number of scan points from the calculation plane can be finally formulated as follows:

$$\{\breve{a}^{(i)}\}_{n^*} = \varnothing \quad \forall n^* \in [1, N] \quad s.t. \quad \delta_{n^*} > \mu \tag{2. 39}$$

The scan points labelled by all the indices n^* satisfying the criterion of Eq.(2. 39), i.e. whose amplitude values are beyond the optimal dynamic range defined by μ, are therefore discarded and they will not be taken into account in the following processing of the calculation plane. The method just described is performed on the results of the PCA step (TSVD) discussed in Section 2.4.1.

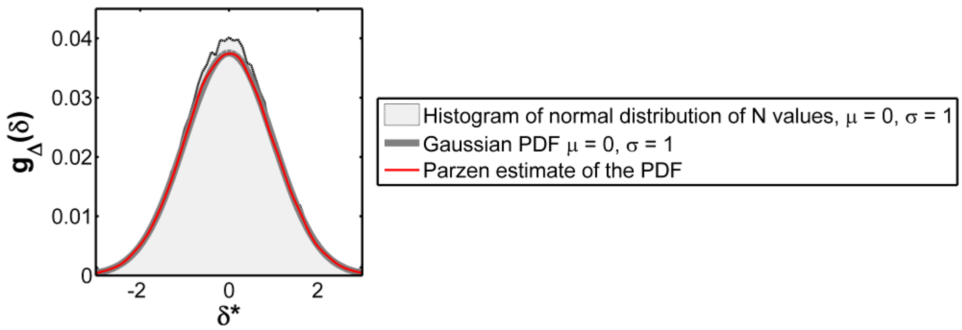

Fig. 2. 16 : example of PDF estimation adopting Parzen method.

Fig. 2. 17 shows results of the application to the $\breve{a}^{(i=1+i=2)}$ matrix of the adaptive method for the selection of the optimal dynamic range. In our example this matrix contains the distribution of two uncorrelated random noise monopole sources (these are marked with a cross in the figures). In particular, Fig. 2. 17(b) reports the PDF, constructed as described previously, of the matrix graphically shown in Fig. 2. 17(a).

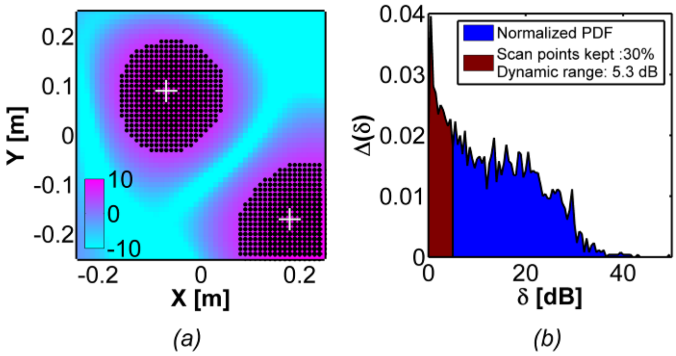

Fig. 2. 17 : (a) Kept scan points (black dots) compared to the full size de-noised matrix $\breve{a}^{(i=1+i=2)}$*. (b) Normalized PDF reporting the selected optimal dynamic range and the percentage of the scan points kept.*

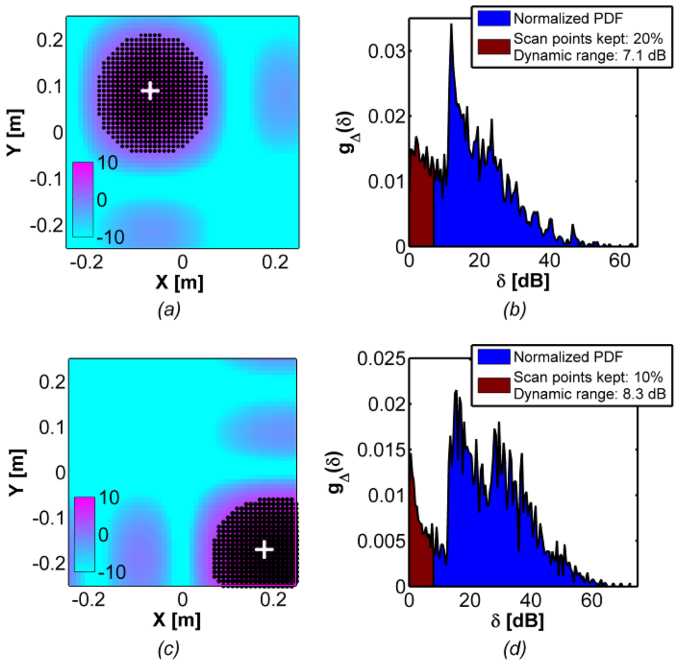

Fig. 2. 18 : Kept scan points (black dots) compared to the full size de-noised matrix (left size). Normalized PDF reporting the selected optimal dynamic range and the percentage of the scan points kept (right side). Results shown in the case of: $\breve{a}^{(i=1)}$ *(a-b) and* $\breve{a}^{(i=2)}$ *(c-d).*

It can be noticed that its shape is right-skewed and it shows a multi- (bi-) modal nature. One part of the distribution is related to the sources distribution, the rest is related to the background noise (to be discarded). The red part of the area plot of Fig. 2. 17(b) reaches the value μ calculated through Eq. (2. 35). The part of the distribution kept for the following steps of the iterative optimization procedure, corresponds to the 30% (the black dots in Fig. 2. 17(a)) of the complete set of equivalent sources covering the entire calculation plane. Looking at the cases shown in Fig. 2. 18(a-b) and Fig. 2. 18(c-d), corresponding to the de-noised matrices $\breve{a}^{(i=1)}$ and $\breve{a}^{(i=2)}$ respectively, it can be noticed that the graphs labelled with (b) and (d) show an evident multi-modal behaviour that can be interpreted as a mixture of multiple mono-modal distributions. The part of the PDF that is of interest is related to the first distribution. However, it is not easy to extrapolate it from the rest using analytical formulations. The use of the proposed method (β factor) demonstrates to be effective in this sense. The entire processing from Eq.(2. 33) until Eq.(2. 39) is summarized in the scheme of Fig. 2. 20.

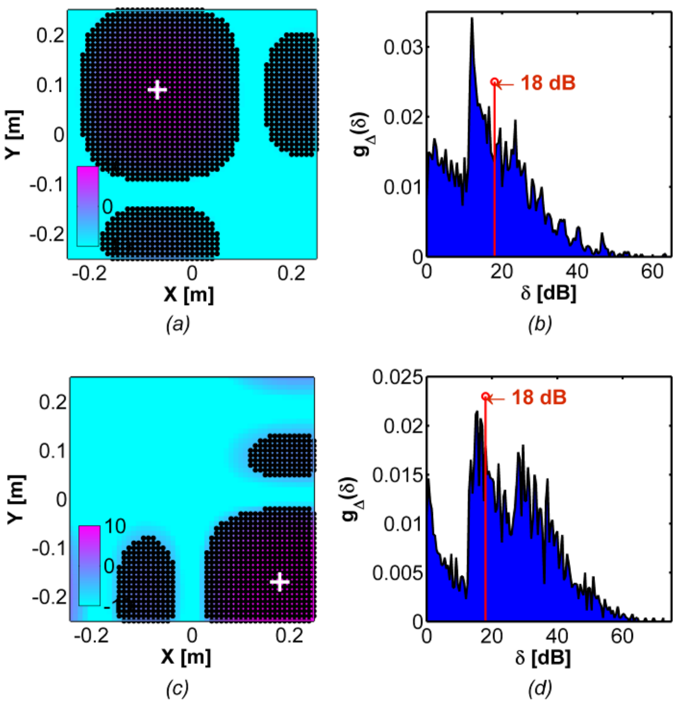

Fig. 2. 19 : Kept scan points (black dots) compared to the full size de-noised matrix (left size) in the case of a manual selection of the parameter μ. Normalized PDF reporting the dynamic range value (18 dB) set manually. Results shown in the case of: $\breve{a}^{(i=1)}$ *(a-b) and* $\breve{a}^{(i=2)}$ *(c-d).*

It is important to notice that the values of the selected optimal dynamic range and the percentage of scan points to be kept are not constant. They rather depend on the specific source distribution. Moreover, the method proves to be able to immediately discard the unwanted ghost sources still present in the $\breve{a}^{(i=1)}$ matrix of equivalent sources. This is not merely due to the application of a linear threshold, but it is the result of an adaptive criterion, based on physical principles, that takes into account the actual information contained in the matrix. In fact, as visible in Fig. 2. 19, another (manual) choice of the parameter μ would lead to a not optimal selection of the scan points to be kept. This could degrade the quality of the final result because it may introduce artefacts.

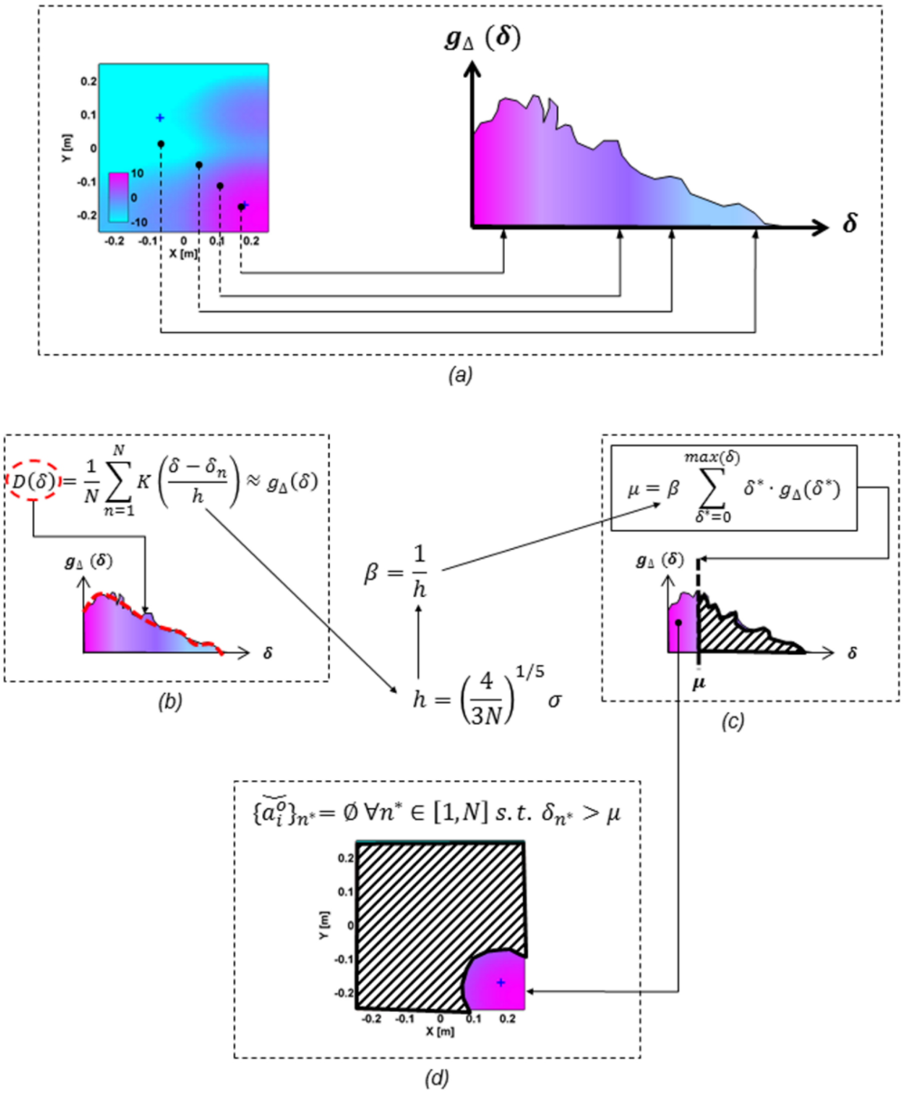

Fig. 2. 20 : (a) Generating the frequency histogram of the random variable Δ as a function of the dynamic range δ. (b) Estimation of the corresponding PDF adopting the Parzen method. (c) Use of the width parameter h for designing the adaptive criterion of reduction of the calculation plane. (d) Adaptive reduction of the calculation plane.

2.4.3. The adaptive criterion as pre-processing step for the iterative optimization algorithm

As already discussed, the first source distributions obtained from the solution of Eq.(2. 6) can be improved by performing an iterative optimization step where the weakest equivalent sources are excluded in order to provide a new inverse problem formulation. Adopting the methods described above, the traditional iterative algorithm of GIBF (see [39]) can be modified as follows:

1) Calculate the initial source vector, $\underline{a}^{(i),k=0}$.
2) Reshape the source vector $\underline{a}^{(i),k=0}$ in a matrix form $\bar{a}^{(i),k=0}$) resembling the scan point distributions on the calculation plane.
    2.1) Perform a PCA on the $\bar{a}^{(i),k=0}$ matrix.
3) Discard the unwanted principal components of $\bar{a}^{(i),k=0}$ through Eq.(2. 29), Eq.(2. 30) and Eq.(2. 31).
4) Truncate the equivalent source vector $\underline{a}^{(i),k=0}$ on the basis of Eq.(2. 39).
5) Calculate a new source vector: $\underline{a}^{(i),k=1}$ with the remaining scan points.
6) Reorder and truncate (10% is the value proposed by Zavala in [37]. However such value can be tuned also in other ways. A good strategy could be relating also this parameter to adaptive criteria.) the equivalent source vector $\underline{a}^{(i),k=1}$, discarding the smallest terms. The number of scan points left is therefore N^*.
7) Calculate a new source vector: $\underline{a}^{(i),k=2} = \{A\}^{+}_{M,N^*} \cdot \underline{p}^{(i)}$.
8) Repeat steps 5) to 7) until a desired number of equivalent sources are reached.

This improved version has several advantages: reduces the computation effort, improves the robustness with respect to the presence of numerical disturbances, it benefits from adaptive criteria that make the optimization more reliable.

2.4.4. The adaptive criterion as pre-processing step for inverse beamforming solution obtained using Bayesian inference

The algorithm proposed in section 2.4.3 foresees an iterative process for improving the accuracy of the results. Such iterative process is clearly aligned with the spirit of an Equivalent Source Method; however its results may be biased by two main factors:

- The wrong decisions of the user of selecting a too much limited number of Equivalent Sources (ES) for describing the acoustic field may lead to a wrong reconstruction of the field itself.

- The iterative process is based on the criterion of discarding always the weakest ES present in the field. Since this is not performed adaptively (no link with the observed physical phenomenon), this criterion may be overly simplistic.

A way to overcome these problems is providing additional information to be put together in the formulation of the inverse problem. Such additional information has to be found in the status before the physical phenomenon is observed. In this manner the space of the possible solutions will be reduced to one of its subsets and the final solution will be enhanced according to principles that are directly linked to the observed physical phenomena. One way to do this is formulating the problem in terms of Bayesian inference. The interested reader can refer to [48, 50, 51] for examples of applications of the Bayesian statistics to inverse acoustic problems.
In this paragraph the concept of confidence level in the occurrence of a given event (presence of a noise source) is introduced. An algorithm combining this vision with the adaptive criterion point of view is proposed below.
Before introducing a possible implementation of such combination between the Bayesian and the adaptive vision of the problem, the Bayesian inference will be contextualized in the previous formulation in order to rigorously describe the operations to be carried out.
In particular the well-known rule of Bayes will be adapted to the acoustic imaging problem under study by defining the following probabilities at the calculation plane, whose geometry is here described by r_π:

$$P_{r_\pi(n)}(R_S|E_S) = \frac{P_{r_\pi(n)}(E_S|R_S) \cdot P_{r_\pi(n)}(R_S)}{P_{r_\pi(n)}(E_S)}, \forall n = 1,..., N \qquad (2.\ 40)$$

The quantities represented in Eq.(2. 40) are:

- $P_{r_\pi(n)}(R_S|E_S)$: Probability that the presence of an non-null equivalent source (random variable E_s) in $r_\pi(n)$, matches with the presence of a real source (random variable R_s).
- $P_{r_\pi(n)}(E_S|R_S)$: Probability that the presence of a real source in $r_\pi(n)$, is identified by a corresponding equivalent source.
- $P_{r_\pi(n)}(R_S)$: A priori probability of finding a real source in $r_\pi(n)$. This probability depends by several factors intrinsic in the problem under study: geometry, type of sources, etc.
- $P_{r_\pi(n)}(E_S)$: Probability of having an equivalent source located in $r_\pi(n)$ if any prior information is available. In our case this probability is trivially equal to 1 in $r_\pi(n)$ for any given n.

The denominator of Eq.(2. 40) is always equal to 1 because any scan point location $r_\pi(n)$ considered in the calculation plane has the same probability of being the location of a non-null equivalent source if any prior information is available.

Combining the Bayesian and the adaptive vision is therefore possible by characterizing the different probabilities by means of the two approaches. This can be done by adopting the following algorithm:

1) Calculate the initial source vector, $\underline{a}^{(i),k=0}$.
2) Reshape the source vector $\underline{a}^{(i),k=0}$ in a matrix form $\bar{a}^{(i),k=0}$) resembling the scan point distributions on the calculation plane.

    2.2) Perform a PCA on the $\bar{a}^{(i),k=0}$ matrix.

3) Discard the unwanted principal components of $\bar{a}^{(i),k=0}$ through Eq.(2. 29), Eq.(2. 30) and Eq.(2. 31).
4) Truncate the equivalent source vector $\underline{a}^{(i),k=0}$ on the basis of Eq.(2. 39).
5) Assign to each scan point $r_\pi(n)$ of the calculation plane a probability $P_{r_\pi(n)}(R_S)$ based on a priori observations. If such observations are not available, can be set: $P_{r_\pi(n)}(R_S)=1\,,\forall n$ and proceed as in the algorithm shown in section 2.4.3.
6) Set a threshold of confidence t_c and discard the scan points n^* such that: $P_{r_\pi(n^*)}(R_S)<t_c$.
7) Calculate a new source vector: $\underline{a}^{(i),k^*=1}$ with the remaining scan points.

A demonstration of the potential of such approach is given below, where the algorithm is applied on experimental data. The main advantage of this approach is that, in presence of reliable a priori information, accurate results can be achieved even without further iterative optimization processes. However, such iterative optimization is always applicable if more accuracy is required.

The proposed approach should not be confused with the so called *Bayesian focusing* presented in [49]. In fact in that case the Bayesian statistics is directly injected in the formulation of the inverse problem allowing the optimal choice of the regularization parameter through Bayesian regularization and the power estimation of the field through the so-called *aperture function*. In the proposed algorithm, instead, the Bayesian inference is exploited in a modular approach in which a priori spatial information and a posterior adaptively obtained information about the sources distribution are nested to give an optimized solution.

2.4.5. Test of the proposed method on numerical simulations

In this section results of the use of the proposed adaptive method are presented on the numerical simulations already introduced in section 2.4. and Fig. 2. 9. The comparison with the method at the state-of-the-art is proposed in terms of accuracy and computational effort. With reference to such simulation, the two optimization methods can be compared looking at Fig. 2. 21(a-b) and Fig. 2. 21(c-d), representing the final result of the inverse beamforming solution obtained respectively with the algorithm proposed in section 2.4.2 and with the algorithm inspired by Suzuki [36] and described in section 2.1.

In Fig. 2. 21(c-d), it can be noticed that the two uncorrelated sources are correctly separated and localized without any numerical issue. It can be also noticed that the results are presented with a dynamic range of 15 dB (which is much higher than the one possible at the first step of the optimization problem).

In Fig. 2. 21(a-b) the solution of the same problem has been reached without applying the proposed new adaptive optimization algorithm and it can be noticed the presence of the partial leak of one source distribution in the other.

The computational effort is much reduced by means of the adaptive method proposed because it allows focusing at the most important part of the equivalent sources distribution at the very first stages of the optimization process, getting more quickly to the desired number of equivalent sources to be used for reconstructing the source distribution. In order to highlight this aspect, a comparison of the trend of the number of scan points (equivalent sources) remaining over the iterative optimization process is shown in Fig. 2. 22 for the traditional GIBF iterative optimization algorithm of section 2.1 and for the optimization processes with the adaptive pre-processing method for the cases of $\underline{a}^{(i=1+i=2)}$, $\underline{a}^{(i=1)}$, $\underline{a}^{(i=2)}$.

The initial number of scan points that discretize the calculation plane is the same (N = 2601) for all the scenarios, while the percentage of scan points discarded at the first iteration is:

- 10% (or other fixed value) as suggested by Zavala in [37].
- 70% for the case of $\underline{a}^{(i=1+i=2)}$ treated with the adaptive method.
- 80% and 90% respectively for the cases of $\underline{a}^{(i=1)}$ and $\underline{a}^{(i=2)}$ processed with the adaptive method.

Being adaptive, the proposed pre-processing optimization method adapts the decision of the part of the calculation plane to be discarded at the first iteration on the basis of physical considerations linked to the type of acoustic field under study (complexity, presence of correlated and/or uncorrelated unwanted background noise).

This latter aspect, allowing reducing the computational effort on equal calculation requirements, is particularly interesting if related to cases where inverse beamforming is applied iteratively, as for example in the use of the microphone clustering approach, described in references [132] and [136], which will be introduced in Chapter 3.

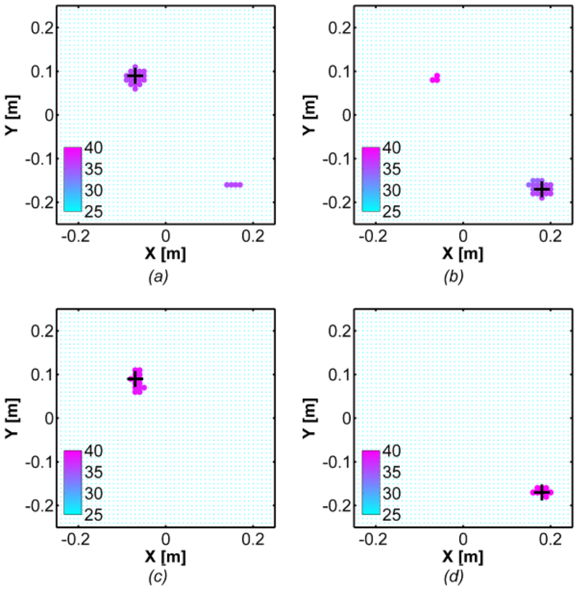

Fig. 2. 21 : Optimized inverse beamforming solution using the adaptive method. SPL maps @ 2 kHz (dB_{ref} = 20 μPa) related to: (a) Solution $\underline{a}^{(i=1)}$ no adaptive pre-processing. (b) Solution $\underline{a}^{(i=2)}$ no adaptive pre-processing. (c) Solution $\underline{a}^{(i=1)}$ with adaptive pre-processing. (d) Solution $\underline{a}^{(i=2)}$ with adaptive pre-processing.

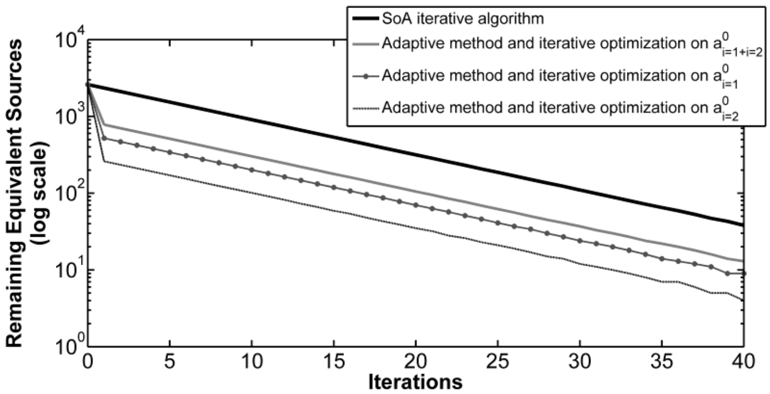

Fig. 2. 22 : Comparison of the trends for the number of remaining of equivalent point sources in different cases.

2.4.6. Test of the proposed method on experimental data

The numerical simulation presented so far has been replicated in a real test scenario by working with loudspeakers in an anechoic environment.
Fig. 2. 23 shows the experimental setup and the geometry of the problem. The two sources are fed with uncorrelated band limited (2 kHz-8 kHz) broadband noise with the same strength. For sake of clarity the representation of Fig. 2. 23(c) will be used for showing the results instead of plotting the beamforming maps on top of the picture of the scene.
In Fig. 2. 24 the optimization process proposed in section 2.4.1 is described. In fact, Fig. 2. 24(a-b) show the results of applying Eq.(2. 6) to a fully populated radiation matrix $\{A\}_{M,N}$. A high density of high-amplitude equivalent sources is present in the areas corresponding to the actual sources. Nevertheless a relevant distribution of lower-amplitude equivalent sources is present also. As already discussed, such ghost patterns are mainly caused by two factors: numerical issues due to the inverse solution of a highly undetermined problem, presence of mixture of uncorrelated noise sources of similar strength [39]. Such undesired phenomena may limit the capability of localization and quantification of the acoustic sources acting in the field. Fig. 2. 24(c-d) and Fig. 2. 25(c-d) show that the problem can be successfully addressed and solved by the adaptive method described in sections 2.4, 2.4.1 and 2.4.2. The numerical issues are no longer present in the solution and the equivalent sources are distributed only in the areas in which the sources are actually acting. The reader should notice, moreover, that the two uncorrelated phenomena are correctly separated. Once this result is obtained, the iterative process described in section 2.4.2 can be applied reaching, acting in the spirit of an ESM, the desired number of equivalent sources needed for describing the acoustic field generated by the identified actual source.

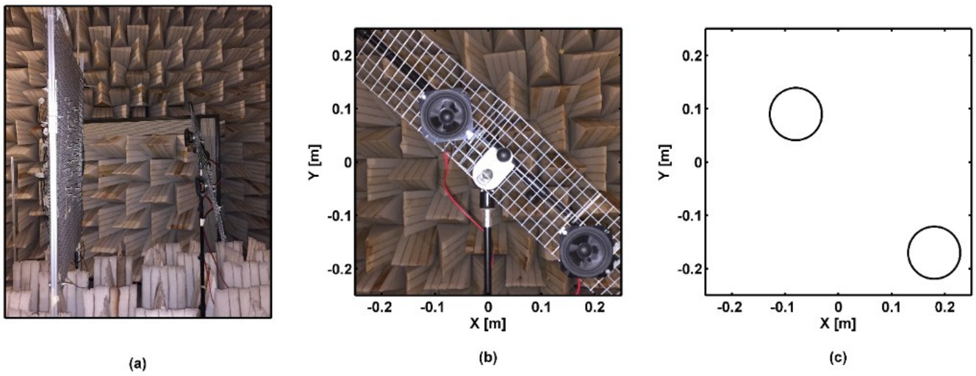

Fig. 2. 23 : Experimental setup of beamforming measurements on loudspeakers in anechoic conditions.

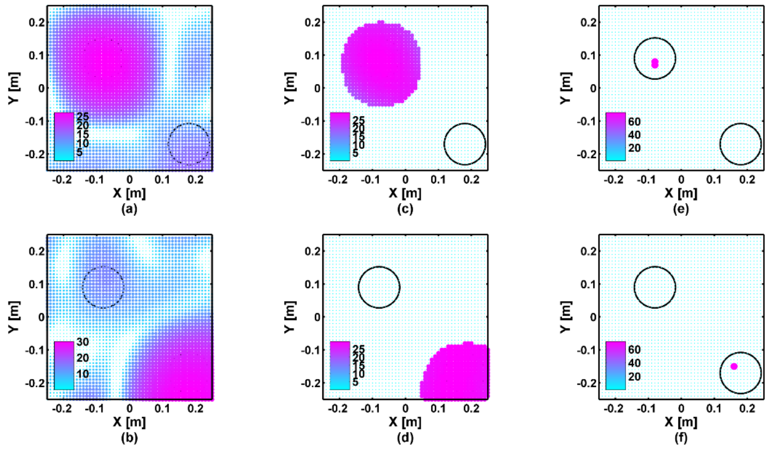

Fig. 2. 24 : Results of the algorithm proposed in section 2.4.2 applied on a real test scenario of two uncorrelated random sources of same strength. SPL maps (dB_{ref} = 20 µPa) presented at 2 kHz. (a-b) Step 1. (c-d) Steps 2-5. (e-f) Steps 6-8.

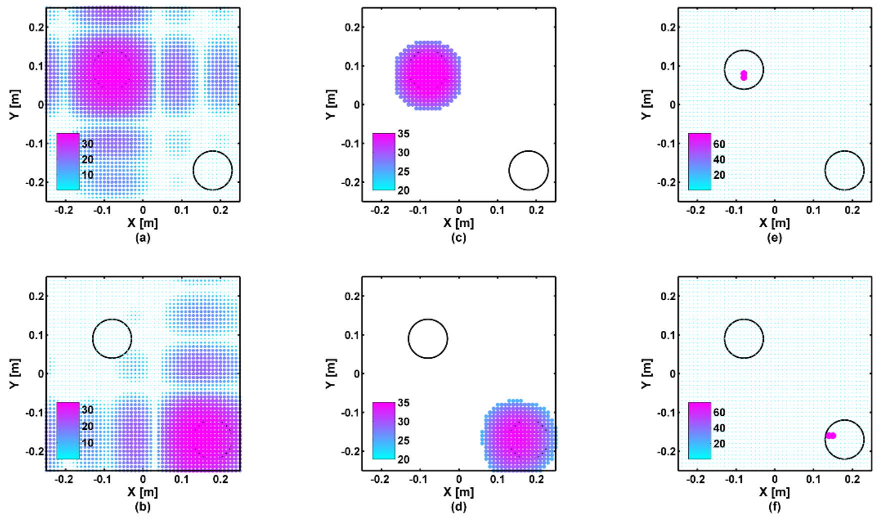

Fig. 2. 25 : Results of the algorithm proposed in section 2.4.2 applied on a real test scenario of two uncorrelated random sources of same strength. SPL maps (dB_{ref} = 20 µPa) presented at 3.5 kHz. (a-b) Step 1. (c-d) Steps 2-5. (e-f) Steps 6-8.

This aspect of the method requires a blind involvement of the user, whose decision of the number of equivalent sources (or number of iterations) is not hooked to tangible physical evidences and this may eventually lead to inaccuracy in the results.

In section 2.4.4 a method based on the combination of the adaptive pre-processing and the Bayesian vision of the problem was presented. This approach is mainly based on the option of avoiding the iterative optimization process by substituting it with the adoption of a Bayesian inference: i.e. by combining the output of the adaptive processing with an a priori confidence level distribution based on information available before performing the measurements. In Fig. 2. 24 the entire process is shown on the real test case depicted above where two loudspeakers are acting (simultaneously) producing uncorrelated broadband noises of the same strength. The result of the adaptive pre-processing method (Fig. 2. 24(a-b)) is combined with a level of confidence distribution (shown in Fig. 2. 24(c)) which has its maximum in the proximity of the center of the two loudspeakers (meaning: maximum a priori probability of finding a real source in those corresponding locations). In the proposed example, then, the threshold of confidence t_c (algorithm described in section 3.4) is set to 0.9 (meaning 90% level of confidence) and eventually Fig. 2. 24(d-e) show the final results where the ultimate solution of the inverse problem is obtained by keeping only the intersection of the equivalent sources locations indicated by both the adaptive and the Bayesian criteria.

Notice that, in the case of the very controlled experiment proposed in this paper, accurate results are achieved with no need of further iterative optimizations. It is worth to point out that the added values brought by the introduction of the adaptive pre-processing method are valuable regardless the need to further improving the solution by means of other processing. In fact it resulted to be effective mainly in avoiding numerical issues in the inverse problem solutions and most of all in allowing a perfect separation of uncorrelated noise sources.

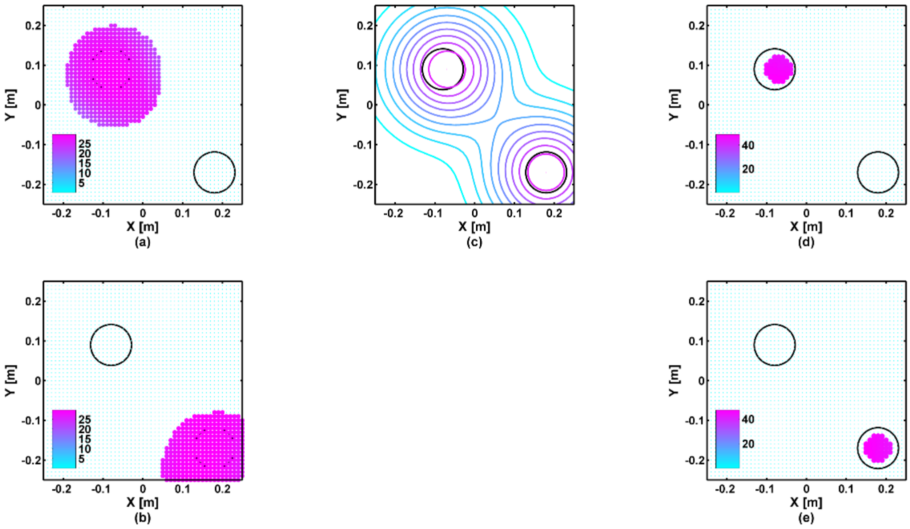

Fig. 2. 26 : Results of the algorithm proposed in section 2.4.4 applied on a real test scenario of two uncorrelated white noise sources of same strength. SPL maps (dB$_{ref}$ = 20 μPa) presented at 2 kHz. (a-b) Steps 1-4. (c) Step 5. (d-e) Step 6-7.

2.4.7. Comparison of the proposed optimization methods

Two inverse beamforming calculation options have been proposed: one adopting an iterative optimization process (section 2.4.3) and another one exploiting the Bayesian inference concept where no further iterative processing is required (section 2.4.4). Both the combinations have shown excellent results on numerical and experimental data, meaning that both are applicable and even a combination of the two is possible.
Where not differently specified, the colour code used for the representation of the acoustic images is reported in Fig. 2. 27.

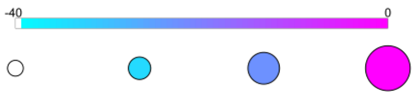

Fig. 2. 27 : colour code for the representation of the acoustic images.

The acoustic images will be represented normalized on their maximum value in a dB scale with a dynamic range of 40 dB. The size of the markers in the scatter plots is proportional to the value assumed by the equivalent source in the corresponding location.

Fig. 2. 28 reports the results obtained with these methods compared to the ones achieved with GIBF and no further optimizations. The reported case, experiment with uncorrelated random noise sources of the same strength, has been chosen for emphasizing the strengths and weaknesses of each approach. In particular it can be noticed that in the worst cases the use of GIBF in presence of uncorrelated sources (Fig. 2. 28(a)) may introduce numerical issues that can make the correct identification of the sources almost impossible. As already explained the advantage of adopting a PCA-based adaptive pre-processing allows separating correctly the uncorrelated source distributions (Fig. 2. 28(b)), thus avoiding the previously visible numerical instabilities related to the wrong source separation. The difference between the results shown in Fig. 2. 24(f) and the ones shown in Fig. 2. 28(b) is in the number of iterations taken for reaching the final solution. The exploitation of the Bayesian inference concept, without any additional pre-processing, grants sparsity in the results as shown in Fig. 2. 28 (c), although it is not able to completely avoid the leakage of one uncorrelated source into the distribution of the other. This additional improvement can be achieved by combining the two methods (Fig. 2. 28(d)) obtaining a perfect separation of the sources, correct localization and optimal ranking and quantification.

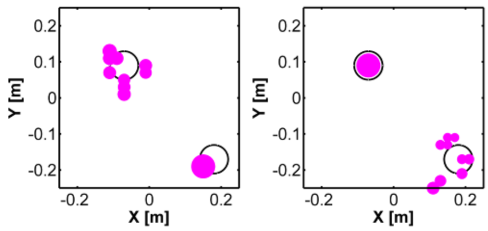

(a)

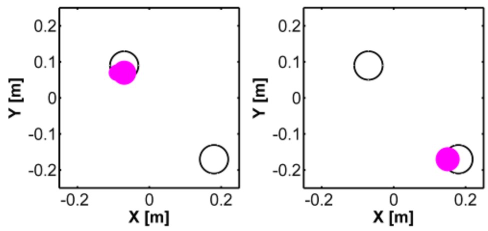

(b)

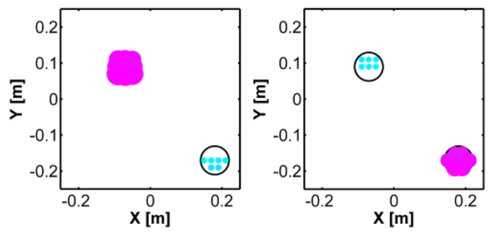

(c)

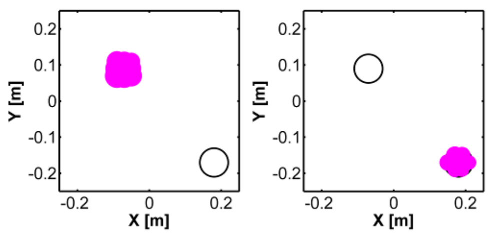

(d)

Fig. 2. 28 : Comparison of methods in the identification of two uncorrelated white noise sources active in the experiment of Fig. 2. 23. Calculation frequency: 2 kHz. Principal components: i=1 and i=2 for all methods. (a) GIBF without additional processing. (b) GIBF and PCA-based adaptive pre-processing. (c) GIBF and Bayesian inference. (d) GIBF with PCA-based adaptive pre-processing and Bayesian inference.

2.4.8. PCA-based methods and spatially joint and disjoint, uncorrelated and correlated sources

The results reported so-far show the potential of the PCA-based methods in separating the investigated acoustic field into uncorrelated source distributions. As already pointed out in section 2.3, the use of PCA as uncorrelated sources separation technique has also downsides mainly related to two aspects: the first one, already discussed, is that it is a *virtual* decomposition that requires additional criteria to ascertain the physical properties of the retrieved uncorrelated sources distributions; the second one is the requirement that the uncorrelated sources distributions sought in the acoustic field have to be spatially disjoint [127]. If, on the contrary, two or more uncorrelated sources are spatially overlapped the decomposition yielded by the described PCA-based methods is not optimal. The following numerical simulations have been performed in order to understand how severely this could affect results of a GIBF algorithm if the equivalent sources distribution is calculated on the basis of the eigen-structure of the CSM. In order to do so two uncorrelated random noise sources of the same strength have been placed almost in the same location in space as depicted by Fig. 2. 29.

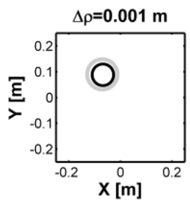

Fig. 2. 29 : numerical simulation of two uncorrelated sources not spatially disjoint.

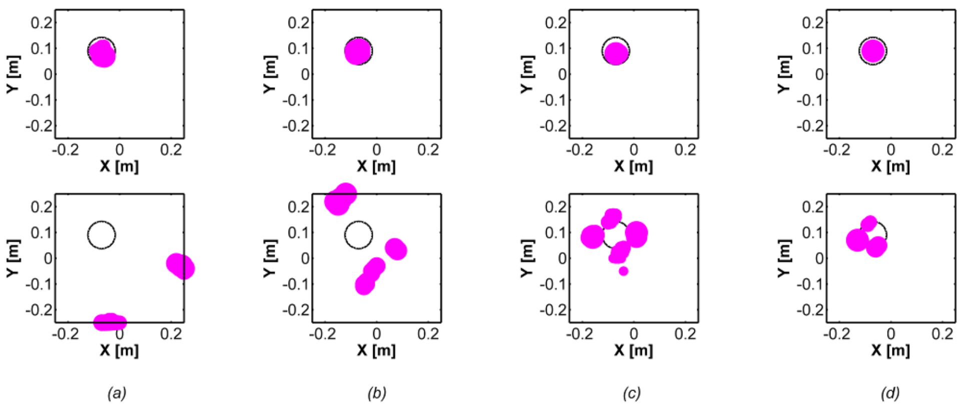

Fig. 2. 30 : GIBF solution with PCA-based adaptive pre-processing with spatially joint uncorrelated sources. Results at (a): 1000 Hz; (b): 2000 Hz; (c) 5000 Hz; (d): 7000 Hz.

The GIBF results obtained per principal components, adopting also the previously described PCA-based adaptive pre-processing, are reported in Fig. 2. 30 for the frequencies: 1000 Hz, 2000 Hz, 5000 Hz and 7000 Hz. It is observed the strange case of one principal component yielding the correct localization of the obtained “virtual” source distribution, whereas the other principal component seems to try to arrange as well as possible the corresponding virtual sources distribution in order to match the far-field without overlapping, at the source plane, with the other equivalent sources. This example highlights that the presence of overlapping uncorrelated sources in the acoustic field under study adversely affects the results of GIBF based on PCA pre-processing. Despite such a combination of spatially joint uncorrelated sources is not the most frequent in industrial applications, this aspect should be carefully considered when exploiting such tools. The following numerical simulation has been performed in order to understand the GIBF performance when disjoint sources, placed at short distance, can be considered partially overlapped as a function of frequency. Several cases have been studied and two of them, depicted in Fig. 2. 31, are reported hereafter.

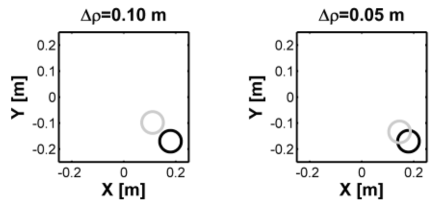

Fig. 2. 31 : numerical simulation of two uncorrelated random noise sources, identified in grey and black, spatially disjoint with short distance.

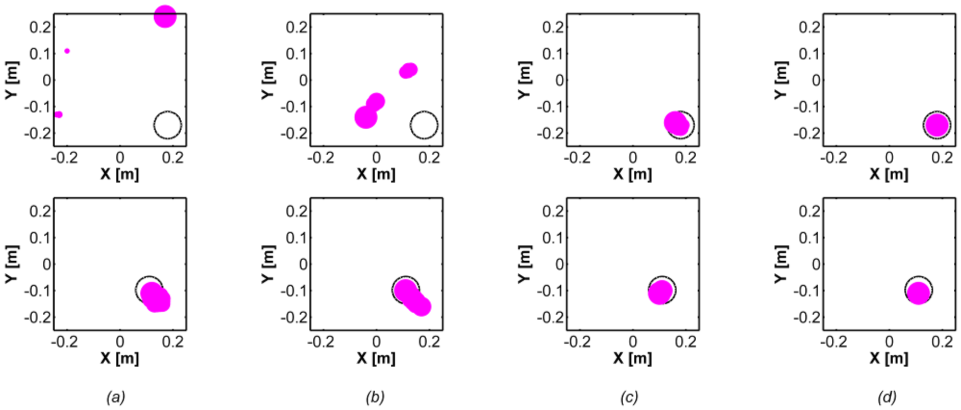

Fig. 2. 32 : GIBF solution with PCA-based adaptive pre-processing with spatially disjoint uncorrelated sources with short distance Δρ = 0.10 m . Results at (a): 1000 Hz; (b): 2000 Hz; (c) 5000 Hz; (d): 7000 Hz.

In Fig. 2. 32 and Fig. 2. 33 it can be noticed that the two uncorrelated sources start to behave as spatially joint at different frequencies depending on their physical spacing. In fact the two sources are correctly identified as uncorrelated and disjoint only for frequencies greater than 2000 Hz in the case of *Δρ* = 0.10 m (Fig. 2. 32) and only for frequencies greater than 5000 Hz in the case of *Δρ* = 0.05 m (Fig. 2. 33).

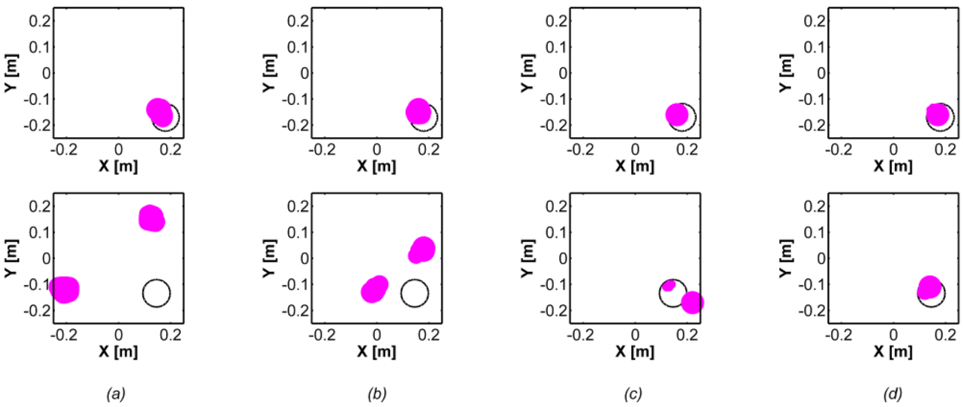

Fig. 2. 33 : GIBF solution with PCA-based adaptive pre-processing in presence of spatially disjoint uncorrelated sources with short distance Δρ = 0.05 m . Results at (a): 1000 Hz; (b): 2000 Hz; (c) 5000 Hz; (d): 7000 Hz.

The limitations just pointed out may insidiously influence the interpretation of the user if the results are not critically interpreted. One instrument that the user has to mitigate such risks is to compare the results obtained through GIBF per principal components with the ones obtained computing all the main principal components of the CSM at once. In the latter case the mutual interaction between the sources active in the field is automatically taken into account. In the cases described above, this practice demonstrated to greatly improve the results allowing to better identifying the closely spaced, but spatially disjointed uncorrelated sources in one acoustic image with the same performance as the one obtained in the next example for correlated sources. The examples reported so far, in fact, treated the case of uncorrelated broadband noise sources. In the next application will be tested the effectiveness of the PCA-based adaptive pre-processing on correlated sources. In this case the PCA-based pre-processing will not give its main effect in helping the separation of the acoustic image into uncorrelated phenomena, rather in de-noising the initial acoustic image and in helping discarding adaptively the insignificant equivalent sources. In this way the following GIBF iterative optimization results more robust and more effective. For this purpose a numerical simulation with two correlated random noise sources of equal strength have been performed. Four different distances, as visible in Fig. 2. 34, have been tested at three different calculation frequencies: 1500 Hz, 2000 Hz and 3000 Hz.

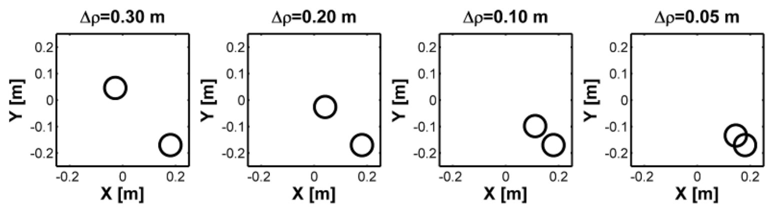

Fig. 2. 34 : numerical simulations of two correlated random noise sources with equal strength placed at progressively closer distance Δρ: geometry of the problem.

The results shown in Fig. 2. 35 demonstrate that the two correlated sources are correctly identified as long as their distance is not comparable with half of the wavelength corresponding to the calculation frequency. Beyond this limit the two sources are interpreted as one located in the middle between the two ideal locations.

This example concludes the demonstration and validation on numerical simulations and experimental cases of the PCA-based adaptive pre-processing method for enhancing the solution of an inverse beamforming. It has been shown that the proposed approach is suitable for better tackling issues typical of inverse acoustic problems such as numerical instabilities and ill-conditioning. The method showed a high impact on the quality of the final result, proving that also undesired numerical mixtures of uncorrelated source distributions can be tackled and avoided with excellent results and less computation effort. Two inverse beamforming calculation options have been proposed: one adopting an iterative optimization process (paragraph 2.4.3) and another one exploiting the Bayesian inference concept where no further iterative processing is required (paragraph 2.4.4). The method has been successfully tested with both uncorrelated and correlated sources opening up several application scenarios ranging from aero-acoustics to interior noise problems.

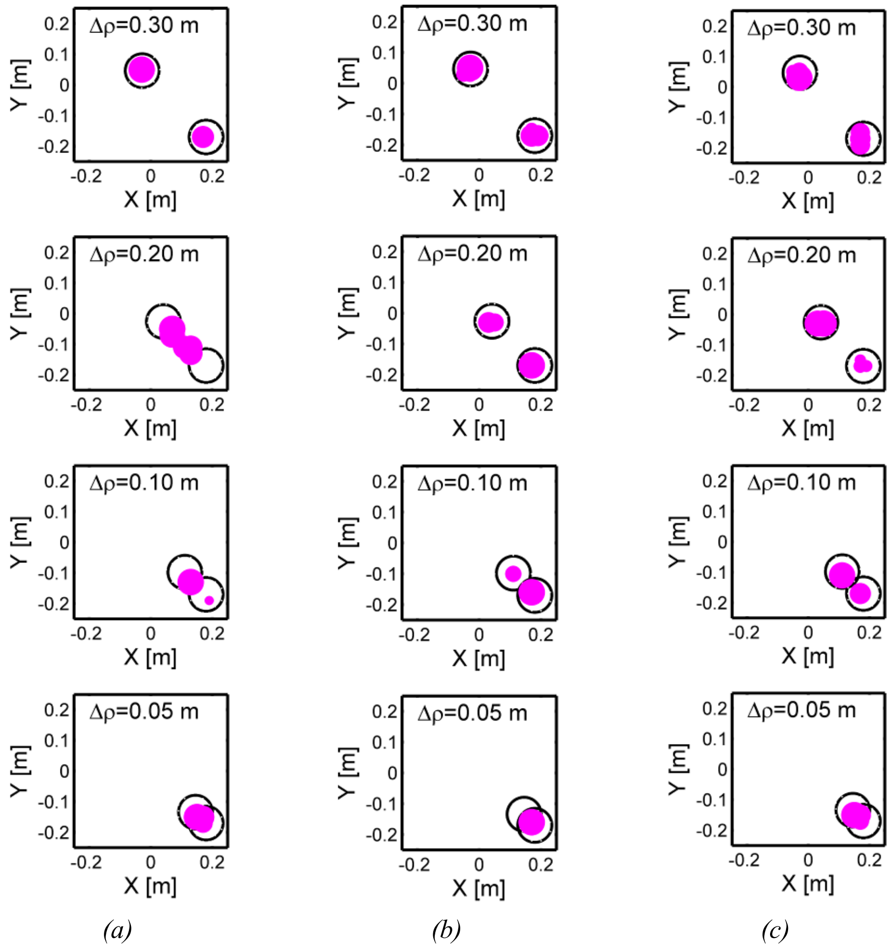

Fig. 2. 35 : GIBF and PCA-based adaptive pre-processing on simulated cases of random noise sources of equal strengths placed at decreasing distances (Δρ=0.3m, 0.2m, 0.1m, 0.05m). Results presented at: (a) 1500 Hz; (b) 2000 Hz; (c) 3000 Hz.

2.5. An adaptive criterion for selecting the calculation points

The inverse problem that GIBF try to solve is very under-determined because the scan points should cover the entire calculation plane in order to make sure to include the source(s) region(s). GIBF aims at iteratively discarding those scan points that are not representative of physical sources based on the strength of the corresponding equivalent sources. As shown in section 2.4, this iterative discarding procedure can be improved adopting adaptive criteria that introduce additional information. In paragraph 2.4.4 a method that benefit from an *a priori* knowledge of the probability of the geometrical regions of the calculation plane to be the location of the sought noise sources was introduced and its use in synergy with the PCA-based adaptive pre-processing described in section 2.4 was discussed. It has been also proven in paragraphs 2.4.6 and 2.4.7 that it can improve the localization and quantification results. However in general the *a priori* knowledge about the acoustic field might be very limited and its related geometrical information might be not available. In these cases such a priori information could be replaced by an a posteriori evaluation of the regions of the calculation plane most likely to host a physical acoustic source. The idea of the criterion proposed in this section is to obtain this geometrical information by performing a preliminary ESM analysis of the acoustic field by formulating a well-determined problem adopting a number of equivalent sources lower than the number of microphones available in the array and refining the analysis performing GIBF on a distribution of scan points distributed according to the outcome of the previous solution. Fig. 2. 36 and Fig. 2. 37 describe the proposed method with an application on the test case already described in paragraph 2.4.6. The corresponding algorithm is the following:

1) Formulate and solve an ESM problem adopting a number of equivalent sources lower than the number of microphones available. We will call the locations of such equivalent sources "*anchors*".
2) Normalize the obtained equivalent sources strengths values to the maximum of the distribution.
3) Select those anchors whose equivalent source strength is above a wanted threshold.
4) Distribute scan points around each anchor according to a wanted pattern.
5) Apply GIBF on the optimized distribution of scan points.

In our example the result of point 1 and 2 is reported in Fig. 2. 36. It can be noticed the equivalent sources with higher strength are located in correspondence of the two loudspeakers locations.

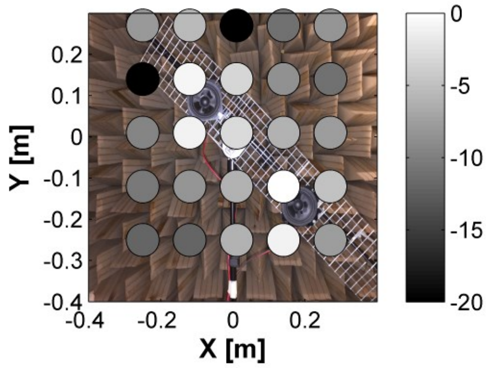

Fig. 2. 36 : Inverse beamforming solution of the well-determined formulation of the inverse problem of two uncorrelated band-passed random noise generated by the two loudspeakers. The solution has been calculated adopting 25 equivalent sources using 43 microphones signals.

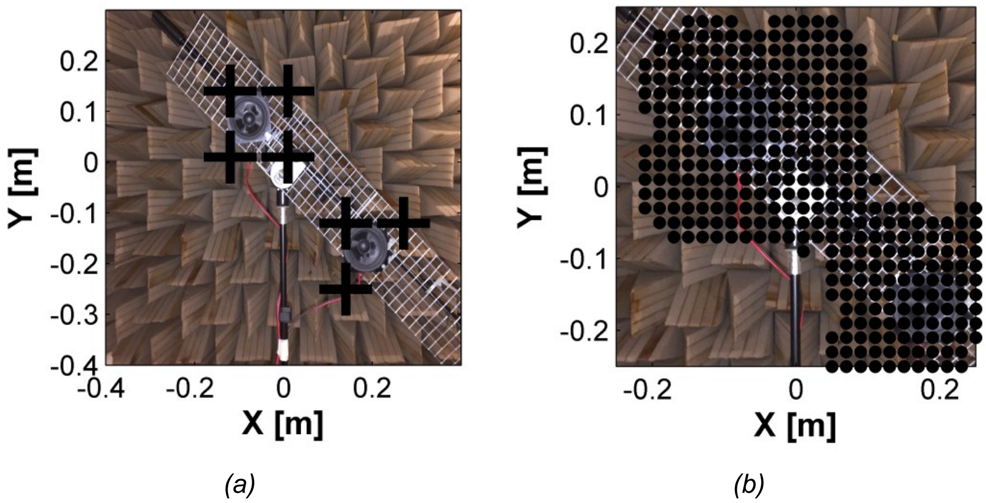

Fig. 2. 37 : adaptive selection of the scan points grid. (a): the crosses mark the anchor locations. (b): the black dots map the scan points positioned around each anchor location.

The anchors whose equivalent source strength is above -5 dB have been kept. This will select the anchors marked with a cross in Fig. 2. 37(a). Around each anchor a distribution of scan points, equally spacing of 0.02m in *x* and *y* direction, has been defined created within a circular region of 0.08m radius. As visible in Fig. 2. 37(b) such optimized scan points distribution allows to focus only on the region where the noise sources are actually present. This will mitigate the unwanted effect of numerical instabilities and inaccuracy related to the under-determination of the problem because it relates the mathematical solution of the inverse problem to physical information. However the problem remains under-determined and ill-conditioned, therefore the strategies described above in this chapter are still required to achieve an optimal result (Fig. 2. 38).

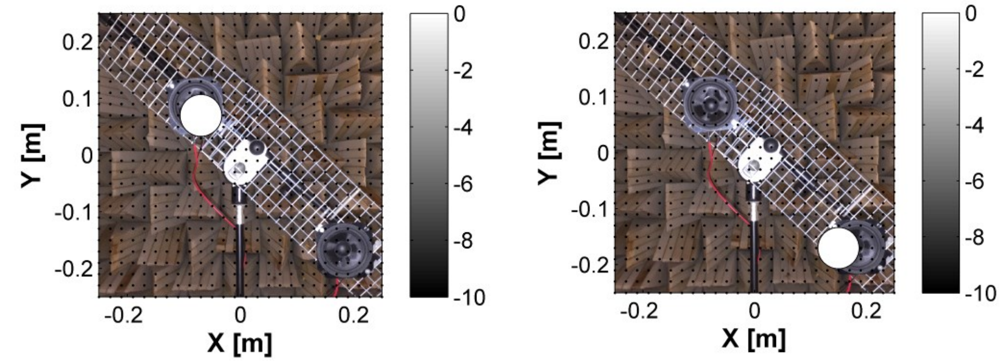

Fig. 2. 38 : optimized GIBF solution on the basis of the adaptive scan point selected.

Chapter 3.

The microphone clustering approach

The inverse beamforming approach presented in Chapter 2 aims at enhancing the capability in resolving complex acoustic fields wherein both correlated and uncorrelated source distributions are present. The method presented in the previous chapter consists in a modular approach in which several tools can be combined for improving a Generalized Inverse Beamforming solution. Such tools are: regularization, PCA of the CSM, iterative solution of the inverse problem, pre-processing based on the PCA of the acoustic image at the scan plane, exploitation of a priori information, etc. For the sake of a compact formulation, the inverse beamforming solution obtained by this entire package of combinable techniques will be identified exploiting the operator Y as follows:

$$\underline{a}^{(i)} = \Upsilon(A, \underline{p}^{(i)}, ...) \, . \tag{3. 1}$$

Recalling that:

- $\underline{a}^{(i)}$ is the solution of the inverse beamforming problem, i.e. the set of coefficients related to the Equivalent Sources defined in the scan plane, whose elementary acoustic contribution is able to reconstruct the acoustic field sampled at the array level.
- $\underline{p}^{(i)}$ is the vector of the pressure values sampled at the array level. In Chapter 2 it has been shown that very often it is obtained by means of a PCA of the CSM. It also possible to exploit the complex spectra of the microphone signals provided that they need to share a common phase reference.
- A is the radiation matrix that defines the propagation of the equivalent sources' sound field from the scan plane level towards the array plane level.

The field '$\cdots$' is left for accounting for any other processing technique compatible with the ones already defined. One of those will be described below.

In this chapter, in fact, a brand new approach for improving the potential of the just recalled inverse beamformer is introduced. The solution *Y(A,*$\underline{p}^{(i)}$*)* is optimized using a microphone clustering algorithm for reducing numerical instabilities and separating uncorrelated contributions. The whole process makes it possible to decompose the acoustic field into absolute and quantified contributions of the partial fields produced by the main active sources. The idea behind the method is to process the acoustic images iteratively obtained performing GIBF on different clusters of microphones taken from the same array. The identification of the main source is expected to be similar during all iterations, while everything else that is related, for instance, to other numerical issues as ghost images, leakage of one principal component in another, etc., is expected to be different per each taken cluster of microphones. By combining such maps, the actual source distribution will be highlighted, while any further negative effect is suppressed. It will be shown that this method, called *Clustering Inverse Beamforming* (CIB), allows absolute source quantification and identification of correlated and uncorrelated source distributions, without any help from any additional reference sensor.

CIB is therefore a processing technique for improving the results of an inverse beamformer based on GIBF. However, its implementation adopting alternative ESM approaches is theoretically possible. The crucial aspect in the formulation of the clustering approach is in the statistical nature of the data that are manipulated. Such vision has been inspired by the statistical nature of the so-called average beamforming method proposed by Castellini et Al. in [58, 59] already described in section 1.1 of the introduction. The concept of combining different areas of a microphone array has been exploited also in other ways in literature. Guidati and Sottek in [137] discuss pros and cons the use of a modular microphones array adopting a "flexible" geometry allowing to adjust the aperture of the array to the targeted acoustic scene or to combine results of arrays with larger and smaller aperture. Such a flexible geometry is exploited and the results reported in the paper on a wind tunnel application. Elias proposes in [138] a so-called *multiplicative beamforming* (MBF) whose main purpose is enhancing the SSL solution by suppressing the unwanted effects of side-lobes of a direct beamformer. In its original formulation it is conceived for cross/star shaped arrays and requires the use of direct beamforming methods. The method has been applied, under these assumptions, in flyover applications [139]. A device referring to this principle has been patented [140]. The extension of the idea towards interior applications is obtained by exploiting the "double-sphere" concept. The two arrays' performances are combined together in the mid-frequency range and exploited to the best of their individual potential elsewhere for covering the largest frequency range possible. The implementation of these main ideas yields benefits in industrial applications ([53, 139]) mainly in terms of localization. The quantification capacity is increased if MBF only if combined with further post-processing with inverse methods. Despite a full description of the adopted methods seems to be not available in literature, the MBF appears on the one hand simple to implement, but on the other hand it presents some severe intrinsic limitations such as the difficulties in correctly identifying complex source distributions.

Contrarily to the reported cases, which share the characteristics of being deterministic and of exploiting direct beamforming methods, CIB is an inverse method that combine in a statistical formulation the results of ESM algorithm on clusters of data belonging to the same microphones array. CIB was presented for the first time in [132] and then extended in [136]. The inner statistical nature of CIB makes it versatile because it can be applied using any kind of array shape and geometry; moreover CIB is also general because it can be applied in exterior as well as interior applications without any change to the processing strategy. These characteristics (and the detailed analyses already performed) make this method a very appealing solution for advanced SSL applications such as aero-acoustics and interior noise identification.

The formulation of the method will be reported in section 3.1. Section 3.2 describes three alternative implementations, whereas sections 3.3 and 3.4 will report respectively on exterior and interior noise automotive applications.

3.1. The Clustering Inverse Beamforming formulation

The clustering approach aims at improving the conventional GIBF performances and it is based on the principle that the solution of an inverse beamforming problem is strongly dependent to the radiation matrix A considered. Indeed, by selecting only certain rows of A, i.e. considering a subset - cluster - of microphones among those constituting the whole array, the mathematical formulation of the problem changes, while the physical problem remains obviously the same. The regularization strategy and the iterative solution of GIBF will act differently depending on the radiation matrix considered: in this way, any numerical instability that give rise to ghost sources will vary, while the actual sources will be constantly identified.
This evidence is exploited performing the GIBF iterative process N_c times on N_c different clusters composed of N_m microphones. The set of GIBF solutions obtained in this way ($\underline{\tilde{a}}^{(i)}{}_c$, c=1, … , N_c) for each one of the main principal components (or for the overall acoustic field if $\underline{p}$ is used instead of $\underline{p}^{(i)}$), will be processed in order to obtain a so-called "clustering mask matrix". This matrix will be used to enhance the capabilities of GIBF to identify the main sources active in the acoustic field under study.
The clusters are more effective if the distribution of their microphones is as much homogeneous as possible with respect to the area of the full array. By means of the set of solutions $\underline{\tilde{a}}^{(i)}{}_c$ two functions will be obtained: the *normalized mean matrix* and the *normalized occurrences matrix*. The first one is defined as the averaged map, per principal components, of the GIBF acoustic images calculated for each cluster, the second matrix emphasizes the effect of the averaging process put in place by the mean matrix whenever the number of clusters considered may result exiguous for providing statistical consistency. It is obtained adopting the function ε which returns value 1 if its argument is non-zero, 0 otherwise:

$$\varepsilon(\underline{\tilde{a}}^{(i)}{}_c) \quad s.t. \quad \begin{cases} \varepsilon(\underline{\tilde{a}}^{(i)}{}_c(n)=0)=0 \\ \varepsilon(\underline{\tilde{a}}^{(i)}{}_c(n)\neq 0)=1 \end{cases} \quad \forall n=1,\ldots,N. \tag{3. 2}$$

The two matrices are then combined in the *clustering mask matrix*, whose expression, in which the *mean matrix* and the *occurrences matrices* are Hadamard multiplied, is the following:

$$\gamma^{(i)} = \overbrace{\frac{\sum_{c=1}^{N_c} \underline{\tilde{a}}^{(i)}{}_c}{\max\left(\sum_{c=1}^{N_c} \underline{\tilde{a}}^{(i)}{}_c\right)}}^{Mean\,matrix} \cdot \overbrace{\frac{\sum_{c=1}^{N_c} \varepsilon(\underline{\tilde{a}}^{(i)}{}_c)}{\max\left(\sum_{c=1}^{N_c} \varepsilon(\underline{\tilde{a}}^{(i)}{}_c)\right)}}^{Occurrences\,matrix}. \tag{3. 3}$$

The combined use of the inverse beamformer defined by Eq.(3. 1) (and described in Chapter 2) and the exploitation of the microphone clustering approach gives birth to the so-called *Clustering Inverse Beamforming* (CIB). In CIB the solution is obtained as a function of the acoustic image $Y(A,p^{(i)})$ calculated through the inverse beamforming formulation as described in Chapter 2 and the mask matrix $\gamma^{(i)}$ obtained through Eq.(3. 3). This approach is formalized in the expression:

$$\underline{a}^{(i)} = \Upsilon(A, \underline{p}, \gamma^{(i)}) \tag{3. 4}$$

and depicted in Fig. 3. 1.

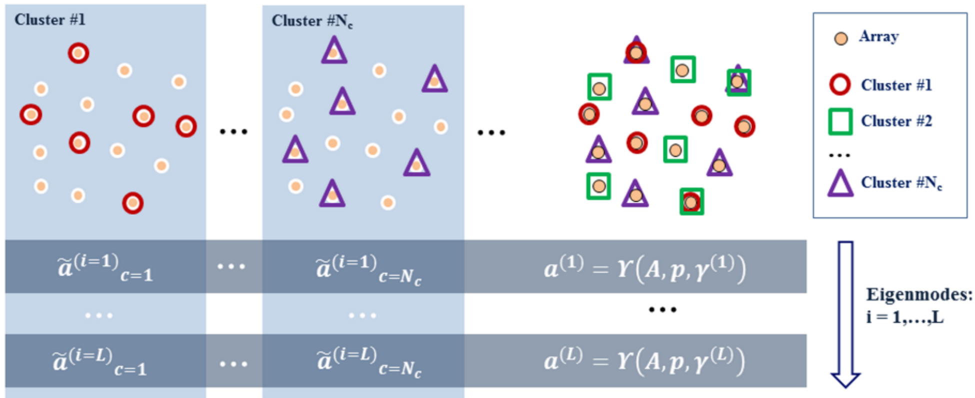

Fig. 3. 1 : Description of the Clustering Inverse Beamforming.

Eq.(3. 4) represents a general formulation of the method. The ways to exploit such formulation are manifold and the best approach can be selected according to the specific problem under investigation. Before listing some alternative methods, interesting aspects related to the effectiveness of the microphone clustering approach deserve to be investigated more in detail through the sensitivity analysis reported in the following section.

3.1.1. Sensitivity to the number of clusters (N_c) and the number of microphones in the cluster (N_m)

The number of microphones (M) to be included in the array, the minimum number of microphones (N_m) that is possible to use without reducing the effectiveness of the processing and the number of clusters (N_c) to be chosen play an important role in the CIB approach presented in this thesis. This section discusses the sensitivity of the method to such variables. The analysis is presented on a simulated beamforming problem with two

uncorrelated random noise sources (monopole-like) placed 0.6 m far from the array in free field conditions.
Two types of array, one with 43 (Fig. 3. 2(a)) and one with 100 (Fig. 3. 2(b)) randomly distributed microphones have been used in these analyses.

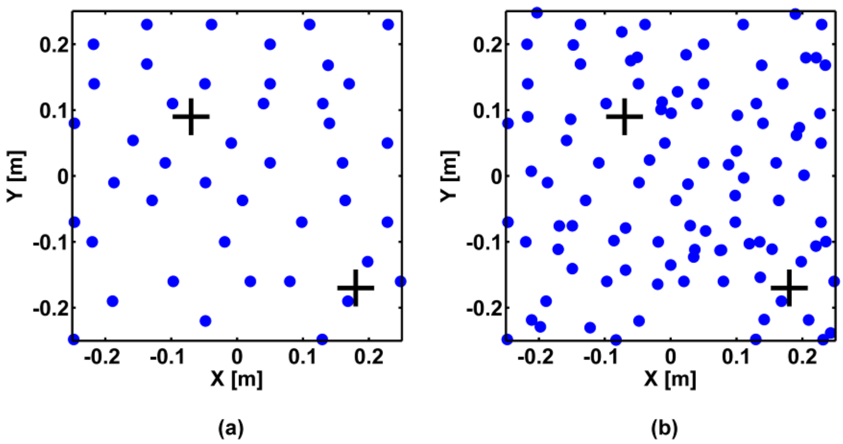

Fig. 3. 2 : problem stating with randomly distributed microphones. (a) M=43. (b) M=100. In both cases the sources locations are: Source#1: [-0.07 m , 0.09 m], Source#2: [0.18 m , -0.17 m].

Since the two sources are uncorrelated, their distributions should be retrieved by GIBF algorithm in the solutions $\underline{a}^{(i=1)}$ and $\underline{a}^{(i=2)}$. The objective of this analysis is to study the effect of the parameters M, N_c and N_m on the effectiveness of the clustering approach to avoid unwanted numerical issues as the leakage of the source distribution of one solution in the other one (see [39]): such effect is obtained by means of the mask matrix $\gamma^{(i)}$ in Eq.(3. 4).
Fig. 3. 3 and Fig. 3. 4 report some examples of this analysis. On the left side of the figures are reported the mask matrices related to Source#1 and on the right one the ones related to Source#2 in different configuration of the parameters M, N_c and N_m. Fig. 3. 3 gives a visual comparison of the mask matrices obtained increasing the number of microphones within each cluster given and fixed the setting of the other parameters. It can be noticed that the increase of N_m makes the mask matrix contribution becoming more uniformly distributed around the ideal location of the source and the spots due to numerical instabilities are almost no longer present. However, despite much lower than the ideal source location, the contribution corresponding to the leakage of the other source becomes more aggregate and its pattern more clearly detectable. Despite this is an undesired behaviour, because it emphasizes the mutual leakage of principal components, it is in line with the spirit of the method. This in fact proves that the statistical nature of the microphone clustering approach tends to pull up the deterministic information, filtering out the rest. The mutual leakage of the principal components is in fact due to limitations of the PCA processing of the CSM, but it is related to physical phenomena. If those physical phenomena are still energetically relevant after the PCA, if compared to the main source, they will be captured by the

microphone clustering approach. This is not a limitation of the technique: the mask matrix is the outcome of a statistical process that makes it possible to interpret $\gamma^{(i)}$ as a most-likelihood indicator, i.e. defining $\gamma^{(i)}(n)$ as the probability that the n^th^ equivalent source belongs to a physical source distribution. With such assumption in mind the interpretation of the mask matrices of Fig. 3. 3 tells the user that the ideal source locations are always identified with "confidence level" ≈*1*. In the locations corresponding to the mutual leakage of principal components such "confidence level" is much poorer. This aspect will be exploited and further deepened in section 0.

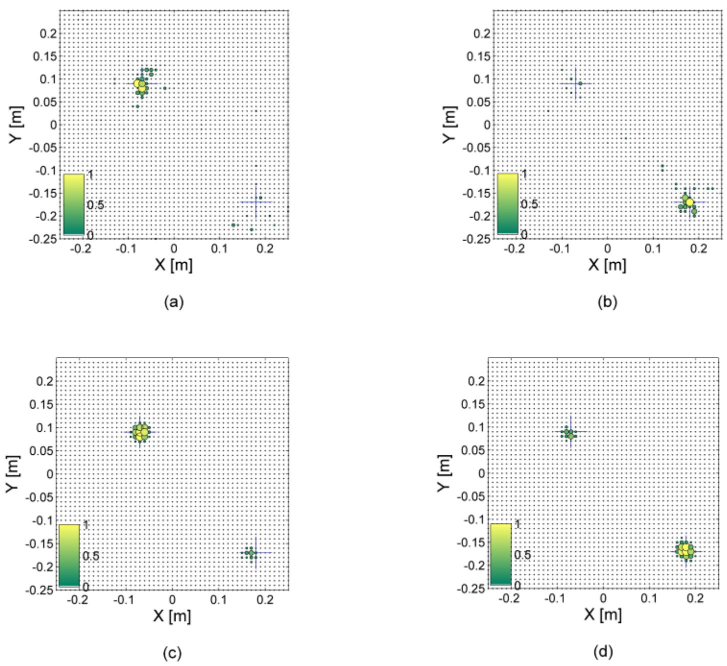

Fig. 3. 3 : Clustering mask matrices (left: $\gamma^{(i=1)}$, right: $\gamma^{(i=2)}$) with different parameters settings. (a-b) $M=43$, $N_c = 30$, $N_m = 5$. (c-d) $M=43$, $N_c = 30$, $N_m = 15$. Example of results @ 2 kHz.

Fig. 3. 4(a-b) and Fig. 3. 4(c-d) show what happen to the mask matrices when the used number of clusters (N_c) is increased from 30 to 100. The effect appears not as evident as the one obtained varying the N_m parameter and the visual comparison of the results do not give enough detail about the sensitivity of the method to these parameters.

For a more systematic interpretation of the results of the analysis, a quantitative instrument is now introduced. CIB aims at enhancing the source identification capability of GIBF mainly by reducing the numerical instabilities linked to the solution of GIBF inverse problem. Numerical instabilities result in ghost sources and noise in the acoustic image, hence lowering the contrast of the sources with respect to the background of the map.

Looking at the acoustic imaging problem from this point of view, CIB improves therefore the contrast.

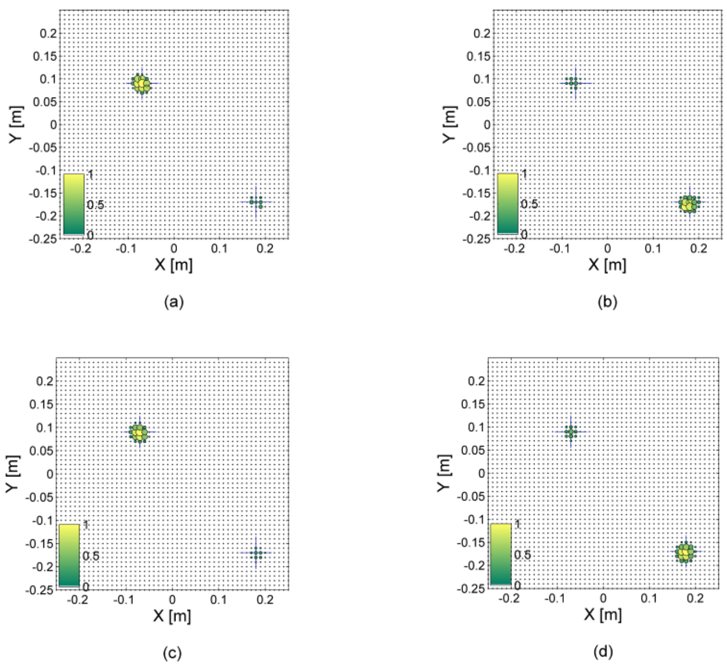

Fig. 3. 4 : Clustering mask matrices (left: $\gamma^{(i=1)}$, right: $\gamma^{(i=2)}$) with different parameters settings. (a-b) M=100, N_c = 30, N_m = 15. (c-d) M=100, N_c = 100, N_m = 15. Example of results @ 2 kHz.

An interesting estimator to prove such concept is the Contrast to Noise Ratio (CNR) [141]. The CNR is a well-known parameter in the community of image processing, since it expresses the quality of an image in terms of contrast (task related image content vs background). It is defined as:

$$CNR = \frac{\left(\overline{P}_{ROI,I} - \overline{P}_{ROI,background}\right)}{\sqrt{\sigma^2_{ROI,I} + \sigma^2_{ROI,background}}} \tag{3. 5}$$

where:

$\overline{P}_{ROI,I}$ represents the mean value of the target structure in the Region of Interest (ROI);

$\overline{P}_{ROI,background}$ is the mean value of the image background in the Region Of Interest (ROI) – target region excluded;

$\sigma^2_{ROI,I}$ is the variance of the target structure in the Region Of Interest (ROI);

$\sigma^2_{ROI,backgorund}$ is the variance of the target structure in the Region Of Interest (ROI) – target region excluded.

Fig. 3. 5 shows a study carried out to test the influence of the parameter N_c by varying the number of clusters in the range: {5,30,100,150,200,250,300,500,1000,5000} for a fixed number of microphones per cluster (N_m=15). Increasing the number of clusters considered in the computation of the mask matrix increases the statistical sample giving more stability to the mean matrix. In order to measure such trend, the CNR function has been calculated on the *mask matrix* and the so-called *squared mean matrix* as a function of N_c. Results are presented in semi-logarithmic scale (horizontal axis) for sake of clarity. The trend show in Fig. 3. 5(a) confirms, as expected, that:

$$\uparrow N_c \quad \Rightarrow \quad \gamma^{(i)} \rightarrow \left(\frac{\sum_{c=1}^{N_c} \underline{\tilde{a}}^{(i)}{}_c}{\max\left(\sum_{c=1}^{N_c} \underline{\tilde{a}}^{(i)}{}_c \right)} \right)^2 \tag{3. 6}$$

The same observation can be confirmed and further highlighted by plotting the evolution of the Root-Mean-Squared Deviation (RMSD, Eq.(3. 7), expressed in percentage with respect to the maximum mean deviation that can be obtained, i.e. 1) at varying N_c values.

$$RMSD = \sqrt{\frac{1}{N} \sum_{n=1}^{N} \left(\gamma^{(i)}(n) - \left(\frac{\sum_{c=1}^{N_c} \underline{\tilde{a}}^{(i)}{}_c(n)}{\max\left(\sum_{c=1}^{N_c} \underline{\tilde{a}}^{(i)}{}_c \right)} \right)^2 \right)^2} \tag{3. 7}$$

Fig. 3. 5(b) reports the RMSD as a function of N_c showing that it tends to zero when N_c becomes very high. The results just obtained confirm also the important role played by the *occurrences matrix* when working with an exiguous number of clusters ($\downarrow N_c$). In fact such matrix allows compensating for the exiguous statistical sample for the computation mean matrix keeping the statistical result still meaningful. When N_c increases, instead, the information carried by the occurrences matrix becomes redundant in the sense of Eq.(3. 6). Numerically speaking it means that the two matrices become more and more similar when

N_c increases. This is confirmed by Fig. 3. 6 and Fig. 3. 7 that report mean matrix, occurrences matrix and their differences in the case of the identification of Source#1 setting N_c=30 and N_c=1000 respectively.

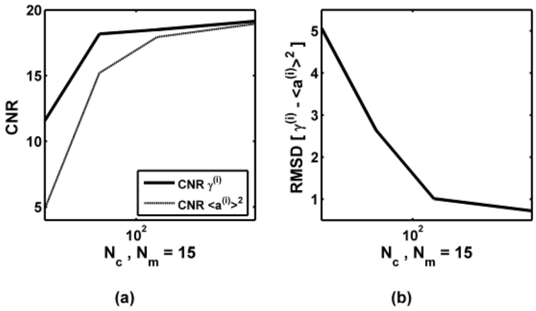

Fig. 3. 5 : (a) CNR achievable exploiting the mask matrix and the squared mean matrix with different N_c. (b) Root Mean Squared Deviation of the difference between the mask matrix ($\gamma^{(i)}$) and the squared mean matrix ($<a^{(i)}>^2$) as a function of the N_c parameter. (c) CNR of the mask matrix obtained for a fixed N_c , varying the number of microphones in each cluster.

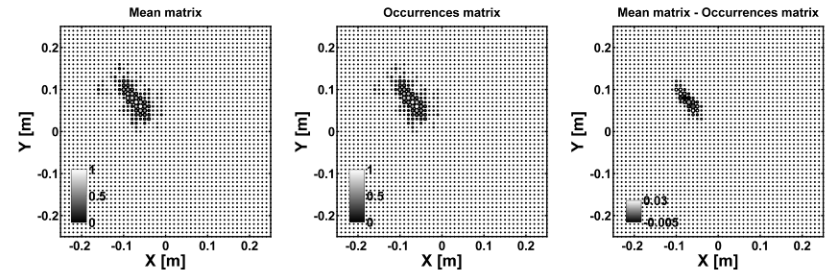

Fig. 3. 6 : Identification of Source#1. Mean matrix, occurrences matrix and their difference in the case of: M=100, N_c=30, N_m=15.

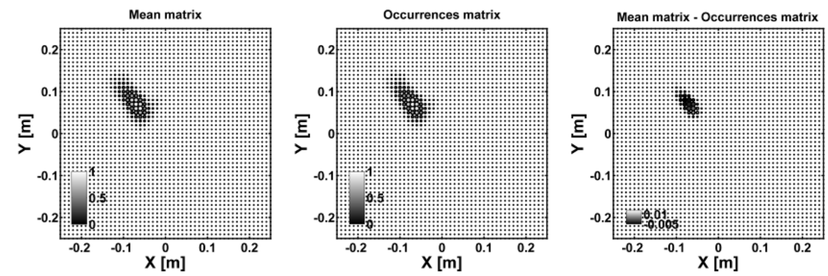

Fig. 3. 7 : Identification of Source#1. Mean matrix, occurrences matrix and their difference in the case of: M=100, N_c=1000, N_m=15.

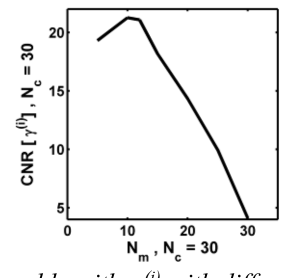

Fig. 3. 8 : CNR achievable with $\gamma^{(i)}$ with different N_m. M=43, N_c=30.

What turns out from this study is that the microphone clustering approach is indeed a statistical method which stably converges to the desired solution thanks a weighted averaging process of the microphone clustering results. The use of the occurrences matrix strengthen such statistical formulation making it possible to compensate for a limited information (limited number of clusters) providing stability and saving computational costs.
It is also interesting to show the effect of changing the number of microphones per cluster by keeping constant the number of clusters. Fig. 3. 8 reports the CNR dependence from the parameter N_m (range: $N_m=\{5,10,12,15,20,25,30\}$) when the mask matrix is estimated using Eq.(3. 3).
The curve presents a clear convexity and a maximum for $N_m=10$ in this case. Such behaviour can be explained observing that the maximum number of microphones available for creating different clusters is 42 (max $N_m=M-1$). Therefore: on the one hand the probability of having consistently different patterns of microphones in each cluster increases if the number N_m decreases; on the other hand, too few microphones per cluster lead to bigger numerical issues for the solution of the inverse problem. The balance between these two opposite effects leads to an optimal value (range) for N_m.
This sensitivity analysis aimed at illustrating how the three main parameters involved in the clustering approach, i.e. M, N_m and N_c, impact on the *mask matrix* and therefore influence the results of the overall source localization approach. The following considerations can be derived:

- The increase of the number M of microphones in the array, as expected, does not produce any advantage to the mask matrix for the same values of N_m and N_c, as long as a full coverage of the array area is guaranteed.
- A high number of taken clusters N_c produces a better localization of the source distribution. It tends to remove all the numerical artefacts except the leakage of one source in the source distribution of the other principal component. This phenomenon is significantly attenuated, but not completely removed.
- The algorithm demonstrated to be robust also when a reduced number of microphones within each cluster is considered. A reduction in N_m produces mask matrices with more spots due to numerical issues, but minor and randomly distributed in the map, while the source localization remains good and the attenuation of the numerical leakage of one principal component in the other is even more efficient with respect to the other cases.

It turns out that the technique is robust and yields good results in all the investigated cases, meaning that there is not only one optimal combination of such parameters. They rather can be tuned according to the characteristics of the acoustic field under study.
A big added value of the proposed method is the benefit deriving from the possibility of using arrays with limited number of microphones and with no specific geometry.

3.2. Exploitation of the microphone clustering principle

Eq.(3. 4) formalized that the CIB solution is obtained as a function of the acoustic image calculated through the inverse beamforming formulation as described in Chapter 2 and the mask matrix $\gamma^{(i)}$ obtained through Eq.(3. 3). The idea is, therefore, to combine the statistical information carried by the mask matrix with the physical least squares reconstruction of the acoustic field obtained through ESM. Notice, however, that the mask matrix contains not only accurate information about the localization of the sources, but also about the ranking of the equivalent sources belonging to the same distribution. This multiplex nature of $\gamma^{(i)}$ allows manifold exploitations. In the following paragraphs three possibilities will be described.

Dedicated examples on simulated and experimental data will be used for describing and highlighting strengths and limitations of the proposed methods. Fig. 3. 9 depicts the numerical simulations and experimental setups.

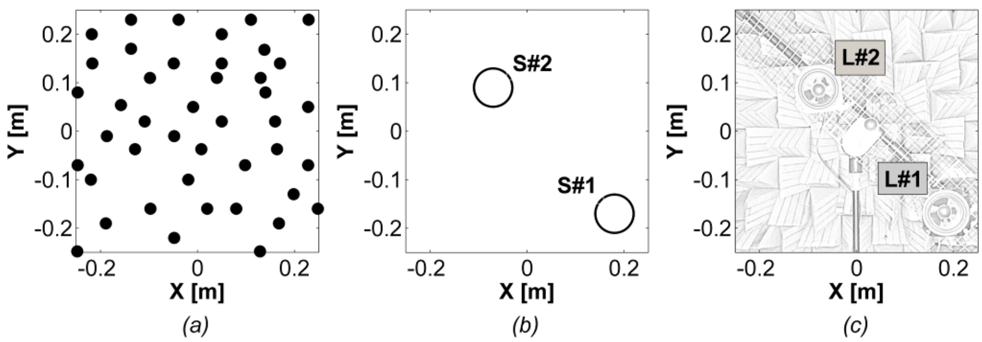

Fig. 3. 9 : numerical simulations and experimental setups. (a): 43 randomly distributed microphones array geometry. (b): locations of the simulated random noise sources S#1 and S#2. (c): experimental test scenario in which two loudspeakers, L#1 and L#2, emit band-limited random noise (range: 1000 Hz – 12000 Hz).

In the numerical simulations represented by Fig. 3. 9(b) S#1 and S#2 are two uncorrelated random noise sources of nominal acoustic power of 41 dB (W_{ref} = 10^{-12} W). Since the Sound Pressure Level (SPL) quantity is more easy to interpret, in Fig. 3. 10(a) is reported the amplitude of the spectra of the two sources as the SPL that a microphone placed 0.04 m far from each source would ideally record is reported in Fig. 3. 10(a).

In the experimental scenario two loudspeakers are used to emit a band-limited random noise signal in the range 1000 Hz – 12000 Hz. The setup is placed in a semi-anechoic room and the geometrical configuration of the sources and the microphones in the array is the same as the simulated case: an array of 43 randomly distributed microphones is placed 0.6 m far from the sources plane and the two sources, L#1 and L#2 in the experimental case, S#1 and S#2 in the numerical simulation, are located in: [0.18 m; -0.07 m] and [-0.17 m;

0.09 m] respectively. The acoustic power of the loudspeakers in the test conditions was not known. In order to obtain quantitative references the speakers have been activated one at the time and the acoustic pressure measured at the microphones location has been back-propagated towards a location placed 0.04 m in front of each loudspeaker. The SPL spectra obtained in this way for L#1 and L#2 are reported in Fig. 3. 10(b).

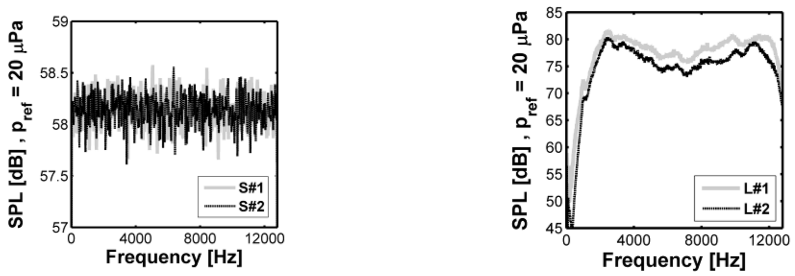

(a) *(b)*

Fig. 3. 10 : SPL spectra computed at 0.04 m far from the sources. (a): numerical simulation. (b) experimental case.

Where not differently specified, the colour code used for the representation of the acoustic images and the mask matrices is reported in Fig. 3. 11.

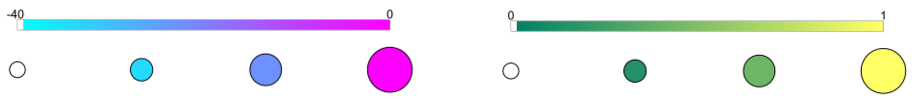

(a) *(b)*

Fig. 3. 11 : colour code for the representation of: (a) acoustic image; (b) mask matrix.

The acoustic images, Fig. 3. 11(a), will be represented normalized on their maximum value in a dB scale with a dynamic range of 40 dB. The size of the markers in the scatter plots is proportional to the value assumed by the equivalent source in the corresponding location. The mask matrices values range by definition from 0 to 1. In this case the colours reported in Fig. 3. 11(b) are used and the size of the markers are proportional to the values assumed by the mask matrix in the corresponding location. The acoustic images maps, therefore, will allow the ranking of the identified sources, but not their absolute quantification. Whenever the quantitative results will be required they will be provided with other graphical instruments. Keeping separated the qualitative and quantitative information should help the interpretation. In fact the reader should be aware that while a conventional beamforming map reports the SPL value "virtually sensed" in each location of the calculation plane through a scanning procedure, an acoustic image reports the discretization of the acoustic field in elementary sources whose acoustic effect can be estimated only considering all of them at once (as described in paragraph 2.3.2 of Chapter 2). This aspect should be considered also in the qualitative ranking of the sources identified in an equivalent sources map.

3.2.1. Method 1: mask matrix adopted as spatial filter

The simplest version of the general function coined in Eq.(3. 4) is the Hadamard product between the inverse acoustic image $Y(A, \underline{p})$ and the clustering mask matrix $\gamma^{(i)}$ as shown in Eq.(3. 8). In this way the mask matrix acts as a spatial filter on the acoustic image:

$$\underline{a}^{(i)} = \mathrm{Y}\left(A, \underline{p}\right) \cdot \gamma^{(i)} . \tag{3. 8}$$

This approach has the advantage of being very simple and robust because it does not require any additional processing. It has the drawback that the multiplicative effect of the function $\gamma^{(i)}$ makes the quantification less accurate because the strength of the equivalent sources are attenuated by the mask matrix whose values range from 0 to 1. Moreover, the masking effect is strongly dependent on the mask matrix shape. To give an example a comparison of the mask matrix computation with two different processing is reported in Fig. 3. 12. In this case the experimental scenario depicted in Fig. 3. 9(c) was chosen because in this case the sound is emitted by loudspeakers instead of ideal point sources. This makes the modelling in terms of equivalent sources more challenging and the choice of the calculation parameters and strategy may strongly influence the final results.

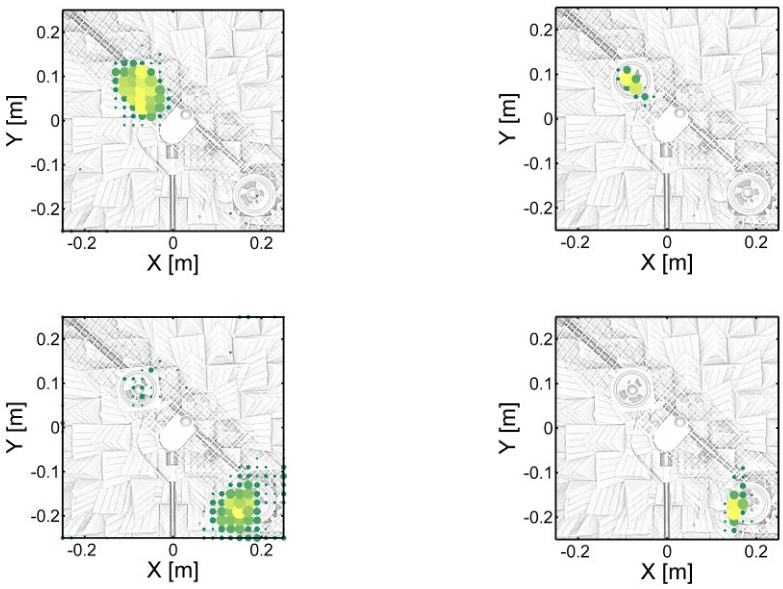

(a) *(b)*

Fig. 3. 12 : comparison mask matrices $\gamma^{(i)}$ computed without, (a), and with, (b), PCA-based adaptive pre-processing.

Fig. 3. 12(a) and Fig. 3. 12(b) show the mask matrices $\gamma^{(1)}$ (top), and $\gamma^{(2)}$ (bottom) in which the clustering solutions $\underline{\tilde{a}}^{(i)}{}_c$ have been obtained without using the PCA-based adaptive pre-processing introduced in Chapter 2, and with this pre-processing technique respectively. The second one is sharper that the first one. Their spatial filtering effect through the application of Eq.(3. 8) is visible in Fig. 3. 13(a) and Fig. 3. 13(b). The sources locations are identified accurately and correctly in both the (a) and (b) cases, while the masking effect is obviously more severe when adopting the sharper version of the mask matrix. This makes this method more suited for improving the localization of the identified noise sources in the acoustic image rather than their quantification.

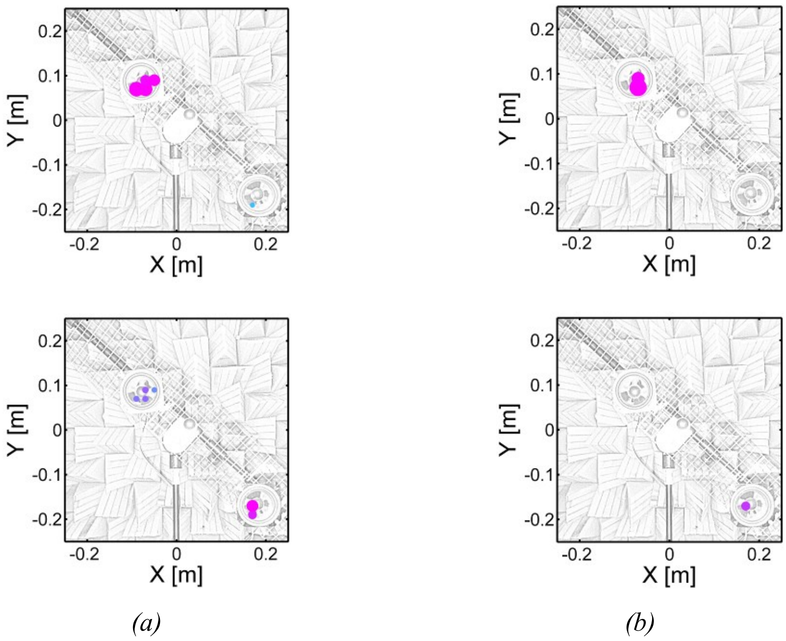

Fig. 3. 13 : comparison of the results obtained adopting method 1 ($Y(A, \underline{p}^{(i)})\cdot \gamma^{(i)}$) computed without, (a), and with, (b), PCA-based adaptive pre-processing.

3.2.2. Method 2: mask matrix adopted for labelling the acoustic image

One way to avoid the masking effect of the mask matrix on the final solution is to use $\gamma^{(i)}$ for labelling the inverse acoustic imaging $Y(A, \underline{p}^{(i)})$. This can be formalized as in Eq.(3. 9):

$$\underline{a}^{(i)} = f\left(\mathrm{Y}\left(A, \underline{p}\right), \gamma^{(i)}\right). \tag{3. 9}$$

The underlying idea is to compare the mask matrix map obtained from each principal component with the overall acoustic image $Y(A, \underline{p})$ (or, alternatively, with its corresponding solution $Y(A, \underline{p}^{(i)})$ computed per principal component) through pattern recognition. The acoustic power of a pattern W_ζ in $Y(A, \underline{p})$ is labelled as part of the ith source distribution whether a pattern $\gamma^{(i)}(n_\xi)$ is recognizable in a similar area in the mask matrix. By doing so $\gamma^{(i)}$ is not used just as a mask map: it rather selects, among the sources patterns in the acoustic image $Y(A, \underline{p})$, those patterns belonging to the same ith principal component. Such approach results in the following algorithm:

1) Identify the recognizable patterns in the acoustic image $Y(A, \underline{p})$, being W_ζ the acoustic power (or any other acoustic quantity with the proper adjustments) of the ζ^{th} pattern using Eq.(2.20).
2) Assuming n_ξ to be the indices of the ξ detectable patterns in the mask matrix, let us define $\eta^{(i)}{}_\xi$ with the following formula:

$$\eta_\xi^{(i)} = \sum_{n \in n_\xi} \gamma^{(i)}(n) \tag{3. 10}$$

3) Select, in the mask matrix, the patterns according to the following condition:

$$\bar{n}_\xi = \left\{ n_\xi \quad s.t. \quad \eta_\xi^{(i)} \geq \alpha \cdot \max\left(\eta_\xi^{(i)}\right) \right\}, \tag{3. 11}$$

where α is an arbitrary threshold depending on the characteristics of the acoustic field under study. The author suggest to set α=0.5.

4) Check intersection between the patterns recognized in $Y(A, \underline{p})$ and in $\gamma^{(i)}$ for determining the solution $a^{(i)}$:

$$\bar{n}_\varsigma = \left\{ n_\varsigma \quad s.t. \quad n_\varsigma \cap \bar{n}_\xi \neq \varnothing \right\} \quad \Rightarrow \quad a^{(i)} = \left\{ \mathrm{Y}\left(A, \underline{p}\right) \right\}_{\bar{n}_\varsigma} \tag{3. 12}$$

Fig. 3. 14 shows an example of comparison between the overall map $Y(A, \underline{p})$ and $\gamma^{(i)}$. The right arrows in the $\gamma^{(i)}$ map indicate the $\gamma^{(i)}(n_\xi)$ patterns of minor entity that have been discarded. In the case of this example, step 4) will yield the $a^{(i)}$ map shown in Fig. 3. 15.

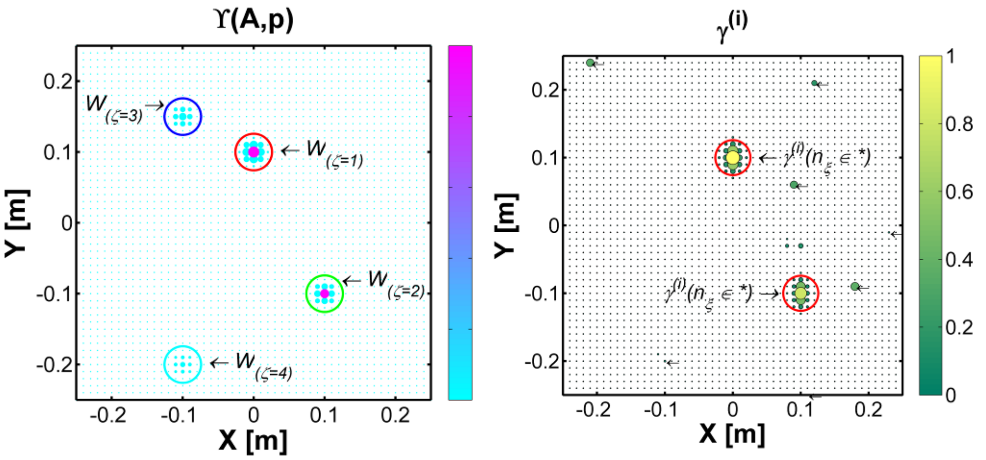

(a) *(b)*

Fig. 3. 14 : example of comparison of Y(A, p) and in $\gamma^{(i)}$ for clustering-based sources labelling and quantification. (a): step 1) quantification of the identified patterns in the overall acoustic image Y(A, p). (b): step 3) selection the mask matrix patterns according to Eq.(3. 11).

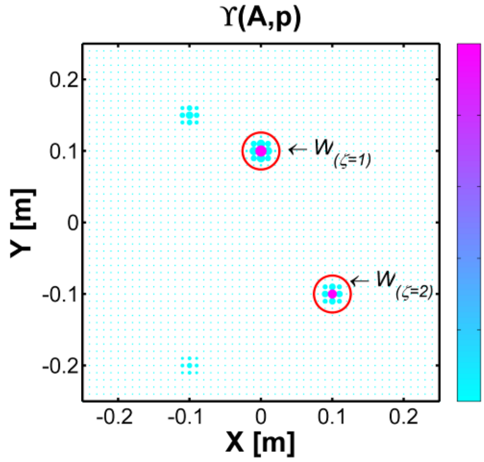

Fig. 3. 15 : step 4) only the patterns corresponding to the criterion given by Eq.(3. 12*) are included in the result obtained through clustering-based labelling and quantification.*

In order to give a practical explanation of the two approaches (method 1 and method 2) described so far, an application on a simulated scenario of Fig. 3. 9(b) will be given below.

Fig. 3. 16 and Fig. 3. 17 report an example, computed at 2000 Hz, of solution adopting GIBF. No PCA-based pre-processing has been used. It can be noticed that the computation of the solution per principal component yields a leakage of one uncorrelated source into the acoustic image of the other (Fig. 3. 16 (a) and (b)) in correspondence of their ideal location.

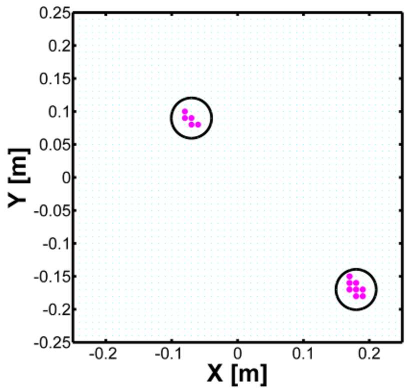

(a)

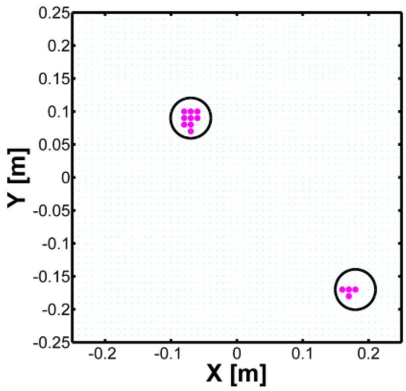

(b)

Fig. 3. 16 : solutions obtained with GIBF per principal component @ 2000 Hz without using the microphone clustering approach and PCA-based adaptive pre-processing. (a): $Y(A, \underline{p}^{(1)})$ (b): $Y(A, \underline{p}^{(2)})$.

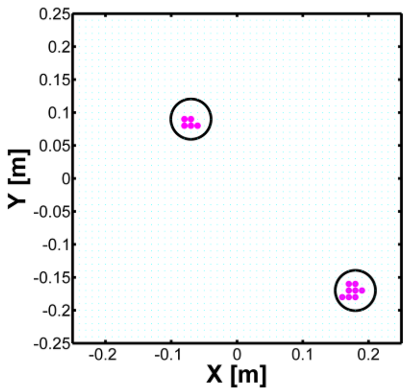

Fig. 3. 17 : overall solution ($Y(A, \underline{p}^{(1)}+\underline{p}^{(2)})$, @ 2000 Hz) obtained with GIBF computing all the main principal components at once without using the microphone clustering approach and PCA-based adaptive pre-processing.

Despite the two solution obtained: $Y(A, \underline{p}^{(1)})$ and $Y(A, \underline{p}^{(2)})$ are mathematically orthogonal, the user is therefore not able to correctly retrieve the physical location of the two uncorrelated sources and it is not even possible to ensure that no numerical issues occurred.

One way to obtain a more robust result is computing all the main principal components at once ($Y(A, \underline{p}^{(1)} + \underline{p}^{(2)})$, as reported in Fig. 3. 17) so that any mutual interaction (physical or mathematical) between the two uncorrelated sources distributions is automatically taken into account. In addition to the one just pointed out, this operation has the benefit of firstly discarding from the array data all the components which are not related to the main acoustic sources (uncorrelated background noise) and secondly to optimally distribute the acoustic strength among the sources thanks to the most likelihood nature of the GIBF solution. However, the so-called *overall solution* does not allow to separate the investigated acoustic field into uncorrelated distribution. Moreover, in complex scenarios (such as the ones that will be reported in paragraphs 0 and 0) numerical issues may pollute the acoustic image.
Fig. 3. 18 describes how the exploitation of the microphone clustering approach through the methods 1 and 2 described above can improve the results. In Fig. 3. 18(a) the clustering mask matrices (left: $\gamma^{(1)}$ and right: $\gamma^{(2)}$) calculated at 2000 Hz are reported, while Fig. 3. 18(b) and Fig. 3. 18(c) report the result of the application of methods 1 and 2 respectively. Method 2 exploits the information carried by the mask matrix for labelling the sources retrieved in the acoustic image. In this case it is preferable to use, as acoustic image to be labelled, the overall solution in order to make it possible, if needed, an optimal quantification. In Fig. 3. 18(c) have been reported also the quantification of the labelled patterns in the acoustic image obtained through the algorithm described in section 2.3.2.

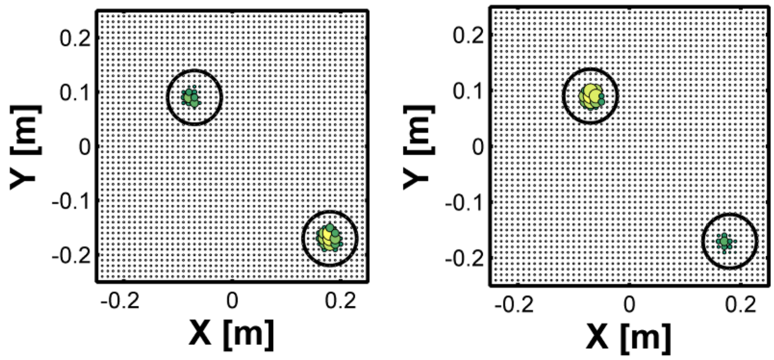

(a)

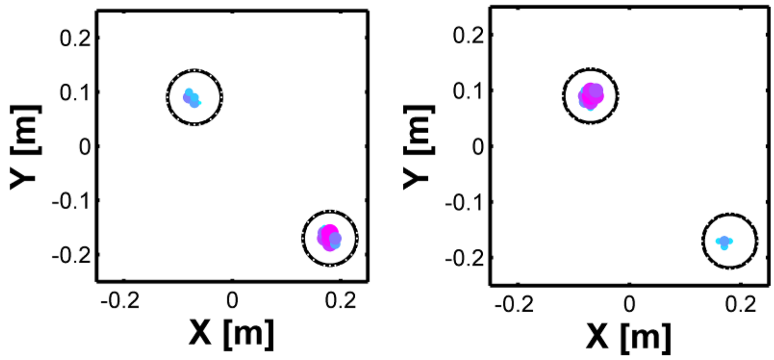

(b)

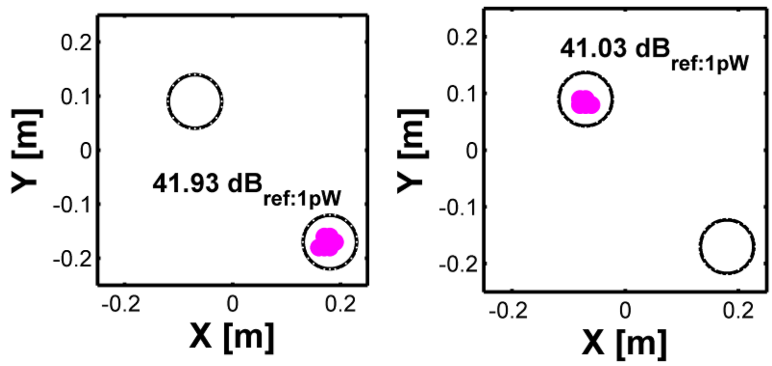

(c)

Fig. 3. 18 : comparison of method 1 and method 2; example @ 2000 Hz. (a): mask matrices $\gamma^{(1)}$ and $\gamma^{(2)}$. (b): solutions adopting Eq.(3. 8). Left: $Y(A, \underline{p}^{(1)})\cdot \gamma^{(1)}$; right: $Y(A, p^{(2)})\cdot \gamma^{(2)}$. (c): solutions adopting Eq.(3. 9). Left: $f(Y(A, \underline{p}^{(1)} + \underline{p}^{(2)}), \gamma^{(1)})$; right: $f(Y(A, \underline{p}^{(1)} + \underline{p}^{(2)}), \gamma^{(2)})$.

3.2.3. Method 3: mask matrix as confidence level distribution

The results shown in Fig. 3. 18 demonstrate that the use of the clustering mask matrix enhances an inverse acoustic imaging solution and that it can be exploited in many ways. The two methods presented so far have pros and cons: method 1, for example, is robust but its masking effect may alter the quantitative results, whereas method 2 does not introduce any masking effect, allowing an optimal quantification of the sources identified in the acoustic image; however it relies on the recognition of patterns within the acoustic image under study. This is a drawback in presence of complex acoustic scenes (an example will be given in section 0) because the pattern matching procedure described in paragraph 0 may fail. For this reason a third method for exploiting the information carried by the clustering mask matrix, which is related to its inner statistical nature, is given in this paragraph. In order to do so it is necessary to interpret the mask matrix $\gamma^{(i)}(n)$ as a function that expresses the probability that the nth equivalent source in the scan grid corresponds to a physical source distribution in the acoustic image. This probability information is obtained *a posteriori* interpreting the equivalent sources corresponding to the values of the mask matrix closer to 1 as the most likely source distribution representative of the investigated acoustic scene.
The idea, formalized as in Eq.(3. 13), is to select in the inverse problem only those equivalent sources locations in the scan grid assuming mask matrix values above a wanted threshold t_L called *confidence level*.

$$\underline{a}^{(i)} = \Upsilon\left(\{A\}_{M,f\left(\gamma_{t_L}^{(i)}\right)}, \underline{p}^{(i)}\right) \tag{3. 13}$$

Fig. 3. 19 explains the concept graphically.

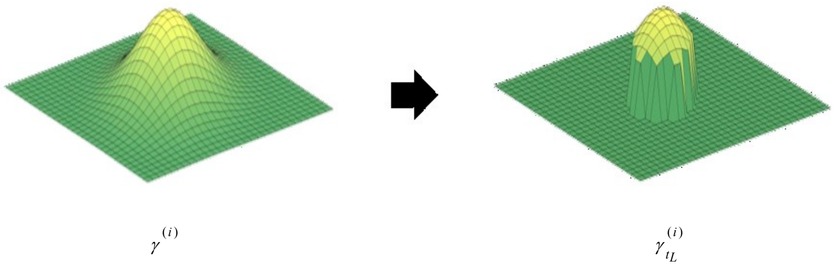

Fig. 3. 19 : the confidence level distribution concept: selecting a confidence level is equivalent to consider only the regions of those scan points in which the clustering mask matrix value is above a wanted threshold t_L.

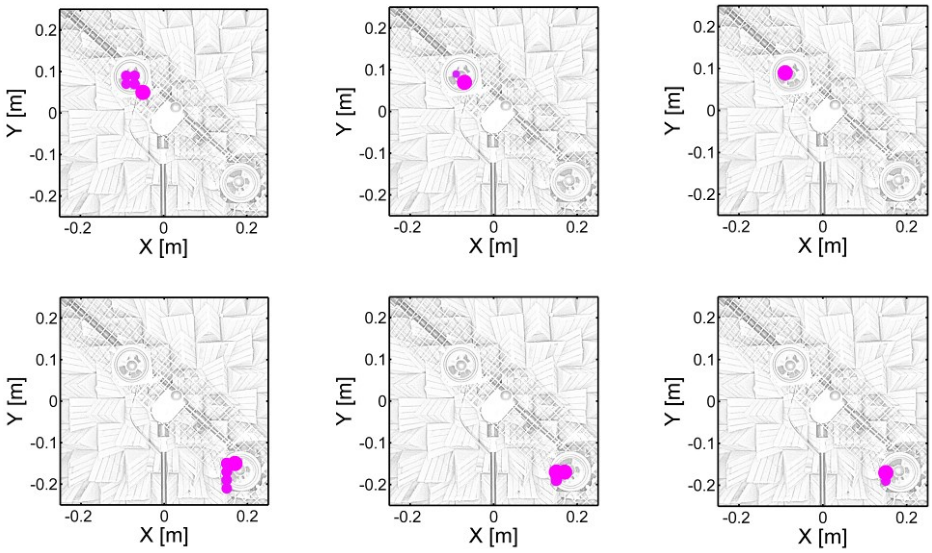

(a) (b) (c)

Fig. 3. 20 : method 3. Solution obtained adopting equation (3. 13); example @ 2000 Hz. Columns: (a), confidence level 20%; (b):confidence level 40%; (c):confidence level 80%.

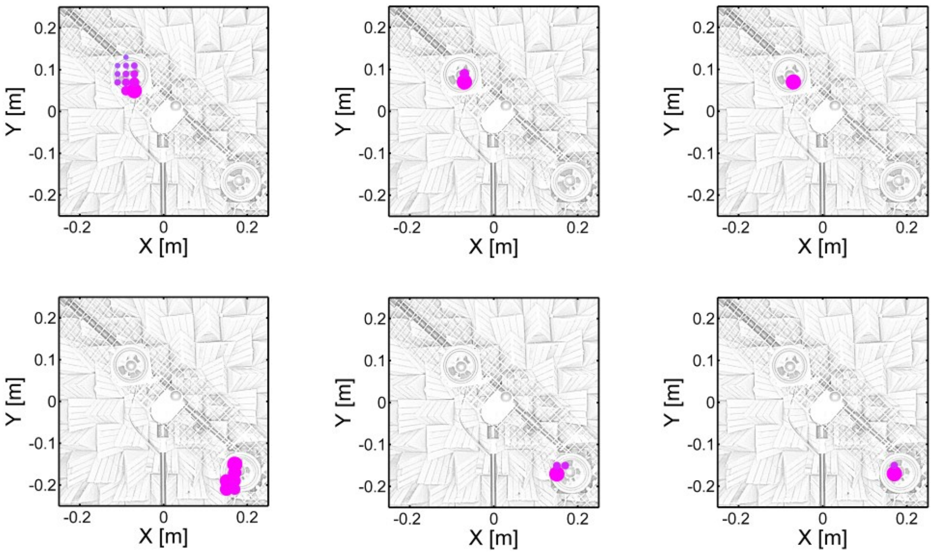

(a) (b) (c)

Fig. 3. 21 : method 3. (a): 1500 Hz. (b): 3000 Hz. (c) 6000 Hz. Confidence level: 50%.

This approach has the advantage of adopting the mask matrix for improving both the localization, selecting the equivalent sources close to its local maxima, and the quantification task, computing the strength of the equivalent sources only in the regions where a physical source is most likely expected. It has the drawback that the threshold t_L selection is user dependent. This may lead to inaccuracy in the reconstruction of sources with complex distributions.

Fig. 3. 20 reports an example of application of method 3 on the experimental case already introduced at the beginning of section 0. In particular it shows the result of the application of Eq.(3. 13) when selecting a progressive confidence threshold level t_L. For the computation, the mask matrices already plotted in Fig. 3. 12(b) have been used.

Fig. 3. 21 shows the results in the same experimental case for increasing frequencies. The confidence level adopted in Eq.(3. 13) is in this case kept constant to the threshold value t_L=0.5 (50% confidence level). Notice that the ranking of the sources is also correct because L#1 is always identified as slightly stronger than L#2 in accordance with the spectra of the SPL level of the two sources reported in Fig. 3. 10(b).

The example just reported shows that method 3 allows for accurate localization and quantitative results. In particular numerical issues and artefacts in the acoustic image are avoided by computing the acoustic field only adopting the equivalent sources corresponding to high values of the mask matrix. The quantification of the patterns identified in the acoustic images computed in this way allows a reliable estimation of the acoustic power radiated by the identified sources through Eq.(2.19) and Eq.(2.20) and the method described in section 2.3.2 of Chapter 2. Fig. 3. 22 reports the quantification results in the just treated experimental case in the range 1500 Hz – 12000 Hz.

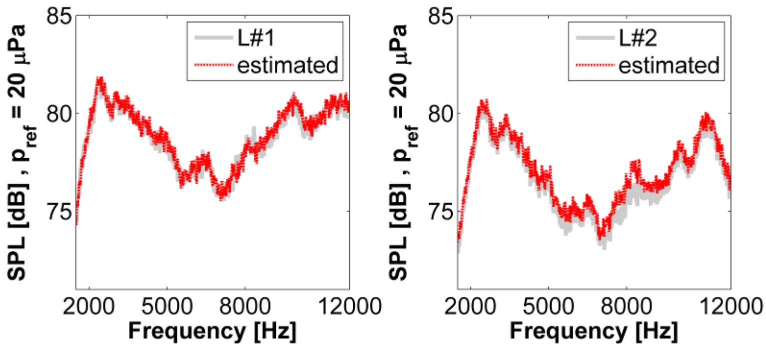

Fig. 3. 22 : SPL spectra estimation at 0.04 m far from the ideal location of L#1 and L#2 of the experimental case described in Fig. 3. 9 and Fig. 3. 10(b). The estimation has been obtained, in the range 1500 Hz – 8000 Hz through the acoustic power quantification of the identified sources.

To conclude this paragraph an application of method 3 on an experimental case in which the two loudspeakers are fed by the same band-limited random noise voltage signal - same amplification settings - is reported in Fig. 3. 23. The acoustic power quantification has been performed adopting the algorithm presented in paragraph 2.3.2 of Chapter 2. Despite an absolute reference is not available for the strength of the two correlated sources in this scenario, it is observed that the equivalent sources are distributed in such a way that the two patterns corresponding to the two loudspeaker sources emit a comparable power. The discrepancy between the two values (corresponding respectively to SPL values of 70.8 dB and 71.6 dB at 0.04 m far from the two sources) can be due, besides the inaccuracy of the proposed method, to the physical characteristics of the two speakers.

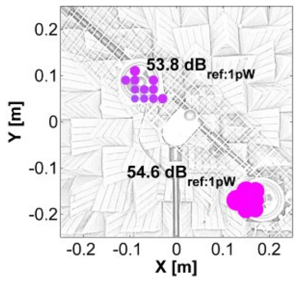

Fig. 3. 23 : acoustic power quantification. Experimental case: L#1 and L#2 are fed with the same band-limited random noise voltage signal. Example of results @ 2000 Hz.

3.3. CIB application to an automotive test case

In this section an application on an automotive test case of the advanced methods introduced so far is presented. Fig. 3. 24 describes the measurement setup adopted. The vehicle is mounted on a double-drum roller bench capable to move both front and rear wheels, in a semi-anechoic room. The drums (simulating the contact tire-ground) have been equipped with the configuration “slick”, therefore the road profile was not included. The measurement campaign was carried out in the frame of an in-door pass-by noise test on a prototype of electric vehicle. The acoustic imaging test, the array used (54 microphones) is visible in Fig. 3. 24(a), was performed simultaneously to the pass-by noise test. The purpose of the acoustic imaging processing shown below is to validate the capability of CIB in separating uncorrelated acoustic phenomena and accurately and reliably ranking the identified sources in terms of radiating acoustic power. Among the several test conditions, two constant speed regimes were selected for the acoustic imaging processing: the first at 50 km/h and the second at 110 km/h.

(a)

(b)

Fig. 3. 24 : test setup. Electric vehicle prototype tested in a semi-anechoic room instrumented with a double roller bench for front and rear wheels and for linear array for in-door pass-by noise test and a 54 microphones star array for acoustic imaging. (a) a view of the vehicle in the instrumented room. (b) the vehicle positioned on the roller bench.

Fig. 3. 25 shows the averaged (over the 54 microphones) Auto-Power Spectrum (APS) computed at the array level. It is clearly visible the difference in levels and frequency content between the two cases. The APS show the presence of broad-band noise as well as tonal components. Three main sources are expected to be responsible of the acoustic field generated by the vehicle: front wheels, rear wheels and the noise related to the engine. The three components are supposed to be uncorrelated because related to different causes. An analysis that allows the separation of the acoustic field in uncorrelated phenomena makes it possible to accurately localize them in space and ranking them in terms of the acoustic power radiated by each of them. For a deeper insight on the quantification of the acoustic

imaging results the reader can refer to [101] for the general theory and to the paragraphs 2.3.2 and 3.2.3 of this thesis for the implementation using CIB.

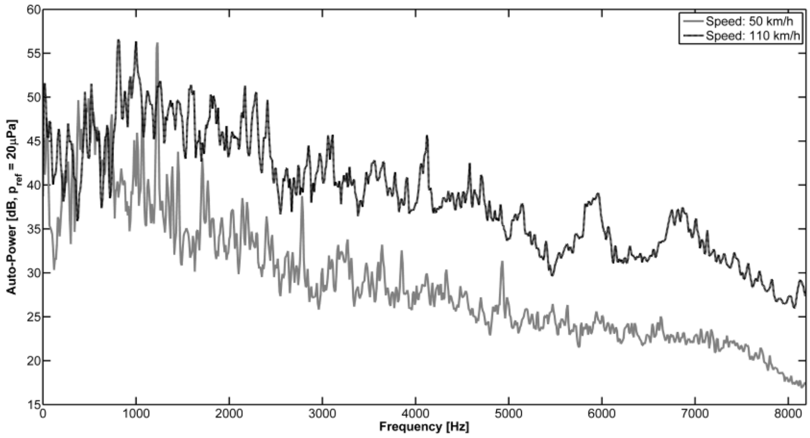

Fig. 3. 25 : Averaged APS at array location for speeds: 50 km/h and 110 km/h.

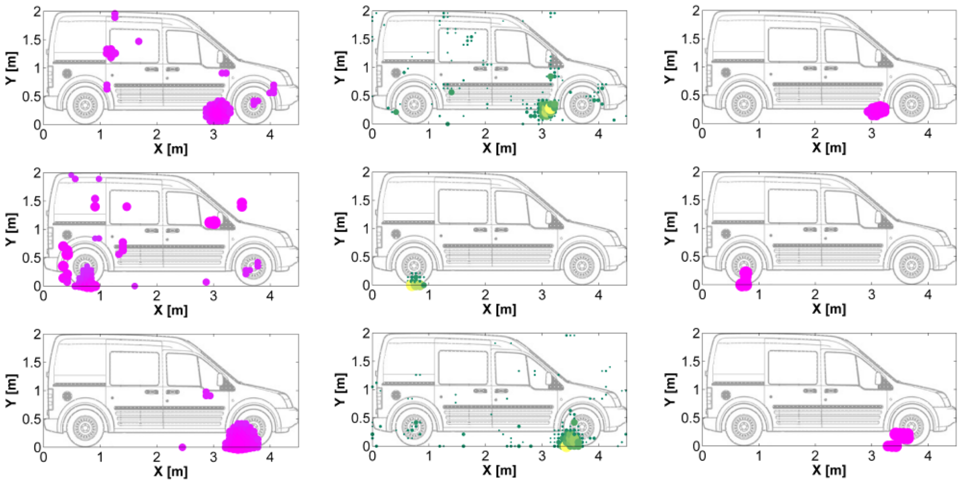

(a) *(b)* *(c)*

Fig. 3. 26 : example of improved solution adopting CIB. Solution computed at 1700 Hz in the scenario @ speed 50 km/h. (a): GIBF solution. (b): clustering mask matrices. (c) CIB solution.

The complexity of investigated acoustic field may dramatically reduce the accuracy of traditional acoustic imaging methods. An example is given in Fig. 3. 26(a) that reports the results obtained applying GIBF as formulated and described in sessions 2.1 and 2.2 of Chapter 2. It can be noticed that the maps corresponding to the three uncorrelated phenomena are polluted by ghost images and numerical issues. It will be shown in this paragraph that the use of CIB, through the exploitation of the clustering mask matrix (Fig. 3. 26(b)) allows to greatly improve the results (Fig. 3. 26(c)) making it possible further quantitative evaluations and the labelling and ranking of the identified acoustic sources.
The PCA-based adaptive pre-processing (theoretical details available in sections 2.3 and 2.4 of Chapter 2) has been adopted in the computation of the clustering mask matrices. Method 3, described in paragraph 0, has been chosen for the CIB processing. The colour code introduced in Fig. 3. 11 was adopted for the representation of the acoustic imaging results. The labelling and quantification of each source distribution has been performed adopting the method described in paragraph 2.3.2 of Chapter 2. Fig. 3. 27 shows some examples of the labelling and quantification of the identified sources in the two scenarios ((a) : 50 km/h and (b) : 110 km/h) at several frequencies in the range 500 Hz – 5000 Hz.

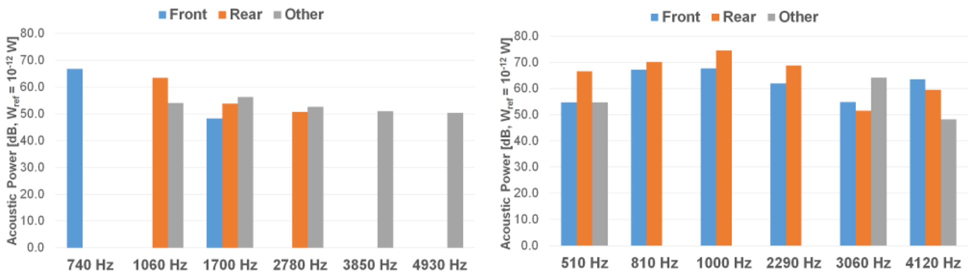

(a) *(b)*

Fig. 3. 27 : Labelling and ranking of the identified uncorrelated sources. The z axis represents the Acoustic Power of the sources in dB. $dB_{ref} = 10^{-12}$ W. (a) Speed: 50 km/h. (b) Speed: 110 km/h.

The labelling and ranking of the uncorrelated sources in the two scenarios allows a deep analysis of the three components. For example it shows that at lower speed (scenario (a) : 50 km/h) the engine contribution is more "audible" in a large frequency range and it is dominated by the tire noise only at low frequency. Whereas the case depicted in Fig. 3. 27(b) shows that the tire noise becomes dominant in the entire frequency range investigated. Rear tires become dominant around 1000 Hz, while the front tires are the dominant noise sources at low speed and low frequency.
The labelling analysis is possible thanks to the localization task reported in Table 3. 1 and Table 3. 2. Thanks to these maps other information becomes also available. In fact they allow an interpretation of the mechanisms of generation and propagation of the identified sources. To give some examples: the front tires noise seems to be generated by the trailing edge, while for the rear tires the leading edge appears more relevant despite in some cases either the contact region and the trailing edge are also interested. Finally it can be noticed

that the engine noise radiates towards the exterior of the vehicle through the front wheels compartment and through the underbody of the center of the vehicle.
As already stated, in the scenario at the speed of 110 km/h (Table 3. 2) the front and rear tire noise become dominant in the entire frequency range under investigation. The engine noise, masked by the tires at low frequency, becomes relevant again at higher frequencies. In the results computed at 2290 Hz two noise sources are clearly related to the rear tire. Despite belonging to two different principal components, the acoustic power radiate by both sources distributions has been accounted to the rear tire in the ranking reported in Fig. 3. 27(b). The explanations to that phenomenon are twofold. One option is that in this specific case the noise generated by the rear tires can be clearly separated into two uncorrelated phenomena: one related to leading and trailing edge and one related to the contact region of the tire; another possibility is that two of the three uncorrelated source distributions are not spatially disjoint. As discussed in paragraph 2.4.8 of Chapter 2, this can be an issue when adopting PCA-based methods for source separation. In fact, the separation in three virtual sources distributions through PCA yields three orthogonal source regions that not necessarily coincide with the physical sources. Besides a critical interpretation of the results obtained through PCA-based blind separation in uncorrelated phenomena, the use of other criteria, such as the one proposed in [127] (see also section 2.3 of Chapter 2), or the computation of the GIBF solution considering all the main principal components at once, can be beneficial to ascertain the validity of the decomposition of the sought source distribution into uncorrelated components.
This example demonstrate the potential of the CIB method when applied to automotive applications. The method has been applied to a test case regarding the study of the noise radiated by the vehicle towards the exterior. However, the accurate identification of the exterior sources is key aspect also for investigating the influence on the in-vehicle noise if the information available through the just described analysis is complemented with the knowledge of the transmissibility properties of the vehicle's cabin.

Table 3. 1: CIB map for the case "Speed 50 km/h" at selected frequencies. Separation in uncorrelated phenomena. Acoustic images normalized to the maximum and plotted in dB with dynamic range: 40 dB.

	Front	Rear	Other
740 Hz		/	/
1060 Hz	/		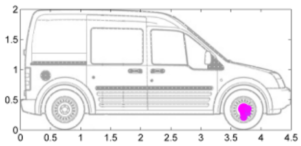
1700 Hz	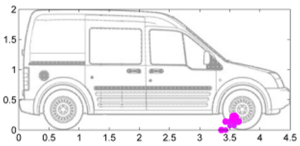	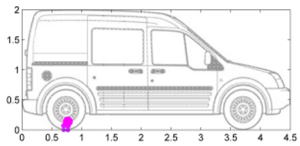	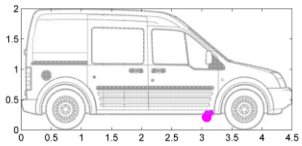
2780 Hz	/	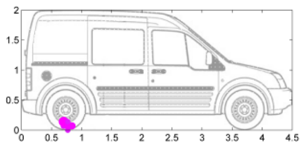	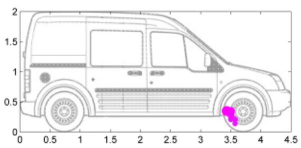
3850 Hz	/	/	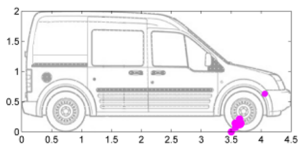
4930 Hz	/	/	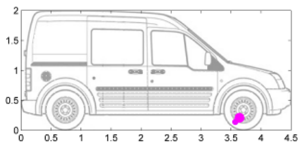

Table 3. 2 : CIB map for the case "Speed 110 km/h" at selected frequencies. Separation in uncorrelated phenomena. Acoustic Power images normalized to the maximum and plotted in dB with dynamic range: 40 dB.

	Front	Rear	Other
510 Hz	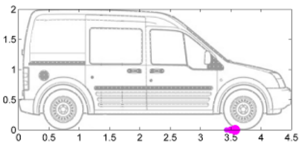	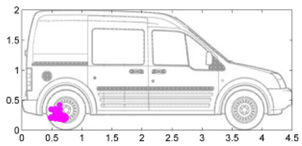	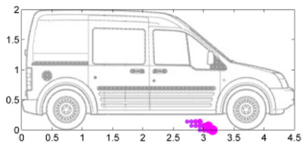
810 Hz	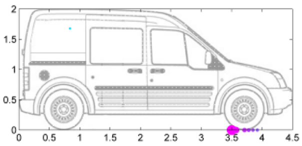	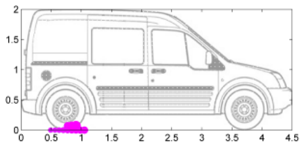	/
1000 Hz	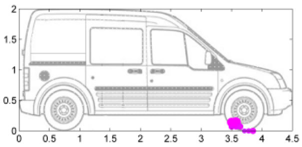		/
2290 Hz	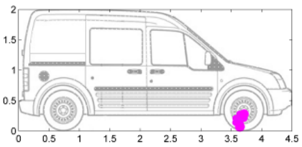	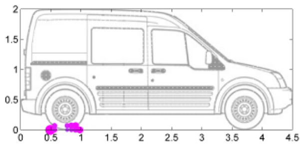 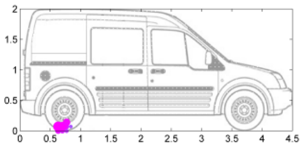	/
3060 Hz	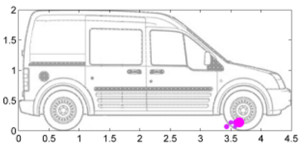	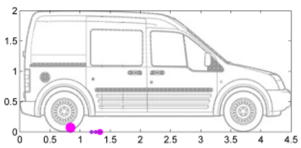	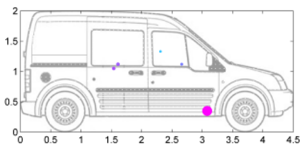
4120 Hz	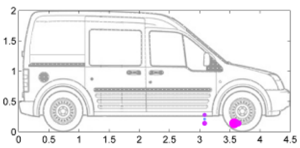	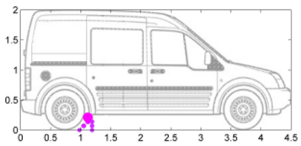	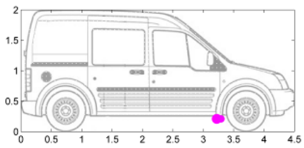

3.4. CIB for interior sound source localization

In-vehicle SSL is gaining more and more importance in NVH, since a correct identification of the noise sources represents the first step towards the improvement of the acoustic experience of a passenger. In this section the CIB technique is applied in interior noise source identification problems. A new formulation adopting a 3D array of microphones randomly distributed in the cavity is presented and compared to a rigid spherical array geometry. Experimental results are presented in a car cabin mock-up. Such formulation aims at improving results in interior testing applications. Indeed the performance of a SSL technique is spoiled by the complexity of the acoustic field characterizing the vehicle cabin. Taking into account complex phenomena like multiple reflections, acoustic and vibro-acoustic modes represents a difficult task, and very often free-field conditions are assumed in SSL algorithms. However, such a simplified assumption might drastically decrease the accuracy of results in terms of both localization and identification. Many solutions have been proposed during the last years to tackle this issue. For instance, Castellini et Al. [58, 59] proposed to reduce the effect of reflections by measuring with the microphone array placed in different positions inside the cabin and then by combining the beamforming output obtained from the processing of each measurement position. The approach assumes that reflections pattern identified by the array differs from position to position, while the actual source pattern remains constant. By combining results of the different tests, reflections fade out while actual sources are enhanced. Stationarity of the acoustic field is of course the main requirement for the exploitability of the method. Pereira [52] suggested to improve the SSL performance in enclosed spaces by extending the ESM formulation [66, 69, 142] to interior problems and coupling it to spherical arrays.

The current standard in interior beamforming applications is to use a rigid sphere. However, the spherical harmonic expansion formulation, on which both direct and inverse methods dealing with scattering arrays are based, and the diameter of the sphere might limit the frequency range. There exist both "hardware-based" [53, 67] and "software-based" [55] methods to cope with low-frequency extension. However, despite valuable, these methods have drawbacks mainly linked to the dimension of the acoustic cavity wherein the test has to be carried out. The closeness of the hardware/software microphones to the walls of the cavity might seriously affect the accuracy of the approach. A distributed array, i.e. an array with microphones randomly distributed inside the cavity, does not suffer of such low frequency issues. Moreover, its random nature matches perfectly with CIB.

The approach presented here can be seen as both an alternative and a complement to the aforementioned methods. Indeed the robustness of CIB makes the approach suitable also for interior testing despite a free field radiation model is assumed. Moreover, the method is versatile and can be exploited with different array geometries, even though some benefits can be achieved in vehicle cabins with a distributed microphone configuration.

3.4.1. Test campaign

In order to prove the applicability of the clustering approach for enhancing interior beamforming results, a test campaign has been carried out on a simplified car cabin mock-up adopting a distributed microphone array. A test with a rigid spherical array was also carried out in order to prove the applicability of CIB to different array geometries. The entire test-rig has been set up into a semi-anechoic room, as visible in Fig. 3. 28, in order to avoid any further influence from the surrounding environment.

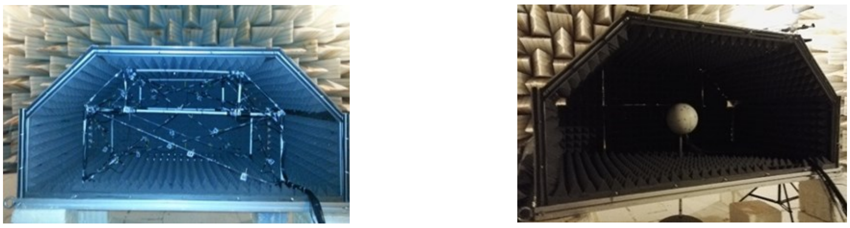

(a) (b)

Fig. 3. 28 : A picture of the car cabin mock-up with trimming material attached to the walls: (a) distributed and (b) spherical array.

The car cabin mock-up consists of an aluminium frame (length × width × max-height : 1.450m×0.950m×0.700m) filled in with panels of different material: wood for the bottom panel, steel for the front vertical panel and PMMA (Polymethyl Methacrylate) for the rest of the panels. The trimming layers are removable and consist of pyramidal-shaped (0.045m×0.045m×0.060m) absorbing foam (density: 21 kg/m^3).
Two microphone arrays were tested: a distributed array and a rigid spherical array. The former consists of 43 microphones randomly distributed over a frame made of aluminium rods and plastic wires. The array shape does not spoil its acoustic transparency in the frequency range 300 Hz – 10 kHz (frequency range of interest). The position of the microphones was randomized adopting two constraints: distance between microphones greater than 0.1m; distance of all the microphones from the panels greater than 0.05 m. The spherical array hosts 40 microphones distributed on a rigid sphere of diameter 0.20 m. The locations of microphones belonging to the two arrays with respect to the mock-up are reported in Fig. 3. 29. Despite challenging, the identification of microphones locations inside a car cabin has been proved to be feasible in recent papers [143, 144]. The higher geometrical complexity in dealing with a distributed array than with a spherical array can therefore be overcome using these strategies.

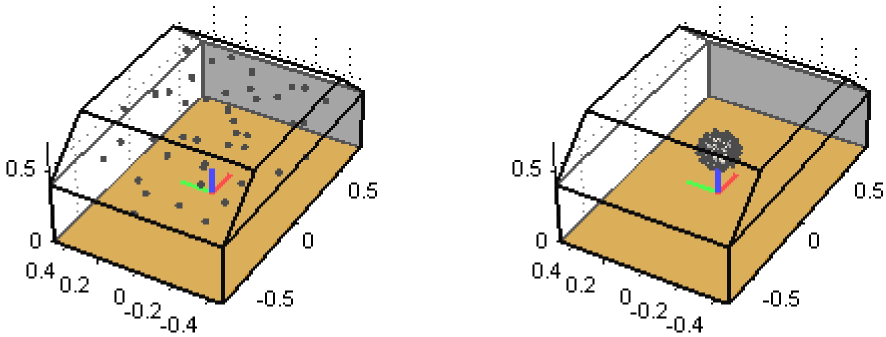

(a) *(b)*

Fig. 3. 29 : Microphone locations with respect to the car mock-up: (a) distributed and (b) spherical array.

Table 3. 3 : Car cabin mock-up in the three configurations tested.

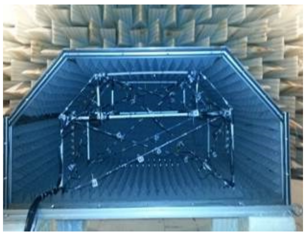		
Total trimmed *ζ=100%*	Car-like *ζ=73.9%*	Naked *ζ=0%*

The mock-up has been tested under three different configurations, as depicted in Table 3. 3. The indicator ζ describes the percentage of the trimmed surface with respect to the total surface of the mock-up. The purpose of investigating these configurations was to test CIB in acoustic fields ranging from a free-field like (Total Trimmed) to a diffuse-field like (Naked) configuration. A configuration resembling a car cabin (Car-like) was also tested. All these aspects well reflect in the values of reverberation time (T30 - Fig. 3. 30) measured in the three configurations. As expected, the reverberation time is dramatically higher in the Naked configuration with respect to the two other cases. It is very interesting to notice that reverberation time is almost the same up to around 1500 Hz in the Total trimmed and Car-like configurations, while for higher frequencies the absorption properties of the trimming panels plays a more evident role.

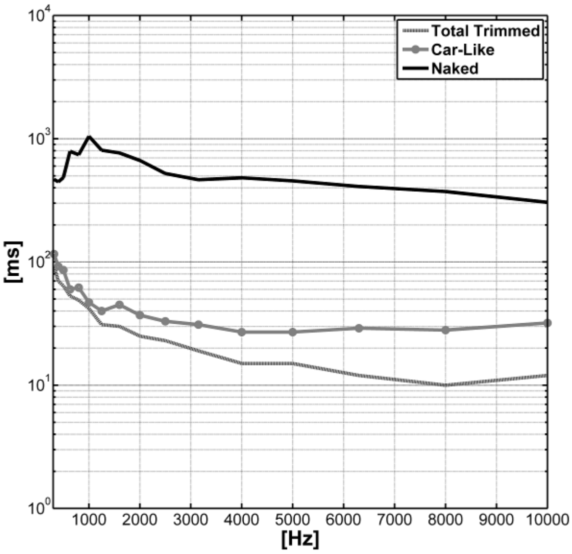

Fig. 3. 30 : mock-up reverberation time (T30) estimated for the three configurations tested.

Three different source scenarios were tested in each configuration (Table 3. 4). The source position with respect to the mock-up is also reported in Fig. 3. 31.

Table 3. 4 : Description of the tested scenarios.

Scenario	Name	Position w.r.t. mock-up
a	Right panel, front bottom	Inside
b	Top panel, front middle	Outside
c	Left panel, front	Outside

When the source is placed outside, noise is radiated towards the interior through the panels and panels also act as noise sources. When the source is placed inside the mock-up, mainly the acoustic and geometrical properties of the cavity come into play. LMS mid-high frequency Q Source was used for generating white noise in the bandwidth 300 Hz – 10 kHz.

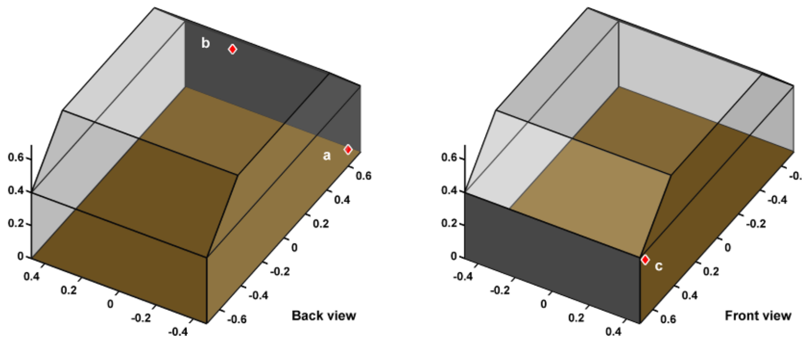

Fig. 3. 31 : Source position in the tested scenarios.

3.4.2. CIB in the mock-up adopting spherical and distributed arrays

The main results of the test campaign will be presented referring to the distributed array. However, for sake of completeness and to demonstrate the versatility of CIB, some results using the rigid spherical array are presented as well in the following.
Clusters of microphones, being subsets of the microphone array, can be selected randomly or under certain constraints. The parameters reported in Table 3. 5 have been adopted for the spherical and the distributed array. A random choice of microphones belonging to each cluster was performed in both cases.

Table 3. 5 : CIB parameters for spherical and distributed array.

	Spherical Array	***Distributed Array***
Number of microphones in each cluster ($\mathbf{N_m}$)	19	15
Number of clusters ($\mathbf{N_c}$)	30	100

Results will be reported adopting the colour code introduced in Fig. 3. 11. Two different methods of implementation of CIB have been tested in this application: method 1 (paragraph 0) and method 3 (paragraph 0). The processing strategy will be indicated in the caption of the figures reporting the results. Method 2 was not used in this application because pattern recognition may fail in the complex acoustic field under study, moreover the main interest of this study was investigating the localization accuracy and the dynamic range capabilities. In this perspective methods 1 and 3 are more suited that method 2.

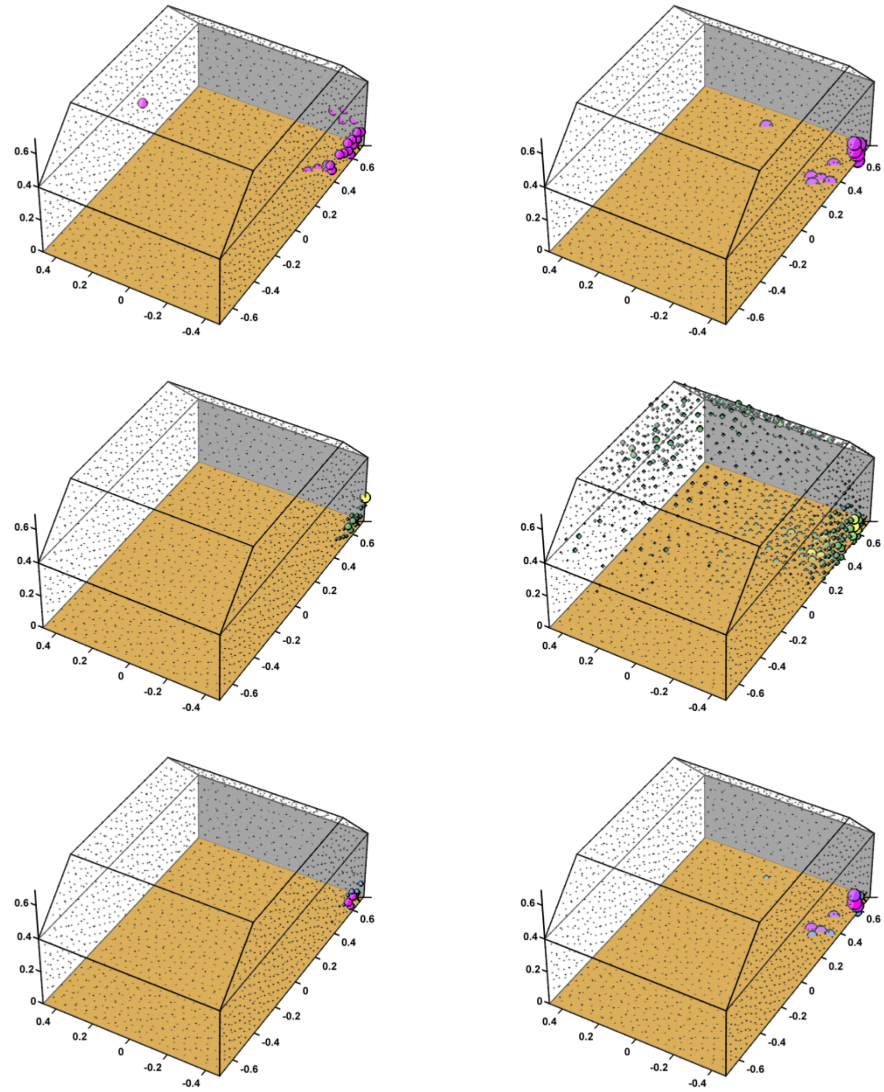

(a) *(b)*

Fig. 3. 32 : Configuration: "Total trimmed". Scenario: a. Frequency: 2.5 kHz. (a) using spherical array. (b) using distributed array. Top: no CIB: Y(A, $\underline{p}^{(1)}$); Middle: mask matrix $\gamma^{(1)}$; Bottom: CIB: method 1.

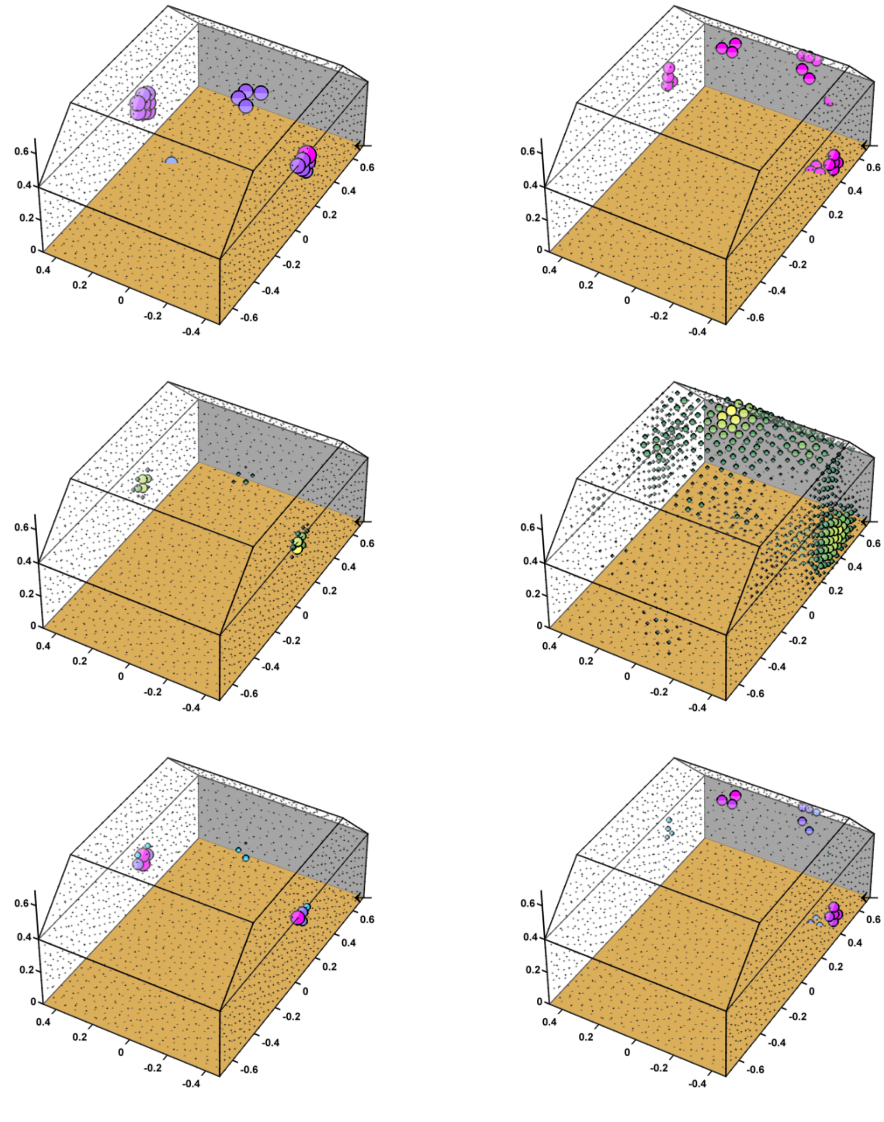

(a) *(b)*

Fig. 3. 33 : Configuration: "Total trimmed". Scenario: a. Frequency: 500 Hz. (a) using spherical array. (b) using distributed array. Top: no CIB: $Y(A, \underline{p}^{(1)})$; Middle: mask matrix $\gamma^{(1)}$; Bottom: CIB: method 1.

Fig. 3. 32 show results in the "Total trimmed" configuration for the "a" scenario, at 2.5 kHz for the spherical and distributed array respectively. Results of standard GIBF are also

reported for sake of completeness, clearly showing that CIB systematically provides better results. The noise source is well located in either cases, but higher dynamic range is obtained using CIB. Both the scattering sphere and the distributed array provide similar performance in terms of localization and quantification capabilities at 2.5 kHz. Moreover, it is interesting to notice that CIB greatly improves results on the rigid sphere. This is also an important goal achieved, since the CIB strategy can be really considered a ready to use solution in those applications of interior sound source localization already faced with scattering spherical arrays. The random array provide more accurate results in the low frequency range (500Hz), as can be seen in Fig. 3. 33. This was expected, since the relative dimensions of the cavity and the sphere did not allow to use any strategy to extend the spherical array performance to lower frequencies. The random array can therefore be thought as an alternative to the spherical one whenever solutions for extending the performance of the scattering sphere at lower frequency cannot be carried out. From now on in this section the presented results are obtained adopting the randomly distributed microphones array configuration. From now on only results adopting the method 3 for the implementation of CIB will be reported.

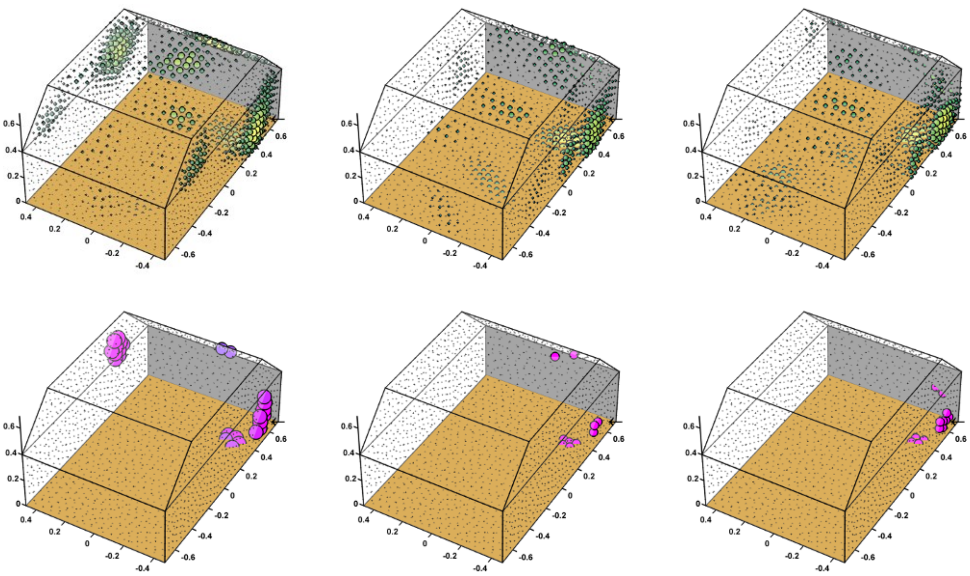

(a) *(b)* *(c)*

Fig. 3. 34 : Configuration: "Total trimmed". Scenario: a. (a) Frequency: 350 Hz. (b) Frequency: 650 Hz. (c) Frequency: 850 Hz. Top: mask matrix $\gamma^{(1)}$; Bottom: CIB: method 3.

The correct identification of noise sources in the low-frequency range is in fact a challenging task. The absorbing efficiency of the trimming material is poor below 1200 Hz (see Table 3. 4), the wavelength of the acoustic waves in this frequency range is

comparable with the three dimensions of the cavity, and therefore strong reflections and acoustic modes of the cavity may result not negligible, also in the “Total trimmed” scenario. These aspects are clearly visible in Fig. 3. 34, where CIB results, in terms of mask matrices and CIB solutions, are reported for the frequency range 350-850Hz.
Table 3. 6 reports the results obtained by applying the proposed method the case of scenario a in the different configurations. Notice that it this particular scenario, the source is placed inside the cabin, therefore there is neither transmission through the cavity walls nor any excitation of the mock-up panels. However, strong reflections may take place. In the low frequency range, these reflections might appear even more relevant than the actual source. This is especially true for the “Naked” configuration.

Table 3. 6 : CIB solutions for source Scenario: a, in all configuration tested.

	Total trimmed	**Car-like**	**Naked**
500 Hz	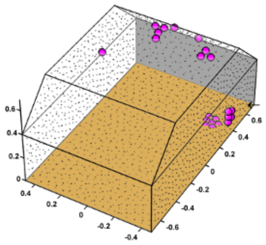	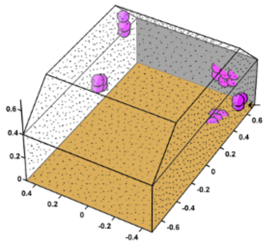	/
2000 Hz	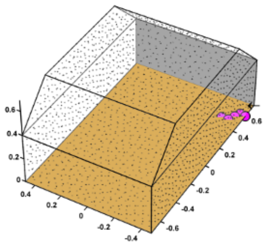	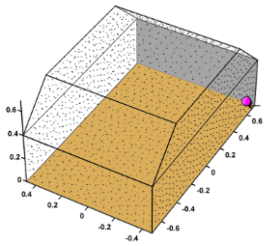	/
4000 Hz	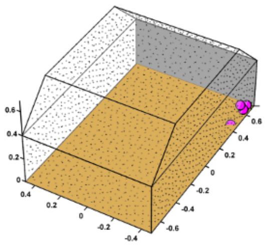	*Localization of the source successful up to 3500 Hz.*	/

In Scenario b the source was place outside the mock-up. Results reported in Table 3. 7 clearly highlight this source configuration turned out to provide better results in terms of localisation accuracy. The same trend can be noticed in Table 3. 8 regarding results obtained for scenario c.

Table 3. 7 : CIB solutions for source Scenario: b, in all configuration tested.

	Total trimmed	**Car-like**	**Naked**
500 Hz	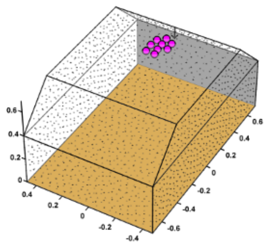	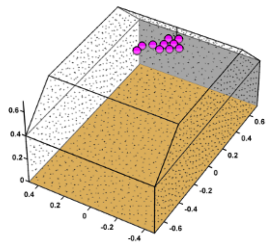	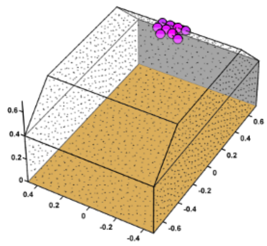
2000 Hz	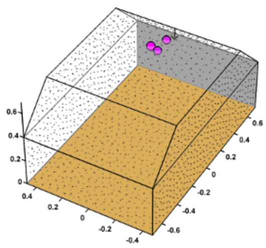	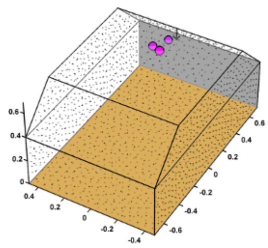	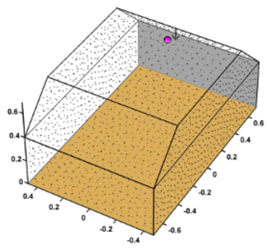
4000 Hz	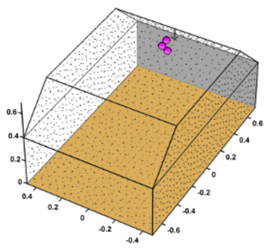	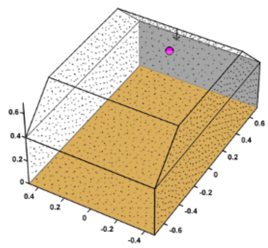	*Localization of the source successful up to 2000 Hz.*

Table 3. 8 : CIB solutions for source Scenario: c, in all configuration tested.

	Total trimmed	**Car-like**	**Naked**
500 Hz	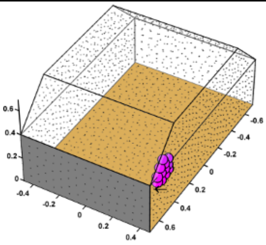	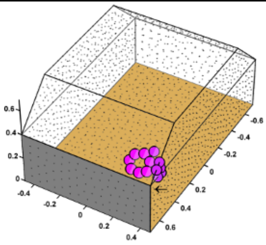	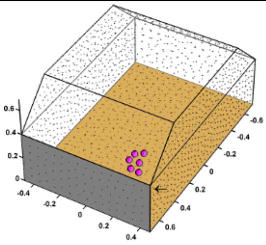
2000 Hz	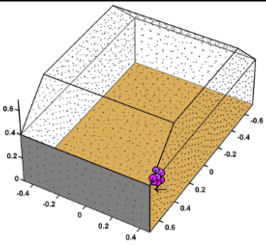	*Localization of the source successful up to 1400 Hz.*	*Localization of the source successful up to 500 Hz.*
/	*Localization of the source successful until 2000 Hz.*	/	/

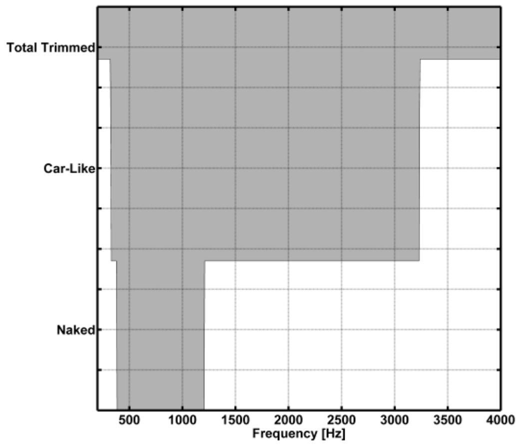

Fig. 3. 35 : Applicability range of CIB for the three mock-up configurations.

Fig. 3. 35 summarises the frequency ranges wherein the noise source could be well localised for the three scenarios and mock-up configurations. Such experimental tests have proved that CIB can be used (with different performances) in reverberant conditions. This can be done, starting from a frequency that is dependent on the geometrical dimensions of the cabin, without any change to the propagation model. To extend this frequency range to lower frequencies the propagation model adopted in the inverse beamforming formulation should be refined.

It has been moreover proven that CIB can be considered a ready to use formulation to be exploited with both a rigid scattering spherical configuration of the microphones or a randomly distributed geometry. Distributed array might represent a valid alternative whenever it is not possible to extend the exploitability of the rigid spherical array (using either hardware or software solutions) to the low frequency range. Moreover, the distributed array might be useful for joint testing with Acoustic Modal Analysis [96, 98, 144, 99] applications.

Chapter 4.

Inverse source identification in time domain

Acoustic imaging techniques allow the user to see what he/she is listening to. This chapter aims at proposing an inverse procedure that allows for retrieving the evolution of the noise source identified in a beamforming map. Such approach overcomes the limit of frequency domain strategies, and opens up different application fields such as auralization, coherence analyses, etc… The source localization step is performed in frequency domain with the goal of accurately identifying the source coordinates. The corresponding time signals are subsequently obtained by convolving in time domain the microphones data with multiple input – multiple output impulse responses corresponding to the back-propagating functions identifying the receiver-source link. The formulation of the algorithm is presented in this chapter and its main strengths and limitations are discussed. Applications are shown in simulated and real experiments.
The proposed technique leverages on the localization step performed in frequency domain for reducing the calculation plane to the few points that host the actual sources. In this way, the further inverse source identification problem, wherein the corresponding time signals are obtained, is no longer underdetermined, since the number of sources active in the field is reasonably lower than the number of microphones available in the array. The above mentioned Impulse Responses are computed by inverting, in frequency domain, the matrix containing the Noise Transfer Functions between the sources' and the microphones' locations (see references [88] and [145]). The obtained inverse Noise Transfer Functions are then inversely Fourier transformed. This set of Impulse Responses intrinsically take into account the mutual interaction between the sources, granting an optimal separation of the corresponding signals as long as all the main sources active in the field are correctly localized and included in the computation. The omission of important contributions could in fact badly compromise the correct identification of the other sources (see also [124]). To prevent this for happening, the sound source localization results must allow large dynamic ranges and accurate calculation of the sources locations. The former aspect is important for correctly identifying the weakest sources as well as the strongest ones; the latter is required in order to properly select the Noise Transfer Functions to be adopted in the time domain source identification step. In order to meet these requirements, the Clustering Inverse Beamforming algorithm (CIB) [132, 136] presented in Chapter 3 is exploited for the sound source localization task, since this method guarantees indeed accurate localization results with large dynamic range also in complex scenarios where multiple correlated and uncorrelated sources are active at the same time.

Once the localization task is completed, the identified sources are synthesized and their time-domain signals become available. It should be considered, however, that the reconstruction of the sources' corresponding signals from far-field data alone must be interpreted in a most likelihood sense because different source distributions can generate an identical far field. In order to understand the influence of this potential ambiguity on the result of the inverse source identification, a preliminary analysis on a virtual experiment will be reported showing, in fact, that this ambiguity is translated in presence of cross-talk between the retrieved sources and/or the presence of a consequent noise disturbance in the retrieved signals. Nevertheless the same analysis ensured also the robustness of the proposed approach in presence of severe SNR conditions and/or complex acoustic fields. Moreover the results that will be presented show a promising correspondence between the synthesized sources and the corresponding reference signals demonstrating the applicability of the method both in presence of correlated sources, where also the time delay between the signals plays a role, and uncorrelated ones.

The exploitation of these ideas enables the user to obtain a realistic estimation of the time evolution of the main acoustic sources under investigation by means of far-field measurements only. This can be a unique advantage in many applications such as aero-acoustics, condition monitoring, etc.

4.1. Description of the methodology

The proposed method requires initial source localization in frequency domain and consequent inverse source identification in time domain. The already described CIB method will be adopted for the source localization task by locating the sought sources through the identification of the local maxima of the mask matrix. Hereafter a theoretical description of the time domain estimation of the sources is reported.
The inverse source identification step is allows for retrieving the time signals of the main noise sources active in the acoustic scene observed with the microphones array. As already mentioned the main idea is convolving the microphones signals with inverse impulse responses. Those are calculated by inverse Fourier transforming (symbol:) a set of MIMO estimated inverse Noise Transfer Functions (NTF) modelled in frequency domain. Those are obtained by inverting per frequency line the direct radiation model (*A* in Eq.(1. 3)) including the candidate N source locations and the M microphones locations. Since the matrix *A* is in general not square, a pseudo-inversion is required. Moreover the system may be ill-conditioned and require regularization. For deepening this aspect the interested reader may refer to [45]. This process allows obtaining the inverse impulse response $h_{n,m}(t)$ between each of the m^{th} microphones locations and each of the nth sources locations.

$$F^{-1}\{A^{+}{}_{n,m}\} = h_{n,m}(t) \tag{4. 1}$$

A is the radiation matrix whose elements describe the radiation model adopted. In case of free-field propagation, each element of the *A* matrix can be expressed as:

$$A_{n,m} = A^{*}\frac{e^{-jkr_{mn}}}{4\pi r_{mn}} \tag{4. 2}$$

where the subscripts m and n represent the m^{th} microphone (over M) and n^{th} calculation point (over N) respectively and r_{mn} represents the distance between the geometrical positions of these two points. The coefficient A^{*} in Eq.(4. 2) depends on the unit of acoustic quantity related to the sought sources q_n. If q_n are the strengths of the sources ([m^3/s]), $A^{*}=j\omega\rho$.
It is very important to notice that, by doing so, the contribution of all the candidate sources is considered together at the same time. This, in one hand, ensures the correct identification of correlated as well as uncorrelated source and provides the best source separation possible because it includes in the model the cross-talk between the sources. In the other hand that means also that all the main acoustic sources should be taken into account. If this is not the case a wrong estimation of all the remaining source signals may most likely occur.
Once the set of inverse impulse responses is available, each source signal can be retrieved adopting Eq.(4. 3) which is valid for source n out of the N active in the acoustic scene.

$$q_n(t) = \sum_{m=1}^{M} h_{n,m}(t) \otimes p_m(t) \tag{4. 3}$$

In order to ensure that all the main sources are taken into account in the computation, an efficient sound source localization strategy is required. In this chapter the already described CIB algorithm will be used. This method in fact: ensures high accuracy in localization almost independently from the frequency range; it moreover allows to correctly identifying correlated sources as well as uncorrelated sources with a large dynamic range. The latter is needed for localizing the weakest sources as well as the strongest ones.

4.2. Preliminary analysis on simulated data

Before applying the just described inverse source identification method on real data, a preliminary study on a simulated scenario has been carried out with the goal of understanding the influence of two potential sources of inaccuracy: the presence of different SNR conditions and the cross-talk between the two sources due to their closeness. Such study has been conducted by considering the beamforming problem depicted in Fig. 4. 1. The source localization step is assumed ideal in this analysis.

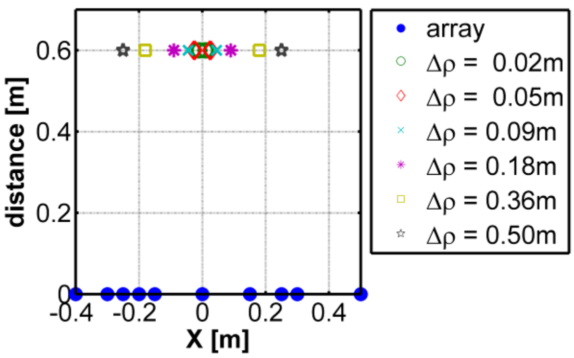

Fig. 4. 1 : simulated scenarios with a randomly distributed linear array (10 microphones) and sources placed at different distances.

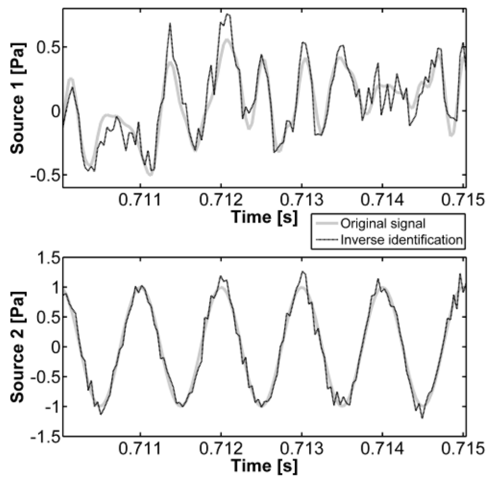

Fig. 4. 2 : example of identification in presence of severe SNR conditions.

Two sources (one 1 kHz sine tone and one white noise band-pass filtered between 0.1-2 kHz) are placed 0.6 m far from a randomly distributed linear array of 10 microphones. The distance between the two sources has been varied between 0.02 m and 0.5 m. The SNR between the microphones clean signal and the added Gaussian background noise has been varied between 25 and 50 dB. Fig. 4. 2 shows one example of results in which the effect of background noise is visible.

Analysing Fig. 4. 2 it is possible to observe that the presence on measurement noise in the microphones is not the only cause of inaccuracy in the retrieved signals. Cross-talk between the sources always occurs and its influence becomes dramatic when the sources become closely spaced (distance < 0.18 m).

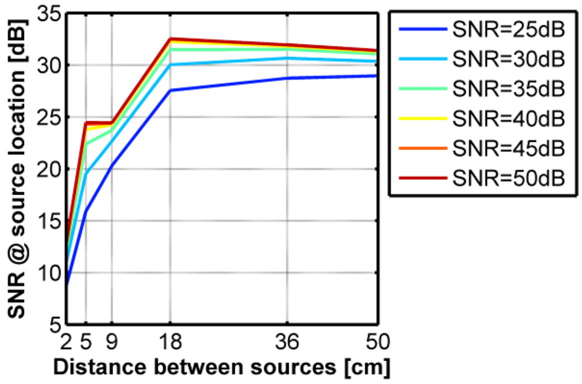

Fig. 4. 3 : Influence of the SNR at microphones location (measurement noise) on the SNR obtained in the retrieved sources signals. Results reported as a function of the distance between the sources.

In the next section the method is applied on real test cases. Two different measurement campaigns will be presented in which the strengths and limitation of the technique in presence of correlated and uncorrelated sources are respectively evaluated.

4.3. Correlated sources

With this validation case two conditions will be tested: the case in which two correlated sources are generated simultaneously by two different devices and the case in which a second correlated source takes place due to the presence of a reflecting surface. In the first case, Fig. 4. 5(a), although correlated, the two signals' signature can be different since they are generated by two different physical devices, while in the other case the main difference between the two signals is the phase shift occurring due to the different travelled path.

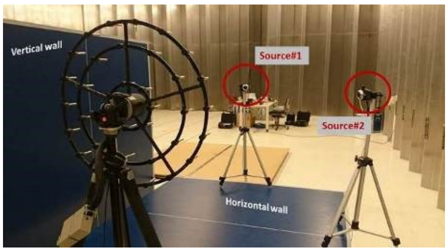

Fig. 4. 4 : Measurement setup for correlated sources identification.

The tests have been performed in a semi-anechoic room, adopting a microphone array of 36 microphones distributed over a pattern of three concentric circles (LMS HDCam36). Two high frequency referenced sources in the range 2 kHz – 20 kHz have been used. Two perpendicular reflecting walls have been used for producing reflections.

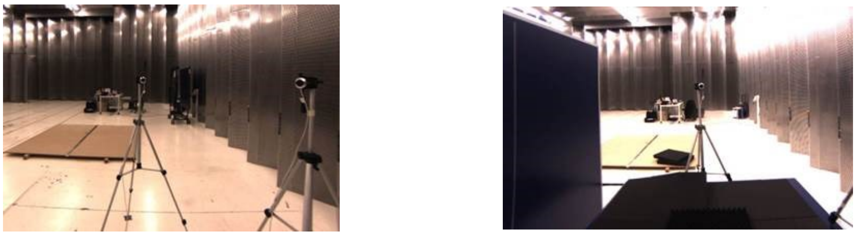

(a) *(b)*

Fig. 4. 5 : (a) Scenario A, two correlated sources. (b) Scenario B, one source and a reflective wall.

Fig. 4. 4 shows the setup. Microphone array: LMS HDCam36. Sources: LMS High Frequency Q Sources (prototype). The origin of the axis coincides with the center of the array which lies in the xy plane. The microphone array points towards –z direction. In all the cases shown in this section the two sources are correlated random noises in the bandwidth 2 kHz – 20 kHz. Table 4. 1 recaps the two configurations.

As shown in Fig. 4. 5(b) absorbing material has been added (in scenario B) for selectively avoiding (damping as much as possible) reflections produced by the horizontal wall. In the case of scenario A the two walls have been removed.

Table 4. 1 : Tested scenarios for correlated sources identification.

Scenario	Source#1	Source#2	Vertical wall	Horizontal wall
A	√	√		
B	√		√	(absorbing material)

4.3.1. Two differently generated correlated sources (Scenario A)

Fig. 4. 6 shows the results of the localization step for the scenario depicted in Fig. 4. 5(a). At this stage of the process the sources are identified among a set of candidate elementary sources (in blue in the picture). The clustering mask matrix presents local maxima in the proximity of the ideal position of the sources. The red diamond marker indicates the local maximum.

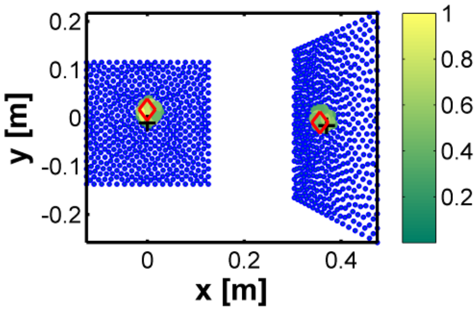

Fig. 4. 6 : Source localization in Scenario A. Frequency range: 3 – 3.1 kHz.

This allows selecting the coordinates of the candidate sources to be identified and at the same time turns the previous undetermined inverse acoustic problem into a well determined one since the number of candidate sources becomes sufficiently lower than the number of available sensors.

Fig. 4. 7 compares the obtained signals (in red) with the reference ones (in black) both in time and in frequency domain. The results obtained in this scenario testify that the method is able to retrieve the two sources active in the acoustic field. The accuracy drops for frequencies greater than 10 kHz.

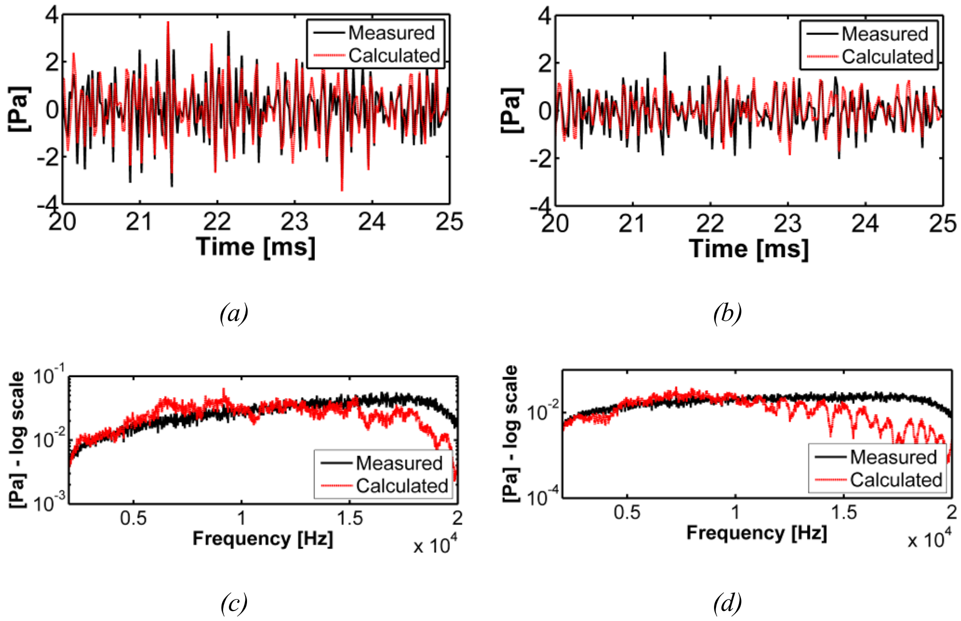

Fig. 4. 7 : scenario A. Comparison with the reference signals in time and frequency domain. (a) and (c) Source#1. (b) and (d) Source#2.

4.3.2. Main source and its reflection (Scenario B)

Fig. 4. 8 shows the results of the localization step for the scenario depicted in Fig. 4. 5(b). The blue dots represent the scanned grid of target points. The red diamond markers represent the coordinates of the retrieved sources that will be identified.

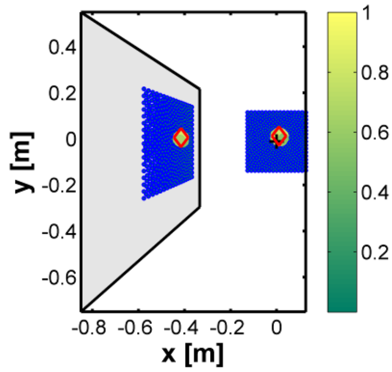

Fig. 4. 8 : Scenario B. CIB for accurate source localization. Frequency range: 3 – 3.1 kHz.

In this case the source localized on the vertical wall is the reflection of Source#1. In order to obtain the reference signal for comparison, a microphone has been placed in correspondence of the theoretical position of such reflection. Such position has been calculated based on geometrical considerations and validated by the beamforming analysis shown in Fig. 4. 9.

Fig. 4. 9 : Conventional beamforming analysis for placing reference microphone in correspondence of the reflection.

The result of the inverse source identification step is reported in Fig. 4. 10 for this scenario. In the sub-cases (b) and (d) of Fig. 4. 10 the match is not optimal, but it is mainly due to the inaccuracy of the used reference signal for the reflection on the vertical wall.

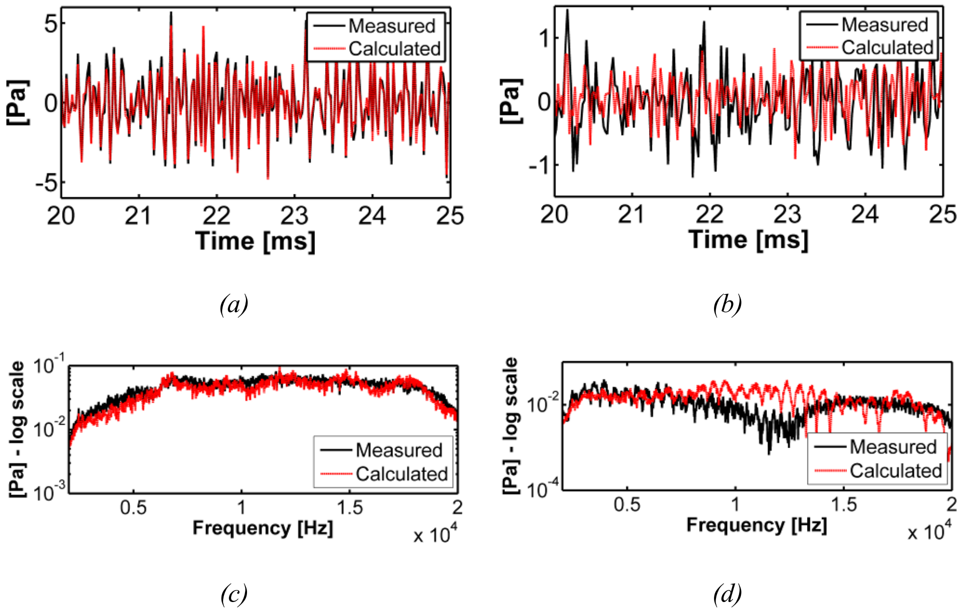

Fig. 4. 10 : scenario B. Comparison with the reference signals in time and frequency domain. (a) and (c) Source#1. (b) and (d) Source#2.

4.3.3. Comparison of the two cases

Reconstruction of source distribution, and their corresponding signals, from far-field data alone is ambiguous since different source distributions can generate an identical far field. From this point of view, the retrieved source distribution and source signals must be interpreted in a most likelihood sense. This considered, the retrieved sources are supposed to be able to reconstruct the acoustic far field. In order to prove this assumption, the two inverse-identified sources have been propagated towards the location of one of the microphones of the array. The spectra of the obtained signal and the microphone's one are compared in Fig. 4. 11.

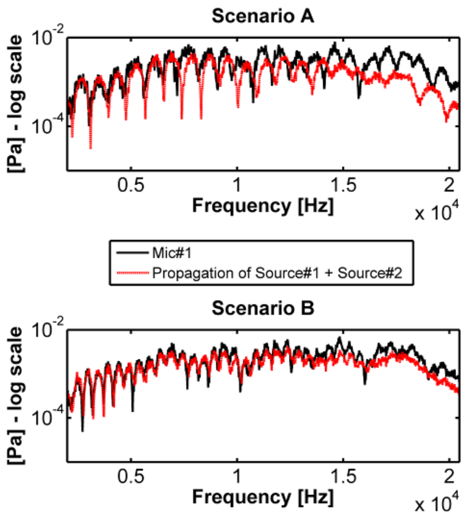

Fig. 4. 11 : Scenario A and B. Mic#1 (array) spectrum vs. propagation of the retrieved sources towards the microphone location.

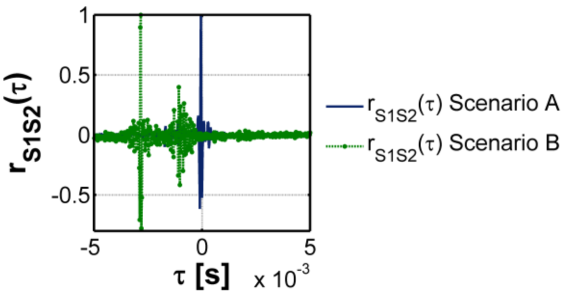

Fig. 4. 12 : Cross-correlation function between the retrieved signals in scenario A and B.

The comparison between the results obtained for scenario A and for scenario B allows to certify also that the proposed method does automatically take into account the phase relationship (time delay or “distance”) between the sources.
This aspect has been investigated by retrieving the distance between the sources by means of cross-correlation. The two cross-correlation functions are reported in Fig. 4. 12.
Table 4. 2 reports that:

- For scenario A, since the Source#1 and Source#2 are acting simultaneously (with no phase shift), as expected, despite the distance between the two sources is 0.927 m, the two retrieved signals present a phase shift quantifiable in ~0.03 m.
- In the case of scenario B, the second source is the reflection of Source#1 on the vertical wall. Therefore between the two sources there must be a phase shift corresponding to the distance covered by the sound emitted by Source#1 before impinging on the wall. The value retrieved in this case is indeed 1.006 m which is very well comparable with the theoretical value (1.088 m) calculated from the geometry.

Table 4. 2 : Source#1 and: Source#2 in Scenario A; its reflection on the wall in scenario B. Time delays and covered distances calculated by cross-correlation and considering speed of sound: 342 m/s.

					d_{12} [m]		
Scenario	**x [m]**	**y [m]**	**z [m]**	**Reflection**	**Geometry**	**Reference**	**Calculated**
A	0.7	-0.002	-0.863		0.927	< 0.03	< 0.03
B	-0.85	-0.014	-0.86	√	1.088	1.022	1.006

4.4. Uncorrelated sources

The following test is used to study the case of two uncorrelated sources simultaneously acting in an acoustic field. The main difference w.r.t. the previous case is that the two signals do not have any deterministic phase relationship.

(a)

(b)

Fig. 4. 13 : setup identification of uncorrelated sources.

Two calibrated volume velocity sources have been positioned as in Fig. 4. 13(b) on a vehicle and measured by using an array of 45 microphones. The two sources (LMS Mid-High Frequency Q Sources) emit two uncorrelated white noises filtered in the band 200 Hz – 10000 Hz. One of the two sources is placed at the tip of the left side mirror of the car. The other source is placed 40 cm distant from the previous one, on the left side window, in the proximity of the B-pillar. The array (LMS HDCam45) is placed 1m far from the vehicle (Fig. 4. 14).

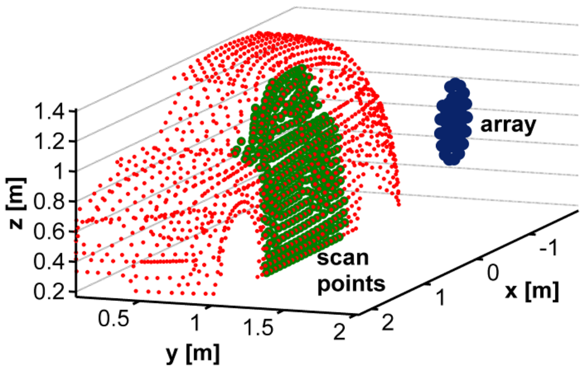

Fig. 4. 14 : identification of uncorrelated sources. Geometry of the problem.

Fig. 4. 15 shows the localization of the two sources adopting CIB and in particular assigning to the two sources the coordinates corresponding to the local maxima of the overall clustering mask matrix. Notice that in the case of the source placed on the tip of the rear mirror, labelled with the number 2, the local maximum of the clustering mask matrix correctly occurs in the corresponding point representative of this component.

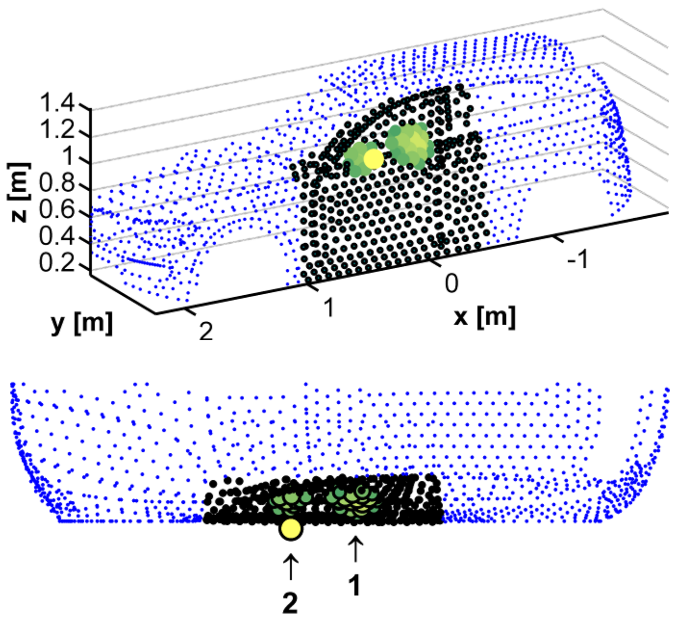

Fig. 4. 15 : CIB localization results. Frequency range: 2 – 2.1 kHz.

The Fig. 4. 16 (a)-(b) and (c)-(d) pairs report the comparison between the calculated source signals and the corresponding reference signals both in time and in frequency domain. In this case the sources' volume accelerations are compared (direct output of the calibrated sources). It is observed an overestimation of the low frequency content in the case of source 2. Fig. 4. 16 (e) and (f) report the clustering mask matrices corresponding to the two uncorrelated source distributions obtained by means of CIB.

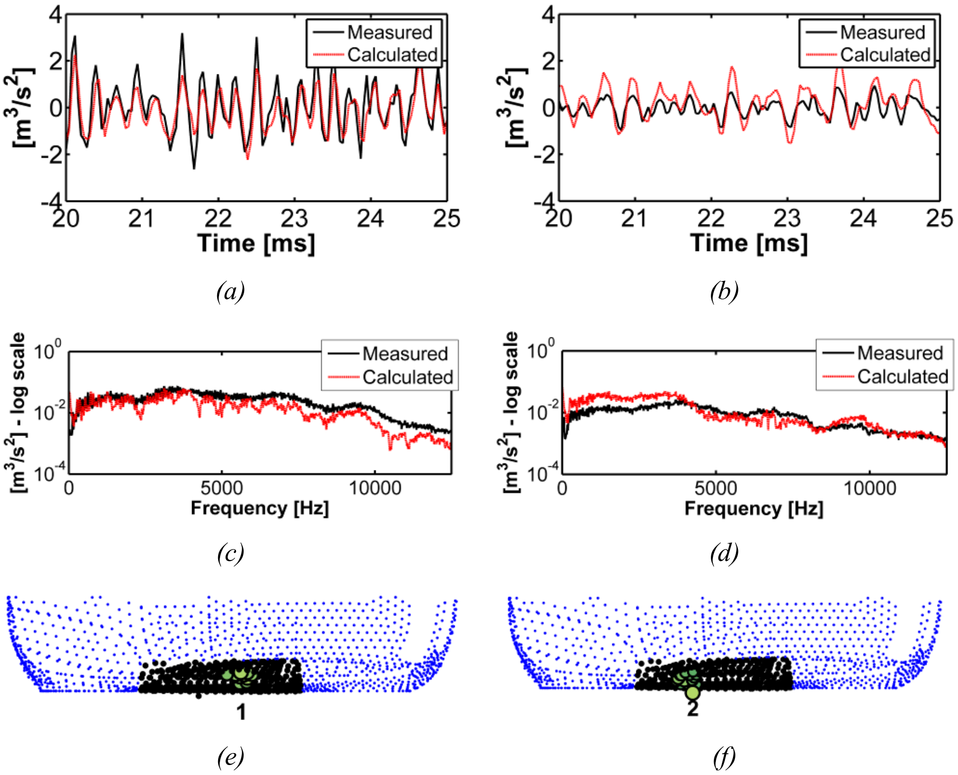

Fig. 4. 16 : inverse identification of the sources. (a) and (b): comparison of measured and calculated time signals (volume acceleration). (c) and (d): comparison of the corresponding spectra. (e) and (f) localization and separation of the two uncorrelated source distributions (frequency range: 2 – 2.1 kHz).

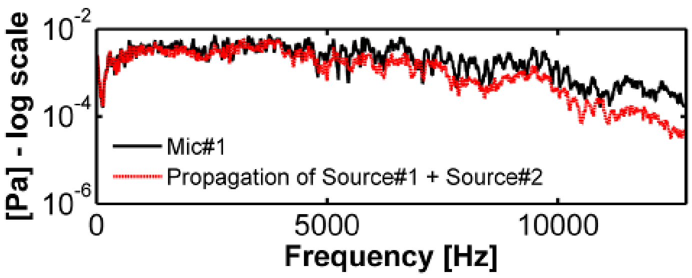

Fig. 4. 17 : Mic#1 (array) spectrum vs. propagation of the retrieved sources at microphone location.

The spectrum of the propagation of the sources towards the location of one of the microphones compared with the spectrum of the signal of the microphone in the same location is shown in Fig. 4. 17. The good match confirms that the retrieved source distribution is indeed able to generate the measured far-field.

Chapter 5.

Acoustic imaging in the angle domain

A relevant cause of discomfort in a vehicle cabin environment is: engine noise. The noise produced by an Internal Combustion Engine (ICE) can be divided into two components: the combustion part, related to combustion process itself, and the mechanical part, which is mainly due to the mechanisms that compose the engine. Such type of noise sources have been deeply studied during the last two decades and several solutions have been adopted for tackling the engine noise problems. This made it possible the advent of more and more quiet engines and more and more isolated vehicle cabins thanks to the reduction of the combustion noise. Despite very beneficial, this reduction made other sources, such as the mechanical noise, which were normally masked by the others, audible again. For tackling such new problems it is useful to understand the mechanism of noise generation by relating the mechanical ICE sources to specific parts of the engine's operation cycle. A methodology named "*angle domain Sound Source Localization (SSL)*" will be presented in this section. This approach assumes the noise sources produced by an engine to be "cyclo-stationary" [146]. This means that the statistical properties of the acoustic and vibration signals produced by the engine are considered periodic in the sense that the random process defined by the signal observed at a given position in the cycle is stationary. The cycle is defined as the angle interval between two identical configurations of the mechanical system. The developed method consists in performing acoustic imaging on array data which are processed by "synchronous averaging". This processing makes it possible to relate the available acoustic information with the angular position of the rotating elements of the engine obtaining an acoustic map reporting the noise sources at any instant of the operating cycle. Similar approaches have been used for condition monitoring of rotating machinery and some examples are reported in [147, 148].

5.1. Description of the methodology

In this paragraph an algorithm that relates the computed acoustic images with the angular evolution of the device under investigation will be proposed. The ambition is obtaining a tool that allows for understanding the causes of the cyclo-stationary noise sources occurring during the functioning of rotating machinery with special focus on impulsive events such as injection noise and piston slap in ICE.

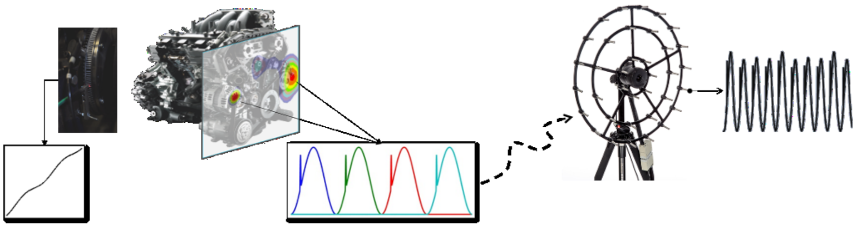

Fig. 5. 1 : a typical application of angle domain SSL is ICE analysis. The array measured signals have to be combined with angular information obtained through a tacho sensor.

Given an array dataset, whose microphones signals are $p_m(\tau)$, m = 1, …, M, the angle domain SSL algorithm requires the information about the angular evolution of the cyclo-stationary event that is responsible for the main acoustic sources sought in the field. This information consists in the rotational speed $\omega(\tau)$ of the rotating element on which to focus the analysis.
The proposed method is based on the following assumptions:

- The acoustic field sampled by the microphone array is cyclo-stationary, therefore it exists a cyclical pattern in the array and in the tacho signals that is repeated over time.
- The abovementioned property makes it possible the so-called synchronous averaging to relate the available acoustic information with the angular position of the rotating elements under investigation.
- The synchronous averaging has also the effect of removing the random fluctuations of the microphones signals and this allows the computation of the Cross-Spectral Matrix (CSM) between the microphones signals without averaging the spectra over several realizations, taking advantage of the synchronous averaging instead.

The angle domain SSL algorithm works as follows:

1. Resampling from time to angle domain.
   Knowing the rotational speed as a function of time $\omega(\tau)$, the angular evolution $\beta(\tau)$ of the element of interest becomes available making it possible to express the microphones signals in the angle domain: $p_m(\beta(\tau))$. The microphones signals are then resampled in order to have them available at a fixed angular increment $d\beta$. The

corresponding equally spaced axis is called β^* and the microphones signals in this domain: $p_m(\beta^*)$.

2. Averaging quantities in angle domain.
In the angle domain β^* every cycle performed by the device under study will last a fixed number of samples (angular intervals) identifying a generalized angular evolution ε, representative of the entire cycle. For example, if the cycle of an ICE takes 720 deg (4π rad) to be completed, the equally spaced angular evolution is: ε = 0, …, 4π. The angular increment $d\beta$ is determined by the resampling performed at point 1. Depending on the duration of the microphones signals, N_ε repetition of the cycle are available in the data. Identifying each repetition of the cycle in the microphones signals with the index n, the averaging process is given by Eq.(5. 1):

$$\tilde{p}_m(\varepsilon) = \frac{1}{N_\varepsilon}\sum_{n=1}^{N_\varepsilon} p_m(\varepsilon_n) \quad , \quad \forall m = 1,..,M \tag{5. 1}$$

The rotational speed evolution is also cyclo-stationary. In fact, all the rotational phenomena that do not have a random cause will occur with the same pattern at every repetition of the cycle. A good example of this are the torsional vibrations of a rotating shaft. Their pattern is constant from cycle to cycle. Therefore, an averaging process in the angle domain can be used also on the rotational speed pursuing at keeping only the cyclo-stationary evolutions:

$$\tilde{\omega}(\varepsilon) = \frac{1}{N_\varepsilon}\sum_{n=1}^{N_\varepsilon} \omega(\varepsilon_n) \tag{5. 2}$$

3. Selecting the angle interval (gate: $\Delta\varepsilon$).
The purpose of the angle domain SSL processing is obtaining an acoustic image at any angular position of the rotating element representative of the cyclo-stationarity of the device under investigation. In order to do so, only the information corresponding to the wanted angular position should be selected for the following acoustic imaging (beamforming) processing. This is obtained by gating the averaged cycle obtaining the dataset: $\tilde{p}_m(\varepsilon)$, m = 1, …, M, as visible in Fig. 5. 2.

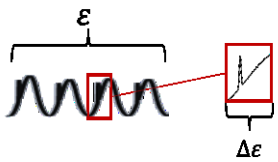

Fig. 5. 2 : example of gate selection, in the angle domain, from the average cycle.

The same gating procedure, applied to the averaged rotational speed, yields: $\tilde{\omega}(\Delta\varepsilon)$.

4. Resampling from angle to time domain.
   For computing the acoustic images corresponding to the selected angular interval $\Delta\varepsilon$, the microphones array signals should be transformed to the time domain again. This is done thanks to the knowledge of the angular evolution within the selected cycle:

$$\tilde{p}_m(\Delta t_\varepsilon) = f(\tilde{p}_m(\Delta\varepsilon)\,,\, \tilde{\omega}(\Delta\varepsilon)) \quad , \quad \forall m = 1,..,M \tag{5. 3}$$

5. Acoustic imaging.
   Thanks to the information in time domain obtained by means of Eq.(5. 3), the computation of a Cross-Spectral Matrix C_M between the microphones array signals is finally possible allowing acoustic imaging. For obtaining such acoustic image three options are possible:
   - Delay & Sum in time domain [151].
   - Focused beamforming in frequency domain (direct method);
   - Equivalent Source Method (inverse method).

   In this document the focused beamforming in frequency domain will be used.

The angle domain SSL algorithm, therefore, consists of a pre-processing of the array data through synchronous averaging followed by a beamforming analysis on special frequency domain data. Such data are in fact obtained processing short signals obtained from a gated averaged cycle in the angle domain and subsequently resampled and transformed to time domain. The data obtained in this way are then combined for the calculation of the CSM. This task is complicated by the type of signals to be processed. In particular:

- The gated time signals are not stationary, instead they are impulsive.
- Since the gated time signals correspond in general to a relatively short angular interval $\Delta\varepsilon$, their duration is also very short. The small number of samples in time results in a poor frequency resolution. This can be an issue for the beamforming analysis.
- Being the CSM a statistical entity it requires a proper averaging process to be correctly estimated. Any parameter or function computed from a random variable will have its own sampling distribution. Only an estimate of such parameter or function can be computed from a finite realization. In the angle domain SSL algorithm the averaging processing occurs in the angle domain and not on the frequency domain spectra. The equivalence between the two procedures is not always granted. In fact temporal averages and ensemble (over many realizations) averages are only asymptotically equivalent and only for ergodic signals [149].

With these critical aspects in mind some sensitivity studies have been carried out to identify strengths and weaknesses of the method. This analysis will allows also to define the optimal settings for an effective use of the algorithm.

5.2. Sensitivity study on the beamforming analysis of impulsive events

In this section it will be shown that the SPL level that the user obtains with angle domain SSL are tricky to interpret because the acoustic phenomena are caused by transient events. In order to make the quantitative results of the beamforming map more reliable, the impulsiveness of the data should be properly taken into account. As pointed out earlier, in an angle domain SSL analysis the investigated phenomena are often impulsive, therefore the energy of the event is concentrated in a short time (or angle) laps. From this point of view a short timeframe of observation is preferable. In fact its increase may be even harmful because it could include phenomena not related with the sought impulsive event. Conversely a short duration of the processed (gated) time/angle signals implies an exiguous number of samples, therefore a poor frequency resolution.

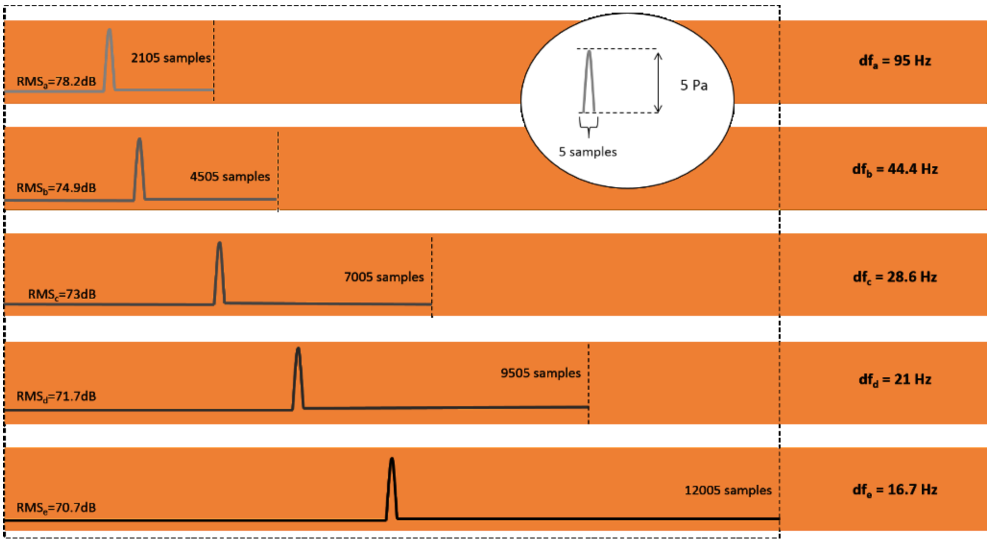

Fig. 5. 3 : Impulsive event preceded and followed by an increasing number of zero-padded values. Sampling frequency: 200 kHz.

The influence of such opposite aspects on the beamforming processing has been studied by simulating a 2D beamforming experiment in which an impulsive source placed in the coordinate [0,0] is propagated towards a linear array of 50 randomly distributed microphones placed 1 m far from the source plane. Five different cases have been simulated in which the duration of the signals has been systematically increased by introducing zero-padded values before and after the same impulsive event. Fig. 5. 3 reports the specs of each scenario: the signals are labelled with letters from a (shortest signal) to e (longest signal).

The RMS value of the signal in the five cases has been reported. It can be noticed that, despite the impulsive event is always the same, the RMS value obtained decreases increasing the number of samples because of the augmented number of zeros in the signal.
Fig. 5. 4(a) compares the spectra of the five impulsive signals. The decrease of the amplitude is in this case not only due to the increase of the number of spectral lines, but also to the lack of energy due to the increased number of zero-padded samples. This implies that the maximum values, corresponding to the theoretical source location, decreases in the beamforming map (fixed frequency range: 1000 Hz – 2000 Hz) from case "a" to case "e" as reported in Fig. 5. 4(b). A third evidence of the observed lack of energy at the increase of the number of samples is given by the energy computation (quantification).

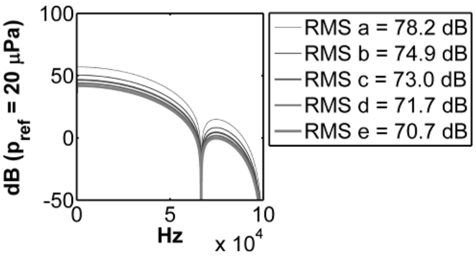

(a)

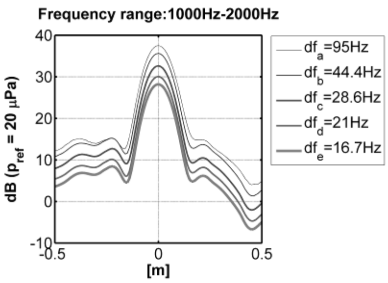

(b)

Fig. 5. 4 : beamforming analysis on an impulsive event with different number of samples. (a): Spectra of the signals a, b, c, d and e. (b): 1D conventional beamforming result in the frequency range 1000 Hz – 2000 Hz adopting a linear array of 50 randomly distributed microphones. The source is placed in the 0 m position. The maximum value of the beamforming map decreases when the number of samples of the signal increases.

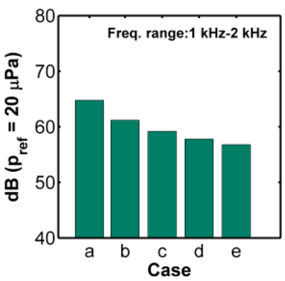

Fig. 5. 5 : energy computation in the same frequency range for the cases a, b, c, d, e.

The observed inverse proportionality can be mathematically explained. In order to do so let us consider the signal *x(t)* represented in Fig. 5. 6.

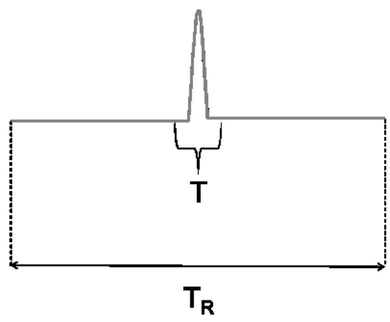

Fig. 5. 6 : impulsive signal characterized by a total length T_R and an impulsive part of length T.

Being *x(t)* an impulsive signal it has a finite energy and its power is zero:

$$E = \int_{-\infty}^{+\infty} |x(t)|^2 dt < +\infty \quad \Rightarrow \quad P = \lim_{a \to +\infty} \left(\int_{-a}^{+a} |x(t)|^2 dt \right) = 0 \tag{5. 4}$$

This allows the calculation of the C_n Fourier coefficients (treating the impulsive event as periodic) to be expressed as follows:

$$C_n = \frac{2}{T_R} \int_{-\infty}^{+\infty} x(t) e^{-i2\pi n f_0 t} dt = \frac{2}{T_R} \int_{-T/2}^{+T/2} x(t) e^{-i2\pi n f_0 t} dt \tag{5. 5}$$

That, compared to the Fourier transform expression (treating the signal as transient) of Eq.(5. 6),

$$X(f) = \int_{-\infty}^{+\infty} x(t) e^{-i2\pi f t} dt = \int_{-T/2}^{+T/2} x(t) e^{-i2\pi n f_0 t} dt \tag{5. 6}$$

yields the wanted relationship between the actual frequency content of the signal and the calculated Fourier coefficient at any discrete frequency line (*nf_0*) as described in Eq.(5. 7).

$$X(f) = \frac{T_R}{2} C_n \quad \forall f = nf_0 \tag{5. 7}$$

The proportionality described by Eq.(5. 7) explains the trend shown in Fig. 5. 5. The lesson learned by this analysis demonstrate that the quantitative results obtained by an angle domain SSL analysis must be particularly critically interpreted: in order to have a reliable ranking between the identified sources, the width of the gate used for the processing must be properly taken into account.

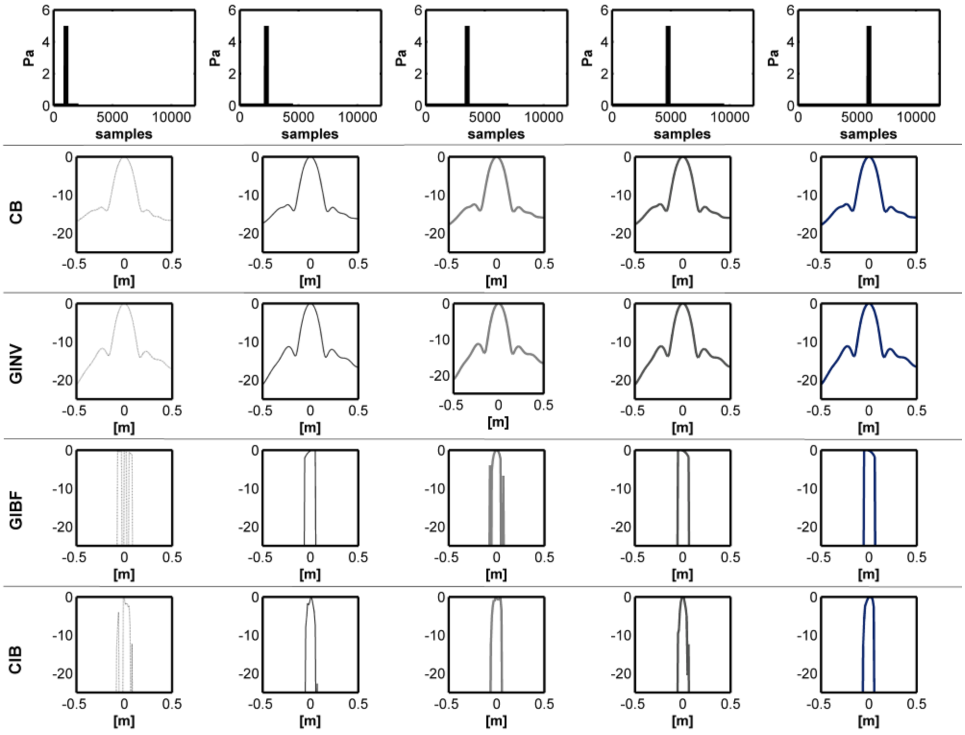

Fig. 5. 7 : beamforming analysis on an impulsive event with different number of samples. Linear array of 50 randomly distributed microphones at 1 m far from the source placed in 0 m position.. Comparison of methods: CB, GINV, GIBF, CIB in the frequency range 1000 Hz – 2000 Hz. Results normalized to the maximum and plotted in dB for comparison.

The particular nature of the signals typically encountered in the targeted applications suggests also to carefully select the acoustic imaging technique. In fact the poor frequency resolution and the particular averaging procedure followed in the execution of the angle domain SSL algorithm, may be insidious for the proper computation of the CSM, required for the acoustic imaging step. Therefore, the choice between direct and inverse approaches is in this case more difficult, because it is made seeking the compromise between the robustness in reliably computing transient signals with poor frequency resolution, on the other hand the need for sufficient spatial resolution and dynamic range to ease the interpretation of the acoustic images obtained over the angular evolution of the investigated machine. A comparison of the performance of different acoustic imaging algorithms already described in this document is reported in Fig. 5. 7: *Conventional Beamforming* (CB), *Generalized Inverse* (GINV) ([112] hybrid formulation adopting Eq.(1.26) in Chapter 1), *Generalized Inverse Beamforming* (GIBF) and *Clustering Inverse Beamforming* (CIB). The application case is the same as before: source placed in location 0 m, line array of 50 randomly distributed microphones placed 1 m far from the source. The adopted source signals are reported in the first row of graphs in Fig. 5. 7. It is observed that CB and GINV yield similar results. It was noticed that different tunings of the *Z* matrix in the GINV formulation (see Eq.(1.26) in Chapter 1) provided a slightly increased spatial resolution, but at the cost of a reduction of the dynamic range (increase of the sidelobes). GIBF yields excellent spatial resolution and dynamic range, but its performance are severely depending on the frequency resolution adopted for the computation. CIB is slightly more robust in this sense, but still suffers of the same limitation.

In this application direct methods appear more stable, at the cost of a limited spatial resolution and dynamic range. It is the vice versa for the case of inverse methods. The latter in fact have demonstrated to outperform CB, but at the risk of instable results. For the sake of a more robustness, this application will be therefore tested adopting CB in the following sensitivity analysis.

5.3. Sensitivity analysis of the proposed angle domain SSL algorithm

Several parameters may influence the results of an angle domain SSL analysis. In this section a simulated experiment has been used for understanding which are the most critical parameters and what is their influence on the final outcome of the analysis. In order to do so a cyclo-stationary problem has been simulated in which 4 cylinders act cyclically emitting an impulsive signal with the sequence 1 – 2 – 3 – 4. The idea is to mimic the behaviour of a 4 cylinders ICE injection (and combustion) noise taking as angular reference its main shaft. The entire cycle is set to have an angular duration of 720 degrees (2 revolutions). The cylinders events are separated 180 deg from each other. The first cylinder acts at 40 deg. The geometry of the problem is described in Fig. 5. 8 for what concerns the source region. The sources have been propagated in time domain towards a 36 microphones array placed 0.6 m far from the source region. The sources signals ($y_1(t)$, $y_2(t)$, $y_3(t)$ and $y_4(t)$ in Fig. 5. 9) have been generated according to the angular evolution described by the signal $\beta(t)$. In the angular evolution of the engine shaft have been simulated constant rotational speed conditions ω_0 polluted by distortions $\Delta\omega$ due to the second order torsional fluctuation of the shaft very typical in common four-stroke ICE.

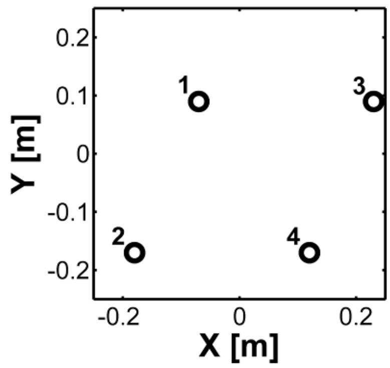

Fig. 5. 8 : geometry of the simulated problem.

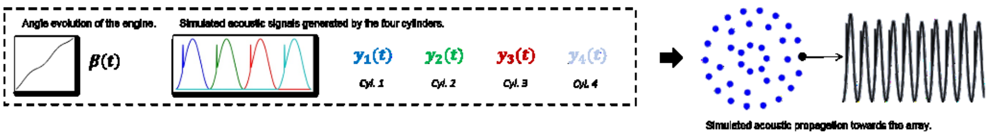

Fig. 5. 9 : simulation strategy. The impulsive event cyclically occurring at each cylinder has been generated and "polluted" by introducing the distortions due to the rotational speed fluctuations.

Seven scenarios have been simulated varying the impulsiveness of the injection component, the presence of the combustion noise and the mean rotational speed. The characteristics of each scenario are summarized in Fig. 5. 10.

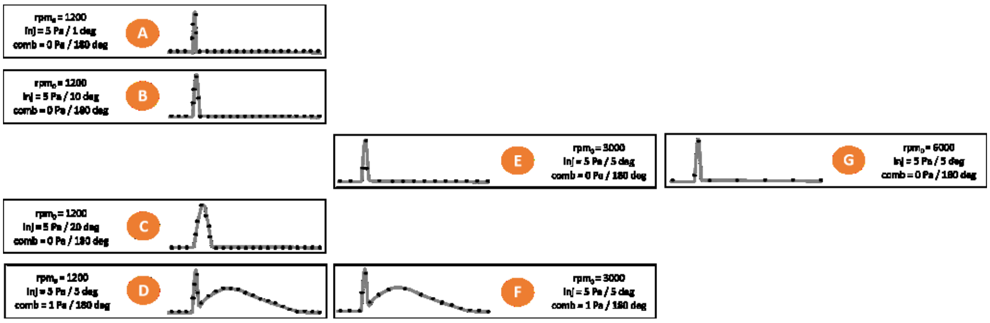

Fig. 5. 10 : Simulated scenarios. Several cyclo-stationary signals have been used tuning the rotational speed, the impulsiveness of the signal and the presence of a low frequency event (simulating the combustion event) happening concomitantly with the more impulsive one (simulating the injection event).

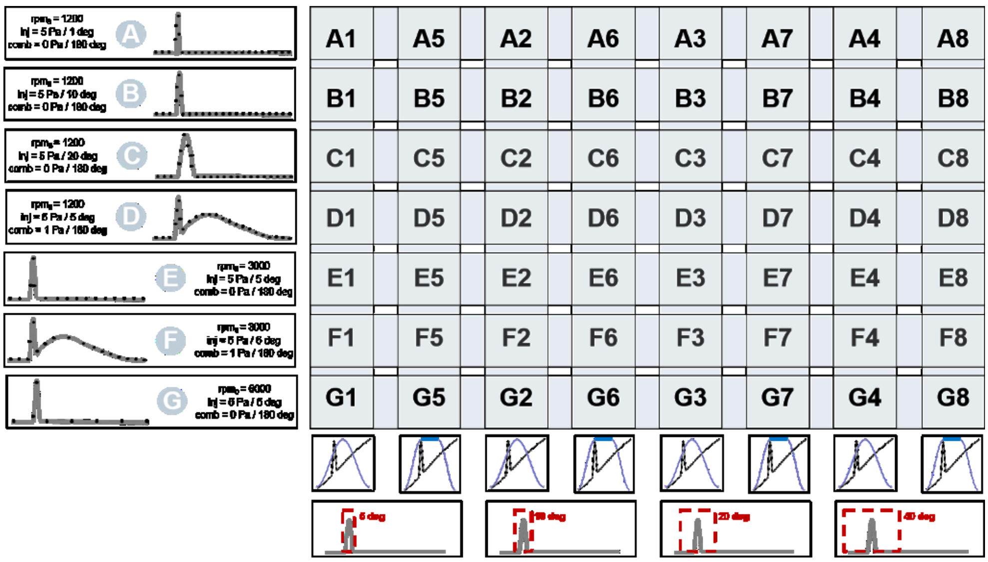

Fig. 5. 11 : Processing cases. Width of the gate has been varied in the range 5 deg – 40 deg and two different windows have been tested.

The impulsive injection components have been simulated with durations of 1 deg, 5 deg, 10 deg and 20 deg. The combustion events, when present, have been simulated with duration of 180 deg. Three different rotational speeds have been tested: 1200 rpm, 3000 rpm and 6000 rpm.
Each scenario has been therefore processed with the angle domain SSL algorithm adopting every time eight different settings of the *width of the gate* and *type of window* parameters. The several processing results have been labelled with codes ranging from A1 up to G8 as described in Fig. 5. 11. Four widths of the gates have been adopted: 5 deg, 10 deg, 20 deg and 40 deg. Two types of windows have been tested: the Hanning window and the Tuckey window, constant and equal to 1 in the central part. The advantage of this latter shape should be that it tends to not suppress the impulsive event if it does not fall in the middle of the considered block.

Fig. 5. 12, Fig. 5. 13, Fig. 5. 14 and Fig. 5. 15 show some examples of angle domain SSL results. Acoustic images, obtained processing the gated information as described in section 5.1, are reported every 30 degrees of rotation of the simulated shaft. The acoustic images are SPL maps with dynamic range of 8 dB. The dB scale is fixed and its maximum is the maximum SPL value detected in all the beamforming maps of the analysis. It can be noticed that the cylinders event, in the sequence 1-2-3-4, are correctly identified at the corresponding angular position. The four cases reported demonstrate that the method is able to correctly identify the four cyclo-stationary sources in the correct location at the correct angular position. The presence of a low frequency component (cases D and F) may cause the presence of artefacts in the acoustic images as visible in Fig. 5. 13. However their level is much lower than the actual sources' level, in fact they disappear in correspondence of the cylinder events. Nevertheless it remains an issue for the algorithm and may reduce it robustness. To mitigate this problem the user can pre-process the data with an high-pass filter (risking to remove important parts of the signals) and/or increase the width of the gate for the angle domain SSL analysis.
The algorithm proved to be less sensitive to the increase of the rotational speed as it is possible to notice by comparing Fig. 5. 12, Fig. 5. 14 and Fig. 5. 15. In fact the only undesired effects are visible in Fig. 5. 15 where artefacts are present right after the end of some cylinder events. In all the cases reported below the Hanning window has been used. Results adopting the Tuckey window will not be shown, but only commented at the end of this paragraph.

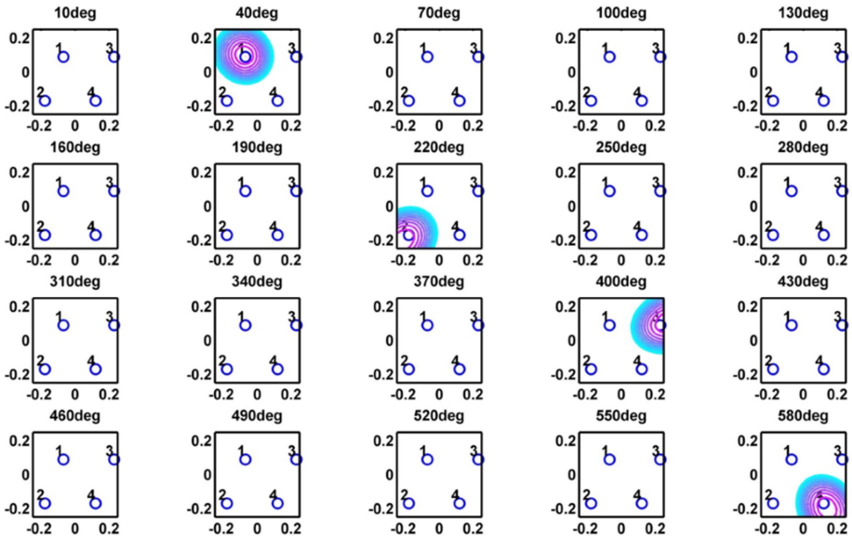

Fig. 5. 12 : simulation 4 cylinders cyclo-stationary events: B3. Rotational speed: 1200 rpm, injection: 10 deg, gate: 20 deg.

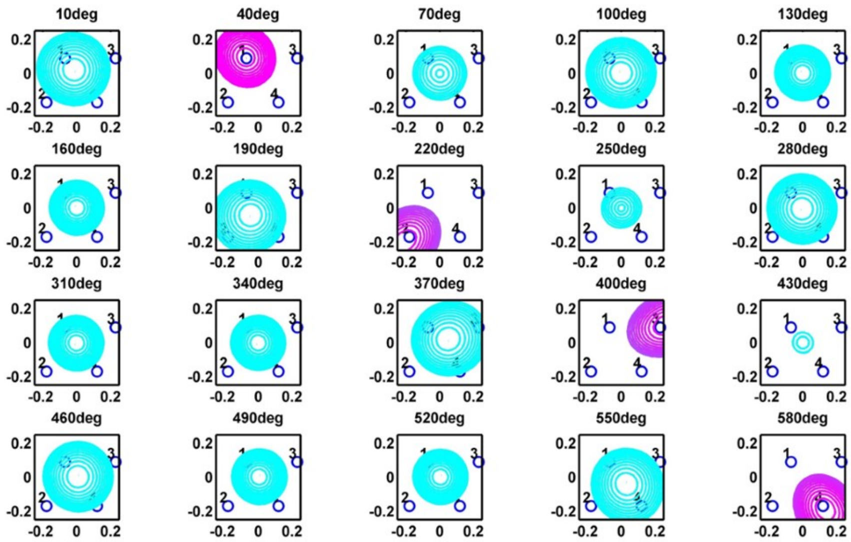

Fig. 5. 13 : simulation 4 cylinders cyclo-stationary events: D3. Rotational speed: 1200 rpm, injection: 5 deg, combustion: 180 deg, gate: 20 deg.

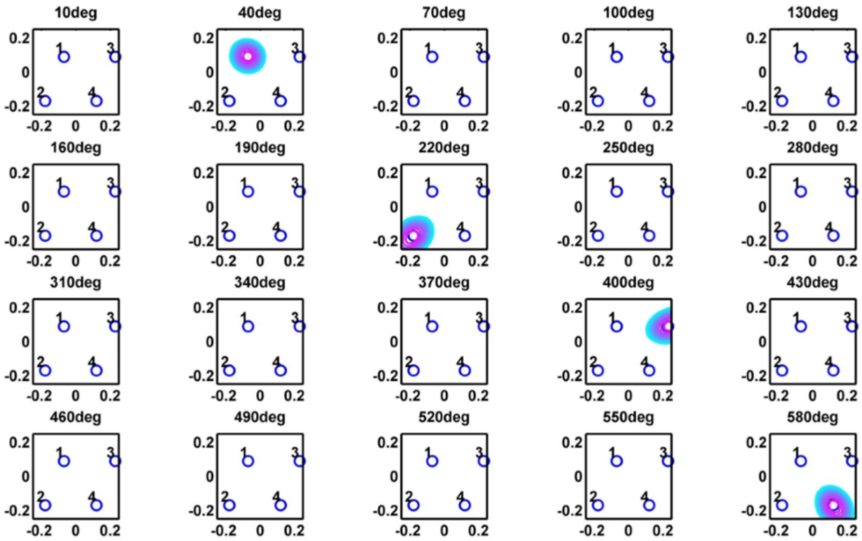

Fig. 5. 14 : simulation 4 cylinders cyclo-stationary events: E3. Rotational speed: 3000 rpm, injection: 5 deg, gate: 20 deg.

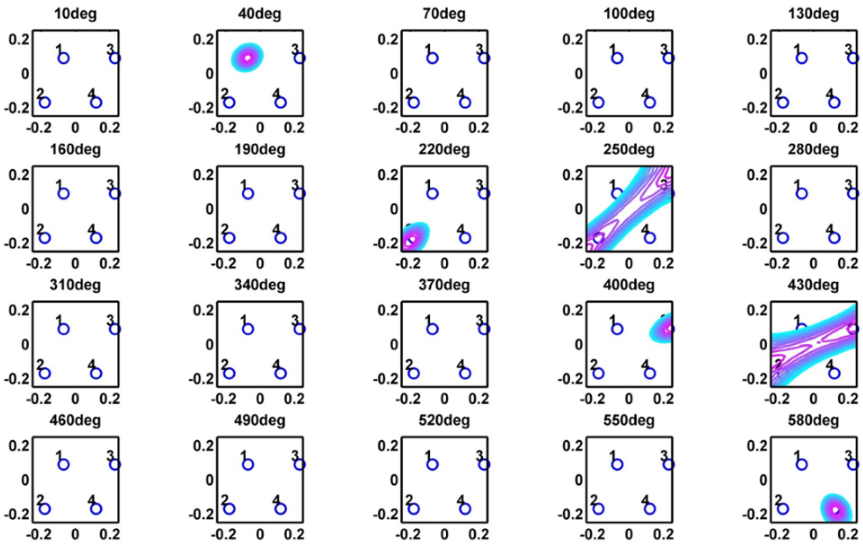

Fig. 5. 15 : simulation 4 cylinders cyclo-stationary events: G3. Rotational speed: 6000 rpm, injection: 5 deg, gate: 20 deg.

Despite very easy to interpret, the acoustic images do not allow a measurable comparison between all the produced cases. The results have been therefore synthesized adopting two indicators: the localization indicator and the dynamic range indicator. Each ideal cylinder location have been associated to a corresponding region of interest visible in Fig. 5. 16(a). The *localization indicator* graph keeps track of the maximum SPL value registered within each cylinder area as a function of the angular position (acoustic images have been calculated every 3 deg: 0, 3, 6, …, 90, 93, …, 717). The *dynamic range indicator* graph reports the difference between the higher localization curve and the one immediately lower as a function of the angular position.

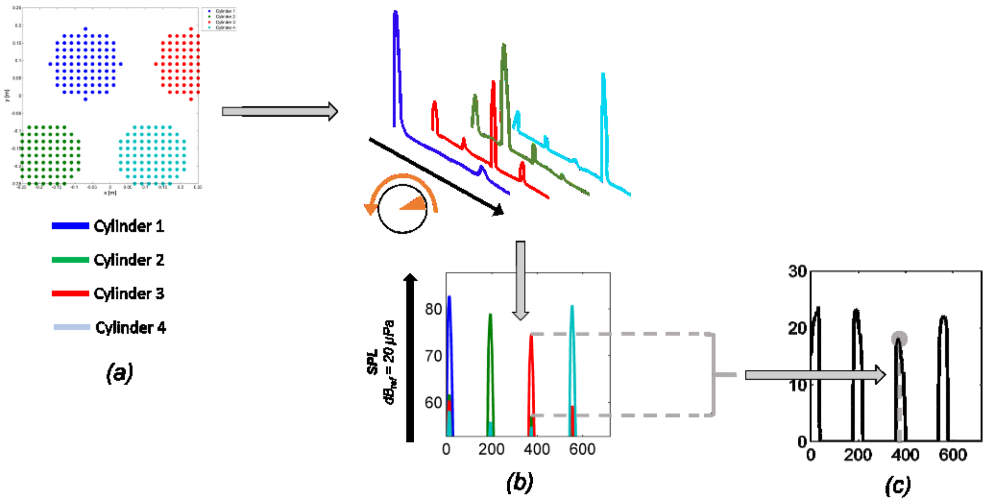

Fig. 5. 16 : (a): regions of interest. (b): the localization indicator graph. Abscissa: the angular position; ordinate: maximum SPL value in the region of interest. (c) : the dynamic range indicator graph. Abscissa: the angular position; ordinate: difference between the higher localization curve and the one immediately lower.

Fig. 5. 17 and Fig. 5. 18 report a comparison of the cases in which the angular width of the impulsive injection event varies from 1 deg up to 10 deg. The comparison shows how results change in terms of localization and dynamic range when adopting gates with different angular widths.

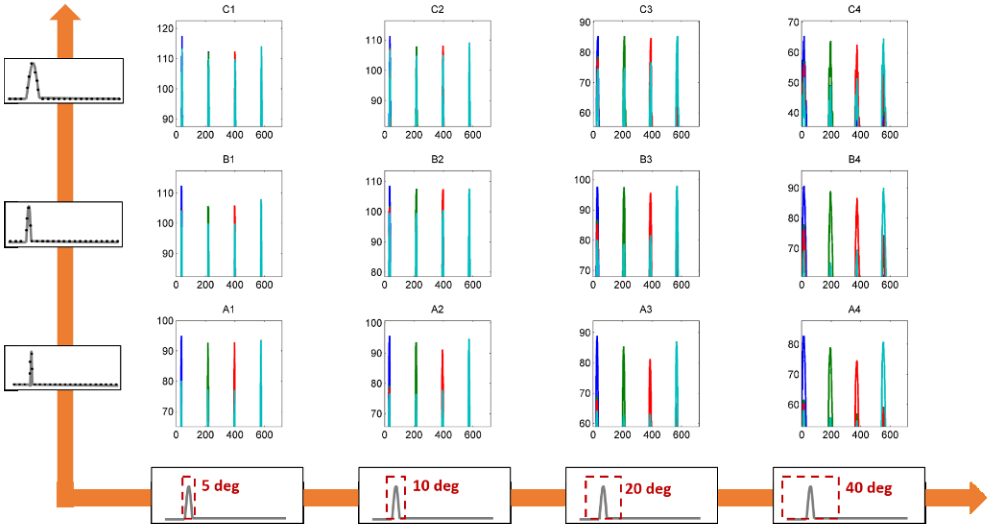

Fig. 5. 17 : localization indicator traced for impulsive events of different angular duration (A: 1 deg, B: 5 deg, C: 10 deg), processed adopting gates of different widths. Hanning window.

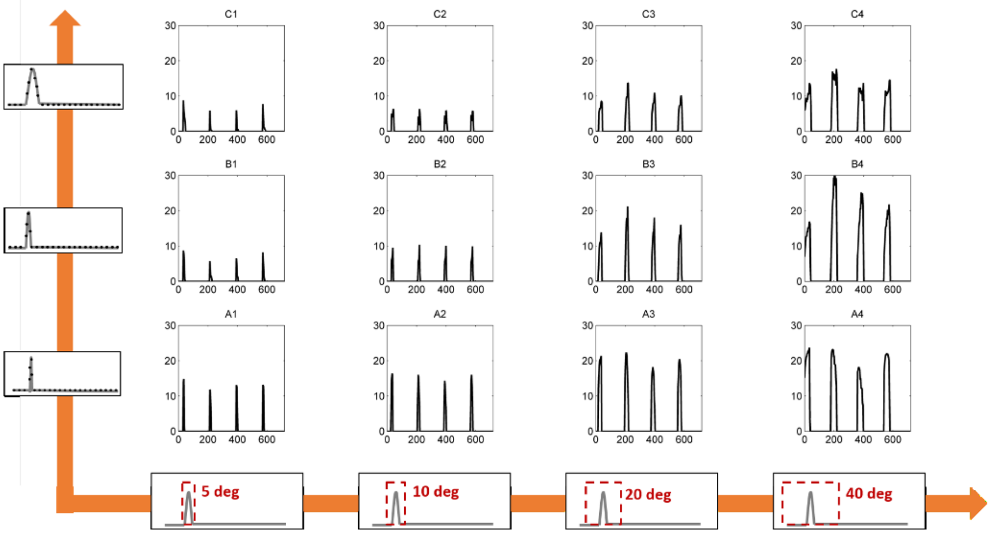

Fig. 5. 18 : dynamic range indicator traced for impulsive events of different angular duration (A: 1 deg, B: 5 deg, C: 10 deg), processed adopting gates of different widths. Hanning window.

The two indicators show that the injection events are correctly localized and in the correct angular positions. In order to have a good dynamic range the width of the gate should be comparable with the width of the investigated impulsive event. The optimal condition is reached when the gate's width is twice the impulse angular width. In this case in fact the maximum SPL value detected is the same for the four cylinders (see cases B2 and C3 of Fig. 5. 17) denoting an optimal ranking of the sources (they are of the same strength). The optimal cases are reported in Fig. 5. 19. An increase of the width of the gate ensures a larger dynamic range, but at the cost of a lower angular resolution (cases A4, B4 and C4 of Fig. 5. 17 and Fig. 5. 18).

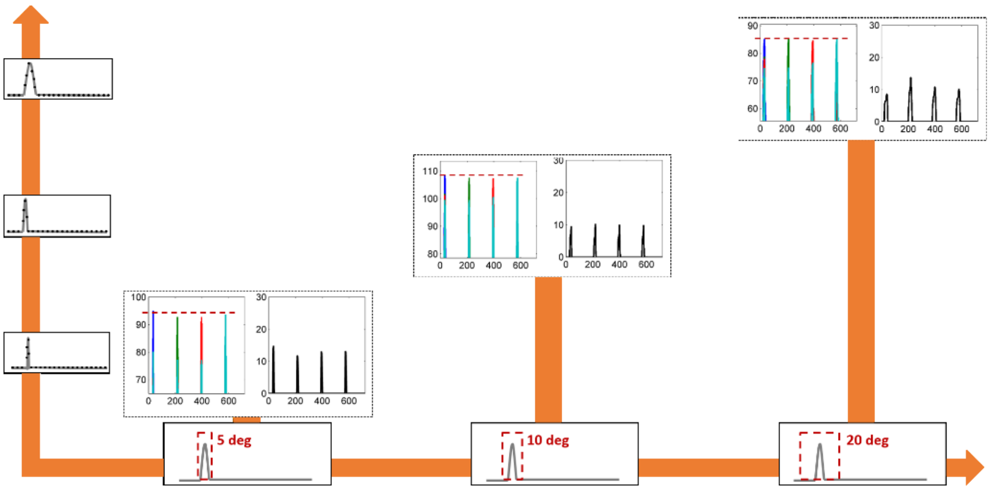

Fig. 5. 19 : optimal gate setting corresponding to the impulsiveness of the signal. Rule of thumb: the gate should have an angular width two times larger than the duration of the sought impulsive events.

The same trends observed in the just described comparison can be observed in Fig. 5. 20 and Fig. 5. 21 where the processing with different gate widths have been tested in cases in which the impulsive event has the same angular width (5 deg), but the nominal rotational speed is changed: 1200 rpm for cases B, 3000 rpm for cases E, 6000 rpm for cases G. Comparing the localization and dynamic range indicators for the cases B2, E2, G2 (where the gate's width, 10 deg, is optimal because twice the impulsive event's width, 5 deg) it can be noticed that the main influence of an increased rotational speed is a reduced angular resolution as denoted by the larger width of the indicators' peaks in correspondence of the angular positions where a cylinder event occurs.

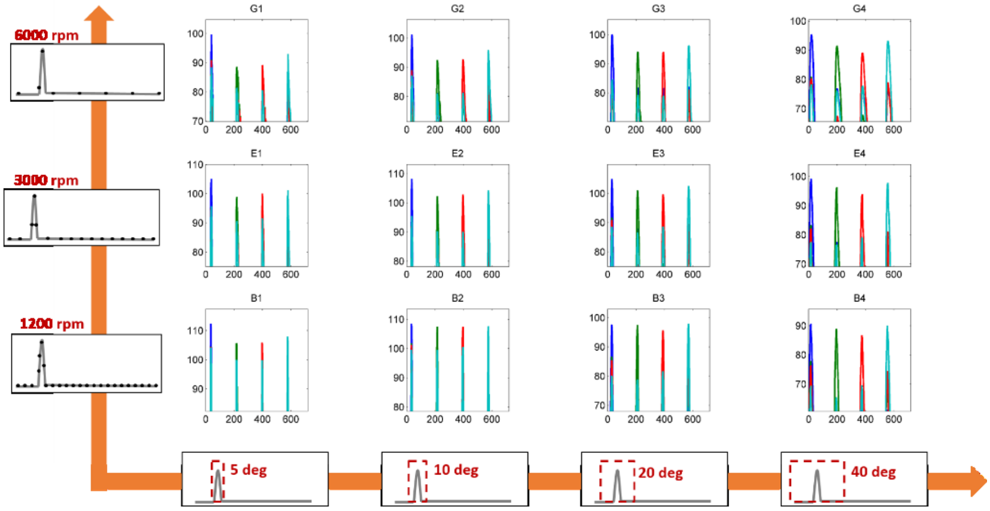

Fig. 5. 20 : localization indicator traced for impulsive events of equal angular duration, but evolving with different rotational speeds (B: 1200 rpm, E: 3000 rpm, G: 6000 rpm), processed adopting gates of different widths. Hanning window.

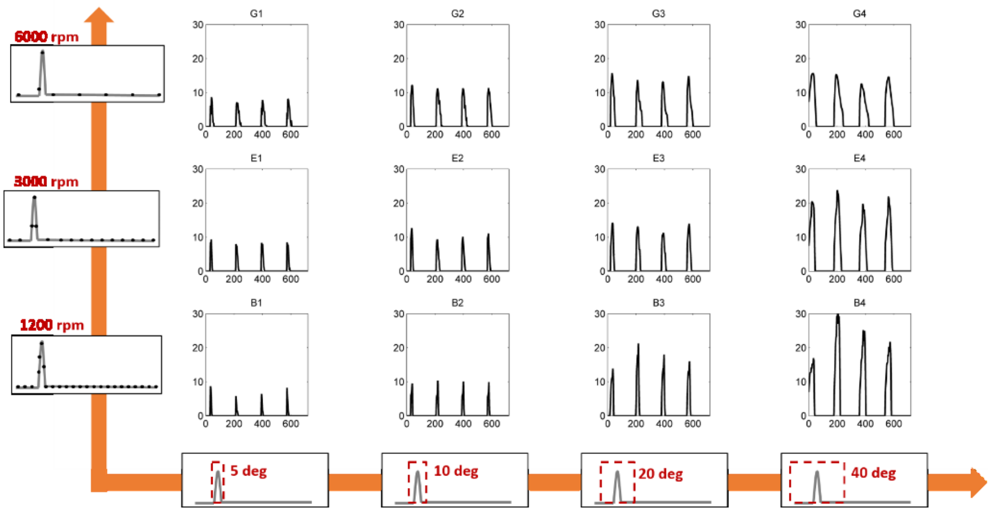

Fig. 5. 21 : dynamic range indicator traced for impulsive events of equal angular duration, but evolving with different rotational speeds (B: 1200 rpm, E: 3000 rpm, G: 6000 rpm), processed adopting gates of different widths. Hanning window.

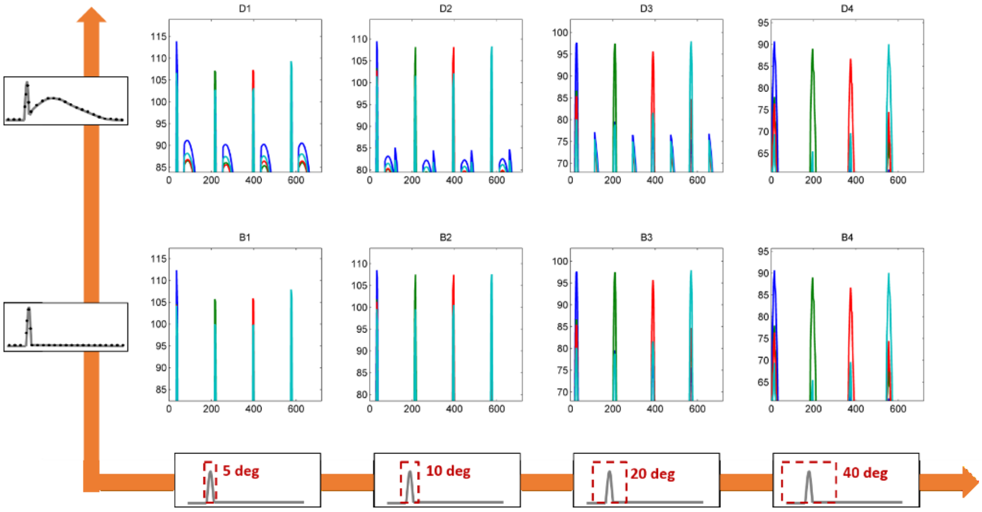

Fig. 5. 22 : localization indicator traced for impulsive events of equal angular duration, with and without an associated low frequency combustion event, processed adopting gates of different widths. Hanning window.

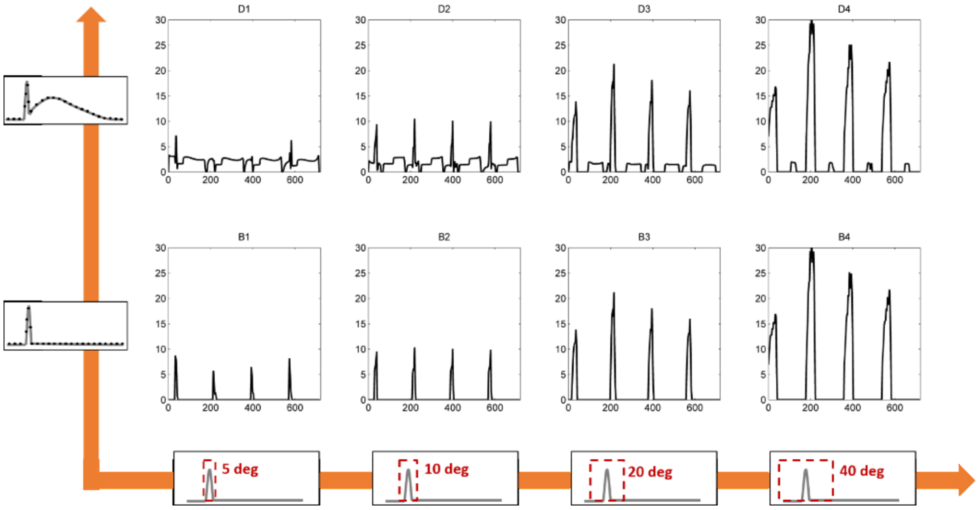

Fig. 5. 23 : dynamic range indicator traced for impulsive events of equal angular duration, with and without an associated low frequency combustion event, processed adopting gates of different widths. Hanning window.

Fig. 5. 22 and Fig. 5. 23 report respectively the localization and dynamic range indicator traced for impulsive events of equal angular duration, with and without a concomitant low frequency combustion event, processed adopting gates of different widths. As already reported commenting Fig. 5. 13 the presence of a concomitant low frequency combustion event may be a source of inaccuracy. In fact it tends to introduce artefacts in the acoustic image if the gate's width is shorter than the angular duration of the low frequency event. In a few words we could conclude that it is not possible to focus at the same time on events of large and narrow angular width. As shown by the graphs corresponding to the processing cases D3 and D4 in Fig. 5. 22 and Fig. 5. 23 the countermeasure to improve the results is increasing the width of the gate.

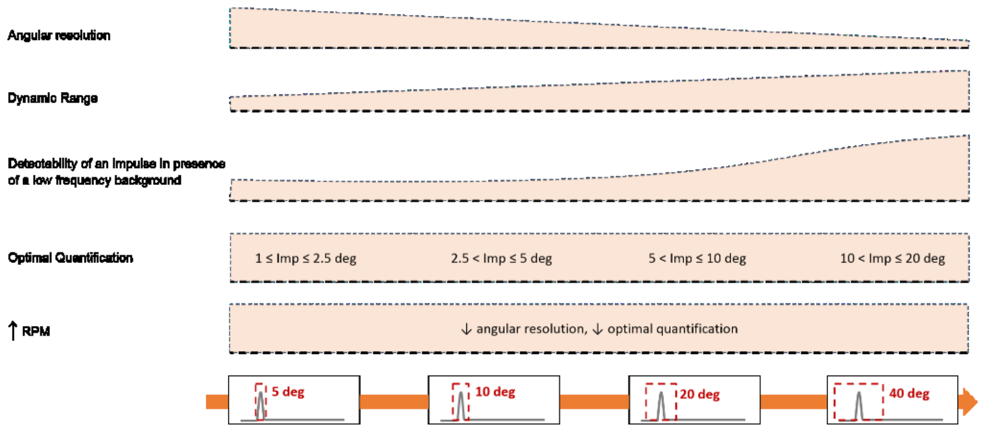

Fig. 5. 24 : influence of different widths of the gate on the main parameters of interest in an angle domain SSL analysis.

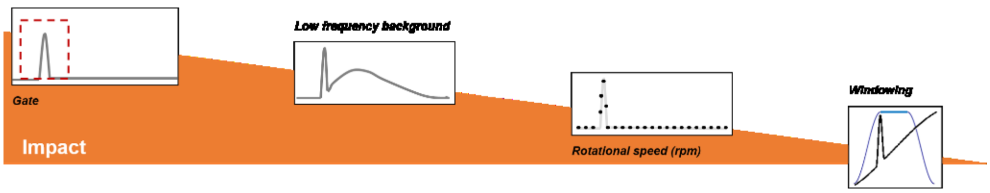

Fig. 5. 25 : ranking of the most relevant parameters influencing angle domain SSL.

In angle domain SSL the user is mainly interested in identifying signals with an impulsive pattern which is repeated in a cyclo-stationary way. This property requires special care in handling the signals both in time/angle and in frequency domain. For this reason the influence of all the parameters related to the length of the treated signals has been investigated: impulsiveness, gate, rpm (influencing the number of samples per angular unit), with the following results:

- The optimal proportion between impulsiveness and angular window of observation is a factor 2. This means that for observing an impulsive phenomenon lasting 5 deg, the best option is using a gate of 10 deg.
- The dynamic range increases proportionally to the width of the gate at the cost of a lower angular resolution.
- The presence of a low frequency background happening with the wanted impulsive event (i.e. combustion event) makes the identification less accurate. For balancing it, larger gates are needed.
- The increase or the rotational speed (RPM) tends to reduce the angular resolution and to degrade the quantitative results, but it does not influence the achievable dynamic range.
- The use of a Tuckey Window slightly increases the angular resolution, but at the cost of "tail effects" at the beginning and the end of the detected impulsive event.

Fig. 5. 24 summarizes the points listed above, while Fig. 5. 25 ranks the sensitivity of the method to the four investigated parameters. The sensitivity analysis has in fact provided a role of thumb that ensures the optimal performance of the techniques if the angular width of the gate is set two times larger than the angular width of the sought impulsive event. Moreover, another consequence of this fact is that the gate acts as a sort of lens that allows the user focusing on events of a wanted impulsiveness. The sensitivity analysis has shown that the method can be successfully applied also in presence of high rotational speeds. Despite it has not broadly discussed in this paragraph, the use of a Tuckey window resulted not beneficial. In addition to these aspects, the authors recommend to select with particular accuracy the sampling frequency balancing the need for a sufficient amount of samples for working with short signals and the potential issues related to resampling. The quality of the tacho signal is another key factor. A good accuracy in the measurement of the angular evolution of the rotating element under analysis certainly improves the quality of the results.

To conclude this chapter let us observe that despite the analysis performed in section 5.2 discouraged the adoption of inverse methods because less stable than direct methods, although better performing, the implementation of CIB into the angle domain SSL algorithm's structure is straightforward and the choice of using it depends essentially by the type of sources signals under investigation.

Chapter 6.

Conclusions

The main results achieved in the development of advanced acoustic imaging methods working in frequency, time and angle domain, for localizing exterior sources affecting in-vehicle noise, interior noise sources and component noise, in vehicles NVH, have been reported in this document. Despite special attention has been dedicated to automotive applications, the proposed techniques are general and ready-to-use in several NVH cases. This multi-domain framework has been designed so that frequency-based, time-based and angle-based techniques can be chosen according to the specific NVH problem that should be tackled.

A novel inverse acoustic imaging method, the so-called Clustering Inverse Beamforming (CIB), working in *frequency domain*, has been invented, validated and positioned with respect to the state-of-the-art. The method has proven to give accurate and reliable results both in academic and in industrial experimental test cases. CIB allows accurate localization, a reliable ranking of the identified sources and their separation into uncorrelated phenomena. It is therefore useful not only for troubleshooting applications, but also for accurate NVH analyses. Another remarkable advantage is that it requires a reduced number of sensors and tests. In several cases, it avoids the use of reference sensors installed close to the investigated object. Moreover, it allows designing flexible and multi-purpose test setup. One example is the use of a randomly distributed microphones array in the car cabin that can be used both for interior acoustic imaging and Acoustic Modal Analysis.

CIB has been adopted also as preliminary step for inverse source reconstruction in *time domain* based on far-field measurements. This technique is particularly suited in those applications that require a detailed knowledge of the main sources and the acoustic field produced by them. The time domain-based method described in this document, therefore, represents an appealing technique for source reconstruction with a reduced computational and experimental effort. This opens up interesting scenarios in which the time domain source reconstruction results are used as input for further analyses. The study of sound and vibration phenomena related to the engine of a car often needs complex experimental setups. The engine has to be instrumented with several sensors requiring several hours (or days) of tests. The possibility to relate the identification of the noise sources produced by the ICE with the angular position of the rotating elements of the engine and the knowledge of the location of such noise sources within the cycle of the ICE, through microphones array measurements, gives therefore several advantages. In fact, on the one hand it allows to understand the causality between the physical phenomena and their acoustic consequences, on the other hand, it allows to optimize the effort for further and more accurate studies, thus saving, once again, time and costs.

The *angle domain* SSL algorithm has been developed for this purpose. The sensitivity analysis presented in this work has proven its robustness on simulated data. Validations of experimental industrial cases have been already successfully performed and will be documented in future publications. The angle domain SSL algorithm is suitable also for condition monitoring applications and even a combined use with the previously described time domain-based inverse source reconstruction is possible.

In conclusion, the proposed *multi-domain* acoustic imaging approaches represents a complete package of technologies for the assessment of advanced NVH analyses with a reduced time and economical effort. This authentic breakthrough in the exploitation of advanced acoustic imaging solutions may represent the beginning of a new generation of experimental techniques for supporting the design of the new generation of ground, marine and air transportation vehicles.

6.1. Critical aspects

The advanced version of GIBF proposed in this thesis in combination with the developed PCA-based adaptive pre-processing algorithms greatly enhances the potential of this inverse acoustic imaging technique both in exterior and in interior noise applications. In fact, this package of methodologies proved to be effective in fairly regularizing the inverse acoustic problem, optimizing the equivalent sources distribution calculation by adaptively discarding insignificant components and providing sufficient criteria to ascertain that the retrieved source distributions correspond to the sought physical sources. The PCA-based pre-processing resulted beneficial in uncorrelated source separation and de-noising of the array data. However, the proposed solutions have demonstrated also limitations. In fact, blind source separation techniques relying on PCA processing of the acoustic data recorded with array-based methods yield a virtual decomposition of the sampled acoustic field that not always correspond to the sought physical phenomena. This is the case when uncorrelated sources distributions are partially joint in space. This issue has been analysed observing a dependency to the analysed frequency. A role can be derived: the proposed PCA-based technique allows to successfully separate uncorrelated noise sources that are disjoint with a distance greater than half the wavelength of the analysed frequency. In this latter case the method yields correct separation into uncorrelated sources distribution. The proposed sufficient criterion for matching virtual and physical source distributions is based on pattern recognition of features in the calculated acoustic image therefore compact sources distributions are more easily identified. Spatially distributed sources make the pattern recognition a more challenging task requiring more refined methodologies that have not been discussed in this document.

The Clustering Inverse Beamforming algorithm proved to be a promising tool for noise source identification in frequency domain with accurate localization and high dynamic range. It relies on the information carried by the so-called clustering mask matrix. This matrix is a function, which is defined in the source region, that assigns to the scan points related to each equivalent source a value ranging from 0 to 1. These values can be interpreted as the confidence level of finding a physical source in the proximity of that location. Several exploitations are possible and its effectiveness has been proven for exterior and interior noise problem on several numerical and experimental validation cases. Further criteria should be introduced to make the setting of the required parameters (number of microphones per cluster, number of clusters, etc.) adaptive. Moreover, the clustering mask matrix entity appears nicely compatible with the concept of “aperture function” adopted in the Bayesian formulation of the ESM problem. This suggest the investigation of further synergies and the extension of CIB towards other ESM approaches (in this thesis it was presented in combination with GIBF).

The reconstruction of the time-domain evolution of the noise sources active in the acoustic scene is obtained in two steps. A preliminary source localization in the frequency domain, exploiting the properties of the clustering mask matrix, is performed first to transform the formulation of the initially under-determined inverse acoustic problem under study into an equivalent over-determined version. Finally, such over-determined problem is solved in time domain. The method has proven to be effective in presence of correlated as well as uncorrelated sources and it was pointed out that the main causes of a not ideal reconstruction of the sources are the cross-talk and the presence of background noise. It is important to point out two other limitations of the technique. The first is that the reconstruction of the sources is granted only in terms of their far-field effect; this could be a limitation in situation in which the not-radiating part of the acoustic excitation produced by the source is relevant to the noise problem under study. The second aspect is that the proposed approach does not model accurately the radiation of distributed sources. This aspect certainly requires further investigations.

The proposed angle domain sound source localization algorithm allows obtaining the acoustic image of the sound source produced by a rotating machinery as a function of the angular evolution of its rotating elements. In order to do so, it requires an ordinary array-based measurements setup and the availability of the main shaft rotational speed information. Direct methods proved to be more robust than inverse approaches in this application. Therefore the methodology was presented adopting CB as acoustic imaging method. In such applications, acoustic imaging faces the additional challenges related to the poor frequency resolution of the information available (due to the intrinsic working principle of the algorithm) and to the presence of impulsive patterns in the processed microphones acoustic signals. It was analysed that these two aspects affect the quantitative part of the identification and the achievable dynamic range. Guidelines for the minimization of the issues related to these aspects have been suggested. In the version presented in this document the approach grants only qualitative results and the accuracy in sources ranking is reduced if the studied signals contain impulsive patterns. Guidelines on how to mitigate these risks have been proposed providing theoretical evidences. The method has been validated on simulated cases and, although not reported in this thesis for confidentiality issues, applications on real test cases have been already successfully carried out. However, the method still needs to be improved through a more extensive experimental validation.

6.2. Recommended future work

Clustering Inverse Beamforming is a promising acoustic imaging technique. Its ability of resolving complex acoustic fields and its compatibility with any kind of array configuration, makes this approach suitable for challenging industrial applications such as aero-acoustic array measurements and interior noise source identification. In the first case, an extension of the radiation model is most probably required for taking into account the effect of the mean flow and other complexities such as the presence of rigid walls in the case of closed test section wind tunnels. CIB is a ready-to-use technique also in the case of the exploitation of 3D configurations of the array and/or the source region. In the case of interior applications the performance already described in this thesis appear to be improvable by exploiting as much as possible the versatility in using the most suitable microphones array configuration.

As already mentioned in section 6.1 the concept of clustering mask matrix appears nicely compatible with the concept of "aperture function" in Bayesian focusing. In fact, despite the big difference between these two entities is that the aperture function is based on a priori information about the source field, while the clustering mask matrix is the statistical result of multiple realizations of a most likelihood fitting of the source region, they share the intrinsic property of a probability density function distribution of finding a physical source in a certain location within the source region. This sisterhood between the two entities suggests a similar use of the clustering mask matrix in a Bayesian approach.

The time domain-based method described in this document represents an appealing alternative for source reconstruction with a reduced computational and experimental effort and with no need of reference sensors. This opens up interesting scenarios for cases in which acoustic imaging quantitative results can be used as virtual sensors. One fascinating case is the possibility of defining an acoustic imaging-based Transfer Path Analysis model suitable for aero-acoustic applications. This will allow considering the wind noise-related problems since the very early stages of the development of the vehicle improving its sound quality performance. Another interesting perspective is the intersection between time-domain and angle-domain information. This is a unique combination in applications, such as condition monitoring, characterized by cyclo-stationary phenomena. In this case the angle domain SSL results should be adopted as pre-processing step for the consequent time domain reconstruction of the identified sources. This implies several challenges mainly related to the fact that the noise sources locations are typically not constant over the angular evolution of the rotating machinery.

Nomenclature

Acronyms

NVH	Noise Vibration and Harshness
TPA	Transfer Path Analysis
AMA	Acoustic Modal Analysis
ICE	Internal Combustion Engine
NAH	Near-field Acoustic Holography
IBEM	Inverse Boundary Element Method
CB	Conventional Beamforming
CSM	Cross-Spectral Matrix
NNLS	Non Negative Least Squares
FFT	Fast Fourier Transform
ESM	Equivalent Source Method
GIBF	Generalized Inverse Beamforming
FRF	Frequency Response Function
IFRF	Inverse Frequency Response Function
SSL	Sound Source Localization
HELS	Helmholtz Least Squares
iPTF	inverse Patch Transfer Function
ASQ	Airborne Sound Quantification
NTF	Noise Transfer Function
SPL	Sound Pressure Level
SVD	Singular Value Decomposition
TSVD	Truncated Singular Value Decomposition
GINV	Generalized Inverse acoustic problem
CNR	Contrast to Noise Ratio

Symbols valid in all the chapters

Constants and counters

M	Number of microphones.
N	Number of scan points.
L	Number of not negligible eigenmodes of the CSM. (L<M).
J	Total number of principal components of the acoustic image.
N_c	Number of clusters.
N_m	Number of microphones per cluster.
i	Counter of the i^{th} eigenmode of the CSM.
j	Counter of the j^{th} principal component of the acoustic image. In Chapter 1 it represents the imaginary identity $\sqrt{-1}$.
k	Counter of the iterations for GIBF optimization.
N_k	Number of scan points left after truncation at kth iteration.
l	Counter of the candidate regularization parameters for Quasi-optimality function.
m	Counter of the m^{th} microphone or any quantity that goes from 1 to M.
n	Counter of the nth scan point or any quantity that goes from 1 to N.
n_x	Number of columns of the rectangular planar scan grid.
n_y	Number of rows of the rectangular planar scan grid.
ρ	Density of the air.

Variables and operators

$\ldots^H$	operator	Hermitian conjugate operator.
$\ldots^+$	operator	Moore-Penrose pseudo-inverse operator.
$\otimes$	operator	Convolution operator.
$F^{-1}\{\ldots\}$	operator	Inverse Fourier transform.

$f(\ldots)$	operator	Function of…
$\Upsilon(A,\underline{p}^{(i)})$	operator	Operator representing the solution of the Equivalent Source problem formulated through the radiation matrix A, the data $\underline{p}^{(i)}$ and including regularization and GIBF iterative optimization.
f	scalar	Frequency. [Hz]
R_r	scalar	Propagation factor.
A	[M×N]	Radiation matrix.
$\{A\}_{m,n}$ or A_{mn}	scalar	Element (m,n) of the radiation matrix.
r_{mn}	scalar	Distance between the mth microphone and the nth scan point.
U	[M×M]	Left singular matrix of the Singular Values factorization of the radiation matrix.
$\underline{u}_m$	[M×1]	mth column vector of U.
V	[N×N]	Right singular matrix of the Singular Values factorization of the radiation matrix.
$\underline{v}_n$	[N×1]	nth column vector of V.
Σ	[M×N]	Singular Values matrix of the radiation matrix.
Σ_{mm}	scalar	mth singular value of Σ.
C_M	[M×M]	Cross-Spectral Matrix (CSM) of the microphones array signals.
I	[M×M]	Identity matrix.

Symbols valid in Chapter 1

Constants and counters

c	Speed of sound. [m/s]
k	Wavenumber. [rad/m]

Variables and operators

Q	scalar	Strength of the monopole source. [m^3/s].
W	scalar	Acoustic power [W].
p_0	scalar	Reference value for the acoustic pressure: 20 μPa.
W_0	scalar	Reference value for the acoustic power: 1 pW.
Ω_0	scalar	Reference surface value: 1 m^2.
C_b	[N×N]	Cross-Spectral Matrix between the elementary sources scanned by a direct beamformer.
C_a	[N×N]	Cross-Spectral Matrix between the equivalent sources of an ESM solution.
$\underline{b}$	[N×1]	Beam pattern. The elements of $\underline{b}$ are: b_n.
$\underline{B}$	[N×1]	Direct beamforming acoustic image. [Pa^2]

Symbols valid in Chapter 2 , Chapter 3 and Chapter 4

Constants and counters

c	Counter of the number of clusters.
l	Counter of the number of candidate regularization parameters.

Variables and operators

E	[M×M]	Eigenvectors matrix of the CSM factorization.
$\underline{e}^{(i)}$	[M×1]	i^{th} eigenvector of the CSM factorization.

$e^{(i)}{}_m$	scalar	m^{th} element of $\underline{e}^{(i)}$.
S	[M×M]	Eigenvalues matrix of the CSM factorization.
$s^{(i)}$	scalar	i^{th} eigenvalue of the CSM.
P	[M×M]	Full eigenmodes matrix of the CSM factorization.
P_L	[M×L]	Eigenmodes matrix of the CSM factorization truncated to the L not negligible eigenmodes of the CSM.
$\underline{p}^{(i)}$	[M×1]	i^{th} eigenmode of the CSM factorization.
$p^{(i)}{}_m$	scalar	m^{th} element of $\underline{p}^{(i)}$.
$\underline{a}^{(i)}$	[N×1]	Linear combination of Equivalent Sources concerning the i^{th} eigenmode of the CSM.
$\underline{a}^{(i),k=*}$	[N_k×1]	Linear combination of Equivalent Sources concerning the i^{th} eigenmode of the CSM at the kth iteration of the GIBF optimization. The size N_k changes according to the truncation operation.
λ^2	scalar	Regularization parameter.
$\lambda^2{}_l$	scalar	Candidate regularization parameter for quasi-optimality function.
$Q(\lambda^2{}_l)$	scalar	l^{th} value of the quasi-optimality function.
Θ_m	scalar	Strength of the m^{th} source.
$\underline{\widetilde{a}}^{(i)}{}_c$	[N×1]	Linear combination of Equivalent Sources concerning the ith eigenmode of the CSM obtained adopting the c^{th} cluster of microphones.
$\varepsilon(\arg)$	operator	Operator of binarization: $\varepsilon(\arg \neq 0) = 1$, $\varepsilon(\arg = 0) = 0$.
$\gamma^{(i)}$	[N×1]	Clustering mask "matrix" concerning the ith eigenvector of the CSM factorization.
$\overline{a}^{(i)}$	[n_y×n_x]	Matrix form of the linear combination of Equivalent Sources concerning the i^{th} eigenmode of the CSM.
Φ	[n_y×n_y]	Left singular matrix of the Singular Values factorization of the matrix form of the linear combination of Equivalent Sources that we can define also "solution matrix" and/or acoustic image.
Ψ	[n_x×n_x]	Right singular matrix of the Singular Values factorization

		of the "solution matrix".
Ω	[ny×nx]	Singular Values of the "solution matrix".
ω_j	scalar	j^{th} Singular Value of the "solution matrix".
$\hat{\omega}_j$	scalar	Normalized j^{th} Singular Value of the "solution matrix".
$\overline{a}_{j=1}^{(i=1+i=2)}$	[ny×nx]	j^{th} Principal Component of the "solution matrix" concerning the i eigenmodes of the CSM considered together.
α	scalar	Weighting factor.
Γ	[1×(J-1)]	Cost function for adaptively select the number of SV of the solution matrix to be taken into account in the PCA.
$\breve{j}$	scalar	Index of the normalized Singular Value corresponding to the minimum of the cost function Γ.
$\breve{a}^{(i)}$	[ny×nx]	Compressed solution matrix: "solution matrix" concerning the i eigenmode/es of the CSM after PCA-based adaptive truncation of $\bar{a}^{(i)}$.
δ_n	[1×N]	Dynamic range distribution of the compressed matrix.
Δ	variable	Random variable corresponding to the values δ_n (it defines its sample space).
g_Δ	function	Probability Density Function of the random variable Δ.
δ^*	variable	Discretization of the values assumed by δ, the continuous statistical variable, defined in the sample space, associated to Δ.
H_{δ^*}	function	Histogram of the values δ_n with discretization δ^*.
μ	scalar	Weighted expectation value of the variable Δ.
β	scalar	Weighting factor.
D	function	Parzen estimate of the Probability Density Function g_Δ.
K	function	Kernel adopted for the Parzen estimation.
h	scalar	Width of the kernel.
σ	scalar	Standard deviation of the distribution of values δ_n.
n^*	scalar	Indices of the scan points to be discarded according to the adaptive method.

Symbols valid in Chapter 5

Constants and counters

N_ε	Number of realization of the generalized angular cycle.
n	Counter of the number of cycles.

Variables and operators

ε	variable	Generalized angular evolution. [rad]
$d\beta$	scalar	Angular increment. [rad]
$\widetilde{p}_m$	variable	Synchronous averaged pressure signal of the mth microphone. [Pa]
ω	variable	Rotational speed. [rad/s]
$\widetilde{\omega}$	variable	Synchronous averaged rotational speed signal. [rad/s]
$\Delta\varepsilon$	scalar	Selected angular interval (gate). [rad]
Δt_ε	scalar	Time interval corresponding to the selected angular interval (gate) after resampling. [s]
E	scalar	Energy of a generic impulsive signal *x(t)*.
P	scalar	Power of a generic impulsive signal *x(t)*.
T	scalar	Total duration of the signal *x(t)*. [s]
T_R	scalar	Duration of the impulsive part of the signal *x(t)*. [s]
C_n	scalar	nth Fourier coefficient of signal *x(t)*.
f_0	scalar	Frequency resolution of the discrete Fourier Transform. [Hz]
X	variable	Fourier transform of the generic impulsive signal *x(t)*.

References

[1] Sanderson, M. A. & Onsay, T. “CAE interior cavity model validation using acoustic modal analysis”. *SAE Technical Paper, 2007.*

[2] Young, S. “Vehicle NVH development process and technologies”. *ICSV 21th Conference, 2014.*

[3] Adams, M. & Van de Ponseele, P. “Sound quality equivalent modeling for virtual car sound synthesis”. SAE Technical Paper, 2001.

[4] Jacobsen, F. “Sound intensity measurements”. *Handbook of Noise and Vibration Control, 534-548.*

[5] Leclère, Q.; Pereira, A.; Bailly, C. & Picard, C. “A unified formalism for acoustic imaging techniques: illustrations in the frame of a didactic numerical benchmark”. Berlin Beamforming Conference, 2016.

[6] Wu, S. F. “Methods for reconstructing acoustic quantities based on acoustic pressure measurements”. *The Journal of the Acoustical Society of America, 2008, 124, 2680-2697.*

[7] Williams, E. G. “Fourier acoustics: sound radiation and nearfield acoustical holography”. *Academic press, 1999.*

[8] Sarradj, E. “Three-dimensional acoustic source mapping with different beamforming steering vector formulations”. *Advances in Acoustics and Vibration, 2012, 292695.*

[9] Allen, C. S.; Blake, W. K.; Dougherty, R. P.; Lynch, D.; Soderman, P. T.; Underbrink, J. R. & Mueller, T. J. “Aeroacoustic measurements”. *Springer Science & Business Media, 2013.*

[10] Billingsley, J. & Kinns, R. “The acoustic telescope”. Journal of Sound and Vibration, 1976, 48, 485-510.

[11] Michel, U. “History of acoustic beamforming”. *Berlin Beamforming Conference, 2006.*

[12] Fisher, M.; Harper-Bourne, M. & Glegg, S. “Jet engine noise source location: the polar correlation technique”. *Journal of Sound and Vibration, 1977, 51, 23-54.*

[13] Billingsley, J. “A comparison of the source location techniques of the acoustic telescope and polar correlation”. Journal of Sound and Vibration, 1978, 61, 419-425.

[14] Dougherty, R. P. “Functional beamforming”. *Berlin Beamforming Conference, 2014.*

[15] Sijtsma, P. “CLEAN based on spatial source coherence”. *International journal of aeroacoustics, 2007, 6, 357-374.*

[16] Sijtsma, P. & Snellen, M. “High-resolution CLEAN-SC”. *Berlin Beamforming Conference, 2016.*

[17] Brooks, T. F. & Humphreys, W. M. “Effect of directional array size on the measurement of airframe noise components”. AIAA paper, 1999, 99-1958.

[18] Brooks, T. F. & Humphreys, W. M. “A deconvolution approach for the mapping of acoustic sources (DAMAS) determined from phased microphone arrays”. Journal of Sound and Vibration, 2006, 294, 856-879.

[19] Brooks, T. F. & Humphreys, W. M. “Extension of DAMAS phased array processing for spatial coherence determination (DAMAS-C)”. AIAA paper, 2006, 2006-2654.

[20] Dougherty, R. P. “Extensions of DAMAS and benefits and limitations of deconvolution in beamforming”. *AIAA paper, 2005, 2961.*

[21] Lawson, C. L. & Hanson, R. J. “Solving least squares problems”. *SIAM, 1995, 15.*

[22] Richardson, W. H. “Bayesian-based iterative method of image restoration”. *Journal of the Optical Society of America, 1972, 62, 55-59.*

[23] Lucy, L. B. “An iterative technique for the rectification of observed distributions”. *The astronomical journal, 1974, 79, 745.*

[24] Fish, D.; Walker, J.; Brinicombe, A. & Pike, E. “Blind deconvolution by means of the Richardson-Lucy algorithm”. *Journal of Optical Society of America, 1995, 12, 58-65.*

[25] Chu, Z. & Yang, Y. “Comparison of deconvolution methods for the visualization of acoustic sources based on cross-spectral imaging function beamforming”. *Mechanical Systems and Signal Processing, 2014, 48, 404-422.*

[26] Ehrenfried, K. & Koop, L. “Comparison of iterative deconvolution algorithms for the mapping of acoustic sources”. *12th AIAA/CEAS Conference, 2006, 2006-2711.*

[27] Yardibi, T.; Zawodny, N. S.; Bahr, C.; Liu, F.; Cattafesta, L. N. & Li, J. “Comparison of microphone array processing techniques for aeroacoustic measurements”. *International Journal of Aeroacoustics, 2010, 9, 733-761.*

[28] Ravetta, P. A.; Burdisso, R. A. & Ng, W. F. “Noise source localization and optimization of phased-array results”. *12th AIAA/CEAS Conference, 2009, 2520-2533.*

[29] Holland, K. & Nelson, P. “The application of inverse methods to spatially-distributed acoustic sources”. *Journal of Sound and Vibration, 2013, 332, 5727-5747.*

[30] Kim, B.-K. & Ih, J.-G. “On the reconstruction of the vibro-acoustic field over the surface enclosing an interior space using the boundary element method”. *The Journal of the Acoustical Society of America, 1996, 100, 3003-3016.*

[31] Bai, M. R. “Application of BEM (boundary element method)-based acoustic holography to radiation analysis of sound sources with arbitrarily shaped geometries”. The Journal of the Acoustical Society of America, 1992, 92, 533-549.

[32] Leclère, Q. “Acoustic imaging using under-determined inverse approaches: Frequency limitations and optimal regularization”. *Journal of Sound and Vibration, 2009, 321, 605-619.*

[33] Lanslots, J.; Deblauwe, F. & Janssens, K. “Selecting sound source localization techniques for industrial applications”. Sound and Vibration, 2010, 44, 6.

[34] Van Der Linden, P.; Keppens, T.; Raff, J. & Schnur, J. “Determination of the noise contributions of engine surfaces”. *SAE Technical Paper, 2001, 2001-01-1482.*

[35] Dumbacher, S. & Brown, D. “Source imaging of irregularly shaped surfaces using inverse FRF method”. *ISMA 21 Conference, 1996, 499-507.*

[36] Suzuki, T. “Generalized Inverse Beam-forming Algorithm Resolving Coherent/Incoherent, Distributed and Multipole Sources”. *14th AIAA/CEAS Conference, 2008, 2008-2954.*

[37] Zavala, P.; De Roeck, W.; Janssens, K.; Arruda, J.; Sas, P. & Desmet, W. “Generalized inverse beamforming with optimized regularization strategy”. *Mechanical Systems and Signal Processing, 2011, 25, 928-939.*

[38] Presezniak, F.; Zavala, P. A.; Steenackers, G.; Janssens, K.; Arruda, J. R.; Desmet, W. & Guillaume, P. “Acoustic source identification using a Generalized Weighted Inverse Beamforming technique”. *Mechanical Systems and Signal Processing, 2012, 32, 349-358.*

[39] Colangeli, C.; Chiariotti, P. & Janssens, K. “Uncorrelated Noise Sources Separation Using Inverse Beamforming”. *Experimental Techniques, Rotating Machinery, and Acoustics, Volume 8, Springer, 2015, 59-70.*

[40] Gade, S.; Hald, J. & Ginn, K. “Wideband acoustical holography”. *Sound and Vibration, 2016, 50, 8-13.*

[41] Gomes, J. & Hansen, P. C. “A study on regularization parameter choice in near-field acoustical holography”. *Journal of the Acoustical Society of America, 2008, 123, 3385-3385.*

[42] Kim, Y. & Nelson, P. “Optimal regularisation for acoustic source reconstruction by inverse methods”. *Journal of sound and vibration, 2004, 275, 463-487.*

[43] Gauthier, P.-A.; Gerard, A.; Camier, C. & Berry, A. “Acoustical inverse problems regularization: direct definition of filter factors using Signal-to-Noise Ratio”. *Journal of Sound and Vibration, 2014, 333, 761-773.*

[44] Dong, B.; Antoni, J. & Zhang, E. “Blind separation of sound sources from the principle of least spatial entropy”. *Journal of Sound and Vibration, 2014, 333, 2643-2668.*

[45] Hansen, P. C. “Regularization tools: A Matlab package for analysis and solution of discrete ill-posed problems”. *Numerical algorithms, 1994, 6, 1-35.*

[46] Tomlinson, M. “Partial source discrimination in near field acoustic holography”. *Applied acoustics, 1999, 57, 243-261.*

[47] Nam K. & Kim Y. “A partial field decomposition algorithm and its examples for near-field acoustic holography”. *The Journal of the Acoustical Society of America, 2004, 116, 172-185.*

[48] Antoni, J. “Bayesian focusing - a unified approach to inverse acoustic radiation”. *ISMA Conference, 2010.*

[49] Antoni, J. “A Bayesian approach to sound source reconstruction: optimal basis, regularization, and focusing”. *The Journal of the Acoustical Society of America, 2012, 131, 2873-2890.*

[50] Antoni, J. “Bayesian vision of inverse problems in acoustics”. *NOVEM Conference, 2015.*

[51] Pereira, A.; Leclère, Q. & Antoni, J. “A theoretical and experimental comparison of the equivalent source method and a bayesian approach to noise source identification”. *Berlin Beamforming Conference, 2012.*

[52] Pereira, A. “Acoustic imaging in enclosed spaces”. *INSA de Lyon – PhD thesis, 2013.*

[53] Lamotte, L.; Minck, O.; Paillasseur, S.; Lanslot, J. & Deblauwe, F. “Interior Noise Source Identification With Multiple Spherical Arrays In Aircraft And Vehicle”. *20th ICSV Congress, 2013.*

[54] Haddad, K.; Hald, J.; “3D localization of acoustic sources with a spherical array”. *Euronoise Conference, Paris, 2008.*

[55] Tiana-Roig, E.; Torras-Rosell, A.; Fernandez-Grande, E.; Jeong, C.-H. & Agerkvist, F. T. “Enhancing the beamforming map of spherical arrays at low frequencies using acoustic holography”. *Berlin Beamforming Conference, 2014.*

[56] Fenech, B. A. & Takeda, K. “Towards more accurate beamforming levels in closed-section wind tunnels via de-reverberation”. *AIAA Paper, 2007, 3431.*

[57] Nau, C. “Beamforming within the modal sound field of a vehicle interior”. *Berlin Beamforming Conference, 2016.*

[58] Castellini, P. & Sassaroli, A. “Acoustic source localization in a reverberant environment by average beamforming”. *Mechanical Systems and Signal Processing, 2010, 24, 796-808.*

[59] Castellini, P.; Sassaroli, A.; Paonessa, A.; Peiffer, A. & Roeder, A. “Average beamforming in reverberant fields: Application on helicopter and airplane cockpits”. *Applied Acoustics, 2013, 74, 198-210.*

[60] Villot, M.; Chaveriat, G. & Roland, J. “Phonoscopy: An acoustical holography technique for plane structures radiating in enclosed spaces”. *The Journal of the Acoustical Society of America, 91, 187-195.*

[61] Tamura, M. “Spatial Fourier transform method of measuring reflection coefficients at oblique incidence. I: Theory and numerical examples”. *The Journal of the Acoustical Society of America, 1990, 88, 2259-2264.*

[62] Tamura, M.; Allard, J. F. & Lafarge, D. “Spatial Fourier-transform method for measuring reflection coefficients at oblique incidence. II. Experimental results”. *The Journal of the Acoustical Society of America, 1995, 97, 2255-2262.*

[63] Hallman, D.; Bolton, J.; Dumbacher, S.; Brown, D.; Libbey, B. & Lally, M. “Acoustic source location in vehicle cabins and free-field with nearfield acoustical holography via acoustic arrays”. *Proc. of the 19th International Seminar on Modal Analysis, Leuven, Belgium, September 1994.*

[64] Hald, J.; Nielsen, F. K. & Blaabjerg, C. “Patch NAH for noise source mapping in cabin environments”. *SAE Technical Paper, 2005.*

[65] Sklanka, B.; Tuss, J.; Buehrle, R.; Klos, J.; Williams, E. & Valdivia, N. “Acoustic Source Localization in Aircraft Interiors Using Microphone Array Technologies”. *12th AIAA/CEAS Conference, 2006, 10.2514/6.2006-2714.*

[66] Koopmann, G. H.; Song, L. & Fahnline, J. B. “A method for computing acoustic fields based on the principle of wave superposition”. *The Journal of the Acoustical Society of America, 1989, 86, 2433-2438.*

[67] Pereira, A.; Leclère, Q.; Lamotte, L.; Paillasseur, S. & Bleandonu, L. “Noise source identification in a vehicle cabin using an iterative weighted approach to the ESM method”. *ISMA Conference, 2012.*

[68] Schmitt, A.; Lamotte, L. & Deblauwe, F. “Source identification inside cabin using inverse methods”. *Berlin Beamforming Conference, 2010.*

[69] Jeans, R. & Mathews, I. “The wave superposition method as a robust technique for computing acoustic fields”. *The Journal of the Acoustical Society of America, 1992, 92, 1156-1166.*

[70] Wang, Z. & Wu, S. F. “Helmholtz equation--least-squares method for reconstructing the acoustic pressure field”. *The Journal of the Acoustical Society of America, 1997, 102, 2020-2032.*

[71] Wu, S. F. “Hybrid near-field acoustic holography”. *The Journal of the Acoustical Society of America, 2004, 115, 207-217.*

[72] Vigoureux, D.; Totaro, N.; Lagneaux, J. & Guyader, J.-L. “Inverse Patch Transfer Functions method as a tool for source field identification”. *Journal of Vibration and Acoustics, 2015, 137, 021006.*

[73] Aucejo, M.; Totaro, N. & Guyader, J.-L. “Identification of source velocities on 3D

structures in non-anechoic environments: Theoretical background and experimental validation of the inverse patch transfer functions method". Journal of Sound and Vibration, 2010, 329, 3691-3708.

[74] Totaro, N. & Guyader, J.-L. "Efficient positioning of absorbing material in complex systems by using the patch transfer function method". *Journal of Sound and Vibration, 2012, 331, 3130-3143.*

[75] Forget, S.; Totaro, N.; Guyader, J.-L. & Schaeffer, M. "A Noise Source Identification Method as an Analysis Support Technique to Improve NVH Performances of 3D Structures". *SAE Technical Paper, 2016.*

[76] Gajdatsy, P. "Advanced transfer path analysis methods". *KU Leuven, Department of Mechanical Engineering, PhD Thesis, 2011.*

[77] Gajdatsy, P.; Janssens, K.; Desmet, W. & Van Der Auweraer, H. "Application of the transmissibility concept in transfer path analysis". *Mechanical Systems and Signal Processing, 2010, 24, 1963-1976.*

[78] Van de Ponseele, P.; Van der Auweraer, H. & Janssens, K. "Source-Transfer-Receiver approaches: a review of methods". *ISMA Conference, Leuven, Belgium, 2012, 17-19.*

[79] Janssens, K.; Gajdatsy, P.; Gielen, L.; Mas, P.; Britte, L.; Desmet, W. & Van der Auweraer, H. "OPAX: A new transfer path analysis method based on parametric load models". *Mechanical Systems and Signal Processing, 2011, 25, 1321-1338.*

[80] Rissler, K. Applying the reciprocal Transfer Path Analysis (TPA) for the airborne sound of power train components". *Chalmers University of Technology, 2011.*

[81] Morgan, P.; Phillips, S. & Watts, G. "The localisation, quantification and propagation of noise from a rolling tyre". *TRL Limited, 2007.*

[82] Hald, J.; Tsuchiya, M.; Blaabjerg, C.; Ando, H.; Yamashita, T.; Kimura, M. & Ishii, Y. "Panel contribution analysis using a volume velocity source and a double layer array with the SONAH algorithm". *Internoise Conference, 2006, 1465-1474.*

[83] Verheij, J. W. "Inverse and Reciprocity Methods for Machinery Noise Source Characterization and Sound Path Quantification Part 1: Sources". *International Journal of Acoustics and Vibration, 1997.*

[84] Verheij, J. W. "Inverse and reciprocity methods for machinery noise source characterization and sound path quantification. Part 2: Transmission Paths".

International Journal of Acoustics and Vibration, 1997, 2, 103-112.

[85] Nelson, P. A. & Yoon, S.-H. “Estimation of acoustic source strength by inverse methods: Part I, conditioning of the inverse problem”. *Journal of sound and vibration, 2000, 233, 639-664.*

[86] Yoon, S.-H. & Nelson, P. A. “Estimation of acoustic source strength by inverse methods: Part II, experimental investigation of methods for choosing regularization parameters”. *Journal of sound and vibration, 2000, 233, 665-701.*

[87] Janssens, K.; Aarnoutse, P.; Gajdatsy, P.; Britte, L.; Deblauwe, F. & Van der Auweraer, H. “Time-domain source contribution analysis method for in-room pass-by noise”. *SAE Technical Paper, 2011.*

[88] Janssens, K. & Bianciardi, F. “Time-domain ASQ method for pass-by noise engineering”. *Internoise Conference, 2013, 246, 810-818.*

[89] Bianciardi, F.; Janssens, K.; Choukri, M. & van der Auweraer, H. “Indoor pass-by noise engineering: a motorbike application case”. *JSAE Symposium, 2014, 20145419.*

[90] Vercammen, S.; Kindt, P.; Bianciardi, F. & Desmet, W. “Noise rariation analysis of a loaded and rotating slick tyre on a rough road surface”.

[91] Hartmann, M.; Ocker, J.; Lemke, T.; Mutzke, A.; Schwarz, V.; Tokuno, H.; Toppinga, R.; Unterlechner, P. & Wickern, G. “Wind Noise caused by the A-pillar and the Side Mirror flow of a Generic Vehicle Model”. *18th AIAA/CEAS Aeroacoustic Conference, 2012, 2205.*

[92] Badaoui, M. E.; Daniere, J.; Guillet, F. & Servière, C. “Separation of combustion noise and piston-slap in diesel engine—Part I: Separation of combustion noise and piston-slap in diesel engine by cyclic Wiener filtering”. *Mechanical Systems and Signal Processing, 2005, 19, 1209-1217.*

[93] Wyckaert, K.; Augusztinovicz, F. & Sas, P. “Vibro-acoustical modal analysis: Reciprocity, model symmetry, and model validity”. *The Journal of the Acoustical Society of America, 1996, 100, 3172-3181.*

[94] Yoshimura, T.; Saito, M.; Maruyama, S. & Iba, S. “Modal analysis of automotive cabin by multiple acoustic excitation”. *ISMA Conference, Leuven, Belgium, 2012.*

[95] Tsuji, H.; Maruyama, S.; Yoshimura, T. & Takahashi, E. “Experimental method extracting dominant acoustic mode shapes for automotive interior acoustic field coupled with the body structure”. *SAE International Journal of Passenger Cars-*

Mechanical Systems, 2013, 6, 1139-1146.

[96] Peeters, B.; El-Kafafy, M.; Accardo, G.; Knechten, T.; Janssens, K.; Lau, J. & Gielen, L. "Automotive cabin characterization by acoustic modal analysis". *JSAE Annual Congress, 2014, 114-20145437.*

[97] El-Kafafy, M.; Accardo, G.; Peeters, B.; Janssens, K.; De Troyer, T. & Guillaume, P. "A fast maximum likelihood-based estimation of a modal model". *Topics in Modal Analysis, Volume 10, Springer, 2015, 133-156.*

[98] Accardo, G.; El-Kafafy, M.; Peeters, B.; Bianciardi, F.; Brandolisio, D.; Janssens, K. & Martarelli, M. "Experimental acoustic modal analysis of an automotive cabin". *Experimental Techniques, Rotating Machinery, and Acoustics, Volume 8, Springer, 2015, 33-58.*

[99] Accardo, G.; Chiariotti, P.; Cornelis, B.; El-kafafy, M.; Peeters, B.; Janssens, K. & Martarelli, M. "Experimental acoustic modal analysis of an automotive cabin: challenges and solutions". *ISMA Conference, 2016.*

[100] Kinsler, L. E.; Frey, A. R.; Coppens, A. B. & Sanders, J. V. "Fundamentals of acoustics". *4th Edition, ISBN 0-471-84789-5. Wiley-VCH, 1999.*

[101] Muller T.J. "Aeroacoustic measurements". *Springer, 2002.*

[102] Petersen, E. C. "An Overview of Standards for Sound Power Determination". *Brüel & Kjær, 1995.*

[103] Zavala, P. A.; De Roeck, W.; Janssens, K.; Arruda, J. R.; Sas, P. & Desmet, W. "Monopole and dipole identification using generalized inverse beamforming". *16th AIAA/CEAS Conference, 2010, 2010-3740.*

[104] Zavala, P.; Janssens, K. & Arruda, J. "Dipole source identification on subsonic airflow through structures". *ISMA Conference, 2012.*

[105] Suzuki, T. "L1 generalized inverse beam-forming algorithm resolving coherent/incoherent, distributed and multipole sources". *Journal of Sound and Vibration, 2011, 330, 5835-5851.*

[106] Griveaux, M. & Martin, V. "Model selection in inverse acoustic problems". *NOVEM Conference, 2015.*

[107] Sarradj, E. "A fast signal subspace approach for the determination of absolute levels from phased microphone array measurements". *Journal of Sound and*

Vibration, 2010, 329, 1553-1569.

[108] Oerlemans, S. & Sijtsma, P. "Determination of absolute levels from phased array measurements using spatial source coherence". AIAA paper, 2002-2464, 2002.

[109] Ben-Israel, A. & Greville, T. N. "Generalized inverses: theory and applications". *Springer Science & Business Media, 2003, 15.*

[110] Rakha, M. A. "On the Moore--Penrose generalized inverse matrix". *Applied Mathematics and Computation, 2004, 158, 185-200.*

[111] Hansen, P. C. "The truncated svd as a method for regularization". *BIT Numerical Mathematics, 1987, 27, 534-553.*

[112] Dougherty, R. P. "Improved generalized inverse beamforming for jet noise". *International Journal of Aeroacoustics, 2012, 11, 259-289.*

[113] Zavala, P. "Aeroacoustic source and moving source identification". *PhD thesis, Faculty of Mech. Eng., University of Campinas, Sao Paulo, 2012.*

[114] Zavala, P.; De Roeck, W.; Janssens, K.; Arruda, J.; Sas, P. & Desmet, W. "Aeroacoustic source identification using generalized inverse beamforming". *ISMA Conference, 2010.*

[115] Zavala, P. A.; De Roeck, W.; Janssens, K.; Arruda, J. R.; Sas, P. & Desmet, W. "Generalized inverse beamforming investigation and hybrid estimation". *Berlin Beamforming Conference, 2010.*

[116] Harker, B. M.; Gee, K. L. & Neilsen, T. B. "Application of beamforming methods to extended partially correlated sources". *Berlin Beamforming Conference, 2016.*

[117] Sas, Q. Y. P. & Van der Auweraer, D. O. H. "Estimation of the number of uncorrelated sources by means of time series modelling". *12th IMAC Conference, 1994, 1, 310.*

[118] Guillaume, P.; Parloo, E. & De Sitter, G. "Source identification from noisy response measurements using an iterative weighted pseudo-inverse approach". *ISMA Conference, 2002.*

[119] Golub, G. H.; Heath, M. & Wahba, G. "Generalized cross-validation as a method for choosing a good ridge parameter". *Technometrics, 1979, 21, 215-223.*

[120] Hansen, P. C. & O'Leary, D. P. "The use of the L-curve in the regularization of discrete ill-posed problems". *SIAM Journal on Scientific Computing, 1993, 14,*

1487-1503.

[121] Magalhaes, M. B. S. & Tenenbaum, R. A. "Sound sources reconstruction techniques: A review of their evolution and new trends". *Acta Acustica united with Acustica, 2004, 90, 199-220.*

[122] Schuhmacher, A.; Hald, J.; Rasmussen, K. B. & Hansen, P. C. "Sound source reconstruction using inverse boundary element calculations". *The Journal of the Acoustical Society of America, 2003, 113, 114-127.*

[123] Pereira, A.; Antoni, J. & Leclère, Q. "Empirical Bayesian regularization of the inverse acoustic problem". *Applied Acoustics, 2015, 97, 11-29.*

[124] Bianciardi, F.; Janssens, K. & Britte, L. "Critical assessment of OPA: effect of coherent path inputs and SVD truncation". *20th ICSV Congress, 2013.*

[125] Nam, K. & Kim, Y. "Visualization of multiple incoherent sources by the backward prediction of near-field acoustic holography". *The Journal of the Acoustical Society of America, 2001, 109, 1808-1816.*

[126] Dong, B. & Antoni, J. "Blind Separation of Uncorrelated Sound Sources from the Principle of Least Spatial Complexity". *19th ICSV Congress, 2012.*

[127] Dong, B.; Antoni, J.; Pereira, A. & Kellermann, W. "Blind separation of incoherent and spatially disjoint sound sources". *Journal of Sound and Vibration, 2016, 383, 414-445.*

[128] Allemang, R. J. "The modal assurance criterion - twenty years of use and abuse". *Sound and vibration, 2003, 37, 14-23.*

[129] Bishop, C. M. "Pattern recognition and machine learning". *Springer, 2006, 128.*

[130] Jain, A. K.; Duin, R. P. W. & Mao, J. "Statistical pattern recognition: A review" *IEEE Transactions on pattern analysis and machine intelligence, 2000, 22, 4-37.*

[131] Mudrova, M. & Prochazka, A. "Principal component analysis in image processing". *MATLAB Technical Computing Conference, Prague, 2005.*

[132] Colangeli, C.; Chiariotti, P.; Janssens, K. & Castellini, P. "A microphone clustering approach for improved Generalized Inverse Beamforming formulation". *NOVEM Conference, 2015, 48984.*

[133] Parzen, E. "On estimation of a probability density function and mode". *The annals*

of mathematical statistics, JSTOR, 1962, 33, 1065-1076.

[134] Tanaka, T.; Shimada, A.; Arita, D. & Taniguchi, R.-i. "A fast algorithm for adaptive background model construction using Parzen density estimation". *IEEE Conference on Advanced Video and Signal Based Surveillance, 2007, 528-533.*

[135] Bowman, A. W. & Azzalini, A. "Applied smoothing techniques for data analysis: the kernel approach with S-Plus illustrations". *OUP Oxford, 1997, 18.*

[136] Colangeli, C.; Chiariotti, P.; Battista, G.; Castellini, P. & Janssens, K. "Clustering inverse beamforming for interior sound source localization application to a car cabin mock-up". Berlin Beamforming Conference, 2016.

[137] Guidati, S.; Sottek, R.; "Advanced Source Localization Techniques Using Microphone Arrays". *SAE - Mechanical Systems, 2011.*

[138] Elias, G. "Source localization with a two-dimensional focused array: optimal signal processing for a cross-shaped array". *Office national d'études et de recherches aérospatiales, 1995.*

[139] Lamotte, L.; Beguet, B.; Cariou, C. & Delverdier, O. "Qualifying the noise sources in term of localization and quantification during flight tests". EUCASS Conference, 2009.

[140] Beguet B. & Lamotte L. "Device for localizing acoustic sources and measuring their intensities". Patent Pub. No.: US 2007/0172078 A1, 26/07/2007.

[141] Stock, M.; Pasler, M.; Birkfellner, W.; Homolka, P.; Poetter, R. & Georg, D. "Image quality and stability of image-guided radiotherapy (IGRT) devices: A comparative study". *Radiotherapy and Oncology, 2009, 93, 1-7.*

[142] Lamotte, L.; Robin, M. & Deblauwe, F. "Noise mapping and sound quantification in the space using spherical array". *Euronoise Conference, 2009.*

[143] Accardo, G.; Cornelis, B.; Janssens, K.; Peeters, B.; Chiariotti, P. & Martarelli, M. "A non-line-of-sight identification algorithm in automatic microphone localization for experimental acoustic modal analysis". *Internoise Conference, San Francisco, USA, 2015.*

[144] Accardo, G.; Cornelis, B.; Janssens, K. & Peeters, B. "Automatic microphone localization inside a car cabin for experimental acoustic modal analysis". *ICSV Congress (Florence, Italy), 2015.*

[145] Verheij, J. W. “Inverse and reciprocity methods for machinery noise source characterization and sound path quantification. Part 2: Transmission Paths”. *International Journal of Acoustics and Vibration, 1997, 2, 103-112.*

[146] Leclère, Q. & Hamzaoui, N. “Using the moving synchronous average to analyze fuzzy cyclostationary signals”. *Mechanical Systems and Signal Processing, 2014, 44, 149-159.*

[147] Cardenas Cabada, E.; Hamzaoui, N.; Leclère, Q. & Antoni, J. “Acoustic imaging applied to fault detection on a rotating machine bench”. *ISMA Conference, 2016.*

[148] Antoni, J.; Abboud, D. & Xin, G. “Cyclostationarity in Condition Monitoring: 10 years after”. *ISMA Conference, 2016.*

[149] Braun, S. “Discover signal processing: An interactive guide for engineers”. *John Wiley & Sons, 2008.*

[150] Jain, A. K.; Duin, R. P. W. & Mao, J. “Statistical pattern recognition: A review”. *IEEE Transactions on pattern analysis and machine intelligence, 2000, 22, 4-37.*

[151] Johnson, D. H. & Dudgeon, D. E. “Array signal processing: concepts and techniques”. *Simon & Schuster, 1992.*